KU LEUVEN

SCK•CEN
STUDIECENTRUM VOOR KERNENERGIE
CENTRE D'ETUDE DE L'ENERGIE NUCLEAIRE

LOW-TEMPERATURE OXIDATION OF FINE UO_2 POWDERS

Gregory Leinders

Supervisors:

Prof. Dr. Koen Binnemans, KU Leuven
Prof. Dr. Thomas Cardinaels, SCK•CEN

Members of the Examination Committee:

Prof. Dr. Luc Van Meervelt, KU Leuven
Prof. Dr. Tatjana N. Parac-Vogt, KU Leuven
Prof. Dr. Ir. Jozef Vleugels, KU Leuven
Prof. Dr. Gustaaf Van Tendeloo, UAntwerpen
Dr. Marc Verwerft, SCK•CEN

Dissertation presented in partial fulfilment of the requirements for the degree of PhD in Chemistry

© 2016 KU Leuven, Science, Engineering & Technology
Uitgegeven in eigen beheer, Gregory Leinders, Leuven, Belgium

Alle rechten voorbehouden. Niets uit deze uitgave mag worden vermenigvuldigd en/of openbaar gemaakt worden door middel van druk, fotokopie, microfilm, elektronisch of op welke andere wijze ook zonder voorafgaandelijke schriftelijke toestemming van de uitgever.

All rights reserved. No part of the publication may be reproduced in any form by print, photoprint, microfilm, electronic or any other means without written permission from the publisher.

Acknowledgments

Looking back at the past four years I realize that the completion of the book in your hands has only been possible by the collaboration of many people. I could have never accomplished this work without the guidance and support that I have received, nor the laughter and tears I have shared. Many people are to thank, and to those not mentioned here explicitly I repeat what I hopefully have already said to you personally: Thank You!

My PhD research could not have been realized without the financial support of SCK•CEN. I am grateful for the confidence the SCK•CEN Academy has shown in my candidacy. Furthermore, I would like to thank my university promoter Prof. Dr. Koen Binnemans for sharing his knowledge, and for helping with the organization of the thesis. Your comments have been invaluable for the completion of this work. To my co-promoter Prof. Dr. Thomas Cardinaels I would like to express my gratitude for helping me navigate throughout the journey. You showed me to conduct scientific research as an independent scientist. My sincere thanks go to Dr. Marc Verwerft. Your interest and enthusiasm has been an indispensable motivator to pursue my goals. The synergy of all of you have allowed me to succeed on this mission.

The contribution of my assessors within the supervisory committee, Prof. Dr. Tanja Vogt and Prof. Dr. Ir. Jef Vleugels, has been greatly appreciated. Your constructive comments encouraged me to question the statements I presented, and to improve the quality of the work.

I wish to thank all my dear colleagues from the FMA group, and especially: My "big sister" Dr. Angela Baena, for sharing a lot of joy, experience, and cookies; Dr. Janne Pakarinen and Dr. Rémi Delville, for spending countless hours in solitary confinement behind the microscope; Koen Vanaken and Peter Dries, for assisting in the laboratory. The experimental work could also not have been performed without the dedication of people in the MNA, RCA and HPH groups: Many thanks!

The award for most caring and loving person undoubtedly goes to my girlfriend. Meid, thanks for your patience and support, I could not have imagined a better soon-to-be wife. To the three musketeers from Neeroeteren: Rob, Dom, Niels, thanks for relieving me with regular intervals from the world of numbers and letters. Kristof and Natalia, my fellow Hasselaren, thanks for the relaxing evenings, and also the not-so-relaxing exercise sessions in the park. Kris, thank you for listening to my scientific tales, and for reminding me of the beauty that awaits outside. And last but not least I want to thank Choufleur for keeping me company when working from home.

Bedankt mama en papa om alle jaren zo goed voor me gezorgd te hebben. Jullie hebben mijn broers en mij de kans gegeven om te kunnen verder studeren. Geoffrey en Laurens, bedankt voor de nodige afleiding wanneer het nodig was. Aan mijn fijne schoonouders Carlo en Patricia: Bedankt voor al jullie steun en het onderdak dat jullie me gegeven hebben. Peetje, door alle jaren heen heb ook jij me gesteund, bedankt om zo'n goede meter voor me te willen zijn. Tenslotte wil ik graag alle grootouders bedanken: Make en bompa, grote oma, opa en oma, … jullie liefde heeft ons allemaal grootgebracht.

Abstract

Globally the most used nuclear fuel material is uranium(IV) oxide (UO_2) which is produced by powder metallurgical processing. Powders are first compacted into cylindrical pellets, and are subsequently sintered at high temperature to increase their density. The UO_2 nuclear fuel cycle is also inseparable from wet-chemical routes: uranium is leached from ore bodies and is further purified via, for example, ion exchange or solvent extraction techniques. Additionally, used nuclear fuel can be reprocessed to separate the elements which contain fissile nuclides (U, Pu) from the fission products. Such reprocessing involves the dissolution of used fuel. Ultimately, the compounds produced via wet-chemical routes −irrespective of their nature, "fresh" or reprocessed− are converted into fine oxide powders.

UO_2 powder shows a tendency to react with oxygen, especially if the grains have a high specific surface area. Uncontrolled uptake of oxygen is usually undesirable in the fuel production stage, and in very fine UO_2 powders exposure to normal air at room temperature may even lead to a pyrophoric reaction. Passivation treatments are required to decrease the reactivity of such UO_2 powders. Additionally, if oxidation can proceed continuously the higher oxide U_3O_8 is formed, and this crystallographic transformation is associated with a volume increase of about 36%. Such a volume increase can result in rupture of storage containers or vessels when not accounted for. Evidently, the reactivity of UO_2 towards oxygen may pose a risk. Despite continued research in this domain the oxidation process is still not completely understood, especially in fine powders and at low temperatures (< 100 °C).

In this PhD thesis the reaction between UO_2 and oxygen has been investigated under conditions related to nuclear fuel production and to storage of UO_2 powders and pellets. The research focused on assessing the crystal structure of the different phases which are formed, and also evaluated the mechanisms and kinetics involved in the oxidation reaction. Results of this study allow a better understanding of the issues related to UO_2 oxidation, and can be applied to improve the handling of UO_2 powders and to evaluate the effects of storage conditions.

The crystal structure of UO_2, seen as the reference state throughout the research, was first investigated. A discrepancy was found with reported values of the unit cell lattice parameter. Therefore, high-quality UO_2 samples were prepared which allowed accurate measurement of the lattice parameter via X-ray diffraction. An improved, more precise value was reported which replaces the existing "generally accepted" value dating from the 1950s.

An important intermediate uranium oxide is U_3O_7. It is the main precursor for U_3O_8 formation at temperatures below 350 °C. However, the crystal structure of U_3O_7 remains subject to debate. Polycrystalline U_3O_7 powders were therefore prepared and investigated using X-ray and selected-area electron diffraction techniques. A comprehensive analysis revealed that the crystal structure consists of fluorite-type ordered uranium and oxygen atoms as in UO_2, with excess anions grouped in so-called cuboctahedral oxygen clusters and forming a long-range ordered defect structure.

At temperatures below 100 °C the oxidation reaction is not well understood. To shed more light on this temperature domain, fine UO_2 powders were oxidized at temperatures ranging from 40 °C to 250 °C and with a different oxygen content in the gas supply. The oxidation process was followed *in-situ* by simultaneous thermal analysis and the oxidized powders were subsequently analyzed using X-ray diffraction and high-resolution transmission electron microscopy. The initial oxidation reaction is characterized as a rapid chemisorption reaction, corresponding with formation of an amorphous phase on the surface of the grains. As the extent of the oxidation reaction increases different kinetic regimes are distinguished, and separate higher oxides form as nanosized domains throughout the grains.

Samenvatting

De meest gebruikte kernbrandstof wereldwijd is uranium(IV) oxide (UO_2). Deze wordt geproduceerd via poeder-metallurgische processen. Poeders worden eerst samengeperst in cilindervormige pillen waarna deze op hoge temperatuur worden gesinterd om een hoge dichtheid te bekomen. De UO_2 brandstofcyclus is onafscheidelijk verbonden met nat-chemische processen: uranium wordt uit ertsen geloogd en verder opgezuiverd via, bijvoorbeeld ionenuitwisseling of solventextractie. Gebruikte kernbrandstof kan ook verder verwerkt worden om de elementen met splijtbare nucliden af te scheiden van de andere fissieproducten. Tijdens zulke verwerkingsprocessen wordt de gebruikte brandstof opnieuw opgelost. Uiteindelijk worden de producten die via nat-chemische weg gevormd zijn −onafhankelijk of ze van "vers" of herwerkt uranium afkomstig zijn− omgevormd tot fijne oxidepoeders.

UO_2 poeders vertonen de neiging om te reageren met zuurstof, vooral als de korrels een hoog specifiek oppervlak hebben. Ongecontroleerde opname van zuurstof is meestal niet wenselijk tijdens de productie van kernbrandstof. In zeer fijne UO_2 poeders kan een pyrofore reactie optreden na blootstelling aan lucht en dit reeds bij kamertemperatuur. De reactiviteit van zulke poeders kan verminderd worden door ze te passiveren. Als oxidatie onbeperkt kan optreden, wordt uiteindelijk het hogere oxide U_3O_8 gevormd en bij deze kristallografische overgang treedt een volume expansie van ongeveer 36% op. Wanneer geen rekening wordt gehouden met deze uitzetting bestaat het risico dat opslagcontainers scheuren. Het is duidelijk dat de reactiviteit van UO_2 tegenover zuurstof een risico vormt. Hoewel in dit domein reeds lange tijd onderzoek gedaan wordt, is het oxidatieproces nog steeds niet volledig begrepen, vooral niet voor fijne poeders en bij lage temperaturen (< 100 °C).

In dit doctoraatsonderzoek werd de reactie tussen UO_2 en zuurstofgas onderzocht onder dezelfde omstandigheden als die van toepassing zijn bij de productie van kernbrandstoffen en bij de opslag van UO_2 poeders en pillen. De focus van het onderzoek lag bij de kristalstructuur van de verschillende fasen die gevormd kunnen worden en er werd tevens een evaluatie gemaakt van de oxidatiemechanismen en de kinetica van het proces. De resultaten van deze studie dragen bij tot een beter begrip van de moeilijkheden gerelateerd aan de oxidatie van UO_2. Ze kunnen worden toegepast om het verwerken van UO_2 poeders te verbeteren en om de omstandigheden voor opslag te evalueren.

De kristalstructuur van UO_2, dewelke als de referentietoestand gezien wordt doorheen het onderzoek, werd eerst bestudeerd. Er werd een tegenstrijdigheid vastgesteld tussen de verschillende vroeger gerapporteerde waarden van de roosterparameter. Daarom

werden UO_2 stalen van hoge kwaliteit aangemaakt, die toelieten om de roosterparameter nauwkeurig te bepalen via X-stralendiffractie. Een verbeterde en meer precieze waarde werd gerapporteerd en deze vervangt de huidige “algemeen aangenomen” waarde die dateert uit de jaren 1950.

Een belangrijk intermediair uraniumoxide is U_3O_7. Het is de voornaamste precursor voor de vorming van U_3O_8 bij temperaturen lager dan 350 °C. De kristalstructuur van U_3O_7 is echter nog niet tot in de details beschreven. Polykristallijne U_3O_7 poeders werden om deze reden aangemaakt en onderzocht door middel van X-stralendiffractie en elektronendiffractie in geselecteerde oppervlakken. Uitgebreide analyse toonde aan dat de kristalstructuur uit een fluoriet-soort ordening van uranium- en zuurstofatomen bestaat, gelijkaardig als in UO_2, maar waarbij toegevoegde anionen gegroepeerd zitten in zogenoemde kuboctaëder zuurstofclusters dewelke aanleiding geven tot een lang-periodisch geordende structuur.

De oxidatiereactie is nog niet goed begrepen bij temperaturen lager dan 100 °C. Om meer duidelijkheid te verkrijgen in dit temperatuurgebied werden fijne UO_2 poeders geoxideerd bij temperaturen tussen 40 °C en 250 °C en ook bij verschillende zuurstofconcentraties in de gastoevoer. Het oxidatieproces werd *in-situ* opgevolgd door gelijktijdige thermische analyse en de geoxideerde poeders werden vervolgens geanalyseerd door X-stralendiffractie en hoge-resolutie transmissie elektronen microscopie. De initiële oxidatiereactie wordt gekarakteriseerd als een snelle chemisorptie reactie, waarbij er een amorfe fase gevormd wordt op het oppervlak van de korrels. Bij meer vergevorderde oxidatie worden verschillende kinetische regimes onderscheiden, en afzonderlijke hogere oxides worden gevormd in domeinen doorheen de korrels op een nanoschaal.

Table of contents

List of abbreviations

ADU	Ammonium diuranate
ALARA	As low as reasonably achievable
ASTM	American Society for Testing and Materials
AUC	Ammonium uranyl carbonate
BET theory	Brunauer, Emmett, Teller theory
BF	Bright field
BR1	Belgian Reactor 1
CCD	Charge-coupled device
DSC	Differential scanning calorimetry
EELS	Electron energy loss spectroscopy
FBFC	Franco-Belge de Fabrication du Combustible
FFT	Fast Fourier transform
FOM	Figure of merit
FWHM	Full width at half-maximum
$\Delta G_f°$	Standard Gibbs free energy of formation
GWd/t	Gigawatt-days per metric ton of heavy metal
$\Delta H_f°$	Standard enthalpy of formation
HR-TEM	High-resolution transmission electron microscopy
IAEA	International Atomic Energy Agency
ICPMS	Inductively coupled plasma-mass spectroscopy
IDR	Integrated dry route
kBq g^{-1}	KiloBecquerel per gram
LEU	Low-enriched uranium
LFF	Long fine focus
LWR	Light-water reactor
MeV	Megaelectron-volt
MIMAS	Micronized master blend
MOX fuel	Mixed oxide fuel
MW	Megawatt (10^6 Watt)
NIST	National Institute of Standards and Technology
O/U	Molar O-to-U ratio
PUREX	Plutonium uranium extraction
PWR	Pressurized-water reactor

RU	Reprocessed uranium
S°	Standard molar entropy
SAED	Selected area electron diffraction
SCK•CEN	Studiecentrum voor Kernenergie, Centre d'étude de l'Energie Nucléaire
SE	Secondary electron
SEM	Scanning electron microscopy
SG	Space group
SSA	Specific surface area
SSG	Superspace group
STA	Simultaneous thermal analysis
TBP	Tri(*n*-butyl)phosphate
TD	Theoretical density
TEM	Transmission electron microscopy
TGA	Thermogravimetric analysis
TIMS	Thermal ionization mass spectroscopy
vol.%	Volume percent
wt.%	Weight percent
XPS	X-ray photoelectron spectroscopy
XRD	X-ray diffraction
Z	Atomic number

Chapter 1.

Introduction

1.1 Uranium dioxide as nuclear fuel

1.1.1 Nuclear fission

Nuclear fission is the reaction during which the nucleus of an atom splits into several (in most cases two) smaller fragments, thereby releasing a very large amount of energy. The process was demonstrated on uranium (actually on the ^{235}U isotope) by German chemists Otto Hahn and Fritz Strassmann in 1938,[1] following the experimental work of the group of Enrico Fermi in the 1930's.[2] The physics of the fission process was interpreted shortly afterwards by Lise Meitner and Otto Frisch in 1939.[3, 4] For their role in the discovery of nuclear reactions with neutrons and the fission of heavy nuclei, Enrico Fermi and Otto Hahn were awarded the Nobel Prize in Physics (1938) and in Chemistry (1944), respectively.[5, 6]

Spontaneous fission occurs in some of the natural isotopes of thorium and uranium, however its probability is extremely low.[7] Alternatively, fission can be induced by bombarding the nucleus of an atom with neutrons. The process is generally described in three stages (shown schematically in Figure 1.1): (1) absorption of a neutron by the nucleus, (2) oscillation of the unstable compound nucleus formed, (3) fission of the compound nucleus into several fission fragments and release of neutrons, gamma radiation, and a very large amount of energy.

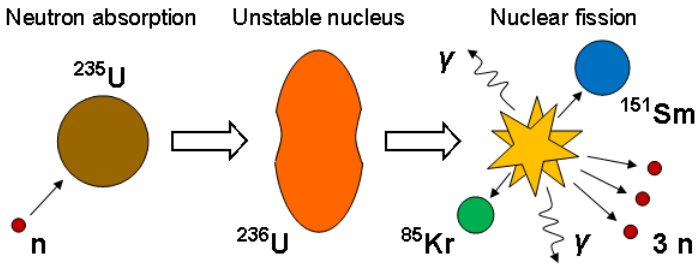

Figure 1.1. Schematic overview of the neutron induced nuclear fission reaction in a ^{235}U nucleus.

The fission process is a statistical nuclear reaction and is generally explained via the liquid-drop model proposed by Niels Bohr.[8] Fission of a ^{235}U nucleus induced by thermal neutrons (discussed further) yields, on average, two smaller fragments (fission products) which can have atomic masses distributed in the range 80−110 and 130−150.[9] Additionally, two or three neutrons are ejected and gamma radiation is released.[10] The corresponding energy release adds up to about 200 MeV per fission event, most (~160 MeV) in the form of kinetic energy of the fission fragments.[4] The associated energy from mass defect considerations between original nucleus and the sum of the newly formed fragments was the first experimental proof of the equivalency between mass and energy as put forward by Albert Einstein in 1905.[11, 12]

The probability for fission depends on the type of nucleus involved and energy of the bombarding neutron.[13] Newly-created fission neutrons typically have energies in the MeV range. Nuclei having an even number of neutrons (e.g. ^{232}Th, ^{238}U, ^{240}Pu) are only fissionable by such highly energetic ”fast” neutrons.[10] On the other hand, elements containing an uneven number of neutrons (e.g. ^{233}U, ^{235}U, ^{239}Pu) also have a fission probability with neutrons which are moderated to lower energies (“slow” or thermal neutrons). Importantly, the probability for nuclear interaction is significantly higher for thermal neutrons, as compared to fast neutrons.[9] Of all naturally occurring isotopes, the ^{235}U isotope is the only one capable to undergo induced fission by thermal neutrons.

A sustainable chain reaction can occur in a sufficiently large body of fissile material when fission yields multiple neutrons. In July 1941 a UK committee, codename MAUD, under direction of prime minister Winston Churchill published two reports stating that the nuclear fission reaction of uranium may be used in a bomb, as well as a source of power.[11] At that time, during World War II, research on the bomb project was pursued in the UK. In the USA research was initially focused on the nuclear power aspect (for example in naval applications), despite earlier attempts by physicist Leó Szilárd to convince the US government of the necessity for research on the bomb project (e.g. his request to Albert Einstein for writing a letter to President Roosevelt).[11] However, in the aftermath of the attacks on Pearl Harbor in December 1941, huge resources were applied without reservation to develop atomic bombs. Nuclear fission research in the USA soon took the lead under the Manhattan project.

The potential for nuclear energy was sadly demonstrated by the deployment of two USA-developed nuclear bombs, detonated over the cities of Hiroshima and Nagasaki (Japan) in 1945. After these events and following the end of World War II the world became divided in two fronts (the capitalist west and communist east), and embarked in a nuclear arms race during the era known as the Cold War. Over 2000 nuclear bomb tests were carried out over the course of 50 years.[14]

The nuclear fission related research fortunately also resulted in the development of various nuclear reactor designs for commercial power production and research purposes. One typically categorizes nuclear reactors based on the moderator and coolant type, each reactor type using a specifically designed nuclear fuel. Belgium’s first nuclear research reactor, the BR1 in Mol (Figure 1.2) which has been operating since 1956, is a graphite-moderated, air-cooled reactor which uses natural metallic uranium as fuel.[15] A second research reactor, the BR2, became critical for the first time in 1962 and is a water moderated and cooled reactor which uses a uranium-aluminum alloy with high enrichment (89−93% ^{235}U) as fuel elements.[16] An experimental low-power reactor, VENUS, was commissioned in 1964 as a water-moderated type, but underwent a major modification in 2008 and is now operating as a fast lead reactor (VENUS-F) to support R&D of future reactor types.[17]

Figure 1.2. The BR1 reactor in Mol with a close up of the platform for loading and unloading of the reactor. Platforms shown on the right give also access to the top of the reactor for maintenance purposes. Reproduced with permission of SCK•CEN.

West-Europe's first demonstration commercial power reactor was also built in Mol (the BR3), and supplied electricity to the grid from 1962 to 1987.[18] It was a USA-designed Light-Water Reactor (LWR) of the subtype Pressurized-Water Reactor (PWR), which used normal, pressurized water both as moderator and as coolant. The BR3 was used as a test reactor for prototype nuclear fuels and served as an education center for the operating personnel of nuclear power plants. The plant is currently being decommissioned. In addition to these research reactors, seven PWR-type commercial power reactors (four in Doel, three in Tihange) are currently operational in Belgium, generating about 55% of the electricity demand.[19] Nuclear fuel of such reactors consists of either low-enriched ^{235}U (3−5%) uranium(IV) oxide (UO_2) or mixed uranium-plutonium oxide (MOX), see also section 1.1.2.

Oxide-based compounds, and more specifically UO_2, have been used as principal type of nuclear fuel material, and they remain widely used today.[20] Ceramic materials in general show a higher corrosion resistance with respect to the coolant as compared to metals, and high physical stability (i.e. a limited amount of swelling under irradiation).[20] The oxides in particular present very high melting points (> 2000 °C), but their inherent low thermal conductivity limits the working temperature of the fuel elements. For this reason other types of ceramics such as carbides, nitrides and silicides have also been considered.[21] Of the non-metal atoms in the possible ceramic fuel materials, oxygen shows the lowest tendency to absorb thermal neutrons,[a] which would otherwise decrease the efficiency of the chain reaction.[13]

Data compiled by the World Nuclear Association for the year 2014 show that nuclear energy accounted for 11.5% of the world's electricity generation.[22] About 80% of the

[a] The tendency for neutron absorption by a given nuclide is expressed by its thermal neutron cross-section, having unit barn: ^{16}O = 0.0002 barn, ^{12}C = 0.0045 barn, ^{14}N = 1.78 barn, ^{28}Si = 0.13 barn.

nuclear capacity is provided by LWR's (60% PWR, 40% other types) which are loaded with UO_2 or MOX fuel.[23] At the time of writing this PhD thesis (2016) about 440 nuclear power reactors are in use around the world, with 65 reactors still under construction and another 173 scheduled to start construction in the coming years.[22] UO_2-based nuclear fuels form the basis for operating most of these reactors, and its production cycle will be discussed in more detail in the following section.

1.1.2 UO_2 nuclear fuel cycle

The nuclear fuel cycle is the whole of processing steps for the production of nuclear energy, starting from the mining of the ore and ending with disposal of the final waste. One distinguishes between the front end and the back end of the cycle.[24] The front end envisages the steps related to the production of nuclear fuel, while the back end involves the steps after irradiation of the nuclear fuel. The UO_2 nuclear fuel cycle is presented schematically in Figure 1.3. One considers open fuel cycles (once through, no reprocessing) and closed fuel cycles including reprocessing and recycling of U and Pu. Each process step will be discussed more in detail in the following paragraphs.

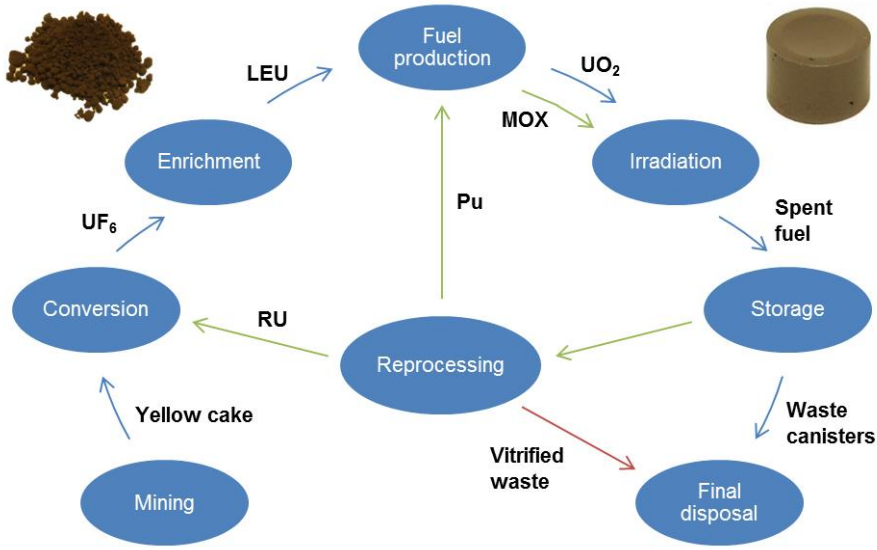

Figure 1.3. UO_2 nuclear fuel cycle. A detailed description of the various process steps is given in the text. Used acronyms: uranium hexafluoride (UF_6), low-enriched uranium (LEU), uranium dioxide (UO_2), mixed-oxide fuel (MOX), reprocessed uranium (RU).

Mining: Uranium is a naturally occurring element found in minerals such as pitchblende (= uraninite) and schoepite, but also dissolved in sea water.[25, 26] Its

concentration in the Earth's crust extends from as little as 1 ppm to over 500,000 ppm (50 wt.%) in some pitchblende deposits.[24] Uranium was discovered by the German chemist Martin Heinrich Klaproth (1789), who named it after the planet Uranus.[27] In nature it exists as a mixture of three isotopes: ^{234}U, ^{235}U and ^{238}U. The average abundance of these nuclides are 0.0054(5)%, 0.7204(6)% and 99.274(1)%, respectively.[28] Uranium is always encountered in its (partially) oxidized form, see also section 1.2.2.

Minerals which contain over 350 ppm U in weight may be considered ore bodies, depending on the ease of extraction.[24] Australia currently holds the largest reserves of uranium resources.[29] Uranium ores were conventionally gathered by excavation, either via open pit or underground mining. The uranium itself, along with some other impurity elements, was then extracted in a leaching operation (typically using sulfuric acid, Eq. (1.1)).[30] Nowadays, direct *in situ* leaching of the ore bodies is the preferred method, and uranium-containing waste streams are also obtained as a byproduct from, for example, gold mining.[31]

$$2\,U_3O_8 + O_2 + 6\,H_2SO_4 \rightarrow 6\,UO_2^{2+} + 6\,SO_4^{2-} + 6\,H_2O \qquad \textbf{(1.1)}$$

Purified uranium solutions are recovered from leach liquors using methods such as ion exchange and solvent extraction.[31] Solid uranium compounds are eventually obtained after chemical precipitation methods. A typical precipitate is ammonium diuranate (ADU, $(NH_4)_2U_2O_7$), which consists of yellow flakes of material. The precipitates are subsequently calcined into oxides before being subjected to further purification steps. The final product of the mining process is called "yellow cake", which consists of a mixture of uranium oxides (UO_2, U_3O_8 and UO_3), and thanks its name to the yellow color of the mixture (due to the orange UO_3), see Figure 1.4.

Figure 1.4. From left to right: dried ADU precipitate, uranium(VI) oxide (UO_3) obtained after calcination at 550 °C in air, triuranium octoxide (U_3O_8) obtained after calcination at 650 °C in air.

Conversion: Yellow cake is usually not sufficiently pure to be "nuclear grade". Impurity elements which have a high thermal neutron cross-section must be removed,

which in practice corresponds with decreasing their concentrations to levels of 1−10 ppm.[31] The yellow cake product is first re-dissolved in nitric acid (Eq. (1.2)), thus forming uranyl nitrate ($UO_2(NO_3)_2$), to allow selective tri(*n*-butyl)phosphate (TBP) extraction of uranyl nitrate complexes (see Eq. (1.4)).[31]

$$U_3O_8 + 8\,HNO_3 \rightarrow 3\,UO_2(NO_3)_2 + 2\,NO_2 + 4\,H_2O \qquad \textbf{(1.2)}$$

Uranyl nitrate is then stripped from the organic phase and denitrated or converted via chemical precipitation and calcination into an oxide form.[30, 31] Refined, nuclear grade UO_2 powder is obtained after a final reduction treatment with hydrogen (Eq. (1.3)). To allow isotopic enrichment (the next process step) UO_2 is first hydrofluorinated into UF_4 powder and subsequently fluorinated into UF_6 (which sublimes at temperatures above 57 °C).[31]

$$U_3O_8 + 2\,H_2 \rightarrow 3\,UO_2 + 2\,H_2O \qquad \textbf{(1.3)}$$

Enrichment: Most reactor designs which employ UO_2 as principal nuclear fuel require that the fraction of the thermally fissile isotope ^{235}U is increased to 3-5% in order to sustain a nuclear chain reaction. It correspondingly belongs to the low-enriched uranium category (< 20% ^{235}U). As already mentioned, natural uranium only contains about 0.7% of ^{235}U, the remaining part being largely ^{238}U.

Since the chemical properties of the different uranium isotopes are identical, physical separation methods based on the slight difference in atomic mass between the different isotopes (~1 wt.%) have been developed. These processes are highly specialized and details are not made public due the risk of proliferation, since the methods are equally applicable for the production of high-enriched uranium to be used in nuclear weapons.[30] Two main enrichment processes are applied: gas diffusion and ultracentrifugation.

Fuel production: After the enrichment process the UF_6 needs to be reconverted into UO_2 powder, the starting product for fuel fabrication. Different procedures have been developed, each producing different types of powder. More specifically, three process have been applied industrially.[20] The ammonium diuranate (ADU) process and the ammonium uranyl carbonate (AUC) process both employ a wet chemical route. The dry route process is known as the integrated dry route (IDR).

Reconverted UO_2 powder is compacted into cylindrical pellets (diameter and height ~10 mm), see Figure 1.5. The quality of the pressed pellets is affected directly by the morphology and size distribution of the particles. Ideally, a normal size distribution and

spherical particles give best results. Additionally, for continuous production at an industrial scale a good flowability of the powder must be obtained.

The cylindrical pellets are subsequently sintered at high temperature to achieve a high density, typically around 95% of the theoretical density. Here also morphology, and more importantly specific surface area of the powder have a deciding effect on the densification process ("sinterability"). High surface area powders generally show increased sinterability. However, such powders also have an increased tendency to oxidize when exposed to air and pose a risk due to pyrophoricity. A high oxygen content in the powders is also disadvantageous with respect to sinterability. A more comprehensive discussion on reconversion routes and powder properties is given in section 1.1.3.

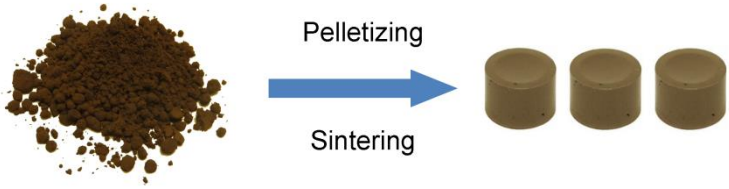

Figure 1.5. UO_2 powder is compacted into cylindrical pellets which are subsequently sintered to high density at high temperature (1500 – 1800 °C).

Irradiation: In a typical PWR with an electrical power output of 1100 MW some 200 fuel assemblies, each containing an array of 17×17 fuel rods, are arranged in the reactor.[20] This corresponds with a load of approximately 18 million fuel pellets.[32] Every 12 to 18 months about one third of the load is replaced with fresh fuel, while the remainder is reorganized to optimize the fission process depending on the remaining content of fissile material.[24] Fuels are thus usually discharged after a total residence time of three years. As an example, in the specific case of an initial ^{235}U enrichment of 4.6% and a burn-up[b] of 50 GWd/t_{HM} the abundance of fissile isotopes has changed to 0.83% ^{235}U, 0.51% ^{239}Pu, 0.10% ^{241}Pu five years after discharge.[33]

Interim storage: Spent fuel which has been removed from the reactor presents a high level of radioactivity accompanied by large heat generation. Therefore, it is transferred directly to an interim storage pool which allows cooling until the radioactivity has decreased to levels which permit handling in other facilities. The general idea is that spent fuel will either be reprocessed or at some point moved to dry storage, followed by permanent repository.[24]

[b] Burn-up is a measure of the energy output per unit mass of fuel. It is typically specified in megawatt-days of thermal output per metric ton of heavy metal (U or U, Pu) initially present in the fuel.

Reprocessing: Spent fuel still contains an appreciable amount of fissile content. To increase the efficiency of the fuel cycle U and Pu can be extracted and reused in the fuel production process. The industrially applied, well-known plutonium uranium redox extraction (PUREX) method is used to recycle U and Pu, and involves dissolution of the spent fuel in nitric acid followed by a complex solvent extraction process.[34] Under the PUREX conditions TBP selectively extracts tetravalent (Pu^{4+}) and hexavalent (U^{6+}) actinide ions (Eqs. (1.4)-(1.5)), while most of the fission products and other actinides (having tri- and pentavalent oxidation states) are not or very poorly extracted.[35] Over 99.5% of the U and Pu content is removed by this method.[36] Pu can subsequently be selectively stripped from the organic phase by adjusting its oxidation state to Pu^{3+} (typical reducing agents: Fe^{2+} and U^{4+}).[35]

$$UO_2^{2+}\,(aq) + 2\,NO_3^-\,(aq) + 2\,TBP\,(org) \rightarrow UO_2(NO_3)_2(TBP)_2\,(org) \qquad \textbf{(1.4)}$$

$$Pu^{4+}\,(aq) + 4\,NO_3^-\,(aq) + 2\,TBP\,(org) \rightarrow Pu(NO_3)_4(TBP)_2\,(org) \qquad \textbf{(1.5)}$$

Nuclear fuels produced from a reprocessing route are mixtures of plutonium and uranium oxide (MOX). In thermal reactors MOX fuel with a Pu content of about 7-9% can be used to replace the otherwise enriched ^{235}U fraction. The most commonly used fabrication route is the micronized master blend (MIMAS) process, which relies on dry-route milling and mixing of oxide powders.[20] The MIMAS process was originally developed by Belgonucléaire in the early 1980s and the commercial plant in Dessel (Belgium) produced over 60% of the world's MOX fuel during the 1990s.[37]

Final disposal: The remainder of spent fuel after reprocessing is high-level waste and consists of fission products, including the long-lived minor actinides (Np, Am, Cm). It is transformed into solid form, incorporated into borosilicate glass (vitrified) and stored in metallic canisters.[24] Such waste canisters are stored at specific sites, awaiting decision on permanent repository. Alternatively, research related to separation and transmutation of the minor actinides in dedicated nuclear reactor systems is on-going.[38] Such processes would drastically decrease the impact associated with nuclear waste from power production.

1.1.3 Reconversion routes

The UO_2 fuel cycle is inseparable from wet chemical processes: uranium-containing ore bodies are leached, uranium is separated and purified in solution, spent fuel is dissolved to allow reprocessing. Nevertheless, the fuel pellet production stage is characterized by powder-metallurgical processing. Transformations of uranium compounds into oxide powders occur in the front end of the UO_2 fuel cycle (see section

1.1.2). A mixture of uranium oxides (yellow cake) is first obtained after calcination of the leach liquors from the milling and extraction process. Yellow cake can be subsequently converted into UO_2 powder, but usually it is first converted into UF_6 as input for the enrichment process. After enrichment, in a process termed reconversion, the final UO_2 powder is obtained. A comprehensive understanding of the reactions involved in the reconversion process allows one to tune powder properties such as morphology, size and specific surface area.

UO_2 powder shows a tendency to further oxidize when in contact with oxygen (see also section 1.2.2), which generally is undesirable. Freshly reduced, very fine UO_2 powders (i.e. which have a high specific surface area) might even burn when exposed to air already at room temperature.[39] In order to limit oxygen uptake passivation procedures are often applied after reconversion. Passivation is associated with low-temperature oxidation of the powder under controlled conditions, thus forming a protective oxide layer.[c] Such processes have been developed in industry, and are usually only applicable to the specific type of powder obtained via the reconversion route in use.

Reconversion routes which have been investigated in the current work are here discussed more in detail.

Integrated dry route (IDR): The route utilizes a rotating furnace system in which gaseous UF_6 (from the enrichment process) first reacts with superheated steam, forming uranyl fluoride (UO_2F_2) powder. The powder then travels down the furnace where it meets a countercurrent flow of steam and hydrogen gas, resulting in formation of UO_2.

IDR powder typically consists of dendritically shaped crystallites whose size is of the order 100 nm, accumulated in loosely packed, soft agglomerates having sizes between 1-20 μm (Figure 1.6). The specific surface area lies in the range 2-3 $m^2\ g^{-1}$. The dry process has some advantages over the wet procedures by being a relative simple process with compact equipment. An important aspect is the omission of liquid waste treatment and the reduced risk of criticality.

The IDR powders can be passivated from excessive oxygen intake by exposing them to an inert atmosphere containing a low quantities of oxygen (1-6 vol.%) near room temperature. Typically this is an integrated part following the reconversion process. In the setup used throughout this PhD thesis project, freshly reduced UO_2 powder was prepared by heating as-received IDR powder to 600 °C under a flow of H_2:Ar (5 vol.%). Cooling was performed under a flow of inert gas (Ar) and upon reaching room temperature (~20-40 °C) a limited supply of oxygen was admitted (1-6 vol.%, the exact

[c] Passivation commonly occurs during oxidation of certain metals, a well-known example is the formation of a very thin (~4 nm) Al_2O_3 layer on the surface of Al which effectively protects against further oxidation.

content increasing over the course of several hours). By performing such a process the oxygen intake was limited to about $UO_{2.03}$.

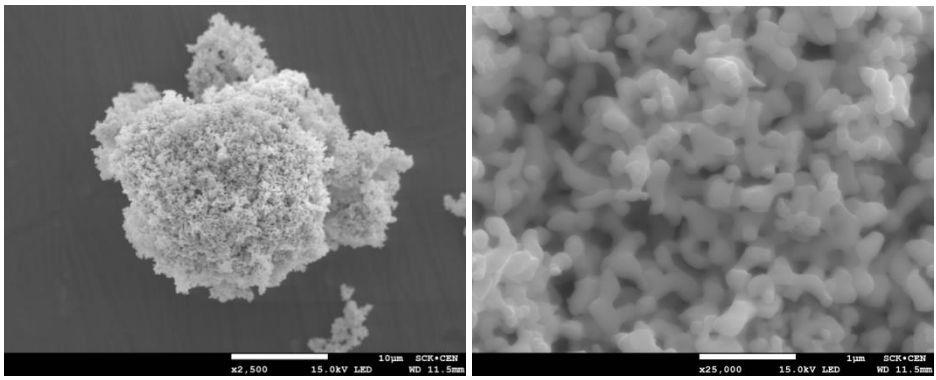

Figure 1.6. Secondary electron (SE) micrographs of IDR obtained UO_2 powder. Large, loosely-packed agglomerates (1−20 µm) consist of many dendritically-shaped crystallites (~100 nm).

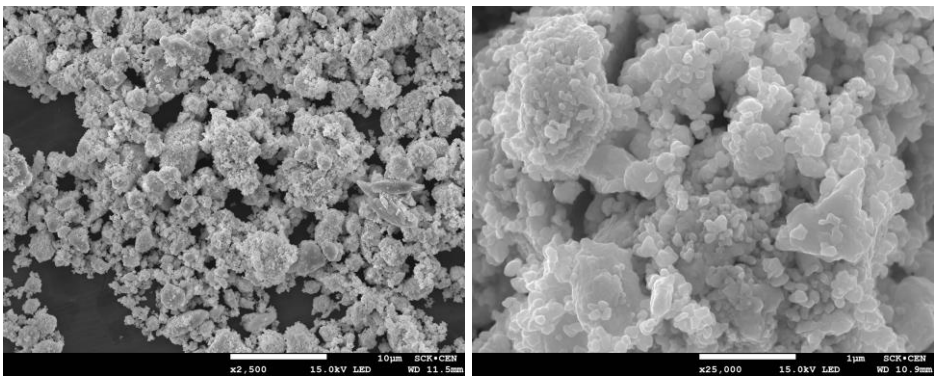

Figure 1.7. Secondary electron (SE) micrographs of ADU route obtained UO_2 powder. Small, rounded crystallites (50−100 nm) are densely packed in much smaller agglomerates (< 5 µm) as compared to IDR powder.

Ammonium diuranate (ADU) route: The ADU route was the first industrially applied reconversion process and it has been widely used. In a two-step process, gaseous UF_6 is first injected into an ammonia solution to hydrolyze and uranium eventually precipitates as ADU. The precipitate is collected on filters, dried and calcined, and in a second step reduced with hydrogen to UO_2.

This process was mimicked on a laboratory scale in this PhD project by first dissolving the supplied UO_2 powder in nitric acid to obtain a uranyl nitrate solution. By titration

with an excess of a NH_3 aqueous solution (Eq. (1.6)) yellow ADU precipitates formed which were subsequently separated by vacuum filtering (see also Figure 1.8). The precipitate was then dried, calcined into U_3O_8 and subsequently reduced to UO_2 with hydrogen.

$$2\,UO_2(NO_3)_2 + 6\,NH_3 + 4\,H_2O \rightarrow (NH_4)_2U_2O_7 + 4\,NH_4NO_3 + H_2O \qquad \textbf{(1.6)}$$

Figure 1.8. Left to right: homogeneous uranyl nitrate aqueous solution, ADU precipitate formed after addition of NH_3 aqueous solution, filtered ADU transferred into a petri dish.

The ADU route obtained UO_2 powder is markedly different from the IDR route powder. Somewhat rounded crystallites with sizes in the range 50-100 nm are densely packed in much smaller agglomerates (< 5 μm), see Figure 1.7. Depending on calcination and reduction conditions (temperature and time in particular) powders with specific surface areas in the range 4−20 $m^2\,g^{-1}$ can be prepared.

When such powders are exposed to air near room temperature (40 °C) the extent of oxidation may reach as high as $UO_{2.22}$, depending on specific surface area. Exposure to reduced oxygen concentrations does not seem to significantly limit the amount of oxidation, hence the passivation treatment utilized for IDR-produced powders fails (this is explained more in detail in Chapters 4 and 5). Usually, ADU-route powders first undergo additional heat treatment to decrease their reactive surface area before being able to be passivated. To better understand the phenomena at play more insight in the oxidation mechanisms at low temperature is required.

1.2 The uranium-oxygen system

1.2.1 Oxidation states of the actinides: uranium

Uranium, having an atomic number Z = 92, is an element of the actinide series of the periodic table (89 < Z < 103). Its atomic weight is equal to 238.02891(3) g mol^{-1}, assuming the natural abundance of its isotopes.[40] The electron configuration of the actinides is characterized by a progressive filling of the 5f orbital, in general of the type [Rn] $7s^2 5f^n$ (n = 0 – 14). Compared to the 4f electrons in the lanthanide series the radial extent of the 5f orbital is greater. As a result the 5f electrons show a more diverse character and are able to participate in bond formation.[41] A wide range of oxidation states is observed, especially in the early actinides. With increasing Z, due to the higher effective nuclear charge and relativistic effects, the chemical behavior starts to resemble more that of the lanthanides. An overview of the electronic configurations and oxidation states is given in Table 1.1.

All naturally occurring isotopes of uranium are radioactive. ^{238}U is the parent isotope for the $4n + 2$ radioactive decay series, in which through a sequence of alfa and beta decay eventually the stable element ^{206}Pb is formed.[24] The specific activity of ^{238}U is 12.4 kBq g^{-1}, while that of ^{235}U is somewhat higher at 80 kBq g^{-1}. The decay time is dominated by the ^{238}U half-life, approximately 4.5×10^9 years,[42] a timespan equal to the age of planet Earth.[43] Heat generated by the radioactive decay of uranium, thorium and potassium are the primary source of energy driving convection in Earth's mantle.

Table 1.1 Overview of the most stable valence states in the actinides and their electronic configuration in ground state. [41, 44]

Element	Valence states [Rn] +					Electronic configuration in ground state
	+II	+III	+IV	+V	+VI	
Ac		$5f^0$				[Rn] $7s^2$ $6d^1$
Th			$5f^0$			[Rn] $7s^2$ $6d^2$
Pa				$5f^0$		[Rn] $7s^2$ $6d^1$ $5f^2$
U			$5f^2$		$5f^0$	[Rn] $7s^2$ $6d^1$ $5f^3$
Np				$5f^2$		[Rn] $7s^2$ $6d^1$ $5f^4$
Pu			$5f^4$			[Rn] $7s^2$ $5f^6$
Am		$5f^6$				[Rn] $7s^2$ $5f^7$
Cm		$5f^7$				[Rn] $7s^2$ $6d^1$ $5f^7$
Bk		$5f^8$				[Rn] $7s^2$ $5f^9$
Cf		$5f^9$				[Rn] $7s^2$ $5f^{10}$
Es		$5f^{10}$				[Rn] $7s^2$ $5f^{11}$
Fm		$5f^{11}$				[Rn] $7s^2$ $5f^{12}$
Md		$5f^{12}$				[Rn] $7s^2$ $5f^{13}$
No	$5f^{14}$					[Rn] $7s^2$ $5f^{14}$
Lr		$5f^{14}$				[Rn] $7s^2$ $6d^1$ $5f^{14}$

1.2.2 Thermochemistry of uranium and oxygen

The wide range in valence states of uranium ions are reflected clearly in its oxidation chemistry. The uranium-oxygen phase diagram (Figure 1.9) is remarkably complex, and although the U-O system has been investigated already for over 70 years new insights are still obtained today.[45-48] One observes a wide phase domain for $UO_{2\pm x}$ starting at a temperature of about 450 °C and ranging up to 2900 °C (not shown here). Two single-valence compounds are uranium(IV) oxide (UO_2) and uranium(VI) oxide (UO_3). In addition, several mixed-valence compounds exist (U_4O_9, U_3O_7, U_3O_8), i.e. compounds in which the uranium ions exhibit a variety in valence states +IV, +V, +VI.[49-51] Most of these oxides also have the tendency to show some amount of non-stoichoimetry.[31] The terminology most often used to identify the various uranium oxides is the O-to-U ratio (O/U), for example UO_2 (O/U = 2), U_4O_9 (O/U = 2.25), etc.

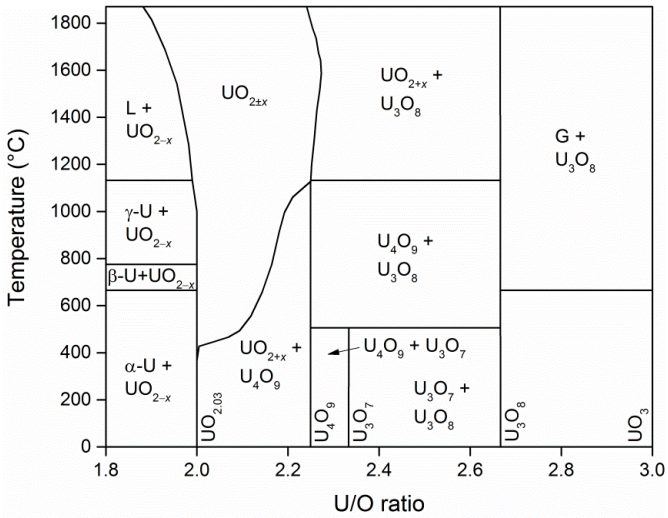

Figure 1.9. Excerpt of the U-O phase diagram, a simplified version adapted from critical reviews of Chevalier *et al.*,[45] Labroche *et al.*,[46] Higgs *et al.*[47] and Guéneau *et al.*[48] Greek letters are used to distinguish between different solid polymorphs, L refers to the liquid state, G refers to the gaseous state.

At low temperatures (< 250 °C) the boundary of the $UO_{2\pm x}$ domain is reduced to about $UO_{2.03,}$[52] and at higher O/U ratios the system becomes more complex. A biphasic region of UO_{2+x} + U_4O_9 is first encountered. Possibly a triphasic region of UO_{2+x} + U_4O_9 + U_3O_7 exists (not shown in Figure 1.9). The thermodynamically most stable oxide formed in dry air is U_3O_8, which evidently is encountered in most parts of the phase diagram. The higher oxide UO_3 is typically obtained as a decomposition product from compounds produced via wet chemical routes.[31] At temperatures above 650 °C UO_3 disproportionates into U_3O_8 and O_2.

The thermodynamic stability of the various oxides depends on conditions of temperature and oxygen partial pressure, and is evaluated via the Gibbs energy function (ΔG). For a generalized oxidation reaction one finds:

$$M\,(s) + O_2\,(g) \rightarrow MO_2\,(s) \quad \textbf{(1.7)}$$

$$\Delta G = \Delta G^0 - R \cdot T \cdot \ln(p_{O_2}) \quad \textbf{(1.8)}$$

where ΔG^0 is the Gibbs energy change in standard conditions (J mol^{-1}), R is the universal gas constant (J K^{-1} mol^{-1}), T is absolute temperature (K) and p_{O_2} is the oxygen partial pressure (atm). When the system is in equilibrium $\Delta G = 0$ and $p_{O_2} = p_{O_2,eq}$:

$$p_{O_2,\mathrm{eq}} = \exp\left(\frac{\Delta G^0}{R \cdot T}\right) \quad \textbf{(1.9)}$$

Substituting Eq. (1.9) in Eq. (1.8) we obtain:

$$\Delta G = R \cdot T \cdot \left(\ln(p_{O_2,eq}) - \ln(p_{O_2})\right) \quad \textbf{(1.10)}$$

Thus, for $p_{O_2} > p_{O_2,eq}$ the oxidation reaction (Eq. (1.7)) is thermodynamically favored. Whether the reaction will proceed at a detectable rate will depend on the kinetics of the oxidation mechanism. Equilibrium curves displaying tabulated values of the standard Gibbs energy for various metal/metal oxide systems as a function of temperature are called "Ellingham diagrams". In such diagrams Gibbs energy is usually represented as the oxygen potential, defined as:

$$\mu_{O_2,\mathrm{eq}} = \Delta G^0 = R \cdot T \cdot \ln(p_{O_2,eq}) \quad \textbf{(1.11)}$$

Figure 1.10 shows an Ellingham diagram with compiled values for UO_{2+x}/U_4O_9, U_4O_9/U_3O_8 and UO_{2+x}/U_3O_8.[53] Interpretation of this diagram is as follows: at a given temperature, if the oxygen partial pressure p_{O_2} in the system is increased such that its corresponding oxygen potential value ($\mu_{O_2} = R \cdot T \cdot \ln(p_{O_2})$) lies above an equilibrium curve, oxidation is thermodynamically favored.

Oxygen potential values as a function of the oxygen content x in UO_{2+x} are also available (see Chapter 2).[54] Thermodynamic data of the most common uranium oxides are presented in Table 1.2.[31, 55] Heat capacity functions of these compounds can be found in the referred works.

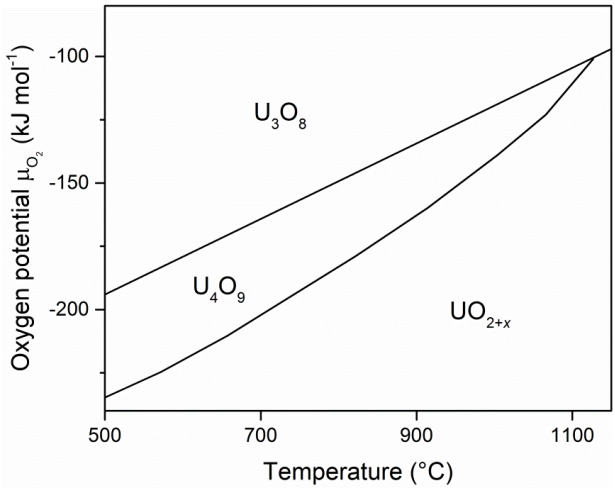

Figure 1.10. Gibbs energy (represented as oxygen potential) as a function of temperature for formation of different uranium oxides. The figure is compiled from critically reviewed data by Guéneau *et al*.[53]

Table 1.2. Thermodynamic data of some of the uranium oxides.[31, 55]

	UO_2	U_4O_9	U_3O_7	U_3O_8	β-UO_3
$\Delta H_f°$ (kJ mol^{-1})	−1085 ± 1	−4512 ± 7	−3423 ± 6	−3575 ± 3	−1220 ± 1
S° (J K^{-1} mol^{-1})	77.0 ± 0.2	334.1 ± 0.7	250.5 ± 0.6	282.6 ± 0.5	96.3 ± 0.4
$\Delta G°$ (kJ mol^{-1})	−1032 ± 1	−4276 ± 7	−3239 ± 6	−3370 ± 3	−1142 ± 1

1.2.3 Uranium oxide crystal chemistry

In the present PhD research solid state phenomena related to low-temperature oxidation of UO_2 are investigated. In an important part of the work the crystallographic changes which occur as a result of oxidation are analyzed and interpreted. For this reason a more detailed overview of the uranium oxide crystal chemistry is given here.

The UO_2 crystal structure has been identified in the $Fm\bar{3}m$ space group (SG).[56] The U atoms occupy face-centered (cubic coordinated) positions and O atoms occupy tetrahedrally coordinated sites (Figure 1.11 (a)).[57] This setting is usually referred to as "fluorite-ordered" after the CaF_2 (fluorite) structure.[58] The generally accepted value for the lattice parameter of stoichiometric UO_2 equals a_0 = 547.04(8) pm, and relates to measurements performed in the 1950s.[59] A re-evaluation of the lattice parameter value was performed in this PhD thesis (see Chapter 2): a_0 = 547.127(8) pm at room temperature.

Upon oxidation, additional O atoms are incorporated into the crystal lattice, the U sublattice remaining largely undisturbed.[60] To maintain charge balance, however, some of the U^{4+} ions need to be oxidized to a higher valence state. One of the resulting effects is the lattice contraction in UO_{2+x} proportional with increasing oxygen content x:

$$a_x = a_0 - c \cdot x \qquad \textbf{(1.12)}$$

with a_x the lattice parameter as a function of oxygen content x in UO_{2+x}, and c the contraction ratio which has reported values between 5.5 and 15 pm per molar excess in oxygen.[61-67] Eq. (1.12) is valid over an appreciable range $0 \leq x \leq 0.125$, provided that the temperature is adequately elevated (see Figure 1.9).

The fluorite structure possesses octahedrally coordinated sites at the cell center ½,½,½ and at symmetry equivalent positions halfway in-between the unit cell axes (see grey dots marked in Figure 1.11 (a)). These lattice sites, which are unoccupied in stoichiometric UO_2 present the largest interstitial holes and are susceptible to accommodate foreign elements. The incorporation of additional oxygen atoms during oxidation results in a reorganization of the anion sublattice, but the cation sublattice remains to a large extent undisturbed and cubic symmetry is maintained.[68] Compounds having an O/U ratio between 2 and 2.5 remain closely related to the original fluorite-type UO_2 structure, the most notable change being a distortion from cubic symmetry with increasing degree of oxidation.[31]

Neutron diffraction studies have shown that the additional O atoms in UO_{2+x} do not exactly occupy the large interstitial sites, but are instead displaced slightly (~1 Å) away from these sites.[60] Further analysis showed that these defects are likely grouped in so-called 2:2:2 Willis clusters, consisting of two additional O atoms displaced along [*u u* 0]-directions (O') and two oxygen atoms displaced along [*u u u*]-directions (O'') leaving two vacancies in the original fluorite-ordered O sublattice (Figure 1.11 (b)).[69] Initially, the defect structure remains disordered, i.e. the defect clusters are distributed randomly throughout the entire crystal.

The uptake of specific amounts of oxygen eventually results in the formation of a long-range ordered defect structure,[70] as was first observed in U_4O_9 (O/U = 2.25).[71, 72] Early assessments considered a linear ordering of 2:2:2 Willis clusters.[73, 74] However, it seemed that with increasing uptake of oxygen a further modification of the anion sublattice occurs. Although, on average, some O atoms remain to be displaced along [*u u* 0]- and [*u u u*]-directions the site occupancy factor for O'' atoms decreases and no longer matches with that expected for a 2:2:2 cluster.[75] In U_4O_9 the defect structure is, in fact, largely characterized by a different type of defect, the cuboctahedral oxygen cluster,[76] and fragments of this cluster may already be assembled in UO_{2+x}.[75, 77]

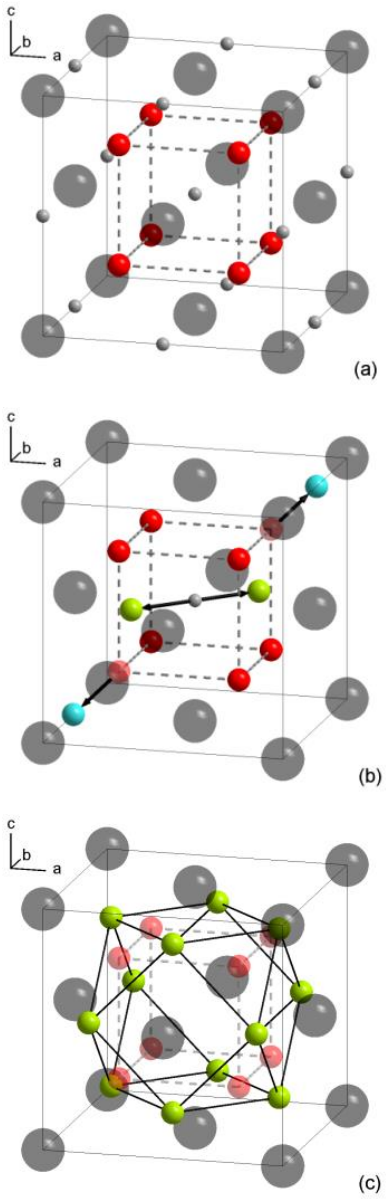

Figure 1.11. UO_2 (fluorite-type) unit cells with black transparent spheres representing uranium atoms, smaller red spheres represent oxygen atoms. (a) Octahedrally coordinated interstitial sites are indicated by small gray spheres. (b) Illustration of the Willis 2:2:2 cluster, consisting of 2 O atoms displaced along [*u u* 0] (green spheres), 2 atoms displaced along [*u u u*] (blue spheres) and two oxygen vacancies (red shaded spheres). (c) Illustration of the cuboctahedral oxygen cluster, consisting of twelve <*u u* 0> displaced oxygen atoms (green spheres).

The cuboctahedral defect model was derived from fluorite-related systems in which anion excess superstructures are recognized.[76, 78] A cuboctahedral oxygen cluster consists of anions which are displaced along twelve <*u u* 0>-directions from the cell center (cf. O' atoms), thus forming the vertices of a regular cuboctahedron (Figure 1.11 (c)). The coordination of such cuboctahedral oxygen clusters in an expanded unit cell forms the basis for solving periodically distorted crystal structures of the fluorite-related uranium oxides.

The U_4O_9 superstructure ($4a_0 \times 4a_0 \times 4a_0$, a_0 = 543.9 pm, SG $I\bar{4}3d$)[76, 79, 80] is described by the spatial ordering of 12 cuboctahedral oxygen clusters (in 64 unit cells).[76, 81] Another higher oxide U_3O_7 (O/U = 2.33) also exhibits a periodically distorted crystal structure.[79, 82-84] Descriptions of the superstructure based on cuboctahedral oxygen clusters have similarly been proposed, but remain subject to debate.[79, 82] A comprehensive description of the U_3O_7 crystal structure is presented in Chapter 3.

Oxidation of UO_2 in dry air is completed with formation of U_3O_8 (O/U = 2.67), and not UO_3. Possibly a large energy barrier exist for UO_3 nucleation on U_3O_8.[52] The high oxygen content of this compound results in a markedly different crystal structure from the fluorite-type. The crystal structure of U_3O_8 is described as a layered structure, closely related to the hypothetical "ideal" UO_3 structure.[85] Two polymorphs are recognized, both having very similar orthorhombic structures: α-U_3O_8 (*a* = 671.6 pm, *b* = 1196 pm, *c* = 414.69 pm, SG *C2mm*) and β-U_3O_8 (*a* = 706.9 pm, *b* = 1144.5 pm, *c* = 830.3 pm, SG *Cmcm*).[85, 86]

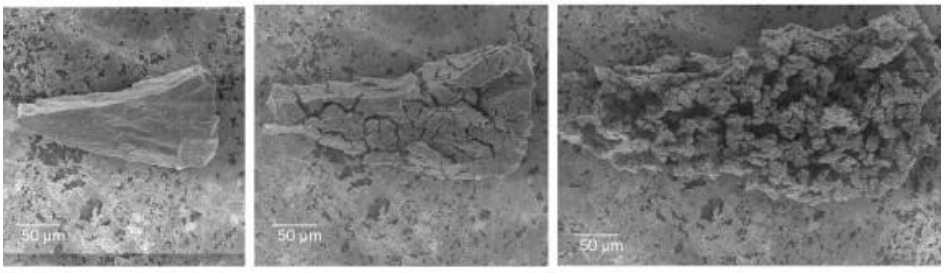

Figure 1.12. Environmental scanning electron micrographs showing the progressive *in-situ* oxidation of a UO_2 pellet fragment at 330 °C. Note that the magnification is identical in all three pictures, clearly illustrating the volume expansion associated with transformation into U_3O_8. Figure reprinted from Quémard *et al*,[87] with permission from Elsevier.

An epitaxial relation exists between the close-packed (111) crystallographic plane in cubic UO_2 and the (001) basal plane of orthorhombic U_3O_8.[88] The U-U interatomic distance is almost identical in both planes.[79] However, the anion arrangement is severely modified, forming pentagonal bipyramid (10-fold) coordination around

uranium atoms.[31] The fluorite structure of UO_2 can be transformed into the layered structure of U_3O_8 by first displacing uranium atoms in (111) planes followed by expanding the distance between such planes along the [111] direction.[89] This expansion is likely responsible for the large volume increase (about 36 vol.%) which is associated with conversion of UO_2 to U_3O_8 (see Figure 1.12).[79, 90] Such a volume increase may ultimately result in rupture of storage containers or vessels.[52]

1.2.4 UO_2 oxidation mechanisms

As already mentioned, solid state phenomena related to low-temperature oxidation of UO_2 are investigated in the current PhD research. For this reason also the literature data on oxidation mechanisms and reaction kinetics are discussed here.

Oxygen is rapidly adsorbed onto the surfaces of freshly reduced uranium dioxide already at temperatures as low as −183 °C (i.e. the boiling temperature of oxygen).[91] In addition to regular physical adsorption, oxygen is also chemically adsorbed. Chemisorption seems to be limited to less than a monolayer of surface coverage, while physisorption does not seem to be limited.[91, 92] The adsorption enthalpy of oxygen onto a freshly reduced surface of UO_2 decreases with surface coverage from −230 kJ mol^{-1} to about −20 kJ mol^{-1} (measured at −183 °C) at the chemisorption limit.[92] The corresponding temperature rise accounts for the pyrophoric behavior of very fine, freshly reduced UO_2 powders. Bannister formulated a simple linear correlation between oxidation extent (ΔO/U) and specific surface area for a chemisorbed monolayer of oxygen at room temperature:[39]

$$\Delta O/U = SSA \times 3.6 \times 10^{-3} \quad \textbf{(1.13)}$$

At temperatures between −130 °C and 50 °C a slow additional reaction between oxygen and UO_2 occurs, and the extent of oxidation seems to increase as a logarithmic function of time.[93] Similar reaction kinetics are also observed during low-temperature oxidation of various metals when very thin (< 5 nm) oxide films grow at the surface.[94-98] The oxidation process at temperatures which are considered too low for thermally activated diffusion is explained by Mott-Cabrera theory.[99, 100] The mechanism is based on the electrostatic field which is set up in the oxide film by adsorption of oxygen on the surface. The electric field lowers the barrier for incorporation and slow migration of ionic species.[101, 102]

Growth of the oxide layer (thickness Δy as a function of time t) under the Mott-Cabrera regime proceeds according to an inverse logarithmic rate law of the type:[103]

$$\frac{1}{\Delta y(t)} = \frac{1}{\Delta y_0} - r \cdot \ln\left(\frac{t-t_0}{\tau} + 1\right) \quad \textbf{(1.14)}$$

where Δy_0 is the thickness of the oxide layer at time t_0, which corresponds with the moment at which the Mott-Cabrera mechanism becomes rate-controlling. The oxidation of metallic uranium also follows this type of kinetics.[104, 105] It is not unlikely that such a mechanism is similarly involved during the initial stage of UO_2 oxidation.[93] Only little experimental data is available in the low temperature range (< 100 °C), but surface oxide layers have been readily observed after oxidation at more elevated temperatures.[106-108] The low-temperature oxidation process in fine UO_2 powders is investigated in detail in Chapter 5.

Bulk oxidation of coarse-grained UO_2 powders or sintered pellets is observed at temperatures above 100 °C.[52] The consensus has been that oxidation of UO_2 proceeds as a diffusion-driven surface reaction involving formation of a product layer (μm scale) at temperatures up to 250 °C.[52, 109, 110] In the most simple interpretation growth of the oxide layer is described by the parabolic (1 dimensional diffusion) rate law:

$$\Delta y = k_p \cdot \sqrt{t} \quad \textbf{(1.15)}$$

where k_p is the rate constant. Formation of an oxide layer on the grain boundaries of irradiated UO_2 pellets has been readily observed by electron[106, 108, 111, 112] and optical[107] microscopy. Similar results have not been reproduced for fine powders and single crystals.[87, 113]

The 1-D diffusion model is only an approximation of the real physical process, which is further complicated by the formation of different intermediate oxide products. Stationary rate laws such as the Jander model,[114] and the Ginstling-Brounshtein model,[115] have been applied to more accurately describe oxidation kinetics in the diffusion-controlled regime.[52, 116-119] However, such models do not distinguish specifically between the different intermediate compounds.

The sequence of crystalline compounds formed upon increasing the oxygen content is: $UO_2 \rightarrow U_4O_9 \rightarrow U_3O_7 \rightarrow U_3O_8$, here disregarding the nonstoichiometric regions in the U-O system.[79, 117] The first two reaction steps are controlled by diffusion. Such a distinction was also made in a recently developed non-stationary model, obtained by solving the diffusion equation in two simultaneous and interdependent reactions $UO_2 \rightarrow U_4O_9$ and $U_4O_9 \rightarrow U_3O_7$.[109] As oxidation progresses the oxidation fronts move towards the unreacted bulk, schematically shown in Figure 1.13, forming discrete surface layers. Experimental mass gain curves can be effectively modelled by employing such a model.[109]

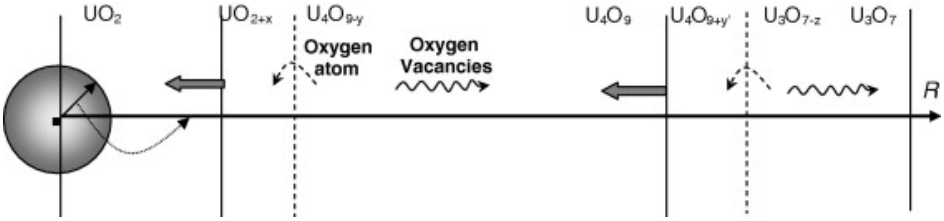

Figure 1.13. Schematic of the discrete-layer oxidation model for spherical UO_2 particles. As oxidation progresses the U_4O_9 and U_3O_7 reaction interfaces penetrate more deeply into the bulk, thus forming surface oxide layers. Figure reprinted from Poulesquen *et al*,[109] with permission from Elsevier.

Fine UO_2 powders (having large specific surface area) appear to behave differently. During room temperature oxidation, limiting compositions in the range $2.1 \leq O/U \leq 2.5$ can be reached, depending on surface area.[39, 120] Formation of UO_3 on the surface may additionally be involved.[120] Despite the high degree of oxidation crystalline intermediate oxides such as U_4O_9 or U_3O_7 are not readily distinguished in diffraction experiments. An interpretation of these phenomena is given in Chapter 4.

Theoretically oxidation of UO_2 completes at the composition UO_3. However, the most stable UO_2 oxidation product formed in dry air is U_3O_8.[121] As already mentioned, this might be due to a large energy barrier for UO_3 nucleation on U_3O_8.[52] At oxidation temperatures between 200 °C and 350 °C one can distinguish formation of the intermediate oxides (U_4O_9, U_3O_7) before U_3O_8 formation, while immediate U_3O_8 formation is observed at more elevated temperatures.[93, 110, 116, 118, 119]

U_3O_8 formation is a process of nucleation-and-growth, and the precursor is considered to be the oxide product layer formed during the diffusion-controlled oxidation stage (U_3O_7 at low temperature, UO_{2+x} at elevated temperature).[87] Continued oxidation of UO_2 into U_3O_8 displays sigmoidal reaction kinetics, but the physical interpretation remains somewhat unclear.[52] Likely, the oxide product layer starts to crack once a critical thickness is reached, thus revealing fresh, unreacted surfaces of UO_2 susceptible for further oxidation.[87] This corresponds with the start of the sigmoidal curve. In fine powders the critical layer thickness is not reached, and as a result no cracking occurs. Such a mechanism explains why a slower U_3O_8 formation rate has been observed in fine powders as compared to in coarse powders.[116]

1.3 Objective and outline

1.3.1 Objective

The aim of this PhD thesis is to obtain a better understanding of the oxidation process in fine UO_2 powders. Under conditions related to nuclear fuel production and to storage of UO_2 powders and pellets the various solid state phenomena are investigated. An in-depth assessment of the crystallographic changes which occur during oxidation is first performed, followed by an evaluation of the reaction thermochemistry and kinetics. The objective is finally to obtain more insight in the oxidation mechanisms at play in the low-temperature range (< 250 °C).

1.3.2 Outline

The results of this PhD research are described in four technical chapters. Each of the chapters are prepared manuscripts which have been submitted, or are planned to be submitted to a peer-reviewed international journal. A summary of the results presented in the technical chapters is given in the closing chapter, and here also an outlook for future research is given.

In addition to the four technical chapters and the closing chapter the background of the research is first presented. The thesis starts with a general introduction to nuclear fission and its associated historical developments. A description of the UO_2 fuel cycle is given and specific attention is paid to different powder reconversion routes. After setting the frame a comprehensive analysis of the uranium-oxygen system is performed, and the state-of-the-art regarding crystallography and oxidation reaction mechanisms and kinetics is presented.

Chapter 2 presents a re-evaluation of the UO_2 crystallographic unit cell lattice parameter, which is a key value in engineering context. Precise measurement is not straightforward since UO_2 shows the tendency to oxidize when in contact with air, and this affects the lattice parameter value. Highly-densified UO_2 samples which presented a negligible intake of oxygen were prepared under specific conditions. Their stoichiometry was accurately measured and an assessment of the lattice parameter was performed via X-ray diffraction. The results were consistent and a more precise value is reported, which replaces the now outdated earlier value.

Chapter 3 presents a structure assessment of U_3O_7, an important intermediate uranium oxide which is formed during oxidation. Although investigated already for over 60 years its crystal structure is still subject to debate. High-quality powder samples were prepared and investigated using X-ray and selected area electron diffraction techniques. The analysis revealed a long-range ordered structure having an atomic arrangement of

fluorite-type ordered uranium and oxygen atoms, with excess anions grouped in distorted cuboctahedral oxygen clusters.

Chapter 4 evaluates the crystallographic changes which occur during low-temperature oxidation of fine UO_2 powders. It has been recognized that fine UO_2 powders behave differently when exposed to air as compared to coarse powders or pellet fragments. A variety of UO_2 powders were oxidized in air at temperatures between 40 °C and 250 °C, and subsequently analyzed by X-ray diffraction and high-resolution transmission electron microscopy. Results showed that higher oxide compounds developed in nanosized domains during continued oxidation. This provided more insight in the oxidation mechanisms at the level of the individual grains.

Chapter 5 gives results of the analysis of thermochemical and kinetic data which were obtained from oxidation experiments on fine UO_2 powders. Particular attention was paid to the oxidation mechanism at temperatures below 100 °C since only limited experimental data were available in this region. A variety of UO_2 powders were oxidized at 40 °C in a limiting supply of oxygen, and also in air at temperatures between 40 °C and 250 °C. Oxidation was followed by *in-situ* thermogravimetric analysis coupled with differential scanning calorimetry. It was found that the initial oxidation reaction corresponds with formation of an amorphous phase on the surface of the grains, which likely induced the development of domains upon further oxidation.

References

(1) O. Hahn, F. Strassmann, *Naturwissenschaften* **1939**, *27*, 11.
(2) E. Fermi, E. Amaldi, O. D'Agostino, F. Rasetti, E. Segre, *Proc. R. Soc. London, Ser. A Mat.* **1934**, *146*, 483.
(3) L. Meitner, O. R. Frisch, *Nature* **1939**, *143*, 239.
(4) O. R. Frisch, *Nature* **1939**, *143*, 276.
(5) Nobel Media AB, *The Nobel Prize in Physics 1938*, **2014**, accessed on: 2016-05-11 http://tinyurl.com/jf8af4s.
(6) Nobel Media AB, *The Nobel Prize in Chemistry 1944*, **2014**, accessed on: 2016-05-11 http://tinyurl.com/hx53dwt.
(7) W. B. Ewbank, Y. A. Ellis, M. R. Schmorak, *Nuclear Data Sheets* **1979**, *26*, 1.
(8) N. Bohr, J. A. Wheeler, *Physical Review* **1939**, *56*, 426.
(9) F. Gönnenwein, *Mass, Charge, and Kinetic Energy of Fission Fragments* in *The Nuclear Fission Process*, CRC Press, Inc., Boca Raton, **1991**.
(10) G. D. James, J. E. Lynn, A. Michaudon, J. Rowlands, G. de Saussure, *Nuclear fission and neutron-induced fission cross-sections*, Pergamon Press Ltd., Oxford, **1981**.
(11) C. Hardy, *Atomic Rise and Fall: The Australian Atomic Energy Commission, 1953-1987*, Glen Haven Publishing, Peakhurst, **1999**.
(12) A. Einstein, *Annalen der Physik* **1905**, *323*, 639.
(13) H. Weigmann, *Neutron-Induced Fission Cross Sections* in *The Nuclear Fission Process*, CRC Press, Inc., Boca Raton, **1991**.
(14) X. Yang, R. North, C. Romney, *Worldwide nuclear explosions*, **2000**, accessed on: 2016-05-11 http://tinyurl.com/zwgg6kn.
(15) J. Van der Auwera, G. Stiennon, J. Goens, L. de Heem, E. M. de Dorlodot, P. Marien, C. Gerard, F. Léonard, *50 Years BR1*, Report CL-3, SCK•CEN, Mol, **2006**.
(16) SCK•CEN, *Belgian Reactor 2 - BR2*, **2016**, accessed on: 2016-05-18 http://tinyurl.com/zgaxz9s.
(17) SCK•CEN, *VENUS-F: an accelerator driven system prototype*, **2016**, accessed on: 2016-05-18 http://tinyurl.com/j8kzukg.
(18) SCK•CEN, *Belgian Reactor 3 - BR3*, **2016**, accessed on: 2016-05-18 http://tinyurl.com/gtqeugw.
(19) ENGIE Electrabel, *Nuclear power at ENGIE Electrabel*, accessed on: 2016-05-11 http://tinyurl.com/jrk4ec3.
(20) T. Abe, K. Asakura, *2.15 - Uranium Oxide and MOX Production* in *Comprehensive Nuclear Materials*, Elsevier, Oxford, **2012**, pp. 393.
(21) A. K. Sengupta, R. Agarwal, H. S. Kamath, *3.03 - Carbide Fuel* in *Comprehensive Nuclear Materials*, Elsevier, Oxford, **2012**, pp. 55.
(22) World Nuclear Association, *World nuclear power reactors & uranium requirements*, **2016**, accessed on: 2016-05-11 http://tinyurl.com/j3urhgj.
(23) D. D. Baron, L. Hallstadius, *2.19 - Fuel Performance of Light Water Reactors (Uranium Oxide and MOX)* in *Comprehensive Nuclear Materials*, Elsevier, Oxford, **2012**, pp. 481.
(24) D. Bodansky, *Nuclear Energy: Principles, Practices and Prospects*, American Institute of Physics, Woodbury, **1996**.

(25) P. C. Burns, *Rev. Miner.* **1999**, *38*, 23.
(26) R. J. Finch, T. Murakami, *Rev. Miner.* **1999**, *38*, 91.
(27) M. H. Klaproth, *Chem. Ann.* **1789**, *2*, 387.
(28) M. Berglund, M. E. Wieser, *Pure Appl. Chem.* **2011**, *83*, 397.
(29) World Nuclear Association, *Supply of Uranium*, **2015**, accessed on: 2016-05-12 http://tinyurl.com/gqagwzd.
(30) L. Grainger, *Uranium and Thorium*, George Newnes Ltd., London, **1958**.
(31) I. Grenthe, J. Drozdzynski, T. Fujino, E. C. Buck, T. E. Albrecht-Schmitt, S. F. Wolf, *The chemistry of the Actinide and Transactinide elements, Vol. 1*, 3 ed., Springer, Dordrecht, **2006**.
(32) World Nuclear Association, *Nuclear Fuel Fabrication*, **2016**, accessed on: 2016-05-13 http://tinyurl.com/h64ltxm.
(33) L. Özdemir, B. B. Acar, O. H. Zabunoğlu, *Annals of Nuclear Energy* **2011**, *38*, 540.
(34) J. P. Glatz, *5.14 - Spent Fuel Dissolution and Reprocessing Processes* in *Comprehensive Nuclear Materials*, Elsevier, Oxford, **2012**, pp. 343.
(35) D. L. Clark, S. S. Hecker, G. D. Jarvinen, M. P. Neu, *Plutonium* in *The Chemistry of the Actinide and Transactinide Elements*, Springer, Dordrecht, **2006**.
(36) J.-Y. Barre, J. Bouchard, *French R&D Stategy for the Back End of the Fuel Cycle* in *Future Nuclear Systems: Emerging Fuel Cycles & Waste Disposal Options, Proceedings of Global '93*, American Nuclear Society, La Grange, **1993**.
(37) D. Haas, A. Vandergheynst, J. van Vliet, R. Lorenzelli, J.-L. Nigon, *Nucl. Technol.* **1994**, *106*, 60.
(38) S. Pillon, *3.05 - Actinide-Bearing Fuels and Transmutation Targets* in *Comprehensive Nuclear Materials*, Elsevier, Oxford, **2012**, pp. 109.
(39) M. J. Bannister, *J. Nucl. Mater.* **1968**, *26*, 174.
(40) J. Meija, B. Coplen Tyler, M. Berglund, A. Brand Willi, P. De Bièvre, M. Gröning, E. Holden Norman, J. Irrgeher, D. Loss Robert, T. Walczyk, T. Prohaska, *Pure Appl. Chem.* **2016**, *88*, 265.
(41) S. Cotton, *Lanthanide and Actinide Chemistry*, Wiley, Chichester, **2006**.
(42) A. H. Jaffey, K. F. Flynn, L. E. Glendenin, W. C. Bentley, A. M. Essling, *Physical Review C* **1971**, *4*, 1889.
(43) G. B. Dalrymple, *Geological Society, London, Special Publications* **2001**, *190*, 205.
(44) H. C. Aspinall, *Chemistry of the f-Block Elements, Vol. 5*, Gordon and Breach Science Publishers, Amsteldijk, **2001**.
(45) P. Y. Chevalier, E. Fischer, B. Cheynet, *J. Nucl. Mater.* **2002**, *303*, 1.
(46) D. Labroche, O. Dugne, C. Chatillon, *J. Nucl. Mater.* **2003**, *312*, 50.
(47) J. D. Higgs, B. J. Lewis, W. T. Thompson, Z. He, *J. Nucl. Mater.* **2007**, *366*, 99.
(48) C. Guéneau, N. Dupin, B. Sundman, C. Martial, J.-C. Dumas, S. Gossé, S. Chatain, F. D. Bruycker, D. Manara, R. J. M. Konings, *J. Nucl. Mater.* **2011**, *419*, 145.
(49) K. O. Kvashnina, S. M. Butorin, P. Martin, P. Glatzel, *Phys. Rev. Lett.* **2013**, *111*, 1.

(50) D. A. Andersson, G. Baldinozzi, L. Desgranges, D. R. Conradson, S. D. Conradson, *Inorg. Chem.* **2013**, *52*, 2769.
(51) S. D. Conradson, D. Manara, F. Wastin, D. L. Clark, G. H. Lander, L. A. Morales, J. Rebizant, V. V. Rondinella, *Inorg. Chem.* **2004**, *43*, 6922.
(52) R. J. McEachern, P. Taylor, *J. Nucl. Mater.* **1998**, *254*, 87.
(53) C. Guéneau, M. Baichi, D. Labroche, C. Chatillon, B. Sundman, *J. Nucl. Mater.* **2002**, *304*, 161.
(54) T. B. Lindemer, T. M. Besmann, *J. Nucl. Mater.* **1985**, *130*, 473.
(55) R. J. M. Konings, O. Beneš, A. Kovács, D. Manara, D. Sedmidubský, L. Gorokhov, V. S. Iorish, V. Yungman, E. Shenyavskaya, E. Osina, *J. Phys. Chem. Ref. Data* **2014**, *43*, 013101.
(56) V. M. Goldschmidt, L. Thomassen, *Videnskapsselskapets Skrifter. I. Mat.-Naturv. Klasse* **1923**, 48.
(57) B. T. M. Willis, *Proc. Phys. Soc., London* **1963**, *274*, 122.
(58) G. L. Miessler, P. J. Fischer, D. A. Tarr, *Inorganic Chemistry (5th Edition)*, Prentice Hall, Instock, **2014**.
(59) F. Grønvold, *J. Inorg. Nucl. Chem.* **1955**, *1*, 357.
(60) B. T. M. Willis, *Proc. Brit. Ceram. Soc.* **1964**, *No. 1*, 9.
(61) P. Perio, *Bull. Soc. Chim. Fr.* **1953**, 256.
(62) L. Lynds, A. W. Young, S. J. Mohl, G. G. Libowitz, *X-Ray and Density Study of Nonstoichiometry in Uranium Oxides* in *Nonstoichiometric Compounds, Vol. 39*, American Chemical Society, **1963**, pp. 58.
(63) V. V. Rachev, V. S. Smurova, L. M. Kovba, E. A. Ippolitova, *Zh. Neorg. Khim.* **1965**, *10*, 2796.
(64) B. Belbeoch, J. C. Boivineau, P. Perio, *J. Phys. Chem. Solids* **1967**, *28*, 1267.
(65) B. Touzelin, M. Dode, *Rev. Int. Hautes Temp. Refract.* **1969**, *6*, 267.
(66) V. A. Alekseyev, L. A. Anan'yeva, R. P. Rafal'skiy, *Int. Geol. Rev.* **1981**, *23*, 1229.
(67) K. Teske, H. Ullmann, D. Rettig, *J. Nucl. Mater.* **1983**, *116*, 260.
(68) B. T. M. Willis, *Nature* **1963**, *197*, 755.
(69) B. T. M. Willis, *Acta Crystallogr. A* **1978**, *34*, 88.
(70) B. T. M. Willis, *J. Phys. (Paris)* **1964**, *25*, 431.
(71) B. Belbeoch, C. Piekarski, P. Perio, *Acta Crystallogr.* **1961**, *14*, 837.
(72) H. Blank, C. Ronchi, *Acta Crystallogr. A* **1968**, *24*, 657.
(73) G. C. Allen, P. A. Tempest, *J. Chem. Soc., Dalton Trans.* **1982**, 2169.
(74) G. C. Allen, P. A. Tempest, *J. Chem. Soc., Dalton Trans.* **1983**, 2673.
(75) A. D. Murray, B. T. M. Willis, *J. Solid State Chem.* **1990**, *84*, 52.
(76) D. J. M. Bevan, I. E. Grey, B. T. M. Willis, *J. Solid State Chem.* **1986**, *61*, 1.
(77) B. T. M. Willis, *J. Chem. Soc., Faraday Trans. II* **1987**, *83*, 1073.
(78) D. J. M. Bevan, O. Greis, J. Straehle, *Acta Crystallogr., Sect. A* **1980**, *A36*, 889.
(79) L. Desgranges, G. Baldinozzi, G. Rousseau, J.-C. Nièpce, G. Calvarin, *Inorg. Chem.* **2009**, *48*, 7585.
(80) R. I. Cooper, B. T. M. Willis, *Acta Crystallogr. A* **2004**, *60*, 322.
(81) J. P. Lauriat, G. Chevrier, J. X. Boucherle, *J. Solid State Chem.* **1989**, *80*, 80.
(82) L. Nowicki, F. Garrido, A. Turos, L. Thomé, *J. Phys. Chem. Solids* **2000**, *61*, 1789.

(83) F. Garrido, R. M. Ibberson, L. Nowicki, B. T. M. Willis, *J. Nucl. Mater.* **2003**, *322*, 87.
(84) H. He, D. Shoesmith, *Phys. Chem. Chem. Phys.* **2010**, *12*, 8109.
(85) B. Loopstra, *Acta Crystallogr. B* **1970**, *26*, 656.
(86) B. O. Loopstra, *Acts Cryst.* **1964**, *17*, 651.
(87) L. Quémard, L. Desgranges, V. Bouineau, M. Pijolat, G. Baldinozzi, N. Millot, J. C. Nièpce, A. Poulesquen, *J. Eur. Ceram. Soc.* **2009**, *29*, 2791.
(88) G. C. Allen, P. A. Tempest, J. W. Tyler, *Philos. Mag. B* **1986**, *54*, L67.
(89) G. C. Allen, N. R. Holmes, *J. Nucl. Mater.* **1995**, *223*, 231.
(90) P. Taylor, D. D. Wood, A. M. Duclos, D. G. Owen, *J. Nucl. Mater.* **1989**, *168*, 70.
(91) L. E. J. Roberts, *J. Chem. Soc.* **1954**, 3332.
(92) I. F. Ferguson, J. D. M. McConnell, *Proc. R. Soc. London, Ser. A Mat.* **1957**, *241*, 67.
(93) J. S. Anderson, L. E. J. Roberts, E. A. Harper, *J. Chem. Soc.* **1955**, 3946.
(94) M. Martin, W. Mader, E. Fromm, *Thin Solid Films* **1994**, *250*, 61.
(95) N. F. Mott, *Trans. Faraday Soc.* **1939**, *35*, 1175.
(96) N. F. Mott, *Trans. Faraday Soc.* **1940**, *35*, 472.
(97) F. J. Graham, H. C. Brookes, J. W. Bayles, *J. Appl. Electrochem.* **1990**, *20*, 45.
(98) A. K. Burnham, G. T. Jameson, *J. Vac. Sci. Technol., A* **1987**, *5*, 1713.
(99) N. F. Mott, *Trans. Faraday Soc.* **1947**, *43*, 429.
(100) N. Cabrera, N. F. Mott, *Rep. Prog. Phys.* **1949**, *12*, 163.
(101) D. Starodub, T. Gustafsson, E. Garfunkel, *Surf. Sci.* **2004**, *552*, 199.
(102) A. T. Fromhold, JR., *Theory of metal oxidation, Vol. 1 - Fundamentals*, North-Holland Publishing Company, Amsterdam, **1976**.
(103) U. R. Evans, *The Corrosion and Oxidation of Metals: Scientific Principles and Practical Applications*, St. Martin's Press, New York, **1960**.
(104) A. G. Ritchie, *J. Less Common Met.* **1984**, *98*, 193.
(105) P. E. Gharagozloo, M. P. Kanouff, *J. Am. Ceram. Soc.* **2013**, *96*, 2943.
(106) L. E. Thomas, R. E. Einziger, R. E. Woodley, *J. Nucl. Mater.* **1989**, *166*, 243.
(107) R. E. Einziger, L. E. Thomas, H. C. Buchanan, R. B. Stout, *J. Nucl. Mater.* **1992**, *190*, 53.
(108) L. E. Thomas, R. E. Einziger, *Mater. Charact.* **1992**, *28*, 149.
(109) A. Poulesquen, L. Desgranges, C. Ferry, *J. Nucl. Mater.* **2007**, *362*, 402.
(110) R. J. McEachern, *J. Nucl. Mater.* **1997**, *245*, 238.
(111) A. Leenaers, L. Sannen, S. Van den Berghe, M. Verwerft, *J. Nucl. Mater.* **2003**, *317*, 226.
(112) A. D. Whapham, B. E. Sheldon, *J. Nucl. Mater.* **1963**, *10*, 157.
(113) J. E. Stubbs, A. M. Chaka, E. S. Ilton, C. A. Biwer, M. H. Engelhard, J. R. Bargar, P. J. Eng, *Phys. Rev. Lett.* **2015**, *114*, 1.
(114) W. Jander, *Z. Anorg. Allg. Chem.* **1927**, *163*, 1.
(115) A. M. Ginstling, B. I. Brounshtein, *Zh. Prikl. Khim. (S.-Peterburg, Russ. Fed.)* **1950**, *23*, 1327.
(116) S. Aronson, B. Roof, J. Belle, *J. Chem. Phys.* **1957**, *27*, 137.
(117) G. Rousseau, L. Desgranges, F. Charlot, N. Millot, J. C. Nièpce, M. Pijolat, F. Valdivieso, G. Baldinozzi, J. F. Bérar, *J. Nucl. Mater.* **2006**, *355*, 10.

(118) P. E. Blackburn, J. Weissbart, E. A. Gulbranson, *J. Phys. Chem.* **1958**, *62*, 902.
(119) D. E. Y. Walker, *J. Appl. Chem.* **1965**, *15*, 128.
(120) H. R. Hoekstra, A. Santoro, S. Siegel, *J. Inorg. Nucl. Chem.* **1961**, *18*, 166.
(121) B. Loopstra, *J. Appl. Crystallogr.* **1970**, *3*, 94.

Chapter 2.

Accurate lattice parameter measurements of stoichiometric uranium dioxide

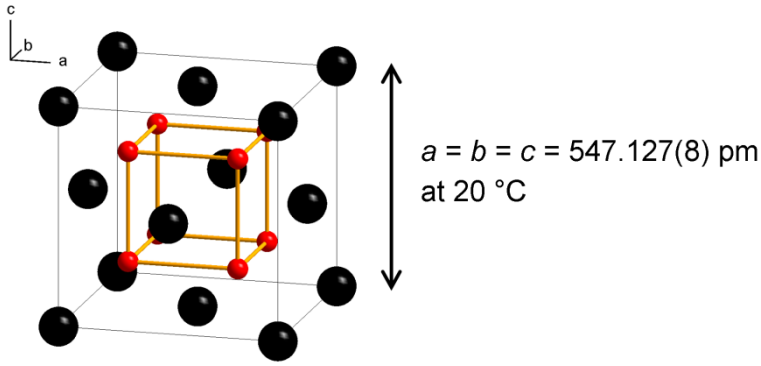

Fluorite-type UO_2 crystal structure

Reproduced from: Gregory Leinders, Thomas Cardinaels, Koen Binnemans, Marc Verwerft, *Journal of Nuclear Materials* **2015**, *459*, 135-142.

Author contributions

Gregory Leinders performed the experimental work and data analysis, including the calibration of the X-ray diffractometer, and the writing of this manuscript. He also contributed to the experimental strategy and the scientific ideas.

2.1 Introduction

UO_2 exhibits a homogeneous range of compositions near exact stoichiometry which have an effect on the lattice parameter. For details about the uranium – oxygen system, see e.g. the reviews of McEachern and Taylor, Guéneau *et al.*, Chevalier *et al.*, Kurepin, Labroche *et al.*, Baichi *et al.* and references therein.[1-8] Given the difficulties to keep UO_2 at exact stoichiometry, precise lattice parameter determination is not straightforward. The lattice parameter has been evaluated as 547.04 ± 0.08 pm at 20 °C by Grønvold in 1955.[9] This value has been adopted as principal reference also by the International Atomic Energy Agency (IAEA).[10] Numerous other values have been published by researchers over the past decades (Table 2.1). Precise knowledge of the lattice parameter of uranium dioxide (UO_2) is important for engineering and research purposes.

When exposed to air, freshly reduced UO_2 powder will rapidly oxidize also at ambient temperatures. Bannister reviewed the low temperature oxidation of UO_2 and found that even for powders with low specific surface area (e.g. 0.5 $m^2\ g^{-1}$), O/U ratios of 2.006 can be found after 24 h of exposure.[11] For powders with a higher specific surface, the limiting amount of hyperstoichiometry can be much higher. The oxidation mechanism is chemisorption of oxygen which starts already at the boiling isotherm of oxygen, i.e. at −183 °C, followed by sub-surface oxidation which starts around −130 °C.[12, 13] The sub-surface oxidation is limited to a depth of approximately 5 nm and it is invariant for temperatures up to 50 °C, the amount of oxygen absorbed being proportional to the surface area.[13] The oxidation of sintered polycrystalline UO_2 follows the same mechanisms and for pellets with high levels of open porosity, macroscopically measurable oxidation can be observed. For pellets which are sintered to densities above 95% of the theoretical density (TD), i.e. when all porosity is closed, the oxidation at ambient conditions is limited to the formation of a thin surface layer. Bulk oxidation is measured only at higher temperatures (> 100 °C), where oxygen diffusion proceeds at a detectable rate.[1, 14]

Upon oxidation the cubic lattice of UO_2 (Figure 2.1) slightly distorts and contracts. Oxygen atoms are incorporated in the cubic-coordinated interstitial sites which are displaced in either the [110] or the [111] directions and oxygen vacancies are formed at the normal sites, with the uranium sublattice remaining undisturbed.[15-17] Willis concluded that the defects cluster together in defect clusters or complexes, with each complex containing interstitial oxygen atoms and vacant normal oxygen sites in the so-called 2:2:2 configuration.[18] The UO_2 lattice contraction is attributed to charge compensation: the excess oxygen is balanced by a valence shift of U^{4+} to $U^{5+/6+}$. The ionic radii of $U^{5+/6+}$ being smaller than that of U^{4+} and the higher specific charge result in a net lattice contraction. This effect is quite substantial and various contraction ratios

have been reported, ranging from -5.5×10^{-3} pm to -15×10^{-3} pm per 0.001 amount of hyperstoichiometry.[19-25]

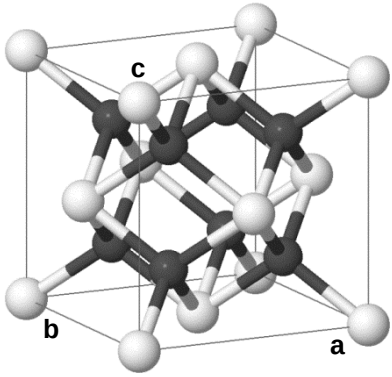

Figure 2.1. Unit cell of the face-centered cubic crystal structure of UO_2. The tetrahedral-coordinated anion sites (oxygen sublattice) are shown in black. The cubic-coordinated cation sites (uranium sublattice) are shown in light grey shade. The normal interstitial sites are found in the cell edge centers 0,0,½; 0,½,0; ½,0,0 and the cell center ½,½,½. Illustration created with Jmol.[26]

Recent work by Cardinaels *et al.* reported a lattice parameter of $UO_{2.001}$ which was higher than the generally accepted value.[27, 28] The focus of that work was on lattice contraction with doping and not specifically oriented on the pure UO_2 material. In the present work, we focus on undoped UO_2 and we pay specific attention to avoid deviations from stoichiometry.

For the experimental assessment of the lattice parameter of stoichiometric UO_2, we have prepared densely sintered polycrystalline pellets (TD > 97%) under two different reducing atmospheres and for one of the conditions, we used two different feed powders. Precise X-ray diffraction and thermogravimetric measurements were performed and yielded a consistent set of data from which an accurate value of the lattice parameter of $UO_{2.000}$ is derived. The parameters influencing the accuracy of the lattice parameter are carefully analyzed and evaluated.

Table 2.1. Selection[a] of the published data on the lattice parameter of UO_2.

Lattice parameter *a* (pm) reported	Temperature reported (°C)	Lattice parameter *a* (pm) at 20 °C[b]	O/U stated	Reference
547.109 ± 0.006	25.3 ± 0.5	547.081	2.001	Cardinaels, 2012[27]
547.0[c]	20	547.0	2[d]	Hutchings, 1987[29]
546.96 ± 0.04[e]			2[e]	Alekseyev, 1981[24]
547.06 ± 0.05	25	547.03	2.001	Lynds, 1963[20]
546.9 ± 0.1			2.00[d]	Blackburn,
547.1 ± 0.1			2.00	1958[14]
547.04 ± 0.08	20 ± 2	547.04	2.00	Grønvold, 1955[9]
546.91 ± 0.01[f]			2.000	Perio, 1953[19]
546.8 ± 0.1[f]			2.00	Herring, 1952[30]

[a] Values were selected from researchers that sufficiently specified their sample preparation methods, analysis methods and uncertainties.
[b] Lattice parameter values reported at a specific temperature are recalculated to 20 °C using the thermal linear expansion coefficient of UO_2.[31]
[c] Measured with neutron diffraction on a single crystal sample.
[d] Assumed value.
[e] Extrapolated result to O/U = 2.
[f] Original value converted from *kX* unit by multiplying a factor 100.2077 pm.[32]

2.2 Experimental

2.2.1 Sample preparation

Three samples were prepared from two batches of depleted uranium oxide powder ($\sim UO_{2.1}$) obtained via Integrated Dry Route (IDR) synthesis and supplied by FBFC International (Dessel, Belgium). The two batches differed in impurity content, both being of nuclear grade. Chemical analysis of the starting material is shown in section 2.3.1.

The samples were prepared using an identical approach. The as-received powder was compacted at 400 MPa into cylindrical pellets. A semi-automatic press (Specac Atlas 8T) was used with a compaction time of 30 s. The pressing die and punches were lubricated with a saturated solution of stearic acid in acetone. This ensured a safe operation of the press and the production of high quality green pellets. Several UO_2 pellets were prepared for each experimental route.

Sintering was performed to reduce the $UO_{2.1}$ to stoichiometry and to densify the green bodies to almost complete density. A Linn HT 1800 Moly high-temperature furnace with an alumina matrix and molybdenum heating elements was used. The sintering atmosphere was monitored with a dew point analyzer and an oxygen analyzer. The dew point of the exiting gas is −80 °C, owing to a very good gas tightness of the system. Green pellets were placed in an alumina crucible fitted with a molybdenum sheet. After placing the crucible containing the samples in the furnace, the system was sealed and flushed until the dew point of the exiting gas reached −60 °C or less.

Table 2.2. Parameters changed between the three samples.

Sample	Powder batch	μ_{O_2} at sintering temp. (kJ mol^{-1})
UO_2 (A)	1	-420 ± 10
UO_2 (B)	1	-540 ± 10
UO_2 (C)	2	-540 ± 10

Two different sintering conditions were used (Table 2.2). A heating rate of 5 °C min^{-1} was always applied. The sintering temperature was 1680 °C and maintained for 4 h. The cooling rate was inherent to the furnace and decreased logarithmic from 5 °C min^{-1} to about 0.5 °C min^{-1} during 15 h. Sample A was sintered under a mixture of 5 vol.% hydrogen and 0.5 vol.% oxygen in argon. Sample B and C were sintered under a gas atmosphere containing 5 vol.% hydrogen in argon. Final density was > 97%, and the remaining porosity was fully closed.

2.2.2 Thermogravimetric analysis

The stoichiometry was measured by thermogravimetric analysis (TGA) with a Netzsch STA 449 ***F1*** Jupiter®. Compounds in the exiting gas flow could be identified with an in-line 403 D Aëolos® quadrupole mass spectrometer. The oxygen and water contents of the exiting gas were monitored with an oxygen and dew point analyzer, respectively. The ASTM C1453-00 standard procedure for measuring the uranium and oxygen-to-uranium atomic ratio by the ignition impurity correction method was used as a basis for the practical procedure using TGA.

Fragments of a sintered pellet (approximately 1 g in total) were placed in an alumina crucible and weighed on an analytical balance in lab environment. After insertion in the TGA apparatus the furnace was sealed, evacuated and refilled with dry argon gas three consecutive times to remove atmospheric impurities. During analysis a constant flow of synthetic air was maintained in the furnace chamber. The sample was heated to 500 °C

and remained at this temperature for 3.5 h. This ensured complete oxidation to U_3O_8 of the initial material. Preliminary tests showed that a preheating step to correct for mass loss due to desorption was not required on these samples.

In the used configuration, the absolute uncertainty on weight readout was measured to be ± 14 μg (1σ), taking drift and noise of the apparatus into account.

2.2.3 X-ray diffraction

Accurate lattice parameter measurements were done by X-ray diffraction. A Philips X'Pert Pro diffractometer utilizing the Bragg-Brentano parafocusing geometry and a θ-θ configuration was employed. Zero point calibration was performed with a sintered Si disc of high purity. Validation is performed against a sintered Al_2O_3 disc (NIST Standard Reference Material 1976b) on a weekly basis. The instrument bias was assessed by verifying the lattice parameter refinement of Si and found to be smaller than 10^{-5} relative (1σ).

An LFF X-ray tube ($CuK\alpha_1$ = 1.5405929 Å)[33] was used as radiation source. The optics of the incident and diffracted beam path were carefully aligned and optimized for the specific samples to ensure a maximum in recorded peak intensity while keeping the scatter from the sample holder as low as possible. A fixed divergence slit in combination with 0.02 rad Soller slits and a copper beam mask ensured the measurement of high-quality diffractograms with low axial divergence. The diffracted beam path was foreseen with 0.02 rad Soller slits and a Ni filter. Detection was done with a position-sensitive detector (PANalytical X'Celerator). This detector operated in scanning mode with an active length of 2.122 ° (2θ). All diffractograms were recorded with a continuous scan in the range 27-141 ° (2θ), using a step size of 0.004 °. The total measuring time was 120 min.

The lattice parameter was calculated using the unit cell refinement method in the PANalytical X'Pert HighScore Plus (v4.1) software. Only $K_{\alpha 1}$ reflections were used in the calculation. This least squares method takes all recorded reflections into account. The uncertainty (1σ) on the lattice parameter is combined with the effect of sample temperature uncertainty (see §2.3.3). Sample displacements were measured and corrected for via the software. Lattice parameters were recalculated to their values at a reference state of 20 °C. For this purpose, the linear thermal expansion coefficient for UO_2 (9.739×10^{-6} °C^{-1} near room temperature) was used.[31]

Sintered pellets were embedded in a conducting phenolic resin by hot mounting in a Struers CitoPress. The side showing the inserted pellet was then ground with SiC sanding paper of successively smaller grain sizes (smallest grain size: 3 μm) and

finished by polishing on cloths with diamond paste (grain size: 1 µm) to achieve a flat and mirror-like surface.

2.2.4 Impurity analysis

A quantitative evaluation of the trace elements in the starting powder was made via inductively coupled plasma-mass spectrometry (ICPMS) using a ThermoFisher XSeries2. In particular, elements such as lead, the lanthanides and some of the actinides were focused on. In total, 50 elements were measured. A sample of the oxide powder (1 g) was dissolved in 8 M nitric acid solution. Aliquots of this solution were further diluted and prepared for analysis.

The instrument was used in the manufacturer's standard configuration. The elements were divided into convenient to measure groups based on their atomic masses, their expected concentrations and potential interferences. Multi-element calibration standards containing the elements in each of these groups were prepared from single-element standards (except for Np and Pu). Internal standards (Sc, Y, Rh, La, Lu, Ir, Th) were used to correct for any internal drift. Quantification was done by external calibration, except for Np and Pu. The instrumental response is almost constant at high masses, so the response at m/z = 235 for a known concentration of a depleted (0.56 at.% ^{235}U) single element U standard can be applied to other actinides and used to quantify the mass fractions of the ^{237}Np and ^{240}Pu and ^{242}Pu isotopes.

The isotope ratios were determined by TIMS (Thermal Ionization Mass Spectrometry) using a VG Sector 54 instrument. The instrument is equipped with 5 Faraday cups and isotope amount ratio measurements were performed in static mode monitoring masses at m/z = 233, 234, 235, 236, 238 using non-zone refined rhenium triple filaments which were loaded with approximately 1 µg of uranium. The samples were evaporated conventionally, once measurements of quality control standards at the start of the analysis sequence were within specification. Mass fractionation was corrected for by using external standard reference materials certified for their $^{235}U/^{238}U$ isotope ratios.

2.3 Results

2.3.1 Chemical analysis

The amount of impurities was as expected for depleted uranium oxide obtained via IDR synthesis (see Table 2.3). The total amount of quantifiable metallic impurities was equal to 93 ± 41 μg g^{-1} for batch 1, and 37 ± 21 μg g^{-1} for batch 2. The remainder of the selected impurity elements were present in quantities below their limit of detection. From the results of TIMS analysis the atomic weight of U is found to be 238.04252 ± 0.00002 g mol^{-1} in batch 1. In batch 2, this value was equal to 238.04104 ± 0.00002 g mol^{-1}.

Table 2.3. Quantifiable impurity levels measured via ICPMS in uranium oxide powder batch 1 and 2[a]. Values given in μg g^{-1}.

	Batch 1	Batch 2		Batch 1	Batch 2
Li	1.0 ± 0.7	0.9 ± 0.7	**Zn**	8 ± 4	1.5 ± 0.8
Be	< 0.06	0.09 ± 0.06	**Zr**	0.09 ± 0.05	0.06 ± 0.04
B	2.9 ± 1.5	1.8 ± 1.3	**Mo**	0.36 ± 0.21	0.18 ± 0.14
Mg	14 ± 7	< 2	**Cd**	0.06 ± 0.04	0.08 ± 0.05
Al	26 ± 8	4.1 ± 1.4	**In**	0.026 ± 0.014	0.018 ± 0.010
Cr	1.2 ± 0.6	0.27 ± 0.17	**Sn**	5 ± 5	4 ± 4
Mn	0.44 ± 0.22	0.28 ± 0.14	**Ba**	0.58 ± 0.23	< 0.5
Fe	15 ± 8	23 ± 12	**La**	0.034 ± 0.010	0.025 ± 0.008
Co	0.035 ± 0.021	< 0.01	**Ce**	0.007 ± 0.003	< 0.001
Ni	15 ± 4	0.53 ± 0.16	**Gd**	0.033 ± 0.017	0.006 ± 0.004
Cu	2.9 ± 1.5	0.15 ± 0.11	**Pb**	0.40 ± 0.20	0.11 ± 0.05

[a] The remainder of the selected impurity elements were Na, Si, P, K, Ca, Ti, V, Rb, Sr, Ag, Nd, Sm, Eu, Tb, Dy, Ho, Er, Tm, Yb, Lu, Ta, W, Hg, Bi, Th, ^{237}Np, ^{240}Pu, ^{242}Pu.

The stoichiometry analysis (see next paragraph) is substantially affected by the presence of impurities. Not only is the calculated metallic fraction of U affected, some species may also react during oxidation thus contributing to the witnessed mass difference. Table 2.4 lists the expected molecular form of the quantifiable impurities present in the sintered and oxidized sample. Using these data, the maximum weight contribution of the quantifiable impurities is recalculated. Samples A and B contain an estimated 136 ± 59 μg g^{-1} of impurity compounds after sintering. After oxidation this value increases to 149 ± 65 μg g^{-1}. Sample C contains an estimated 47 ± 27 μg g^{-1} of impurity compounds after sintering. After oxidation this value increases to 62 ± 33 μg g^{-1}. The stoichiometry analysis is corrected for these effects.

Some impurities are expected to evaporate. In the case of total evaporation of all the compounds indicated in Table 2.4, we calculated the resulting effect on the measured stoichiometry to be < 0.0001.

Table 2.4. Molecular form of selected impurities in the initial and oxidized sample.

Impurity element	Molecular form in	
	Initial sample (sintered)	Oxidized sample
Li	Li_2O	Li_2O
Be	BeO	BeO
B	B_2O_3[a]	B_2O_3
Mg	MgO	MgO
Al	Al_2O_3	Al_2O_3
Cr	Cr_2O_3[a]	Cr_2O_3
Mn	MnO[a]	MnO_2
Fe	Fe	Fe_2O_3
Co	Co	CoO
Ni	Ni	NiO
Cu	Cu	CuO
Zn	ZnO[a]	ZnO
Zr	ZrO_2	ZrO_2
Mo	Mo	MoO_3[a]
Cd	Cd[a]	CdO
In	In[a]	In_2O_3
Sn	Sn[a]	SnO_2
Ba	BaO	BaO
La	La_2O_3	La_2O_3
Ce	Ce_2O_3	CeO_2
Gd	Gd_2O_3	Gd_2O_3
Pb	Pb[a]	PbO_2

[a] Will evaporate during heat treatment.

2.3.2 Stoichiometry measurement

A general way for determining the unknown stoichiometry x in a UO_{2+x} sample is the method based on the weight difference after oxidation to U_3O_8 (cf. ASTM C1453-00). Here, the atomic fraction of uranium is calculated from the amount of U_3O_8 obtained. Ideally, only the reaction

$$3\,UO_{2+x} + \frac{1}{2}(2-3x)\,O_2 \rightarrow U_3O_8 \qquad \textbf{(2.1)}$$

accounts for the weight gain after oxidation, resulting in a straight-forward calculation to obtain the initial stoichiometry. In practice, however, the presence of impurities must be corrected for. Also, if adsorbates are present on either the initial sample with unknown stoichiometry, on U_3O_8, or on both, the recorded weight change differs from the ideal case.

The fraction of uranium per initial sample weight (U_w) was calculated using Eq. (2.2)

$$U_w = \frac{1}{y} \cdot \frac{z \cdot (1 - I_O)}{1 + \frac{8 \cdot M_O}{3 \cdot M_U}} - C_{nq} \quad \textbf{(2.2)}$$

with y the initial sample weight of UO_{2+x} (g), z the resulting U_3O_8 sample weight (g), I_O the total amount of all impurity compounds present per gram U_3O_8 (g g^{-1}), and M_O (= 15.99940 g mol^{-1}) and M_U the atomic weights of oxygen and uranium, respectively. The value of the atomic weight of uranium is the one calculated from its actual isotopic vector as shown in §2.3.1. Additionally, the U_w value is lowered with a constant value (C_{nq} = 0.0001 g g^{-1}, or 100 µg g^{-1}) to correct for the presence of non-quantifiable impurities (ASTM C1453-00). Finally, the stoichiometry (O/U) is calculated using Eq. (2.3)

$$O/U = \frac{M_U}{M_O} \cdot \frac{1 - U_w - I}{U_w} \quad \textbf{(2.3)}$$

with I the total amount of impurity elements and compounds present per initial sample weight (g g^{-1}). Correction for moisture content was left out as our TGA tests showed no detectable mass loss from sintered pellet fragments heated at 150 °C in inert atmosphere for 3 h.

The stoichiometry of the pellets was derived from the *in situ* mass difference at 50 °C, i.e. before and after oxidation. An overview of the results is given in Table 2.5. All three samples can be considered to be stoichiometric, within the error of the measurement.

Table 2.5. Stoichiometry of the different samples.

Sample	O/U	Propagated error
UO_2 (A)	1.999	± 0.001
UO_2 (B)	2.000	± 0.001
UO_2 (C)	1.9997	± 0.0006

The following experimental uncertainties were taken into account for the propagated error on the stoichiometry: quantifiable and non-quantifiable impurities, weight readout, atomic weight, and isotopic vector of uranium. Using the values as shown in Table 2.6 the propagated error on the calculated stoichiometry of samples A and B is equal to ± 0.001 (1σ) while that of sample C is equal to ± 0.0006 (1σ).

Table 2.6. Overview of the various experimental uncertainties and their effect on stoichiometry measurement by TGA.

		Uncertainty	Effect on stoichiometry
Quantifiable impurities (µg g^{-1})	**Batch 1**	Sintered: 59 Oxidized: 65	± 0.001
	Batch 2	Sintered: 27 Oxidized: 33	± 0.0005
Analytical balance uncertainty (µg)		20	± 0.0003
STA balance uncertainty (µg)		14	± 0.0002
Non-quantifiable impurities (µg g^{-1})		10	± 0.0002
Oxygen atomic weight (µg mol^{-1})		10	± 0.0001
Uranium atomic weight (µg mol^{-1})		20	± 0.000008

2.3.3 X-ray diffraction

The measured lattice parameter values (a_T) are shown in Table 2.7. Each sample was measured two times over the course of two weeks. The uncertainty on the as-measured lattice parameter (σ_{a_T}) is obtained from the least squares refinement.

Table 2.7. Lattice parameter results of the different samples.

	a_T (pm)	σ_{a_T} (pm)	Temperature[a] (°C)	Δa (pm)	$\sigma_{\Delta a}$ (pm)	a at 20 °C (pm)	σ_a (pm)
UO_2 (A)	547.159	0.002	24.5 – 26.0	-0.028	0.002	547.131	0.003
	547.157	0.002	25.0 – 26.5	-0.031	0.002	547.126	0.003
UO_2 (B)	547.162	0.002	25.5 – 27.0	-0.033	0.002	547.129	0.003
	547.157	0.002	24.5 – 26.0	-0.028	0.002	547.129	0.003
UO_2 (C)	547.149	0.003	25.0 – 26.5	-0.030	0.002	547.119	0.004
	547.158	0.003	25.0 – 26.5	-0.031	0.002	547.127	0.004

[a] Temperature inside the XRD apparatus after thermal stabilization, directly before and after XRD analysis.

Samples were thermally stabilized in the XRD apparatus overnight. The temperature inside the apparatus was measured directly before and after X-ray analysis. The average of these two values (T) was used to correct for thermal expansion of the lattice (Δa). The as-measured lattice parameter a_T at temperature T is recalculated to its value at 20 °C according to the equation

$$a = a_T \cdot \big(1 - \alpha \cdot (T - 20)\big) \qquad \textbf{(2.4)}$$

with α = 9.739 × 10^{-6} °C^{-1} the linear thermal expansion coefficient for UO_2.[31] The probability distribution of the temperature is conservatively taken as uniform, with central value the average of the two readings (T_2, T_1) and width $\Delta T = T_2 - T_1$. The variance is then $\frac{1}{3}\left(\frac{\Delta T}{2}\right)^2$ and the uncertainty $\frac{\Delta T}{2\sqrt{3}}$. The uncertainty on temperature correction ($\sigma_{\Delta a}$) is calculated using Eq. (2.4). Combination of these uncertainties yields the propagated error on the corrected lattice parameter (σ_a)

The parameters used in this study to assess the quality of the measured X-ray diffractograms are: (1) the net statistical counting error, calculated through the Jenkins and Schreiner figure of merit (FOM),[34] (2) the full width at half-maximum (FWHM) of the (422) peak, measured as 2θ (°), and (3) the scatter on the observed peak positions relative to the theoretical peak positions. This last parameter, which describes the quality of the metric aspects of the powder pattern, is also estimated by the Smith and Snyder FOM.[35] Table 2.8 shows the average results of the quality assessment of the diffractograms used for calculating the lattice parameter of the UO_2 samples. The narrow scatter on the peak positions is recognized in the very high Smith and Snyder FOM values, which indicate excellent quality of the recorded diffractograms.[36] Figure 2.2 shows the recorded XRD pattern of sample B together with the residual on the peak positions. All measured patterns were consistent throughout the analysis period.

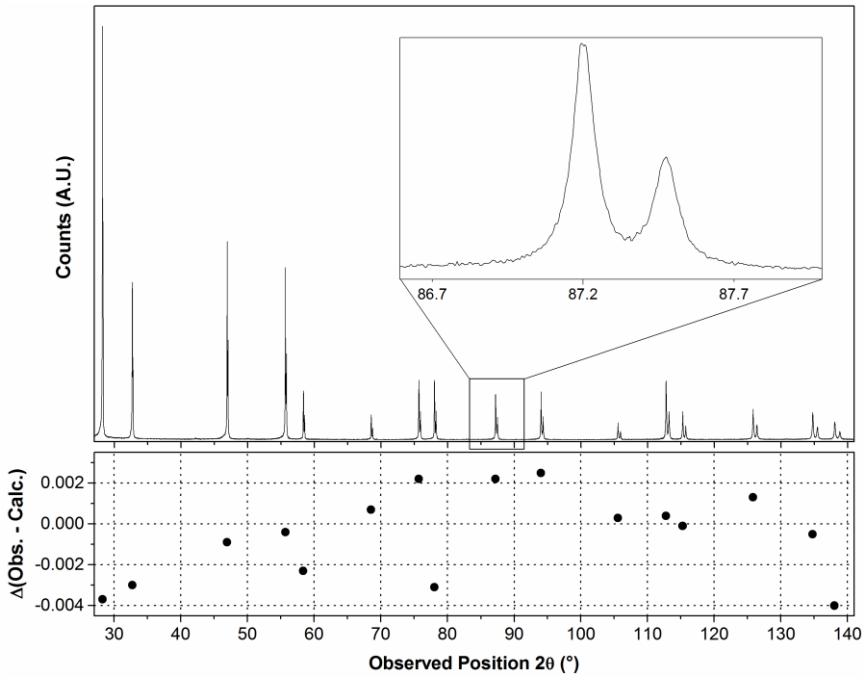

Figure 2.2. XRD pattern of sample B. The inset shows a close up of the UO_2 (422) reflection. At the bottom, the observed peak scatter is plotted.

Table 2.8. Assessment of the quality aspects of the recorded X-ray diffractograms.

Sample	Jenkins & Schreiner FOM	FWHM (422) peak 2θ (°)	Observed peak scatter[a] 2θ (°)	Smith & Snyder FOM
UO_2 (A)	60	0.109	< 0.007	493
UO_2 (B)	65	0.105	< 0.005	498
UO_2 (C)	48	0.146	< 0.007	324

[a] Value taken as the maximum difference between observed and theoretical peak positions.

2.4 Discussion

It is well known that freshly reduced fine UO_2 powder is unstable in air at room temperature, i.e. it will rapidly absorb oxygen.[11-13, 37] To minimize the uptake of oxygen we choose to produce sintered pellets with high densities (> 97% TD). Any oxidation is then confined to the very surface of the sample (less than 5 nm) and will not disturb the XRD analysis which has a substantially larger information depth, varying between 0.6 µm for low-angle to 3.5 µm for high-angle reflections.[1] This behavior is further confirmed by the fact that XRD patterns show no change after several weeks of exposure to the ambient atmosphere.

Two slightly different sintering atmospheres were applied: samples B and C underwent the most reducing condition (-540 kJ mol^{-1} at 1680 °C), while a slightly less reducing condition (-420 kJ mol^{-1} at 1680 °C) was applied for sample A. Using the equations of Lindemer and Besmann equilibrium values for different levels of hypo- and hyperstoichiometry of $UO_{2\pm x}$ as a function of temperature can be calculated (see Figure 2.3).[38] The calculated equilibrium lines of the applied gas mixtures (H_2, O_2 and H_2O) for the two conditions are also presented in the same figure.

The most reducing condition (applied for samples B and C) is expected to yield a slight hypostoichiometry at sintering temperature, whereas the less reducing condition (sample A) is expected to yield a slight hyperstoichiometry. During cooldown, both atmospheres enter a domain of very slight hyperstoichiometry ($2.0000 < O/U < 2.0001$). Sample A is thus always kept in slightly hyperstoichiometric conditions while samples B and C are expected to have gone from slightly hypo- to slightly hyperstoichiometry during cooldown.

Given the sintering and cooling conditions and knowing that below 1200 °C there is no measurable hypostoichiometric UO_{2-x} range,[2, 3, 17, 39] the thermogravimetric results of Table 2.5 indicate that all samples are fully stoichiometric within the experimental uncertainty margin. It would indeed be highly improbable that sample A, which was

kept in slight hyperstoichiometry during the complete sintering and cooldown process would be hypostoichiometric while the two other samples which were sintered at more reducing conditions actually have more elevated O/U values. In fact, the uncertainty on exact stoichiometry may be considered to be single sided towards hyperstoichiometry.

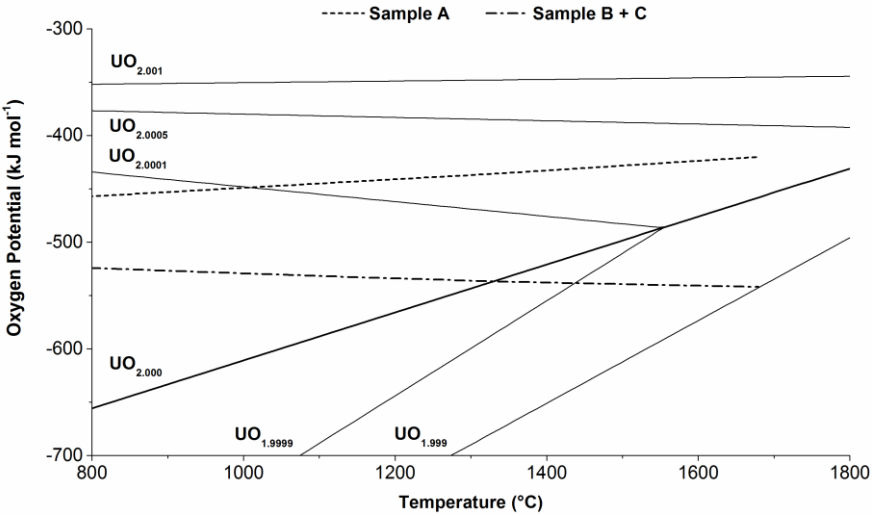

Figure 2.3. Ellingham diagram showing the oxygen potential equilibrium values of $UO_{2\pm x}$ according to the equations presented by Lindemer and Besmann.[38] The temperature dependent value of the oxygen potential according to the applied gas mixtures is shown by a dashed line (sample A) and a dash-dot line (samples B and C).

By far, the largest contribution to the propagated error on stoichiometry originates from the uncertainty on the impurity content (0.001 for batch 1 and 0.0005 for batch 2, see the first two rows in Table 2.6, §2.3.2). It should be mentioned that if the impurity content would be entirely ignored (the terms I_O and C_{nq} in Eq. (2.2) and the term I in Eq. (2.3)) the O/U ratio would be underestimated by 0.002. All other factors combined contribute to an uncertainty of ± 0.0004 on the O/U ratio. The propagated error is ± 0.001 for batch 1 and ± 0.0006 for batch 2.

The used method for stoichiometry analysis is based on but not identical to the ASTM C1453-00 standard procedure. The latter measured a precision of ± 0.002 on O/U value, i.e. interlab tests on a series of reference samples gave a standard deviation of ± 0.002 (1σ). The uranium content in these reference samples was separately measured using two different techniques and had a relative uncertainty of 0.06%, or ± 0.01 on O/U. In this study, the propagated error on a single sample measurement is slightly smaller compared to the ASTM precision because *in situ* TGA measurements were used to define the stoichiometry. The listed O/U values are corrected for non-quantifiable impurities, according to the ASTM standard procedure.

In Table 2.7 (§2.3.3), the results of the lattice parameter analysis of three different samples were given and for each sample two measurements were performed, yielding a total of six measurements. After temperature correction to 20 °C, the 95% confidence interval of the individual observations overlap, and we consider the complete data set to be representative for the lattice parameter determination of UO_2. The uncertainty on the average lattice parameter has several components: the dataset due to impurity content in solid solution, sintering conditions and sample degradation; the uncertainty of the individual refinements; temperature variation; and instrument bias. The contribution of the different sources of uncertainty are given in Table 2.9.

The population variance (σ_{pop}^2) estimates stochastic variations due to impurity effects, sample preparation and sample degradation. Numerous compounds are able to form a solid solution with UO_2, thus influencing the lattice parameter of the unit cell.[27, 28, 40-45] Experimental data, however, is not yet available for every system. The chemical analysis of Table 2.3 was used as a basis for the estimation of the impact of the impurity content on the lattice contraction or expansion. With the given concentrations, the effect on the lattice parameter is two orders of magnitude less than the uncertainty on the lattice parameter and is also part of the variance of the individual measurements (sample C versus samples A and B). Also the difference in sintering conditions (sample A versus samples B and C) is understood to be part of the population variance. Upon exposure of UO_2 to the ambient atmosphere, its oxidation is expected to occur. By using densely sintered samples, this is expected to be sufficiently slow. By repeating measurements, possible degradation is part of the variation between the individual measurements (first versus second measurement of all samples).

The refinement uncertainty was better than 0.003 pm for all analyses (see also Table 2.7), and in the summary of Table 2.9, the maximum uncertainty was taken to calculate the refinement variance ($\sigma_{a_T}^2$).

Table 2.9. UO_2 lattice parameter derived from the results listed in Table 2.7, total uncertainty and individual variances taken into account to derive the uncertainty on the lattice parameter value.

$\langle a \rangle_{20\,°C}$ (pm)	σ_{total} (pm)	σ_{pop}^2 (pm²)	$\sigma_{a_T}^2$ (pm²)	$\sigma_{\Delta a}^2$ (pm²)	σ_{instr}^2 (pm²)	σ_{total}^2 (pm²)
547.127	**0.008**	2.0×10^{-5}	9.0×10^{-6}	4.0×10^{-6}	2.5×10^{-5}	5.8×10^{-5}

The effect of sample temperature should not be underestimated. The variation on the lattice parameter value is 5×10^{-3} pm °C^{-1}.[31] For this reason, all samples were always thermally stabilized in the XRD apparatus overnight. The average value of the temperature inside the apparatus directly before and after the measurement was used to

recalculate the lattice parameter value at 20 °C (see also Table 2.7). The variance due to temperature uncertainty ($\sigma^2_{\Delta a}$) is identical for all samples. The instrument bias was discussed earlier (see §2.2.3) and it appears that the variance due to instrument bias (σ^2_{instr}) has the largest contribution in the total variance (Table 2.9).

At times of the earliest crystallographic studies on UO_2 (1940s) X-ray wavelengths were still defined in terms of the lattice parameter of calcite.[46] The relative unit known as k*X* was used. Values expressed in k*X* units could later be recalculated to Å units using a correction factor based on experimental data at that time. Throughout the years, this correction factor was adjusted. In the early 1950s the CuKα_1 wavelength was defined as 1.53740 k*X*. Recalculation using the factor 1.00202 yielded the absolute value of 1.54051 Å, as used by Grønvold and Lynds *et al.*[9, 20] In the 1960s, the correction factor was adjusted to 1.002056 and another relative wavelength unit was proposed by Bearden.[47] Alekseyev *et al.* utilized a value for CuKα_1 of 1.54056 Å.[24] The current value of the correction factor is 1.002077, or a CuKα_1 value of 1.540593 Å.[48] The most accurate measurement of the absolute wavelength of CuKα_1 was performed by Härtwig *et al.* in 1991.[33] Their value of 1.5405929 Å is the currently accepted value.[49, 50]

Much of the literature on the UO_2 lattice parameter lacks information about the actual source wavelength used, i.e. the authors either mention the combined $K_{\alpha 1,2}$ value or they do not specify any value at all. When the source $K_{\alpha 1}$ value is specified, however, one can recalculate the originally derived lattice parameter simply by multiplying with the ratio of current to old $K_{\alpha 1}$ value. Of the values cited in table 1, only three can be recalculated: the value of Grønvold, that of Lynds *et al.* and that of Alekseyev *et al.*[9, 20, 24] A recalculation using the currently accepted value of 1.5405929 Å (CuKα_1) results in a significant increase of their lattice parameter determinations (Table 2.10). Figure 2.4 presents in a graphical way the data of Table 2.10. It shows that the lattice parameter value determined in this work lies within the uncertainty range of the values reported by Grønvold and Lynds *et al.*, but is not in agreement with the values reported by Alekseyev *et al.* and Cardinaels *et al.*.[9, 20, 24, 27]

Table 2.10. Recalculated lattice parameter values.

Reported value (pm)	Recalculated value (pm)[a]	Corrected to $UO_{2.000}$[b] (pm)	Uncertainty (pm)	Reference
546.96	546.97		± 0.04	Alekseyev *et al.* [24]
547.03	547.06	547.07	± 0.05	Lynds *et al.* [20]
547.04	547.07		± 0.08	Grønvold [9]

[a] Recalculated using CuKα_1 = 1.5405929 Å.
[b] Corrected to stoichiometry using the relation of Lynds *et al.*.[20]

The UO_2 lattice parameter derived in the current study a = 547.127 ± 0.008 (Table 2.9) is higher than many earlier reported values (Table 2.1), even when taking into account the correction for $CuK\alpha_1$ wavelength (Table 2.10). As a result, the theoretical density of UO_2 calculated with the original lattice parameter value of Grønvold at 20 °C (10.9562 ± 0.0048 g cm^{-3}) decreases slightly to 10.9510 ± 0.0005 g cm^{-3} (both calculated for M_{Unat} = 238.02891 g mol^{-1} and M_O = 15.99940 g mol^{-1}). The uncertainty on the theoretical density is dominated by the uncertainty on the lattice parameter. When working with other enrichments, one must obviously take the effective mass of the actual uranium vector. The theoretical density of our samples (depleted uranium, see §2.3.1) is calculated as 10.9515 g cm^{-3}.

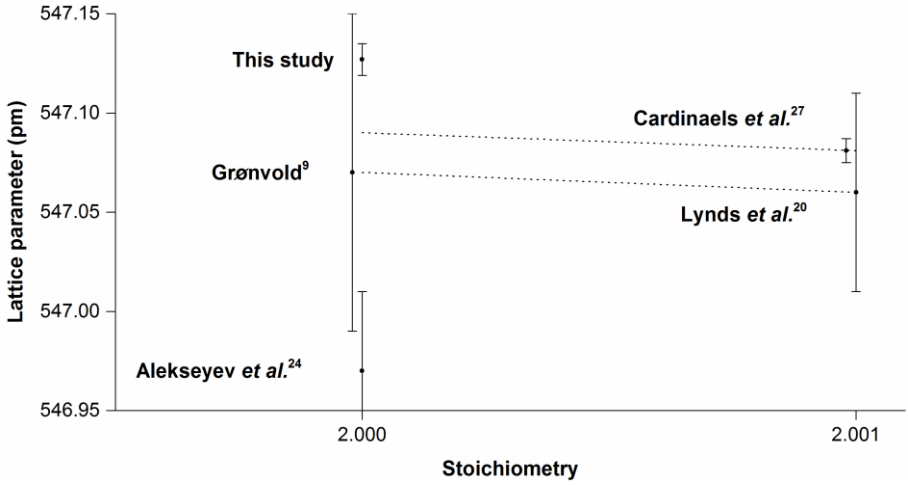

Figure 2.4. Presentation of the recalculated lattice parameter values of UO_2. Additionally, the data of Cardinaels *et al.* is added.[27] For clarification, some of the data points are shifted slightly left of their original position. The dashed lines present the effect of correcting for hyperstoichiometry on lattice parameter value.

A main cause for the increased value of the lattice parameter is attributed to the avoidance of hyperstoichiometry. Ambient oxidation of UO_2 powder may easily induce deviation from stoichiometry well in excess of 0.001. In the present study, the use of densely sintered UO_2 was adopted in order to prevent oxidation, while many of the earlier reported results stem from powder samples for which slight oxidation cannot be ruled out.

Material purity affects both stoichiometry and lattice parameter. As mentioned before, not correcting for the presence of impurities may result in an underestimation of up to 0.002 on stoichiometry, leading to a false interpretation of the measured lattice parameter. Few, if any, of the researchers cited in Table 2.1 performed a detailed impurity assessment. The use of lubricants or binders which contain a metallic

compound should be avoided during pelletizing. The sample discussed by Cardinaels *et al.* was prepared with zinc stearate as a lubricant.[27] Although this compound is expected to evaporate during calcination, it is not unlikely that some Zn remains in the body and forms a solid solution with UO_2, thus influencing the lattice parameter.

2.5 Conclusion

In this paper, the lattice parameter of stoichiometric UO_2 measured by X-ray diffraction on sintered pellets is reported. Furthermore, a discussion is given of the experimental difficulties encountered when preparing and measuring representative samples. The parameters influencing the accuracy of the lattice parameter measurement are carefully analyzed and evaluated.

XRD analysis performed over the course of two weeks gave consistent values for the lattice parameter of UO_2. No significant difference in both stoichiometry and measured lattice parameter was found between samples sintered at very reducing (-540 kJ mol^{-1}) or moderately reducing (-420 kJ mol^{-1}) atmospheres. Also the effect of feed powder with slightly different impurity content was not measurable.

The stoichiometry of the samples could be accurately measured using gravimetric methods based on the ASTM C1453-00 standard procedure for measuring the uranium and oxygen-to-uranium atomic ratio by the ignition impurity correction method. The prepared samples are stoichiometric within the error of the measurement.

The lattice parameter of $UO_{2.000 \pm 0.001}$ is evaluated as 547.127 ± 0.008 pm at a temperature of 20 °C, or 547.154 ± 0.008 pm at 25 °C. The significance of this re-evaluated value should not be underestimated. It is substantially higher than the generally accepted value of 547.04 ± 0.08 pm from Grønvold[9] and it results in a different theoretical density for UO_2 (10.9510 ± 0.0005 g cm^{-3} at 20 °C and $M_{UO2} = 270.0277$ g mol^{-1}), which is a key value in engineering context. Lattice contraction and lattice expansion studies are often performed to better understand the response of the UO_2 lattice to irradiation effects, to understand the effect of doping or the effect of oxidation. Research results are often expressed relative to the value of the undisturbed UO_2 system. Also for theoretical studies, structure data are often used either as input to develop parameterized interatomic potentials or to validate ab-initio calculations.

Older data on the lattice parameter of UO_2 were critically evaluated and suggestions were made to correct some of these values. The generally accepted value of 547.04 ± 0.08 pm from Grønvold should be recalculated to 547.07 ± 0.08 pm as it was originally derived using a now outdated value of the $CuK\alpha_1$ wavelength.[9]

Acknowledgements

G. L. thanks SCK•CEN for the financial support of this study. Also, the authors are indebted to A. Baena for assisting in sample preparatory work, and Dr. A. Dobney for providing ICPMS and TIMS analysis.

References

(1) R. J. McEachern, P. Taylor, *J. Nucl. Mater.* **1998**, *254*, 87.
(2) C. Guéneau, M. Baichi, D. Labroche, C. Chatillon, B. Sundman, *J. Nucl. Mater.* **2002**, *304*, 161.
(3) P. Y. Chevalier, E. Fischer, B. Cheynet, *J. Nucl. Mater.* **2002**, *303*, 1.
(4) V. A. Kurepin, *J. Nucl. Mater.* **2002**, *303*, 65.
(5) D. Labroche, O. Dugne, C. Chatillon, *J. Nucl. Mater.* **2003**, *312*, 21.
(6) D. Labroche, O. Dugne, C. Chatillon, *J. Nucl. Mater.* **2003**, *312*, 50.
(7) M. Baichi, C. Chatillon, G. Ducros, K. Froment, *J. Nucl. Mater.* **2006**, *349*, 57.
(8) M. Baichi, C. Chatillon, G. Ducros, K. Froment, *J. Nucl. Mater.* **2006**, *349*, 17.
(9) F. Grønvold, *J. Inorg. Nucl. Chem.* **1955**, *1*, 357.
(10) IAEA, *Thermophysical properties database of materials for light water reactors and heavy water reactors*, IAEA, Vienna, **2006**.
(11) M. J. Bannister, *J. Nucl. Mater.* **1968**, *26*, 174.
(12) L. E. J. Roberts, *J. Chem. Soc.* **1954**, 3332.
(13) J. S. Anderson, L. E. J. Roberts, E. A. Harper, *J. Chem. Soc.* **1955**, 3946.
(14) P. E. Blackburn, J. Weissbart, E. A. Gulbranson, *J. Phys. Chem.* **1958**, *62*, 902.
(15) C. Keller, *Comprehensive Inorganic Chemistry, Vol. 10*, Pergamon Press, Oxford, **1975**.
(16) B. T. M. Willis, *P. Brit. Ceramic Soc.* **1964**, *1*, 9.
(17) I. Grenthe, J. Drozdzynski, T. Fujino, E. C. Buck, T. E. Albrecht-Schmitt, S. F. Wolf, *The chemistry of the Actinide and Transactinide elements, Vol. 1*, 3 ed., Springer, Dordrecht, **2006**.
(18) B. T. M. Willis, *Acta Crystallogr. A* **1978**, *34*, 88.
(19) P. Perio, *Bull. Soc. Chim. Fr.* **1953**, 256.
(20) L. Lynds, A. W. Young, S. J. Mohl, G. G. Libowitz, in *Nonstoichiometric Compounds, Vol. 39*, American Chemical Society, **1963**, pp. 58.
(21) V. V. Rachev, V. S. Smurova, L. M. Kovba, E. A. Ippolitova, *Zh. Neorg. Khim.* **1965**, *10*, 2796.
(22) B. Belbeoch, J. C. Boivineau, P. Perio, *J. Phys. Chem. Solids* **1967**, *28*, 1267.
(23) B. Touzelin, M. Dode, *Rev. Int. Hautes Temp. Refract.* **1969**, *6*, 267.
(24) V. A. Alekseyev, L. A. Anan'yeva, R. P. Rafal'skiy, *Int. Geol. Rev.* **1981**, *23*, 1229.
(25) K. Teske, H. Ullmann, D. Rettig, *J. Nucl. Mater.* **1983**, *116*, 260.
(26) Jmol: an open-source Java viewer for chemical structures in 3D, <http://www.jmol.org/>
(27) T. Cardinaels, K. Govers, B. Vos, S. Van den Berghe, M. Verwerft, L. de Tollenaere, G. Maier, C. Delafoy, *J. Nucl. Mater.* **2012**, *424*, 252.
(28) T. Cardinaels, J. Hertog, B. Vos, L. d. Tollenaere, C. Delafoy, M. Verwerft, *J. Nucl. Mater.* **2012**, *424*, 289.
(29) M. T. Hutchings, *J. Chem. Soc. Farad. T. 2* **1987**, *83*, 1083.
(30) H. Hering, P. Perio, *Bull. Soc. Chim. Fr.* **1952**, *76*, 351.
(31) J. K. Fink, *J. Nucl. Mater.* **2000**, *279*, 1.
(32) P. J. Mohr, B. N. Taylor, *Rev. Mod. Phys.* **2005**, *77*, 1.

(33) J. Härtwig, G. Hölzer, E. Förster, K. Goetz, K. Wokulska, J. Wolf, *Phys. Status Solidi A* **1994**, *143*, 23.
(34) R. Jenkins, W. N. Schreiner, *Powder Diffr.* **1989**, *4*, 74.
(35) G. S. Smith, R. L. Snyder, *J. Appl. Crystallogr.* **1979**, *12*, 60.
(36) R. Jenkins, R. L. Snyder, in *Introduction to X-ray Powder Diffractometry* (Ed.: J. D. Winefordner), John Wiley & Sons, Inc., **1996**, pp. 287.
(37) H. R. Hoekstra, A. Santoro, S. Siegel, *J. Inorg. Nucl. Chem.* **1961**, *18*, 166.
(38) T. B. Lindemer, T. M. Besmann, *J. Nucl. Mater.* **1985**, *130*, 473.
(39) M. H. Rand, R. J. Ackermann, F. Gronvold, F. L. Oetting, A. Pattoret, *Rev. Int. Hautes. Temp.* **1978**, *15*, 355.
(40) H. Kleykamp, *J. Nucl. Mater.* **1993**, *206*, 82.
(41) H. Kleykamp, *J. Nucl. Mater.* **1985**, *131*, 221.
(42) R. Behera, C. Deo, H. Xu, *J. Nucl. Mater.* **2013**, *433*, 504.
(43) S. C. Middleburgh, D. C. Parfitt, R. W. Grimes, B. Dorado, M. Bertolus, P. R. Blair, L. Hallstadius, K. Backman, *J. Nucl. Mater.* **2012**, *420*, 258.
(44) J. W. McMurray, D. Shin, B. W. Slone, T. M. Besmann, *J. Nucl. Mater.* **2013**, *443*, 588.
(45) S. C. Middleburgh, R. W. Grimes, K. H. Desai, P. R. Blair, L. Hallstadius, K. Backman, P. Van Uffelen, *J. Nucl. Mater.* **2012**, *427*, 359.
(46) R. Jenkins, R. L. Snyder, in *Introduction to X-ray Powder Diffractometry* (Ed.: J. D. Winefordner), John Wiley & Sons, Inc., **1996**, pp. 1.
(47) J. A. Bearden, *Rev. Mod. Phys.* **1967**, *39*, 78.
(48) P. J. Mohr, B. N. Taylor, D. B. Newell, *Rev. Mod. Phys.* **2012**, *84*, 1527.
(49) G. Hölzer, M. Fritsch, M. Deutsch, J. Härtwig, E. Förster, *Phys. Rev. A: At. Mol. Opt. Phys.* **1997**, *56*, 4554.
(50) M. Deutsch, E. Förster, G. Hölzer, J. Härtwig, K. Hämäläinen, C. C. Kao, S. Huotari, R. Diamant, *J. Res. Natl. Inst. Stand. Technol.* **2004**, *109*, 75.

Chapter 3.

Assessment of the U_3O_7 crystal structure by X-ray and electron diffraction

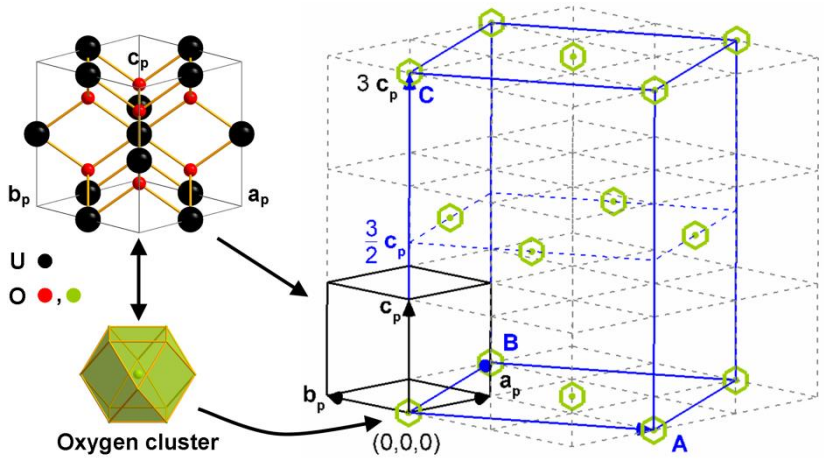

Submitted for review to Inorganic Chemistry: Gregory Leinders, Rémi Delville, Janne Pakarinen, Thomas Cardinaels, Koen Binnemans, and Marc Verwerft

Author contributions

Gregory Leinders performed the main part of the experimental work, the interpretation of the data and the writing of this manuscript. He also contributed to the experimental strategy and the scientific ideas.

3.1 Introduction

Oxidation of UO_2 in dry air at temperatures above about 200 °C results in formation of U_3O_8 (O/U = 2.67), the thermodynamically more stable oxide of uranium.[1] The formation of U_3O_8 from UO_2 is associated with a volume increase of about 36%. This transformation is an important threat for the integrity of storage containers for UO_2, especially when considering long-term storage and final repository of irradiated nuclear fuels.[1-4] The oxidation behavior of UO_2 at ambient to medium temperatures up to 300 °C has been investigated already for many decades, and novel insights continue to be obtained.[5-14]

A wide variety of intermediate oxides can be formed by oxidation of UO_2 under different conditions.[1, 15] Compounds with an O/U ratio between 2 and 2.5 have structures in which the cation arrangement remains closely related to the original fluorite-type UO_2 structure, the most notable change being a deviation from cubic symmetry with increasing oxidation.[16] In the broad hyperstoichimetric range of compositions, commonly referred to as UO_{2+x} ($O/U \leq 2.25$) the excess oxygen develops randomly distributed defects and the structure can be described as defective cubic fluorite.[17-20] At the composition U_4O_9 (O/U = 2.25) an ordered superstructure develops which also has cubic symmetry.[21, 22] When the O/U ratio exceeds 2.25 the symmetry is lowered,[23] but the atomic arrangement remains closely related to the fluorite arrangement until U_3O_8 is formed, which has a different crystal structure.[24, 25] The compounds intermediate to U_4O_9 and U_3O_8 have been assigned tentative formulas based on thermogravimetric data (e.g. U_3O_7, U_2O_5).[26, 27]

Uranium oxides with an O/U ratio close to 2.33 are commonly referred to as U_3O_7,[28] despite possible variations in composition. Their crystal structure is characterized by a distortion of the fluorite-type cubic structure to tetragonal symmetry. In the absence of detailed crystallographic information the accepted criterion for identification has been the axial ratio *c/a*. A few early studies reported the existence of two main polymorphs: α-U_3O_7 ($c/a \sim 0.986$) and β-U_3O_7 ($c/a \sim 1.031$).[27, 29] However, more recent studies have questioned the existence of α-U_3O_7, suggesting that early workers failed to differentiate it from the cubic U_4O_9 phase which is formed at the earlier stage of oxidation.[13, 30] Variations in axial ratio ($1 < c/a \leq 1.031$) are regularly reported, but never exceeding $c/a \sim 1.031$, i.e. the value for β-U_3O_7.[9, 13, 30-34] In what follows the notation U_3O_7 will be used to refer to this state.

For uranium oxides having $2.25 < O/U \leq 2.33$, the formation of a tetragonal phase with gradually increasing *c*/*a* ratio ($1 < c/a \leq 1.031$) has been clearly demonstrated by *in-situ* diffraction experiments at 250 °C and 310 °.[11, 13] The origin of the *c*/*a* variation is often attributed to a deviation from stoichiometry (U_3O_{7-z}),[7, 13, 31, 32] but it has also been considered as a lattice strain effect.[11] Upon further oxidation ($2.33 \leq O/U \leq 2.67$) a

two-phase system $U_3O_7 + U_3O_8$ is formed, where the lattice parameters of the U_3O_7 phase remain unchanged, and the fraction of U_3O_8 increases at the expense of U_3O_7.[11, 13, 35] Thus, the U_3O_7 state is found to be the main precursor for U_3O_8 formation.

The crystal structure of the fluorite-type oxidation products which retain cubic symmetry (i.e. UO_{2+x} and U_4O_9) have been investigated extensively. Oxidation results in a reorganization of the anion sublattice by the incorporation of additional oxygen atoms, while the cation sublattice remains to a large extent undisturbed.[18] In UO_{2+x} the excess oxygen atoms occupy sites in the fluorite-type unit cell which are displaced along <*u u* 0> and <*u u u*> directions from the interstitial holes, and some vacancies appear in the fluorite oxygen sublattice.[19] These defects, generalized in the concept of Willis's 2:2:2 cluster, are initially randomly dispersed.[20] As the composition approaches the O/U ratio of 2.25 the excess oxygen atoms tend to occupy more of the twelve <*u u* 0>-type displaced sites.[22, 36] These sites form the vertices of a regular cuboctahedron, hence the terminology cuboctahedral oxygen cluster.[37, 38] In U_4O_9 spatial ordering of these cuboctahedral clusters occurs, which results in a superstructure ($I\bar{4}3d$) based on the fluorite structure but quadrupled in all three directions: $4\mathbf{a_p}$, $4\mathbf{a_p}$, $4\mathbf{a_p}$ (with a_p the lattice parameter of the fluorite-like subcell).[11, 39]

The concept of the cuboctahedral oxygen cluster has also been used as a basis for the assessment of the U_3O_7 crystal structure.[11, 40-42] Formation of oxygen clusters in U_3O_7 has been confirmed in recent *ab initio* studies,[43] however, due to limitations in the simulation cell the cuboctahedral arrangement could not be proven.[44] Indications for the long-range ordering of these defects have been reported,[11, 40, 41] but a complete and consistent description of the superstructure has not been obtained yet. McEachern and Taylor have cited unpublished work which mentioned the existence of a $\sqrt{5}\mathbf{a}$, $\sqrt{5}\mathbf{a}$, $3\mathbf{c}$ superstructure for U_3O_7.[1] Nowicki *et al.*, citing the same unpublished data, studied different stacking possibilities for cuboctahedral oxygen clusters in U_3O_7 and proposed superstructures of the type $5\mathbf{a}$, $5\mathbf{a}$, $j\,3\mathbf{c}$ (j an integer).[40] In their description the U_3O_7 phase exists as a family of polytypes. Desgranges *et al.* performed a detailed assessment of neutron diffraction data obtained from U_3O_7 (produced *in situ* by oxidation of UO_2 powder at 310 °C).[11] They described the crystal structure as an arrangement of tilted and skewed cuboctahedral oxygen clusters in a $4\mathbf{a}$, $4\mathbf{a}$, $4\mathbf{c}$ superstructure ($I\bar{4}2d$).

Diffraction patterns of crystals having a long-range ordered defect structure typically display a set of strong reflections ("parent structure reflections") that are characteristic for the underlying parent structure, and much weaker "satellite reflections" corresponding to the perturbations. If the periodicity of the perturbations has only rational components with respect to the parent structure basis vectors, the system is commensurately perturbed and it is possible to derive an expanded unit cell. The diffraction patterns of U_3O_7 discussed further are dominated by strong, fluorite-type

parent structure reflections and also display a large number of much weaker reflections corresponding to a commensurate perturbation, similar to what is observed in U_4O_9.[45]

In the present paper, a comprehensive structural analysis of the long-range ordered U_3O_7 crystal structure is performed by combining X-ray powder diffraction (XRD) and Selected-Area Electron Diffraction (SAED) techniques. A consistent structural model based on the coordination of cuboctahedral oxygen clusters in an expanded unit cell is subsequently derived.

3.2 Experimental section

3.2.1 Sample material

Samples were prepared from depleted nuclear grade UO_{2+x}, produced via the Integrated Dry Route (IDR process) and supplied by FBFC International (Dessel, Belgium). The impurity content of this powder was evaluated using Inductively Coupled Plasma Mass Spectroscopy (ICP-MS, ThermoFisher XSeries2). The presence of in total 50 elements was probed for. A summary is presented in Table 3.1, the total metallic impurity fraction was 47 µg g^{-1}. The powder consists of loosely-packed, soft agglomerates of up to 20 µm. Each agglomerate is composed of a large number of small crystals whose size is of the order 100 nm. The specific surface area (BET theory) of the powder was measured using nitrogen gas adsorption (Micromeritics Tristar II 3020), and equaled 2.3 m^2 g^{-1}. The stoichiometry of the UO_{2+x} powder batch was measured using *in-situ* thermogravimetric analysis and equaled 2.088 ± 0.002 (2σ), the exact procedure has been described elsewhere.[46] According to Rietveld analysis of the X-ray diffraction data measured for this powder, it contains about 1.5 wt.% U_3O_8.

Table 3.1. Impurity levels measured via ICP-MS in the as-received UO_{2+x} powder batch. The values are given in µg g^{-1} (2σ).

Li	1 ± 1	**Zn**	2 ± 2
Be	0.1 ± 0.1	**Zr**	0.06 ± 0.08
B	3 ± 3	**Mo**	0.2 ± 0.2
Al	4 ± 3	**Cd**	0.1 ± 0.1
Cr	0.3 ± 0.3	**In**	0.02 ± 0.02
Mn	0.3 ± 0.3	**Sn**	4 ± 8
Fe	23 ± 24	**La**	0.03 ± 0.02
Ni	0.5 ± 0.3	**Gd**	0.006 ± 0.008
Cu	0.2 ± 0.2	**Pb**	0.1 ± 0.1

3.2.2 Thermal analysis

Simultaneous Thermal analysis (STA) using a Netzsch STA 449 *F1* Jupiter, coupled to a quadrupole mass spectrometer (403 D Aëolos®), was performed to investigate conditions for the formation of U_3O_7 from UO_2 and to evaluate the stoichiometry of the UO_{2+x} powder. All used gases were of high purity (99.9992%) and with no measurable water content (dew point < −80 °C). A constant flow of argon gas (20 mL min^{-1}) was maintained through the balance compartment and leading into the furnace chamber, here referred to as the protective gas flow, resulting in increased balance stability. The flushing (active) gas entered the furnace chamber directly through a secondary inlet with a flow of 80 mL min^{-1}. The total exiting gas flow was therefore equal to 100 mL min^{-1}. The gas supply was controlled via various mass flow controllers (Bronkhorst EL-FLOW), individually calibrated to the type of gas used.

Simultaneous thermogravimetric analysis (TGA) and differential scanning calorimetry (DSC) was performed with a type S (Pt-10% Rh / Pt) thermocouple, carrying Pt/Rh crucibles with lids (sample mass ~ 20 mg). Single thermogravimetric analysis was performed with a type B (Pt-30% Rh / Pt-6% Rh) thermocouple, carrying an alumina crucible (sample mass ~ 2000 mg). In both cases, prior temperature calibration was performed by melting standards (In, Sn, Bi, Zn, Al, Au) and validated with a selection of these metals on a regular basis. Tabulated values for heats of fusion of these high-purity metals were used to calibrate the calorimeter. Mass change was continuously recorded with an accuracy of ±28 µg (2σ). The absolute mass readout of the balance was calibrated using a reference weight of 2000.00 mg. All STA runs were corrected for drift and buoyancy by subtraction of a blank run under identical conditions.

A Carbolite TZF1800 tube furnace was used for performing heat treatments on larger quantities of powder (3-50 g). The sintered alumina tube could be sealed from the lab environment by fitting of specifically designed plugs, allowing for a continuous flow of dry gasses (argon or synthetic air, N_2 / 21 vol.% O_2). Also, the furnace was modified with a retractable type K thermocouple for accurate temperature control. Powders were loaded in dried alumina crucibles, weighed and inserted in the furnace at room temperature. The working tube was then sealed gastight and flushed with dry argon until the dew point of the exiting gas reached −74 °C or less. After completion of the thermal treatment, the alumina crucibles were retrieved and weighed on a laboratory balance at room temperature.

3.2.3 X-ray diffraction

X-ray powder diffraction was performed with a Philips X'Pert Pro diffractometer in parafocusing geometry (θ-θ configuration). Validation of zero point calibration was

performed against an Al_2O_3 reference sample (NIST Standard Reference Material 1976b) on a weekly basis. An LFF X-ray tube (Cu $K\alpha_1$ = 1.5405929 Å)[47] was used as radiation source. The beam path consisted of a fixed divergence slit (½°) and copper beam mask in combination with 0.02 rad Soller slit assemblies. A position-sensitive 1D detector (PANalytical X'Celerator) was used, with a nickel filter placed in front to avoid Cu Kβ contribution to the diffracted signal. The goniometer was operated with a step size of 0.008° (2θ) through the range 24-121° (2θ).

Specimens for powder diffraction were carefully prepared via the back-loading technique. During sample preparation, transfer and measurement, the specimens were exposed to the normal lab environment (room temperature, relative humidity ~50%). The lattice parameters presented throughout the text are recalculated to their value at 20 °C, using the linear thermal expansion coefficient for UO_2 of 9.739×10^{-6} °C^{-1} near room temperature.[48] For U_3O_7 the same coefficient was assumed, as was also proposed for U_4O_9 by Martin.[48, 49] Rietveld analysis of the X-ray diffractograms was performed with PANalytical HighScore Plus (v4.1) software. Details on the followed methodology can be found in the supporting information.

3.2.4 Electron diffraction

Transmission Electron Microscopy (TEM) was performed with a 300 kV JEOL 3010 microscope equipped with an in-column Gatan 794 MSC CCD camera and a side-entry double tilt specimen holder. A small amount of powder (< 1 mg) was randomly sampled and dispersed by isopropanol in a beaker. Short intervals (~10 s) of ultrasonic deagglomeration were applied to break up the soft agglomerates into individual grains. The suspension was then pipetted onto a holey carbon grid and the isopropanol was left to evaporate. Data analysis was performed with Gatan Microscopy Suite® (GMS) 2.

3.3 Results

3.3.1 Sample preparation

Conditions for the preparation of U_3O_7 from UO_2 powder were investigated using STA. During one single run a sample of the supplied UO_{2+x} powder was first reduced to stoichiometric UO_2 by heating to 700 °C under a flow of an Ar / H_2 (96:4 vol.%) mixture. Then, after cooling to 35 °C, the gas was switched to pure argon for 1.5 h and subsequently to synthetic air until the end of the run. Complete transformation into U_3O_8 was achieved by heating at a constant rate (5 °C min^{-1}) up to 450 °C. Already during the preceding isotherm at 35 °C, after switching the gas to synthetic air, a slight mass increase O/U = 2.04 ± 0.02 was observed. The mass and heat flux recorded during the heating stage show that further oxidation proceeds in two exothermic

reaction steps (Figure 3.1), the second being much better defined than the first. A region of drastically decreased reaction rate is observed at oxidation temperatures between 265 °C and 295 °C, indicated by the vertical lines. Here, the corresponding O/U ratio lies between 2.36 and 2.37. At higher temperatures oxidation completes with the formation of U_3O_8.

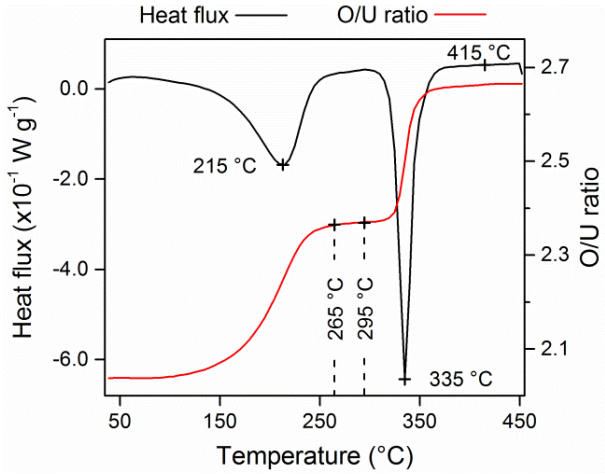

Figure 3.1. STA data recorded during the oxidation of UO_2 powder (5 °C min^{-1} heating rate). Both TGA and DSC signals show a two-step reaction, one peaking at 215 °C and the other peaking at 335 °C.

The reaction enthalpy was quantified by integration of the DSC signal peak area, taking a sigmoidal baseline. The small endothermic peak which is noticed at the start of the heating stage should be disregarded as it is a commonly occurring artefact in DSC analysis (i.e. initially the sample crucible temperature lags slightly behind the empty reference crucible). The starting point of the first exothermic reaction step is set at 95 °C, the temperature at which the mass increase exceeded 28 µg (i.e. higher than the 2σ uncertainty on mass readout). The end point was taken at 265 °C, where the derivative of the mass signal dropped below 28 µg min^{-1}. The second exothermic step, being much better defined, starts at 295 °C and ends at 415 °C where the derivative of the mass signal has decreased to less than 28 µg min^{-1}. The reaction enthalpy per mole UO_2 is measured as −42 ± 2 kJ mol^{-1} and −43 ± 2 kJ mol^{-1}, respectively.

Based on the results obtained by STA (Figure 3.1) the as-received UO_{2+x} powder was oxidized in a controlled way by thermogravimetric synthesis at 250 °C. The progression of the synthesis is presented in Figure 3.2 and it shows a fast increase in mass corresponding to completion of the first exothermic reaction stage. The mass increase levels off upon reaching the target temperature of 250 °C, the average O/U corresponding to about 2.33. During the isothermal stage additional mass increase is

observed and the rate appears to increase slightly towards the end. A stable mass signal is obtained during cooling, while still flushing with synthetic air. The average stoichiometry of the TGA produced sample was 2.371 ± 0.002. Subsequent X-ray analysis on the oxidized powder (see section 3.3.2) showed that it contained a well-developed, crystalline U_3O_7 phase (a = 538.01 ± 0.02 pm, c = 554.89 ± 0.02 pm) and an increased U_3O_8 fraction (8.6 ± 0.2 wt.% as compared to 1.5 wt.% in the as-received powder).

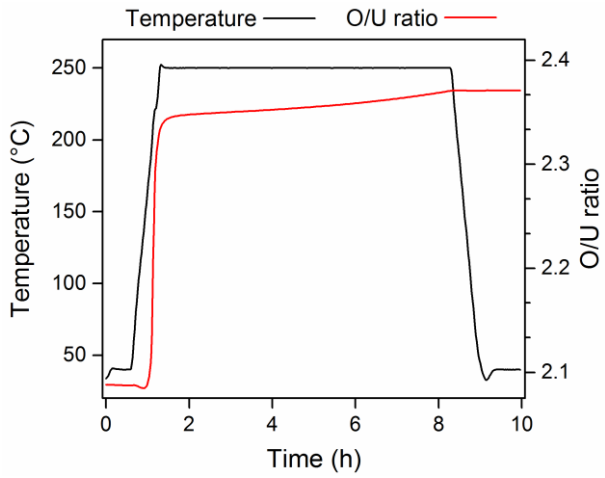

Figure 3.2. TGA data measured during oxidation of the as-received UO_{2+x} powder (5 °C min^{-1} heating rate).

A larger batch of U_3O_7 was subsequently prepared in the tube furnace in order to have sufficient material for further analysis. The as-received UO_{2+x} powder was oxidized at 250 °C (heating and cooling rate 5 °C min^{-1}) under a constant flow of dry, synthetic air for 7 h. The average stoichiometry after heat treatment was measured by gravimetry and equaled an O/U ratio of 2.356 ± 0.002, i.e. slightly lower than that of the powder synthesized in the STA. Subsequent X-ray analysis (see section 3.3.2) again showed well-crystallized U_3O_7 (a = 537.99 ± 0.02 pm, c = 554.91 ± 0.02 pm). A smaller increase in U_3O_8 content was observed (3.8 ± 0.2 wt.%), consistent with the lower weight increment.

The stoichiometry of the U_3O_7 phase formed in both samples can be calculated from the measured average stoichiometry values and U_3O_8 weight fractions. Results are presented in Table 3.2. The O/U ratio of the U_3O_7 phase is identical in both cases, which shows that further oxidation results solely in the formation of additional U_3O_8.

Table 3.2. Determination of the stoichiometry of the U_3O_7 phase from average stoichiometry values $(O/U)_{av}$ and U_3O_8 weight fractions in the two samples.

Sample	$(O/U)_{av}$	wt.% U_3O_8	(O/U) U_3O_7
Uncertainty	± 0.002	± 0.2	± 0.01
(1)[a]	2.371	8.6	2.34
(2)[b]	2.356	3.8	2.34

[a] Powder prepared in TGA setup
[b] Powder prepared in tube furnace

3.3.2 Average structure analysis of U_3O_7

Uranium oxide compounds in the stoichiometry range $2 < O/U \leq 2.5$ all share a fluorite parent arrangement of U and O atoms similar as in UO_2 (space group, SG, $Fm\bar{3}m$).[16] In U_3O_7 the oxygen atoms also occupy positions which are displaced from the large, octahedrally coordinated interstitial sites,[41] much similar as in U_4O_9.[39] As a result, local perturbations of the anion sublattice are induced. The principal type of defect is the cuboctahedral oxygen cluster,[11, 40, 41] which consists of twelve oxygen atoms displaced equally along the <*u u* 0> directions from an interstitial site in the parent structure,[37] and a thirteenth oxygen atom at the cuboctahedron center, although the occupation of the latter position remains subject to debate.[11, 38, 39] A cuboctahedral cluster arrangement is represented by green spheres in Figure 3.3.

Long-range periodicity of the perturbations gives rise to satellite reflections in diffraction experiments, as observed by neutron diffraction (Desgranges *et al*. and Garrido *et al*.)[11, 41] and electron diffraction (this study and unpublished work of Thomas and Taylor).[1] However, no satellite reflections are distinguishable by X-ray diffraction (this study and e.g. Rousseau *et al*.).[13] Therefore, the XRD data are interpreted in terms of the "average" or "parent" structure of U_3O_7. Throughout the text the subscript 'p' will refer to parent structure indexing.

X-ray diffractograms of the powders show a well-defined, crystalline phase of high symmetry (see Figure 3.4). The reflections obey all-face centering reflection conditions (F), $(hkl)_p$: $h + k$, $k + l$, $h + l = 2n$, as is also the case for the UO_2 crystal structure. However, all $(hkl)_p \neq (hhh)_p$ reflections are split into two components $(hkh)_p = (khh)_p \neq (hhk)_p$ evidently breaking the cubic symmetry of the UO_2 structure. Indeed, the incorporation of excess oxygen in U_3O_7 leads to tetragonal distortion of the formerly cubic structure.[29] A model for the parent structure may then be proposed in which the "fluorite atoms" keep the same positions as in UO_2 (see Figure 3.3). This arrangement can readily be described in SG $P4_2/nnm$ (no. 134).[30]

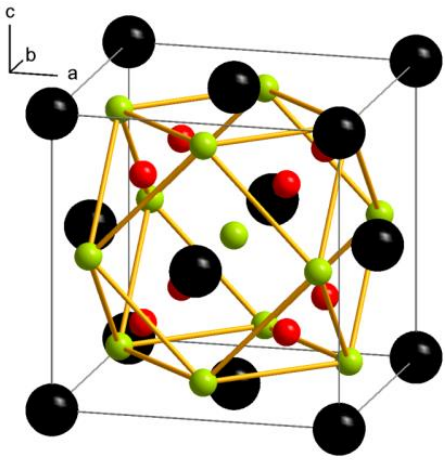

Figure 3.3. Representation of the fluorite parent arrangement of U and O atoms as in UO_2 (black and red spheres, respectively) and a cuboctahedral oxygen cluster (green spheres connected by yellow lines) with occupied cuboctahedron center (central green sphere).

Table 3.3. Average unit cell composition of U_3O_7 in SG *P*4$_2$/*nnm* (origin choice 2). (1) Fluorite-type parent configuration, (2) cuboctahedral oxygen cluster. The oxygen site occupancy factors (o_f and o_c) are such that an O/U ratio of 2.33 is obtained.

Wyckoff sites		*x*	*y*	*z*	occ.	Site symmetry reflection cond.	Notes
U	4*f*	0	0	0	1	$h+k$, $k+l$, $h+l = 2n$	(1)
O1	2*a*	1/4	3/4	1/4	o_f	$h+k+l = 2n$ [a]	
O2	2*b*	3/4	1/4	1/4	o_f	$h+k+l = 2n$ [a]	
O3	4*c*	1/4	1/4	1/4	o_f	$h+k$, $l = 2n$ [a]	
O'c	4*e*	1/2	1/2	1/2	o_c	$h+k$, $k+l$, $h+l = 2n$	(2) $u = 0.41$ [b]
O'1	8*l*	0.5+*u*	0.5+*u*	1/2	o_c	$h+k = 2n$ [a]	
O'2	8*m*	0.5−*u*	0.5+*u*	1/2	o_c	*none* [a]	
O'3	16*n*	0.5	0.5+*u*	0.5+*u*	o_c	*none* [a]	
O'4	16*n*	0.5	0.5−*u*	0.5+*u*	o_c	*none* [a]	
O/U					2.33		

[a] Equal occupation of these sites results in accidental *F* extinctions.

[b] Value measured by Garrido *et al*. from neutron diffraction data.[41]

Fluorite-type anion sites corresponding to the parent structure arrangement can locally be transformed into cuboctahedral oxygen clusters by the incorporation of additional oxygen atoms.[37] The presence of such perturbations in U_3O_7 can be generalized by using the concept of an average unit cell in which the anion sublattice represents both fluorite-type sites and sites related to the cuboctahedra. The combined occupancy of these sites should then yield the average stoichiometry O/U = 2.33. The composition of the average cell, and the corresponding site symmetry conditions in SG $P4_2/nnm$ (origin choice 2) is subsequently presented in Table 3.3.

The cation positions (4*f*) give rise to *F*-type reflection conditions ($h + k$, $k + l$, $h + l = 2n$), and although their contribution to the total scattered intensity is low anyway, the anion positions are also such that *F*-centering reflection conditions apply. Identical site occupation of Wyckoff sites 2*a*, 2*b* and 4*c* (the fluorite-type anion sites) results in accidental *F* extinctions. Anions arranged in a regular cuboctahedral configuration similarly invoke accidental *F* extinctions, i.e. their symmetry is equivalent to that of the cuboctahedron center (an interstitial site 4*e*).[50] Reflections which violate these conditions were not observed in the current XRD analysis, however, they were readily distinguished in SAED patterns (section 3.3.4). Lifting of the accidental extinctions occurs due to deviations from uniform site occupation of the anion sublattice, or due to distortions of the regular cuboctahedral geometry.

Information with respect to the anion sublattice is ineffectively probed by X-ray analysis since the scattering efficiency of oxygen atoms is very poor as compared to that of uranium atoms. Consequently, only lattice metric parameters and the uranium isotropic temperature factor of the U_3O_7 average structure (Table 3.3) were refined, using all observed reflections in the X-ray diffractograms and for both prepared samples. Small angular ranges around 26.0, 34.0 and 51.5 ° (2θ) were excluded as these areas correspond to α-U_3O_8 reflections (see also Figure AII.1 in Appendix II), but they do not overlap with reflections from the U_3O_7 phase.

Results of Rietveld refinement were almost identical for both samples, the only notable difference was a slightly higher temperature factor in sample 2 (see Table 3.4). The agreement between experimental data and fitted profile was very good for both samples, as evidenced by the agreement factors (R_{wp} = 0.099 and 0.090, respectively). The lattice parameters proposed for U_3O_7 are the average of both refinements: c_p = 554.90 ± 0.02 pm and $a_p = b_p$ = 538.00 ± 0.02 pm (c_p/a_p = 1.031).

The weight fraction of U_3O_8 in the two samples was quantified from an independent Rietveld analysis of the XRD data. The reported crystal structure of α-U_3O_8 (*C*2*mm*, a = 671.6(2) pm, b = 1196.0(4) pm, c = 414.7(1) pm) was adopted.[24, 25] The angular ranges which were excluded in the prior analysis of the U_3O_7 parent structure were now included, and the refinement was repeated. The parameter set was equal as that used in

the prior analysis, with the addition of the α-U_3O_8 phase. The weight fraction of U_3O_8 was determined according to the method of Hill and Howard from the refined scale factor values in each sample.[51] The results have been presented in Table 3.2.

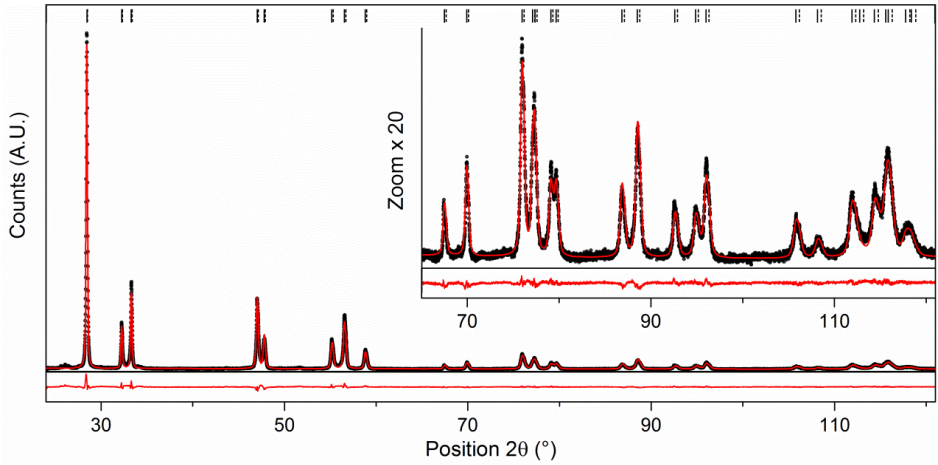

Figure 3.4. Experimental XRD data (dots) and fitted profile (red line) for the sample prepared by oxidation in the tube furnace (R_{wp} = 0.090). The difference profile is shown at the bottom. Peak maxima for CuKα_1 and CuKα_2 are indicated at the top by solid and dashed lines, respectively. The inset shows a zoom-in of the higher order reflections.

Table 3.4. Refined parameters of the U_3O_7 parent structure, according to the Rietveld method on X-ray diffraction data.

Sample	Lattice parameters (pm)		Temperature factor B_{iso}	Agreement factors		
	a_p (= b_p)	c_p	U (Å²)	R_{exp}	R_{wp}	R_{Br}
(1)[a]	538.01(2)	554.89(2)	0.48(1)	0.049	0.099	0.030
(2)[b]	537.99(2)	554.91(2)	0.54(1)	0.048	0.090	0.035

[a] Powder prepared in TGA
[b] Powder prepared in tube furnace

3.3.3 Superstructure analysis of U_3O_7

Individual U_3O_7 crystals were typically a few hundred nm large (see Figure 3.5) and allowed to perform single crystal diffraction investigations in selected-area electron diffraction mode. Both strong reflections, corresponding to the fluorite-like parent structure, and much weaker satellite reflections were observed. After repeated analysis

on the same specimen, the intensity of the satellite reflections further decreased and eventually disappeared. Similar instabilities of satellite reflections have also been reported during TEM analysis on U_4O_9.[52] Measurements were therefore preferentially done on freshly prepared specimens (all from sample 2, since it contained a smaller fraction of U_3O_8).

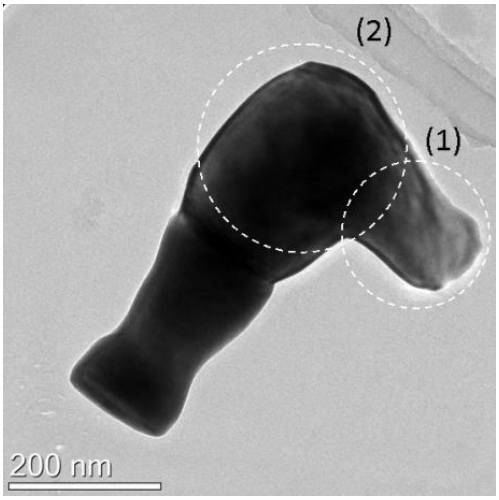

Figure 3.5. Bright field image of a U_3O_7 grain with marked regions from which several SAED patterns were obtained. (1) Patterns presented in Figure 3.6 (b, c, d), Figure 3.7 (a) and Figure 3.8 (a). (2) Pattern presented in Figure 3.8 (b). Other patterns (Figure 3.6 (a) and Figure 3.7 (b)) were obtained from different grains.

In Figure 3.6 diffraction patterns forming a systematic tilt series around the **c***-axis are presented. The lattice expansion along the **c**-axis (c/a = 1.031) is also measurable in the SAED patterns and allows to identify the **c***-axis. Intense main reflections and sharp satellite reflections are observed. The intense reflections can be readily indexed in the parent structure; they obey *F* extinction rules and were observed also in the XRD patterns. The other reflections, which were not previously distinguished, can be subdivided in two types: additional parent structure reflections which violate the *F*-centering conditions, e.g. $(033)_p$ and $(121)_p$, and satellite reflections having non-integer indices with respect to the parent structure unit cell.

The $[3\bar{1}0]_p$-zone axis orientation appears to be the basal plane for the perturbation: each parent structure reflection is surrounded by four first order satellites. The analysis of differently oriented diffraction patterns (Figure 3.6-3.8) leads to conclude that each parent structure reflection is in fact surrounded by eight non-coplanar first order reflections. All eight reciprocal vectors are given in Table 3.5, they are related by 4/*m* point group symmetry operations. A reciprocal space map restricted to satellite

reflections of first- and second order is presented in Appendix II. Satellite reflections can consistently be indexed by linear combinations of three such non-coplanar vectors, e.g.:

$$\mathbf{q_1} = \frac{1}{5}\cdot\mathbf{a}^* + \frac{3}{5}\cdot\mathbf{b}^* + \frac{1}{3}\cdot\mathbf{c}^* = \frac{1}{15}\cdot[395]^*_{\mathrm{p}} \qquad \textbf{(3.1)}$$

$$\mathbf{q_2} = \frac{-1}{5}\cdot\mathbf{a}^* + \frac{-3}{5}\cdot\mathbf{b}^* + \frac{1}{3}\cdot\mathbf{c}^* = \frac{1}{15}\cdot[\bar{3}\bar{9}5]^*_{\mathrm{p}} \qquad \textbf{(3.2)}$$

$$\mathbf{q_3} = \frac{-3}{5}\cdot\mathbf{a}^* + \frac{1}{5}\cdot\mathbf{b}^* + \frac{1}{3}\cdot\mathbf{c}^* = \frac{1}{15}\cdot[\bar{9}35]^*_{\mathrm{p}} \qquad \textbf{(3.3)}$$

Table 3.5. Overview of the 4/*m* symmetry related wave vectors The symbols of the symmetry operations refer to inversion (*−1*), four-fold rotation (*4*) reflection (*m*), and combinations thereof.

Wave vector	Operation	Wave vector	Operation
$\mathbf{q_1} = 1/15\cdot[395]^*_{\mathrm{p}}$		$\mathbf{q_5} = 1/15\cdot[\bar{3}\bar{9}\bar{5}]^*_{\mathrm{p}}$	*−1*
$\mathbf{q_2} = 1/15\cdot[\bar{3}\bar{9}5]^*_{\mathrm{p}}$	*m, −1*	$\mathbf{q_6} = 1/15\cdot[39\bar{5}]^*_{\mathrm{p}}$	*m*
$\mathbf{q_3} = 1/15\cdot[\bar{9}35]^*_{\mathrm{p}}$	*4*	$\mathbf{q_7} = 1/15\cdot[9\bar{3}\bar{5}]^*_{\mathrm{p}}$	*4, −1*
$\mathbf{q_4} = 1/15\cdot[9\bar{3}5]^*_{\mathrm{p}}$	*m, −1, 4*	$\mathbf{q_8} = 1/15\cdot[\bar{9}3\bar{5}]^*_{\mathrm{p}}$	*m, 4*

The $[001]_{\mathrm{p}}$-zone orientation clearly illustrates that the point group symmetry 4/*mmm* of the parent structure is further reduced to 4/*m* for the superstructure, see Figure 3.7 (b). The position of the satellite reflections indeed lifts the mirror planes perpendicular to the **a***- and **b***-axes, and the bisecting mirror planes. This further decrease of point group symmetry results in additional orientation twinning. Thus, upon oxidation of U_4O_9 (point group $m\bar{3}m$ with order 48) to U_3O_7 (point group 4/*m* with order 8) one expects a total of six different orientation domains to be formed: three different orientation possibilities for the **c***-axis (an example of **c***-axis twins is available in Appendix II), and for each of these, two additional orientation twins due to the long-range ordering with loss of mirror planes perpendicular to **a***- and **b***-axes and the bisecting mirror planes. For example, orientations such as $[2\bar{1}0]_{\mathrm{p}}$ and $[\bar{1}20]_{\mathrm{p}}$ are no longer equivalent in the perturbed structure (see Figure 3.8).

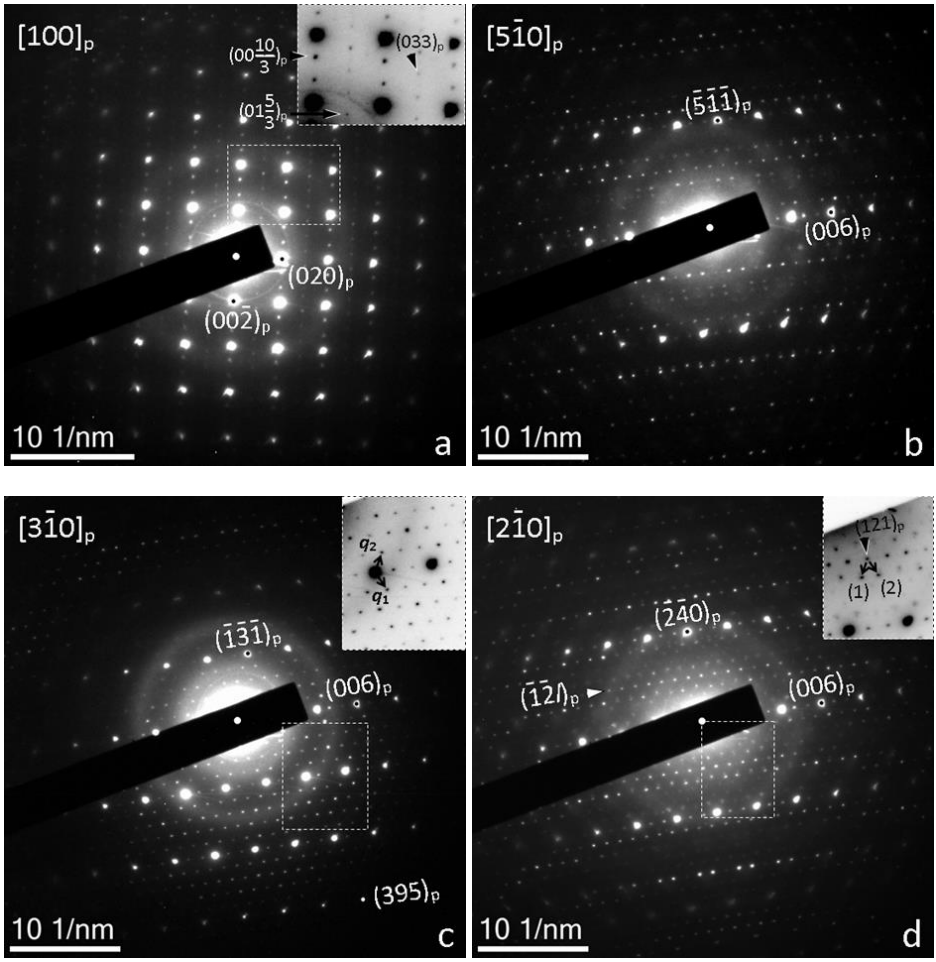

Figure 3.6. SAED patterns forming a systematic tilt series around the **c***-axis. (a) $[100]_p$-zone axis showing weak non-fluorite reflections (e.g. $(033)_p$) and satellites aligned along the **c***-axis: $(0k\lambda)_p$: $\lambda = l \pm ⅔$. (b) Pattern oriented slightly off-axis from the $[5\bar{1}0]_p$-zone. Most of the satellites correspond with reciprocal lattice points in the $[3\bar{1}0]_p$-zone axis, and appear due to the small crystallite thickness. (c) $[3\bar{1}0]_p$-zone axis, the basal plane for two wave vectors $\mathbf{q_1} = 1/15 \times [395]^*_p$ and $\mathbf{q_2} = 1/15 \times [\bar{3}\bar{9}5]^*_p$. Satellites along the **c***-axis can thus be indexed as the sum of $\mathbf{q_1}$ and $\mathbf{q_2}$ (= $1/3 \times [002]^*_p$). (d) $[2\bar{1}0]_p$–zone axis pattern, also showing non-fluorite reflections (e.g. $(121)_p$) and rows of satellites in which the position of every third diffraction spot slightly deviates from the trend. Wave vectors $\mathbf{q_1}$ and $\mathbf{q_2}$ are slightly inclined with respect to the $[2\bar{1}0]_p$–zone axis, however, the first order satellites can still be distinguished directly adjacent to the parent reflections: (1) = $(\frac{6}{5}\frac{13}{5}\frac{2}{3})_p$, (2) = $(\frac{6}{5}\frac{13}{5}\frac{4}{3})_p$.

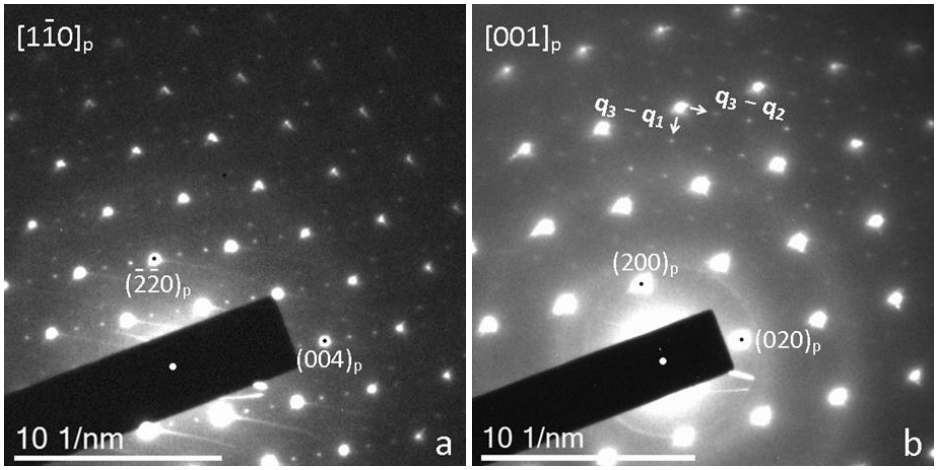

Figure 3.7. (a) $[1\bar{1}0]_p$-zone axis oriented pattern, showing satellites aligned along the **c***-axis (**q**$_1$ + **q**$_2$). (b) $[001]_p$-zone axis diffractogram, in which satellites can be consistently indexed according to **q**$_3$ – **q**$_1$ (= $1/5 \times [\bar{4}\bar{2}0]_p^*$) and **q**$_3$ – **q**$_2$ (= $1/5 \times [\bar{2}40]_p^*$). Evidently, the vector **q**$_1$ – **q**$_2$ (= $1/5 \times [260]_p^*$) can also be constructed. This pattern clearly demonstrates the absence of mirror planes perpendicular to the **a***- and **b***-axes in the perturbed structure. Furthermore, in both patterns reflections of the type $(hkl)_p$: h, $k = 2n + 1$, $l = 2n$ remain extinct (e.g. $(110)_p$, $(112)_p$).

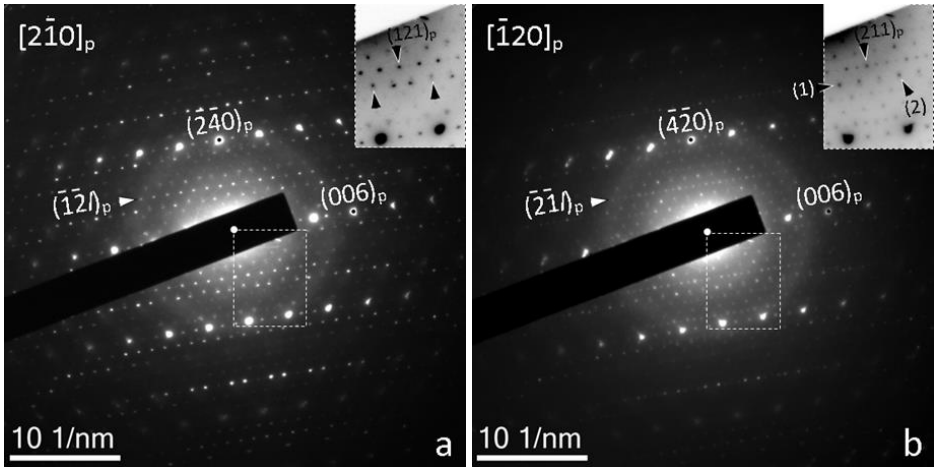

Figure 3.8. SAED patterns of twinned domains oriented along $[2\bar{1}0]_p$ and $[\bar{1}20]_p$, the position of the aperture in a real space image is shown in Figure 3.5. Every third reflection which deviates from the trend in (a), indicated by arrows in the inset, in fact originates from the neighboring $[\bar{1}20]_p$-oriented domain. The reflections indicated in the inset (b) are indexed as (1) = $(\frac{12}{5}\frac{6}{5}0)_p$, (2) = $(\frac{12}{5}\frac{6}{5}2)_p$.

The XRD results (section 3.3.2), as well as the TEM analysis, revealed no indications that the U_3O_7 structure would have a lower point group symmetry than 4/*m*. Within the limits of the observations, three linearly independent wave vectors are thus required to construct all observed reciprocal lattice points while maintaining tetragonal symmetry for the superstructure. Throughout this paper the combination $\mathbf{q_1}$, $\mathbf{q_2}$, $\mathbf{q_3}$ will be used, although other equivalent sets may be chosen.

The observation of sharp satellite reflections is indicative of crystallographic perturbations having a long-range periodicity. Irrespective of the specific type of perturbation, it is the ordering scheme in real space (e.g. a repetition of cuboctahedral oxygen clusters in three dimensions) which defines the wave vectors ($\mathbf{q_1}$, $\mathbf{q_2}$, $\mathbf{q_3}$). Since all wave vectors have rational components with respect to the parent structure basis vectors $\mathbf{a_p}$, $\mathbf{b_p}$, $\mathbf{c_p}$ the long-range ordered structure can be described in an expanded unit cell.

The real space periodicity of the perturbation, hereafter often referred to as the defect structure, is described by a vector space with unit cell vectors $\mathbf{r_1}$, $\mathbf{r_2}$ and $\mathbf{r_3}$ which are conventionally constructed as:

$$\mathbf{r_1} = \frac{(\boldsymbol{q_2} \times \boldsymbol{q_3})}{|\boldsymbol{q_1} \cdot (\boldsymbol{q_2} \times \boldsymbol{q_3})|} = -\frac{1}{2} \cdot (2\mathbf{a_p} + \mathbf{b_p} + 3\mathbf{c_p}) \quad \textbf{(3.4)}$$

$$\mathbf{r_2} = \frac{(\boldsymbol{q_3} \times \boldsymbol{q_1})}{|\boldsymbol{q_1} \cdot (\boldsymbol{q_2} \times \boldsymbol{q_3})|} = \frac{1}{2} \cdot (\mathbf{a_p} - 2\mathbf{b_p} + 3\mathbf{c_p}) \quad \textbf{(3.5)}$$

$$\mathbf{r_3} = \frac{(\boldsymbol{q_1} \times \boldsymbol{q_2})}{|\boldsymbol{q_1} \cdot (\boldsymbol{q_2} \times \boldsymbol{q_3})|} = \frac{1}{2} \cdot (3\mathbf{a_p} - \mathbf{b_p}) \quad \textbf{(3.6)}$$

The unit cell spanned by the three vectors $\mathbf{r_1}$, $\mathbf{r_2}$ and $\mathbf{r_3}$ is the primitive real space unit cell corresponding to the long-range ordering of the defect structure, but obviously, none of the vectors are translation vectors of the parent structure. The smallest supercell which keeps both the parent structure and defect structure invariant is subsequently obtained by the following linear combinations of $\mathbf{r_1}$, $\mathbf{r_2}$ and $\mathbf{r_3}$:

$$\mathbf{A} = \mathbf{r_1} + \mathbf{r_2} + \mathbf{r_3} = \mathbf{a_p} - 2\mathbf{b_p} \quad \textbf{(3.7)}$$

$$\mathbf{B} = -\mathbf{r_1} - \mathbf{r_2} + \mathbf{r_3} = 2\mathbf{a_p} + \mathbf{b_p} \quad \textbf{(3.8)}$$

$$\mathbf{C} = -\mathbf{r_1} + \mathbf{r_2} - \mathbf{r_3} = 3\mathbf{c_p} \quad \textbf{(3.9)}$$

The volume of this unit cell is readily calculated as:

$$V = |\mathbf{A} \cdot (\mathbf{B} \times \mathbf{C})| = 15 \cdot V_p \qquad \textbf{(3.10)}$$

The relation between parent structure unit cell, defect structure periodicity and the expanded unit cell is represented in Figure 3.9.

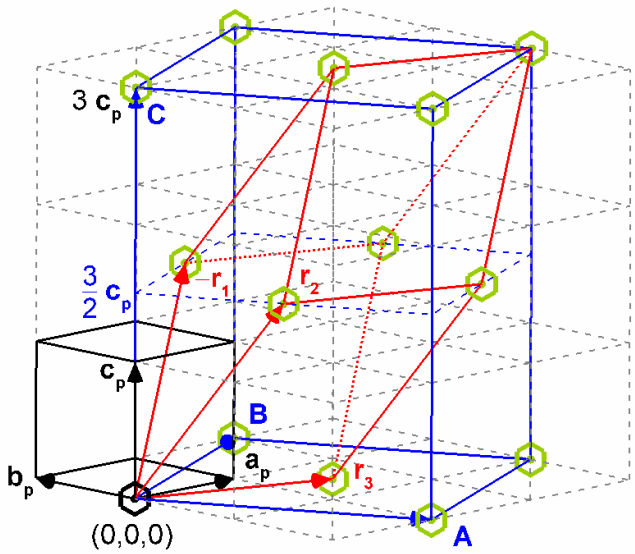

Figure 3.9. Representation of the parent structure unit cell (in black, $\mathbf{a_p}$, $\mathbf{b_p}$, $\mathbf{c_p}$, dashed lines indicate its repetition in three dimensions), the defect structure unit cell (in red, $\mathbf{r_1}$, $\mathbf{r_2}$, $\mathbf{r_3}$) and the expanded unit cell (in blue, unit cell vectors **A**, **B**, **C**). For convenience, the defect structure unit cell is represented with vectors $-\mathbf{r_1}$, $\mathbf{r_2}$ and $\mathbf{r_3}$. The expanded unit cell has a volume of fifteen parent structure cells and four defect structure cells. Green hexagon symbols indicate a possible coordination scheme of defect clusters.

The reflection conditions observed in the SAED patterns, when indexed using the expanded unit cell, allow one to assign the symmetry elements and to propose a space group for the perturbed structure. Reflections having indices (*HKL*) with respect to the expanded unit cell are related to their parent structure index $(hkl)_p$, according to: $H = h - 2k$, $K = 2h + k$, $L = 3l$. An overview of some observed reflections in both notations is presented in Table 3.6. As mentioned, the SAED patterns revealed a point group symmetry of 4/*m* for U_3O_7. Considering further that all reflections are also consistent with the *HK*0: $H + K = 2n$, *H*00: $H = 2n$ and 00*L*: $L = 2n$ general reflection conditions, the space group of the perturbed structure is identified as $P4_2/n$ (no. 86).

Table 3.6. Overview of observed reflections with indices according to the parent cell and expanded unit cell notation.

Parent cell indexation		Expanded cell indexation		Fig.
Zone axis	Reflection	Zone axis	Reflection	
$[\mathbf{100}]_\mathbf{p}$	$(00\frac{2}{3})_p$	$[\mathbf{120}]$	(002)	6 a
	$(01\frac{1}{3})_p$		$(\bar{2}11)$	
$[\mathbf{3\bar{1}0}]_\mathbf{p}$	$(\frac{1}{5}\frac{3}{5}\frac{1}{3})_p$	$[\mathbf{110}]$	$(\bar{1}11)$	6 c
	$(\frac{2}{5}\frac{6}{5}\frac{1}{3})_p$		$(\bar{2}21)$	
$[\mathbf{2\bar{1}0}]_\mathbf{p}$	$(12\frac{1}{3})_p$	$[\mathbf{430}]$	$(\bar{3}41)$	6 d,
	$(121)_p$		$(\bar{3}43)$	7 a
$[\mathbf{001}]_\mathbf{p}$	$(\frac{4}{5}\frac{2}{5}0)_p$	$[\mathbf{001}]$	(020)	7 b
	$(200)_p$		(240)	
$[\mathbf{\bar{1}20}]_\mathbf{p}$	$(21\frac{2}{3})_p$	$[\mathbf{100}]$	(052)	8 b
	$(211)_p$		(053)	

3.3.4 Structural model for U_3O_7

In U_3O_7 the atomic arrangement remains closely related to the parent UO_2 fluorite structure, but the excess oxygen atoms give rise to the formation of so-called cuboctahedral oxygen clusters.[11, 40, 41] Such clusters consist of twelve oxygen atoms arranged at the vertices of a cuboctahedron, and a thirteenth atom is located at its center (see also section 3.3.2).[37] Whether the central oxygen atom occupies exactly the cuboctahedron center, or is somewhat displaced remains subject to debate.[11, 38, 39] Periodic replacement of eight "fluorite-anions" by a cuboctahedral oxygen cluster results in long-range ordered structures: in U_4O_9 a superstructure of 64 fluorite subcells ($4\mathbf{a}_p$, $4\mathbf{b}_p$, $4\mathbf{c}_p$) containing twelve clusters is recognized;[11, 39] in U_3O_7 the occurrence of cuboctahedral oxygen clusters has similarly been confirmed,[41, 43, 44] but their long-range ordering scheme remained subject to debate.[11, 40]

With the cuboctahedral oxygen cluster as defining perturbation underlying to the long-range order of the U_3O_7 crystal structure a structure model can be derived in the expanded unit cell described in the preceding paragraph. If one oxygen cluster is assigned at the corners of the defect structure unit cell (spanned by vectors $\mathbf{r}_1$, $\mathbf{r}_2$ and $\mathbf{r}_3$, see Figure 3.9), then each expanded cell contains four subcells with a cuboctahedral oxygen cluster arrangement (13 anions) and eleven subcells with a fluorite arrangement (8 anions). Evidently, the total number of anions in the expanded cell equals $(4 \times 13) + (11 \times 8) = 140$, and it contains $15 \times 4 = 60$ U atoms. Thus, the resulting O/U

ratio of the expanded unit cell equals 140/60 = 2.33, i.e. the exact stoichiometry which is expected for the U_3O_7 crystal structure.

The origin of the expanded unit cell is chosen at the cell center of a fluorite subcell containing a cuboctahedral cluster (Wyckoff position 4*e* of the fluorite parent structure, see Table 3.3). Consequently to this origin choice, the coordinates *x*,*y*,*z* of the U and O atoms relative to the parent structure basis vectors (Figure 3.3) must be transformed to coordinates *x*',*y*',*z*' relative to the supercell basis vectors (**A**, **B**, **C**), according to (***P***, ***p***):

$$\begin{pmatrix} x' \\ y' \\ z' \end{pmatrix} = \boldsymbol{P}^{-1} \cdot \left[\begin{pmatrix} x \\ y \\ z \end{pmatrix} - \boldsymbol{p} \right] \qquad \textbf{(3.11)}$$

where ***P*** denotes the linear transformation matrix and ***p*** denotes the origin translation vector:

$$\boldsymbol{P}^{-1} = \begin{bmatrix} 1 & 2 & 0 \\ -2 & 1 & 0 \\ 0 & 0 & 3 \end{bmatrix}^{-1} = \begin{bmatrix} 1/5 & -2/5 & 0 \\ 2/5 & 1/5 & 0 \\ 0 & 0 & 1/3 \end{bmatrix} \qquad \textbf{(3.12)}$$

$$\boldsymbol{p} = ½\mathbf{a_p} + ½\mathbf{b_p} + ½\mathbf{c_p} \qquad \textbf{(3.13)}$$

A complete list of the atomic positions in the expanded unit cell is presented in Table 3.7. Fluorite-arranged U and O atoms are labelled as U1-U8 and O1-O15, respectively. Anions corresponding to the cuboctahedra are labelled as O'1-O'6 and those corresponding to the cuboctahedra centers are labelled as O'c. The size of the cuboctahedra is defined by the value *u*, which relates with the displacement of anions along the twelve <*u u* 0> directions from the cuboctahedron center in the average unit cell (see also section 3.3.2). According to the neutron diffraction results of Garrido *et al*. *u* equals 0.41.[41] A schematic of the expanded unit cell using the value *u* = 0.41 is given in Figure 3.10. The cuboctahedra are FCC-like packed, with a dense stacking in the (**A**, **B**) plane: they are separated by 0.5**A** + 0.5**B**, or expressed in terms of the parent structure unit cell $1.5\mathbf{a_p} + 0.5\mathbf{b_p}$. A larger separation between cuboctahedra of two neighboring layers is given by 0.5**A** + 0.5**C**, or in terms of the subcell parameters $0.5\mathbf{a_p} + 1\mathbf{b_p} + 1.5\mathbf{c_p}$.

It is expected that the cuboctahedra in U_3O_7 are in fact distorted from their regular (ideal) geometry. As mentioned in section 3.3.2, when the anions are arranged in a regular cuboctahedron accidental all-face centering (*F*) extinctions occur, but the

introduction of distortion of the cuboctahedron vertices will lift these extinctions. The occurrence of distorted cuboctahedra would indeed explain our observations of parent structure reflections such as $(011)_p$ and $(121)_p$ in SAED patterns. In their latest refinement of the U_4O_9 crystal structure Cooper and Willis also obtained a distorted cluster model,[39] and significant deformation and tilting of the cuboctahedral configuration was similarly found by Desgranges *et al.* from refinement of U_3O_7 neutron diffraction data.[11]

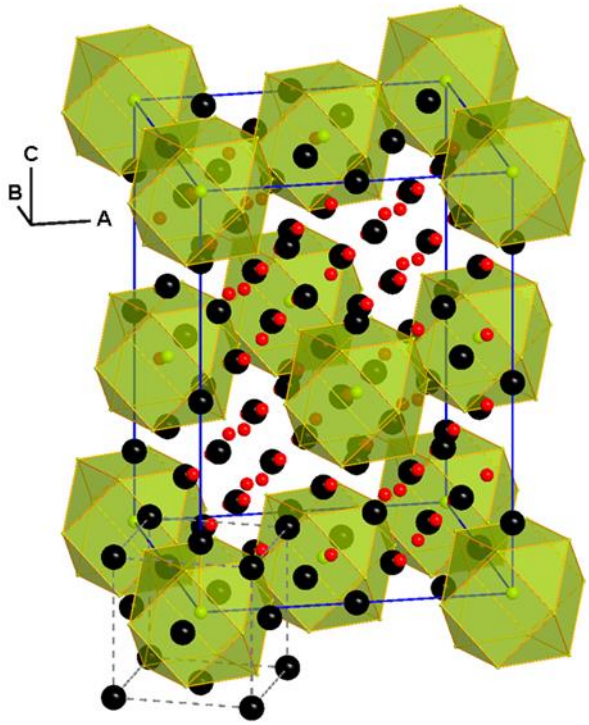

Figure 3.10. Illustration of the U_3O_7 crystal structure in its expanded unit cell (blue lines). U and O atoms located on fluorite-type positions in the parent structure (dashed gray lines) are represented by black and red spheres, respectively. Excess anions are located on the vertices of the cuboctahedra and at the cuboctahedra centers (green spheres).

In our structural model for U_3O_7 distortion of the cuboctahedra can be generated by the introduction of an additional displacement vector $\boldsymbol{\delta}^i$ on symmetry equivalent atoms *i* belonging to the cuboctahedron (see Table 3.7). This allows also to introduce restraints such that reflections of the type $(hkl)_p$: h, $k = 2n + 1$, $l = 2n$ remain extinct (e.g. $(110)_p$, $(112)_p$), since these were never observed in the SAED patterns (section 3.3.3).

Table 3.7. Atomic arrangement in the U_3O_7 expanded unit cell (SG $P4_2/n$, origin choice 2), with cell parameters $A = B = 1203.00 \pm 0.04$ pm, $C = 1664.70 \pm 0.06$ pm. (1) Fluorite-type uranium sites, (2) Fluorite-type oxygen sites, (3) cuboctahedral oxygen cluster.

Wyckoff sites		*x'*	*y'*	*z'*	Notes
U1	4*d*	1/2	0	0	
U2	8*g*	0.500	0.000	0.333	
U3	8*g*	0.100	0.200	0.000	
U4	8*g*	0.100	0.200	0.333	(1)
U5	8*g*	0.300	0.600	0.000	
U6	8*g*	0.300	0.600	0.333	
U7	8*g*	0.600	0.700	0.333	
U8	8*g*	0.700	0.400	0.333	
O1	4*f*	1/4	1/4	0.083	
O2	2*a*	1/4	1/4	1/4	
O3	4*f*	3/4	3/4	0.083	
O4	2*b*	3/4	3/4	1/4	
O5	4*e*	1/4	3/4	0.083	
O6	4*e*	1/4	3/4	0.250	
O7	4*e*	1/4	3/4	0.417	
O8	8*g*	−0.050	0.150	0.250	(2)
O9	8*g*	−0.050	0.150	0.417	
O10	8*g*	0.050	0.350	0.083	
O11	8*g*	0.050	0.350	0.250	
O12	8*g*	−0.050	0.650	0.083	
O13	8*g*	−0.050	0.650	0.250	
O14	8*g*	0.050	0.850	0.250	
O15	8*g*	0.050	0.850	0.417	
O'c	4*c*	0	0	0	
O'1	8*g*	(0−*u*×1/5)	(0+*u*×3/5)	0	
O'2	8*g*	(0−*u*×3/5)	(0−*u*×1/5)	0	
O'3	8*g*	(0+*u*×1/5) −(*δ*)	(0+*u*×2/5) +(*δ*×1/2)	(0+*u*×1/3)	
O'4	8*g*	(0−*u*×1/5) −(*δ*)	(0−*u*×2/5) +(*δ*×1/2)	(0+*u*×1/3)	(3)
O'5	8*g*	(0−*u*×2/5) +(*δ*×1/2)	(0+*u*×1/5) +(*δ*)	(0+*u*×1/3)	
O'6	8*g*	(0+*u*×2/5) +(*δ*×1/2)	(0−*u*×1/5) +(*δ*)	(0+*u*×1/3)	

A *Bond Valence Sum* (BVS) assessment was made to evaluate the validity of the introduction of a cluster distortion parameter δ.[53, 54] The BVS method relies on the principle that the length of a bond d_{ij} between two atoms i and j is a function only of the strength of the bond v_{ij}. The bond strength or bond valence is defined such that the valence of each atom i in the structure equals the sum of the bond valences v_{ij} between atom i and all other atoms in the structure:

$$\sum_j v_{ij} = V_i \qquad \textbf{(3.14)}$$

The variation of the bond length d_{ij} with varying bond valence v_{ij} can be expressed by an exponential relationship:

$$v_{ij} = \exp\left(\frac{R_0 - d_{ij}}{b}\right) \qquad \textbf{(3.15)}$$

Since Eq. (3.15) decays exponentially with increasing distance d_{ij}, the summation given by expression (3.14) needs to be carried out only over a limited number of atom pairs. Bond valence parameters R_0 and b of Eq. (3.15) are both expressed in the same length scale as the bond length d_{ij} and are derived from the analysis of the bond lengths between atom pairs in well-characterized crystal or molecular structures. The BVS analysis has been successfully applied in the investigation of complex uranium oxides and fluorides since more than sixty years already.[55-58] With the atomic coordinates in the expanded unit cell (see Table 3.7), BVS calculations were performed for different values of the deformation parameter d and with the parameter sets (R_0 and b) published by Zachariasen.[56] The parameter sets published by Brese and O'Keeffe, and Brown provided almost identical results.[59, 60]

The nominal valence state of uranium in U_3O_7 is 4.67. When taking the atomic arrangements corresponding to the undistorted cuboctahedra ($d = 0$), the BVS calculations resulted in a substantially deviating value with an average U valence of only 4.3, see Table 3.8. By varying the distortion parameter d, the average sum of the bond valences on the uranium sites increases: for $d = 0.0625$, the average uranium valence was found to be 4.67. The uranium atoms located at elevations $z' = 0$ and $z' = 0.5$ (U1, U3 and U5), i.e. at the equatorial level of the cuboctahedra assume a valence of 4.4. The average valence of cations located on planes in-between the layers with cuboctahedra is 4.8: positions U2 and U8 assume a valence around 4 (3.9 for U2 and 4.0 for U8), positions U4 and U7 assume a valence of 5.0 and the valence sum around U6 is 6.1. Within the accuracy of the BVS method, the results are more than satisfactory for the valence of the cations located in-between the cuboctahedra layers (U2, U4, U6, U7 and U8), and they indicate that further atomic position refinement might be needed to improve the environment of positions U1, U3 and U5.

Table 3.8. BVS-derived charge of the individual cations for undistorted (d = 0) and distorted cuboctahedra (d = 0.0625), using the Zachariasen parameter set. Values which do not correspond with a given valence state have been omitted.

	Multiplicity	δ = 0			δ = 0.0625		
		U^{4+}	U^{5+}	U^{6+}	U^{4+}	U^{5+}	U^{6+}
U1	4	4.3	-	-	4.3	-	-
U2	8	-	4.6	-	4.0	-	-
U3	8	-	4.5	-	4.4	-	-
U4	8	4.2	-	-	-	5.0	-
U5	8	-	4.5	-	4.4	-	-
U6	8	4.2	-	-	-	-	6.1
U7	8	4.2	-	-	-	5.0	-
U8	8	4.2	-	-	3.9	-	-
		Average cation charge			**Average cation charge**		
		4.31			4.67		

A comparison of simulated and experimentally observed SAED patterns is presented in Figure 3.11, illustrating the effect of regular ($\delta = 0$) and distorted cluster arrangements ($\delta = 0.06$); in both cases, the dimensions of the cuboctahedron were kept identical to the value derived by Garrido *et al*. ($u = 0.41$).[41] Only those diffraction patterns corresponding with the distorted arrangement show additional reflections which violate the *F*-centering reflection conditions, consistent with the experimental observations.

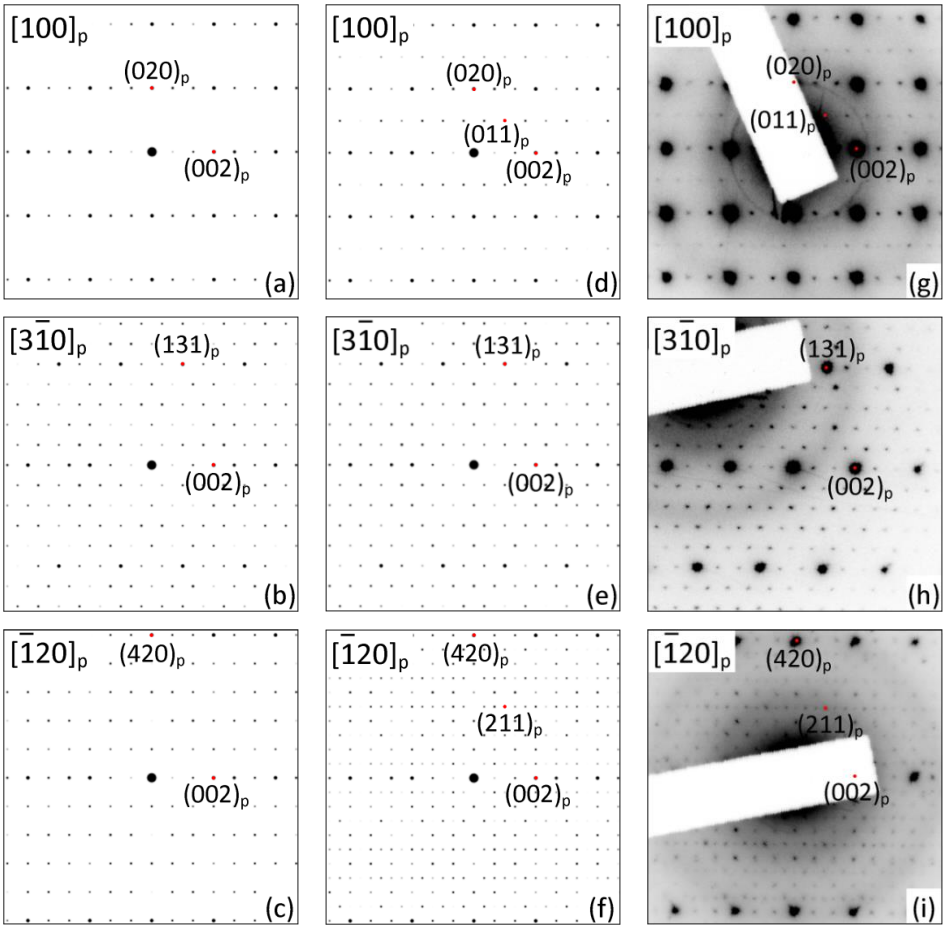

Figure 3.11. Comparison of simulated SAED patterns according to the derived structural model for U_3O_7 when cuboctahedral oxygen clusters have either a regular arrangement (a, b, c) or a distorted arrangement (d, e, f). Excerpts of the corresponding experimentally observed SAED patterns are presented in the right column (the origin of pattern (h) was shifted to allow for a better comparison).

3.4 Discussion

Polycrystalline samples of U_3O_7 were prepared by oxidation of UO_2 powder. The average stoichiometry was accurately measured via gravimetric analysis and was equal to an O/U ratio of 2.34 ± 0.01, in almost perfect agreement with the expected value of 7/3 = 2.33. Lattice parameters of U_3O_7 were determined via Rietveld refinement of X-ray diffraction data: c_p = 554.90 pm and $a_p = b_p$ = 538.00 pm (c_p/a_p = 1.031), also in excellent agreement with reported values.[11, 41] These results confirm that the produced powders are representative of U_3O_7.

Both X-ray and electron diffraction showed intense reflections obeying *F*-centering conditions, due to the fluorite-type parent structure. In addition to the intense parent structure reflections numerous weak satellites were observed in the SAED patterns which remained undetected by XRD. The satellite reflections could be indexed by three wave vectors $\mathbf{q_1} = 1/15 \cdot [395]^*_p$, $\mathbf{q_2} = 1/15 \cdot [\bar{3}\bar{9}5]^*_p$ and $\mathbf{q_3} = 1/15 \cdot [\bar{9}35]^*_p$. Thus, the long-range periodicity of the defect structure which exists in U_3O_7 is commensurate with respect to the fluorite-type parent structure, and the smallest unit cell which keeps both the perturbation and the parent structure invariant is defined by $\mathbf{A} = \mathbf{a_p} - 2\mathbf{b_p}$, $\mathbf{B} = 2\mathbf{a_p} + \mathbf{b_p}$, $\mathbf{C} = 3\mathbf{c_p}$, see Figure 3.9.

Unpublished results due to Thomas and Taylor which were cited in a review paper of McEachern and Taylor mentioned the existence of a tetragonal superstructure for U_3O_7 with cell dimensions $a = b = \sqrt{5}a_p$ and $c = 3a_p$.[1] These dimensions are identical to those of the **A**, **B**, **C** unit cell derived in the present study ($V = 15 \cdot V_p$). Other investigators interpreted the complex perturbation of U_3O_7 in much larger unit cells. Desgranges *et al.* proposed a supercell in which all three parent structure unit parameters are quadrupled: $\mathbf{A}_D = 4\mathbf{a_p}$, $\mathbf{B}_D = 4\mathbf{b_p}$, $\mathbf{C}_D = 4\mathbf{c_p}$ ($V_D = 64 \cdot V_p$).[11] Such a supercell is not compatible with the present observations. Nowicki *et al.*, also referring to the unpublished results of Thomas and Taylor, predicted superstructures of the type $\mathbf{A}_N = 5\mathbf{a_p}$, $\mathbf{B}_N = 5\mathbf{b_p}$, $\mathbf{C}_N = j\ 3\mathbf{c}$ (j an integer) for U_3O_7.[40] The latter expanded cells are consistent with the present findings, but they are not primitive (e.g. $V_N = 75 \cdot V_p$):

$$\mathbf{A}_N = \mathbf{A} + 2\mathbf{B} = 5\mathbf{a_p} \qquad \textbf{(3.16)}$$

$$\mathbf{B}_N = -2\mathbf{A} + \mathbf{B} = 5\mathbf{b_p} \qquad \textbf{(3.17)}$$

$$\mathbf{C}_N = \mathbf{C} = 3\mathbf{c_p} \qquad \textbf{(3.18)}$$

In accordance with literature on the defect structure of U_3O_7,[11, 40, 41] and the U_4O_9 superstructure,[37, 38, 45] long-range order in U_3O_7 is interpreted in terms of the ordering of

cuboctahedral oxygen clusters with 12 or 13 atoms which periodically replace the eight anions of a fluorite subcell. The expanded unit cell (**A**, **B**, **C**) contains four cuboctahedral clusters and eleven fluorite-type subcells. Oxygen atoms which are arranged on the vertices of a regular cuboctahedron, centered in the fluorite subcell would give rise to accidental *F* reflection conditions $(hkl)_p$: $h + k$, $k + l$, $h + l = 2n$.[50] The observation of weak reflections violating these rules further indicated that the cuboctahedra are distorted, in accordance with results of other researchers.[11, 39]

A point of discussion remains the occupation of the cuboctahedron center, i.e. whether the cuboctahedra consist of 12 or 13 oxygen atoms. With cuboctahedra of 13 anions, the total number of anions in the expanded unit cell is 140 and the resulting O/U ratio is 140/60 = 2.33; if the cuboctahedra would contain 12 anions, the O/U ratio would be 136/60 = 2.27. The thermogravimetric results yielded an O/U ratio of 2.34 ± 0.01, and are thus more in line with the assumption that the cuboctahedra contain 13 atoms. The argument of unit cell composition was used by Bevan *et al*. in order to exclude cuboctahedra with empty centers in their description of the U_4O_9 superstructure.[37] Cooper and Willis, however, more recently concluded that in U_4O_9 the anions at the cuboctahedra centers would be displaced along <111> directions.[39] On the other hand, Desgranges *et al*. retained the occupation of cuboctahedra centers in their assessment of the U_3O_7 structure.[11] From a structural point of view it remains unclear how such anions would coordinate with other atoms, and this is definitely a matter for further research.

Bond-valence-sum (BVS) calculations gave a tentative for the distortion of the cuboctahedra, defined by the magnitude of displacement vectors $\boldsymbol{\delta}^{i}$ (see Table 3.7), although intensity data will be required to more accurately refine the atomic positions of the cuboctahedron anions. When the distortion parameter (δ) is varied, the average cation valence increases and an exact match with the nominal U valence in U_3O_7 (4.67) is obtained for $\delta = 0.0625$. With this deformation parameter, two U^{5+} sites (U4 and U7) and one U^{6+} site (U6) could be distinguished (see Figure 3.12). Recent X-ray absorption experiments confirmed that in U_4O_9 the oxidation states U^{4+} and U^{5+} predominate, while in U_3O_8 the oxidation states U^{5+} and U^{6+} predominate.[61] No such experimental data is yet available on the U_3O_7 system, but the current BVS calculations give results which are consistent and illustrate the development of the U^{6+} environment upon further oxidation of U_4O_9, marking U_3O_7 as the important intermediate oxide for U_3O_8 formation.

Oxidation of UO_2 into U_4O_9 is accompanied by an isotropic cell contraction, mainly related to the decreasing ionic radius of cations with a higher valence state.[16] The contraction of the $\mathbf{a}_p$- and $\mathbf{b}_p$-axes and subsequent expansion of the $\mathbf{c}_p$-axis (anisotropy) which occurs upon further oxidation can be understood to be a consequence of the

ordering of the cuboctahedra forming a layered structure in U_3O_7. Compared to U_4O_9, the cuboctahedra are substantially re-ordered in U_3O_7.

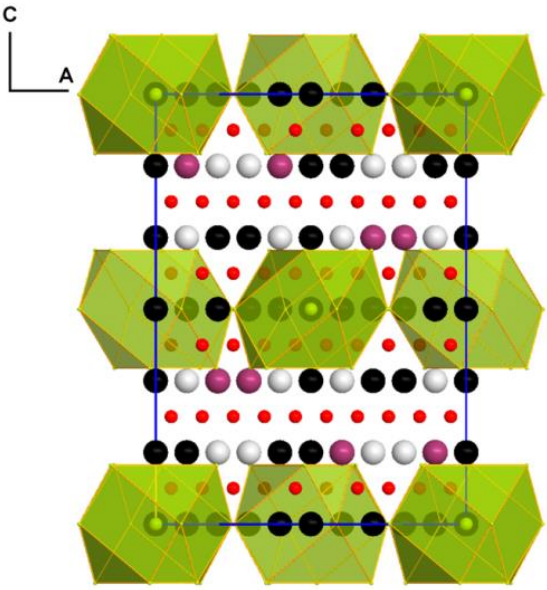

Figure 3.12. AC projection of the U_3O_7 expanded unit cell demonstrating the location of U^{5+} (grey colored) and U^{6+} (purple colored) environments due to distorted cuboctahedra ($\delta = 0.0625$). This projection also clearly illustrates the layered arrangement of cuboctahedra in planes perpendicular to the **C**-axis, at intervals of 0, 1.5, 3 × $\mathbf{c_p}$.

In the U_3O_7 structure cuboctahedra are arranged in layers perpendicular to the **C**-axis with an inter-layer distance of 1.5 × $\mathbf{c_p}$ (see Figure 3.12). The arrangement in U_4O_9 is notably different, the intervals are $0.5\mathbf{a_p} + 1\mathbf{b_p} + 1.5\mathbf{c_p}$ (and all permutation of $\mathbf{a_p}$, $\mathbf{b_p}$ and $\mathbf{c_p}$), i.e. there is no such distinct layer periodicity.[37] A comparison of the cuboctahedra locations in both structures is presented schematically in Figure 3.13, taking the origin at the center of a cuboctahedron. Green and gray hexagons represent cuboctahedra locations in the U_3O_7 crystal structure, at positions 0, 3 × $\mathbf{c_p}$ and 1.5 × $\mathbf{c_p}$, respectively. The projection of the expanded **A**, **B**, **C** unit cell is highlighted in blue. Diamond symbols represent the cuboctahedra in the U_4O_9 crystal structure, whose expanded $4\mathbf{a_p}$, $4\mathbf{a_p}$, $4\mathbf{a_p}$ cubic unit cell is highlighted in red (arbitrary selection of the unit cell axes); they are centered on the 12*b* Wyckoff sites of the $I\bar{4}3d$ space group of U_4O_9.[37]

It is interesting to compare distances between cuboctahedral oxygen clusters in the U_3O_7 structure and in U_4O_9. In U_3O_7 the nearest neighbor distance between two

cuboctahedra is in the planes perpendicular to the **C**-axis. In terms of the fluorite substructure, their respective displacement is given by $1.5\mathbf{a_p} + 0.5\mathbf{b_p}$ and the distance is thus $\sqrt{5/2}a_p$. The next-nearest distances are between two cuboctahedra in different layers, and their displacement is given by $0.5\mathbf{a_p} + 1\mathbf{b_p} + 1.5\mathbf{c_p}$. Ignoring for a moment the small tetragonal distortion ($c_p \approx a_p$), the distance is $\sqrt{7/2}a_p$ which is exactly the nearest neighbor distance between the cuboctahedral defects in cubic U_4O_9.[37]

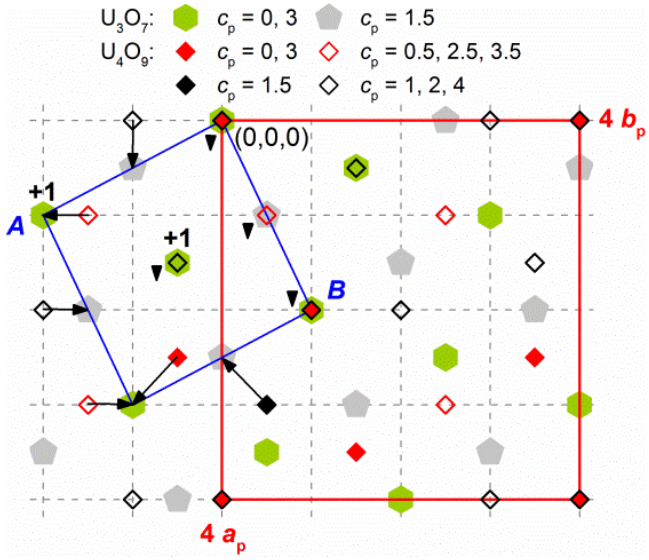

Figure 3.13. AB projection of the real space schematic presented in Figure 3.9, but expanded over a larger range. The location of cuboctahedra in U_3O_7 and in U_4O_9 are indicated by the various symbols, both unit cells are highlighted in blue and red, respectively. Arrowed lines denote displacements having two components along the basis vectors ($\mathbf{w_{1,2}}$) and plain arrows denote displacements along the **c**-axis ($\mathbf{w_3}$).

The defect structure of U_3O_7 can be interpreted as translational movement of cuboctahedra from positions originally occupied in the U_4O_9 structure. The displacement either occurs according to $\pm 0.5\mathbf{a_p} \pm 0.5\mathbf{b_p}$ ($\mathbf{w_1}$) and $\pm 0.5\mathbf{a_p} \pm 0.5\mathbf{c_p}$ ($\mathbf{w_2}$), or to $\pm 1\mathbf{c_p}$ ($\mathbf{w_3}$). A possible scheme is presented in Figure 3.13, where arrowed lines denote displacements along $\mathbf{w_1}$ and $\mathbf{w_2}$, and plain arrows denote displacements along $\mathbf{w_3}$. Next to the rearrangement, two additional cuboctahedra (denoted as "+1") have to be created in each expanded unit cell (**A**, **B**, **C**) in order to obtain an O/U ratio of 2.33. The current analysis illustrates that the transformation of U_4O_9 into U_3O_7 upon oxidation can be seen as a process of cuboctahedra rearrangement into a layered structure and the additional creation of new cuboctahedra due to the incorporation of excess anions.

3.5 Conclusion

U_3O_7 powder was synthesized by oxidation of UO_2 powder under specific conditions. Lattice parameters were accurately measured by X-ray diffraction and were equal to $c_p = 554.90 \pm 0.02$ pm and $a_p = b_p = 538.00 \pm 0.02$ pm ($c_p/a_p = 1.031$), in excellent agreement with reported values. The stoichiometry of the U_3O_7 phase was determined via gravimetric analysis and was equal to an O/U ratio of 2.34 ± 0.01, also in agreement with the expected value of 7/3 = 2.33.

A detailed study of the U_3O_7 crystal structure using X-ray powder diffraction and electron diffraction on single crystal grains was performed. SAED patterns revealed additional, weak reflections which remained undetected by XRD. The U_3O_7 crystal structure exhibits a complex, long-range ordering based on a tetragonal parent structure which is reminiscent of the original fluorite-type structure of UO_2. Satellite reflections in reciprocal space were defined by three linearly independent, commensurate wave vectors $\mathbf{q_1} = 1/15 \cdot [395]_p^*$, $\mathbf{q_2} = 1/15 \cdot [\bar{3}\bar{9}5]_p^*$ and $\mathbf{q_3} = 1/15 \cdot [\bar{9}35]_p^*$. The corresponding real space periodicity was subsequently derived in an expanded unit cell ($V = 15 \cdot V_p$) spanned by the basis vectors:

$$\mathbf{A} = \mathbf{a_p} - 2\mathbf{b_p} \tag{3.7}$$

$$\mathbf{B} = 2\mathbf{a_p} + \mathbf{b_p} \tag{3.8}$$

$$\mathbf{C} = 3\mathbf{c_p} \tag{3.9}$$

The long-range ordered crystal structure of U_3O_7 can be described in the expanded unit cell (SG $P4_2/n$) as a fluorite-derived structure in which the cations keep the same stacking as in UO_2, and where the anions follow an ordered arrangement of eleven fluorite-like subcells (with eight anions) and four subcells in which the anions assume a distorted cuboctahedral arrangement (with thirteen anions). The composition of the expanded unit cell is then $U_{60}O_{140}$ and yields an O/U ratio of 2.33.

The nearest neighbor distance between cuboctahedra equals $\sqrt{5/2}a_p$ and is shorter than the distance between cuboctahedra in the U_4O_9 crystal structure. The rearrangement of cuboctahedra in U_3O_7 as compared to in U_4O_9 can be interpreted as translational movement and creation of new cuboctahedra such that a layered structure is obtained. This explains the anisotropy ($\mathbf{a_p}$, $\mathbf{b_p}$ contraction; $\mathbf{c_p}$ expansion) that is witnessed upon oxidation of U_4O_9 into U_3O_7.

Acknowledgements

G.L. thanks SCK•CEN for a PhD fellowship. The authors thank K. Vanaken, P. Dries and Dr. S. Van den Berghe for laboratory support, and Dr. A. Dobney for providing ICPMS analysis.

Appendix II: Additional information regarding the Rietveld refinement methodology followed and crystallographic information file of the U_3O_7 crystal structure. Additional SAED pattern (**c**-axis twin) and a three-dimensional schematic of reciprocal space in the U_3O_7 structure.

References

(1) R. J. McEachern, P. Taylor, *J. Nucl. Mater.* **1998**, *254*, 87.
(2) L. E. Herranz, F. Feria, *Prog. Nucl. Energy* **2009**, *51*, 201.
(3) M. J. Bannister, *J. Nucl. Mater.* **1968**, *26*, 174.
(4) A. Leenaers, L. Sannen, S. Van den Berghe, M. Verwerft, *J. Nucl. Mater.* **2003**, *317*, 226.
(5) P. Taylor, R. J. McEachern, D. C. Doern, D. D. Wood, *J. Nucl. Mater.* **1998**, *256*, 213.
(6) R. E. Einziger, L. E. Thomas, H. C. Buchanan, R. B. Stout, *J. Nucl. Mater.* **1992**, *190*, 53.
(7) G. C. Allen, P. A. Tempest, J. W. Tyler, *J. Chem. Soc., Faraday Trans. 1* **1988**, *84*, 4049.
(8) P. Taylor, E. A. Burgess, D. G. Owen, *J. Nucl. Mater.* **1980**, *88*, 153.
(9) D. E. Y. Walker, *J. Appl. Chem.* **1965**, *15*, 128.
(10) L. Quémard, L. Desgranges, V. Bouineau, M. Pijolat, G. Baldinozzi, N. Millot, J. C. Nièpce, A. Poulesquen, *J. Eur. Ceram. Soc.* **2009**, *29*, 2791.
(11) L. Desgranges, G. Baldinozzi, G. Rousseau, J.-C. Nièpce, G. Calvarin, *Inorg. Chem.* **2009**, *48*, 7585.
(12) A. Poulesquen, L. Desgranges, C. Ferry, *J. Nucl. Mater.* **2007**, *362*, 402.
(13) G. Rousseau, L. Desgranges, F. Charlot, N. Millot, J. C. Nièpce, M. Pijolat, F. Valdivieso, G. Baldinozzi, J. F. Bérar, *J. Nucl. Mater.* **2006**, *355*, 10.
(14) F. Valdivieso, V. Francon, F. Byasson, M. Pijolat, A. Feugier, V. Peres, *J. Nucl. Mater.* **2006**, *354*, 85.
(15) P. Taylor, *J. Nucl. Mater.* **2005**, *344*, 206.
(16) I. Grenthe, J. Drozdzynski, T. Fujino, E. C. Buck, T. E. Albrecht-Schmitt, S. F. Wolf, *The chemistry of the Actinide and Transactinide elements, Vol. 1*, 3 ed., Springer, Dordrecht, **2006**.
(17) F. Grønvold, *J. Inorg. Nucl. Chem.* **1955**, *1*, 357.
(18) B. T. M. Willis, *Nature* **1963**, *197*, 755.
(19) B. T. M. Willis, *Proc. Brit. Ceram. Soc.* **1964**, *No. 1*, 9.
(20) B. T. M. Willis, *Acta Crystallogr. A* **1978**, *34*, 88.
(21) B. Belbeoch, C. Piekarski, P. Perio, *Acta Crystallogr.* **1961**, *14*, 837.
(22) B. T. M. Willis, *J. Phys. (Paris)* **1964**, *25*, 431.
(23) K. B. Alberman, J. S. Anderson, *J. Chem. Soc.* **1949**, 303.
(24) B. O. Loopstra, *Acts Cryst.* **1964**, *17*, 651.
(25) B. Loopstra, *Acta Crystallogr. B* **1970**, *26*, 656.
(26) H. R. Hoekstra, S. Siegel, F. X. Gallagher, *J. Inorg. Nucl. Chem.* **1970**, *32*, 3237.
(27) H. R. Hoekstra, A. Santoro, S. Siegel, *J. Inorg. Nucl. Chem.* **1961**, *18*, 166.
(28) P. Jolibois, *C.R. Acad. Sci.* **1947**, *224*, 1395.
(29) E. F. Westrum, Jr., F. Gronvold, *Phys. Chem. Solids* **1962**, *23*, 39.
(30) G. Leinders, J. Pakarinen, R. Delville, T. Cardinaels, K. Binnemans, M. Verwerft, *Inorg. Chem.* **2016**, *55*, 3915.
(31) P. E. Blackburn, J. Weissbart, E. A. Gulbranson, *J. Phys. Chem.* **1958**, *62*, 902.
(32) P. A. Tempest, P. M. Tucker, J. W. Tyler, *J. Nucl. Mater.* **1988**, *151*, 269.

(33) G. C. Allen, P. A. Tempest, J. W. Tyler, *J. Chem. Soc., Faraday Trans. 1* **1988**, *84*, 4061.
(34) S. R. Teixeira, K. Imakuma, *J. Nucl. Mater.* **1991**, *178*, 33.
(35) S. Aronson, B. Roof, J. Belle, *J. Chem. Phys.* **1957**, *27*, 137.
(36) A. D. Murray, B. T. M. Willis, *J. Solid State Chem.* **1990**, *84*, 52.
(37) D. J. M. Bevan, I. E. Grey, B. T. M. Willis, *J. Solid State Chem.* **1986**, *61*, 1.
(38) B. T. M. Willis, *J. Chem. Soc., Faraday Trans. II* **1987**, *83*, 1073.
(39) R. I. Cooper, B. T. M. Willis, *Acta Crystallogr. A* **2004**, *60*, 322.
(40) L. Nowicki, F. Garrido, A. Turos, L. Thomé, *J. Phys. Chem. Solids* **2000**, *61*, 1789.
(41) F. Garrido, R. M. Ibberson, L. Nowicki, B. T. M. Willis, *J. Nucl. Mater.* **2003**, *322*, 87.
(42) H. He, D. Shoesmith, *Phys. Chem. Chem. Phys.* **2010**, *12*, 8109.
(43) D. A. Andersson, G. Baldinozzi, L. Desgranges, D. R. Conradson, S. D. Conradson, *Inorg. Chem.* **2013**, *52*, 2769.
(44) N. A. Brincat, M. Molinari, G. C. Allen, M. T. Storr, S. C. Parker, *J. Nucl. Mater.* **2015**, *467*, 724.
(45) H. Blank, C. Ronchi, *Acta Crystallogr. A* **1968**, *24*, 657.
(46) G. Leinders, T. Cardinaels, K. Binnemans, M. Verwerft, *J. Nucl. Mater.* **2015**, *459*, 135.
(47) G. Hölzer, M. Fritsch, M. Deutsch, J. Härtwig, E. Förster, *Phys. Rev. A* **1997**, *56*, 4554.
(48) J. K. Fink, *J. Nucl. Mater.* **2000**, *279*, 1.
(49) D. G. Martin, *J. Nucl. Mater.* **1988**, *152*, 94.
(50) N. C. Popa, B. T. M. Willis, *Acta Crystallogr. A* **2004**, *60*, 318.
(51) R. J. Hill, C. J. Howard, *J. Appl. Crystallogr.* **1987**, *20*, 467.
(52) G. C. Allen, J. T. Buswell, P. A. Tempest, *J. Chem. Soc., Dalton Trans.* **1983**, 589.
(53) I. D. Brown, *Chem. Rev.* **2009**, *109*, 6858.
(54) I. D. Brown, D. Altermatt, *Acta Crystallogr. B* **1985**, *41*, 244.
(55) W. Zachariasen, *Acta Cryst.* **1954**, *7*, 795.
(56) W. H. Zachariasen, *J. Less Common Met.* **1978**, *62*, 1.
(57) S. Van den Berghe, M. Verwerft, J. P. Laval, B. Gaudreau, P. G. Allen, A. Van Wyngarden, *J. Solid State Chem.* **2002**, *166*, 320.
(58) A. Baena, T. Cardinaels, K. Govers, J. Pakarinen, K. Binnemans, M. Verwerft, *J. Nucl. Mater.* **2015**, *467*, *Part 1*, 135.
(59) N. E. Brese, M. O'Keeffe, *Acta Crystallogr. B* **1991**, *47*, 192.
(60) I. D. Brown, *Bond Valence Parameters,* **2013**, accessed on: 2016-07-29 http://www.iucr.org/resources/data/datasets/bond-valence-parameters.
(61) K. O. Kvashnina, S. M. Butorin, P. Martin, P. Glatzel, *Phys. Rev. Lett.* **2013**, *111*, 1.

Chapter 4.

Low-temperature oxidation of fine UO_2 powders: a process of nanosized domain development

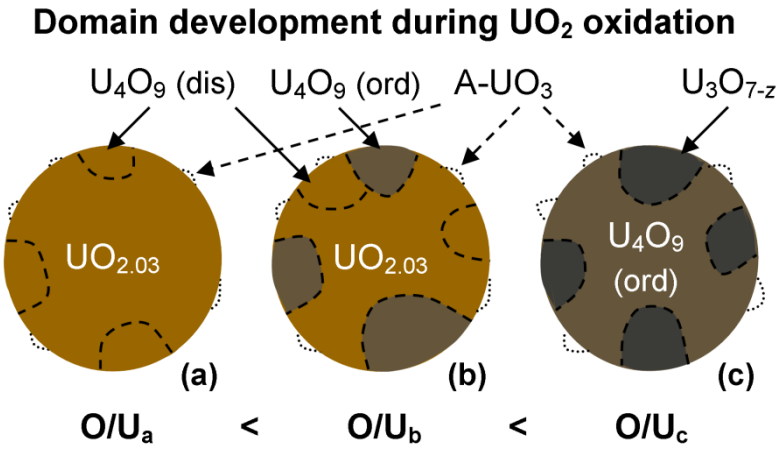

Published as: Gregory Leinders, Janne Pakarinen, Rémi Delville, Thomas Cardinaels, Koen Binnemans, and Marc Verwerft, *Inorganic Chemistry* **2016**, *55*, 3915-3927.

Author contributions

Gregory Leinders performed the main part of the experimental work, the interpretation of the data and the writing of this manuscript. He also contributed to the experimental strategy and the scientific ideas.

4.1 Introduction

Oxidation of uranium(IV) oxide (UO_2) has been the subject of research for more than 70 years. Most of the previous studies have been focused on the behavior at moderate temperatures (100-400 °C), a region of interest in both the front-end and back-end of the UO_2 nuclear fuel cycle. Control of the oxygen intake is of importance for nuclear fuel production, more precisely for the UO_2 powder processing stages. Powder morphology and stoichiometry affect the pellet pressing process (die filling and compaction) and the early stages of sintering. Numerous experimental studies have been performed on powders.[1-13] Also, the handling of freshly reduced 'active' powders, which react pyrophorically when exposed to air has been studied.[14, 15] Additionally, oxidation of UO_2 single crystals has been investigated.[2, 16-18] A significant portion of work has been devoted to the oxidation behavior of both non-irradiated[8, 19-25] and irradiated[26-28] UO_2 fuel pellets in the context of spent fuel stability under medium- and long-term storage conditions. The focus has mainly been on the conversion of UO_2 to the more thermodynamically stable oxide U_3O_8. The formation of U_3O_8 leads to about 36% volume expansion, which may be detrimental for the integrity of the fuel cladding. Also, oxide compounds having U^{5+} and U^{6+} oxidation states show an increased solubility in aqueous environments, which is of concern in the repository of spent nuclear fuel.[29]

Upon oxidation, the fluorite ($Fm\bar{3}m$) crystal structure of UO_2 (a_0 = 547.127(8) pm)[30] contracts linearly while still retaining its cubic symmetry. Excess oxygen is incorporated onto positions which are slightly displaced from the interstitial sites. Additionally, vacancies appear at some of the regular oxygen sites. The resulting effect is a local, but random reorganization of the anion sublattice.[31-34] A wide phase domain of hyperstoichiometric UO_{2+x} ($x \leq 0.25$) exists at temperatures between 250 °C and 2850 °C.[35] At lower temperatures the oxygen solubility limit is considered to be quite small ($x \leq 0.03$).[36] Oxidation in excess of this limit results in a two-phase domain of UO_{2+x} and U_4O_{9-y} ($0.06 \leq y \leq 0.02$).[37] The crystal structure of U_4O_9 is commonly described as a superstructure, based on a fluorite-like parent cell repeated four times in all directions (i.e. $4a_0 \times 4a_0 \times 4a_0$, a_0 = 543.9 pm).[1, 38, 39] The defect structure has been described by an ordering of cuboctahedral oxygen clusters,[1, 38-40] and lately, by split di- and quad-interstitial clusters.[31, 41, 42]

As oxidation proceeds beyond U_4O_9 the structure deforms anisotropically from cubic to tetragonal symmetry, but the exact formation mechanism is still under debate.[1, 43-45] The compound formed is usually classified as U_3O_7, although U_3O_{7-z} is probably a more appropriate designation. The nonstoichiometric character of U_3O_{7-z} is recognized in its variable tetragonal unit cell parameters ($c/a \neq 1$).[3, 8, 13, 46] The variability of the ratio c/a has, however, also been related to the strain produced by topotactic growth (i.e. formation of a new crystalline phase within a reactant) of U_3O_7 within U_4O_9.[1] The solid

solubility limit is expected to be close to O/U = 2.33, and the associated lattice parameters are reported in the range a_0 = 536.3-539.8 pm and c_0 = 553.1-556.5 pm.[3, 46] A generally accepted crystalline structure has not been formulated for the phase or phases commonly referred to as U_3O_7. Several studies described it as fluorite-based and having a defect structure based on the formation of cuboctahedral oxygen clusters.[1, 44, 45] Recent *ab-initio* studies confirmed the formation of oxygen clusters, but failed to reproduce the experimentally observed tetragonal distortion,[41] or to prove the cuboctahedral arrangement due to limitations in the simulation cell.[47] Electron diffraction (Thomas and Taylor, unpublished but cited in other works,[36, 44] and Leinders *et al.*[48]) and neutron diffraction[1, 45] experiments evidence the presence of superstructure reflections indicating an ordered arrangement of the defect clusters. The electron diffraction investigations showed that the modulation is different from that of U_4O_9, but a precise description of the superstructure has not been formulated.

The most stable UO_2 oxidation product formed in dry air is orthorhombic α-U_3O_8.[49] U_3O_8 formation is usually associated with a process of nucleation-and-growth from U_3O_7 in non-irradiated powder and pellets.[2, 3, 50, 51] Theoretically, oxidation of UO_2 completes at the composition UO_3, a pure U^{6+} compound. In contrast, all previously discussed oxidation products are mixed-valence compounds.[41, 52, 53] The UO_3 polymorphs (7 known modifications) are moderately stable in air and dissociate into U_3O_8 and O_2 at temperatures between 450 °C and 700 °C.[54] UO_3 is typically obtained as a decomposition product of uranium compounds prepared via solution chemistry (e.g. uranyl nitrate hexahydrate and ammonium diuranate),[55, 56] but amorphous UO_3 and schoepite ($UO_3 \cdot 2H_2O$) was also reported to form in air-oxidized UO_2 powders and pellets.[7, 21, 57, 58]

The consensus has been that oxidation of UO_2 proceeds, at least initially, as a diffusion-driven surface reaction involving formation of a product layer.[36, 59] The sequence of crystalline compounds formed upon increasing the oxygen content is: $UO_2 \rightarrow U_4O_9 \rightarrow U_3O_7 \rightarrow U_3O_8$, here disregarding the nonstoichiometric regions in the U-O system.[1, 3] Formation of an oxide layer on the grain boundaries of irradiated UO_2 pellets has been readily observed by electron[26, 28, 60, 61] and optical[27] microscopy. Similar results have not been reproduced for fine powders and single crystals.[2, 16] High-resolution transmission electron microscopy (HR-TEM) with a sub nanometer-scale spatial resolution can be a powerful tool for studying the complex oxidation behavior of UO_2.

In this work, the mechanisms of surface oxidation of freshly reduced UO_2 powders are investigated in the low-temperature range from 40 °C to 250 °C. Samples were prepared by solid state synthesis under isothermal and isobaric conditions (dry, synthetic air) and measured via *in-situ* thermogravimetric analysis (TGA). In addition, the effect of particle size on oxidation was studied in three powders with specific surface areas ranging from 4 $m^2 g^{-1}$ to 21 $m^2 g^{-1}$. Crystallographic changes in the

oxidized powders were evaluated by X-ray diffraction (XRD). These bulk-sensitive measurements were complemented with HR-TEM, which provided new insights on the oxidation mechanisms of individual grains.

4.2 Experimental

4.2.1 Sample preparation

Samples were prepared from two depleted UO_{2+x} batches (average O/U ≈ 2.1) produced via the Integrated Dry Route (IDR process) and supplied by FBFC International (Dessel, Belgium). The impurity content of the as-received powder was evaluated using inductively coupled plasma-mass spectroscopy (ICP-MS, ThermoFisher XSeries2). In total, the presence of 50 elements was probed for. The combined metallic impurity fraction was 136 µg g^{-1} and 47 µg g^{-1} in the two batches. In order to obtain samples with different surface areas, a wet route dissolution process was used. The as-received powders were first dissolved in HNO_3 (4M aqueous solution) and subsequently titrated with an excess of a 4M NH_4OH aqueous solution. The precipitate so formed was vacuum filtered and dried at 80 °C for several hours to obtain clear yellow $(NH_4)_2U_2O_7$ (ammonium diuranate or ADU) powder.

Three uranium oxide precursor powders, having low (L), medium (M) and high (H) specific surface areas, were prepared from the produced ADU powder via dry-route processing. Surface areas were measured by nitrogen gas adsorption (BET analysis using a Micromeritics TriStar II 3020), see Table 4.1. The corresponding theoretical spherical particle size (d_{BET}), calculated from the surface area values, is added to this table. Further processing of the powders was performed in a Carbolite TZF1800 tube furnace with continuous flows of dry active gasses (dew point < -80 °C). Powder H was obtained by calcination of the ADU powder in synthetic air (N_2 / 21 vol.% O_2) at 550 °C for 30 min. X-ray analysis showed that the compound thus formed was β-UO_3. Powders M and L were obtained by calcination in synthetic air at 650 °C for 30 min and 4 h, respectively. The compounds thus formed were identified as α-U_3O_8. Small amounts of the precursor powders were subsequently sampled, reduced to stoichiometric UO_2 and oxidized under specific conditions (see section 4.2.2).

Table 4.1. Specific surface area, theoretical spherical particle size and oxide type of the precursor powders.

	L	**M**	**H**
Specific surface area (m^2 g^{-1})	4.0	9.3	21.1
Theoretical particle size d_{BET} (nm)	179	77	34
Type of oxide	U_3O_8	U_3O_8	UO_3

Three powders of uranium oxide with varying stoichiometry in a reference crystalline state ($UO_{2.03}$, U_4O_9, U_3O_7) were additionally produced using the above described thermal equipment. The as-received UO_{2+x} (2 $m^2 g^{-1}$) was first reduced to stoichiometric UO_2 at 700 °C in a flow of Ar / 5 vol.% H_2. After cooling to room temperature and purging with pure Ar, the flushing gas was switched to Ar / 0.01 vol.% O_2 for several hours. This procedure passivates the powdered material from uncontrolled oxidation upon retrieval from the furnace and exposure to the normal atmosphere.[15] The average stoichiometry O/U of the powder thus obtained was 2.03 as measured by gravimetry. U_4O_9 (O/U = 2.24) was produced by heating the as-received powder at 200 °C in Ar / 0.01 vol.% O_2 for 24 h. U_3O_7 (O/U = 2.34) was obtained by heating the as-received powder at 250 °C in synthetic air for 7 h. Small quantities of U_3O_8 were present both in the U_4O_9 and U_3O_7 powders. From an XRD Rietveld refinement, the quantity of U_3O_8 was found to be 1.5 wt.% in our U_4O_9 and 3.8 wt.% in our U_3O_7 samples. These amounts are taken into account in the presented stoichiometry values for U_4O_9 and U_3O_7. The presence of U_3O_8 did not interfere with the reference compound reflections in XRD.

4.2.2 Thermogravimetric analysis (TGA)

Thermogravimetric analysis on various samples of the three precursor powders was performed with a Netzsch STA 449 ***F1*** Jupiter® thermogravimeter, coupled to a quadrupole mass spectrometer (403 D Aëolos®) to analyze the evolved gases. The oxygen and water contents of the exiting gas were monitored with an oxygen analyzer (Setnag OXYBOX'AIR) and dew point analyzer (Alpha Moisture Systems ADHT-BL), respectively. All gases were of high purity (99.9992%) with no measurable water content (dew point < −80 °C). A constant flow of argon gas (20 mL min^{-1}) was maintained through the balance compartment and leading into the furnace chamber, here referred to as the protective gas flow, resulting in increased balance stability. The flushing (active) gas entered the furnace chamber directly through a secondary inlet with a flow of 80 mL min^{-1}. The total exiting gas flow was therefore equal to 100 mL min^{-1}. The gas supply was controlled via various mass flow controllers (Bronkhorst EL-FLOW), individually calibrated to the type of gas used.

Sample powders (30-35 mg each) were loaded in a small Pt/Rh crucible with lid and placed on the sample carrier, foreseen with a type S thermocouple (Pt-10% Rh/Pt).Thereafter the furnace was closed, degassed to 10^{-2} mbar and refilled with dry argon. This purging process was repeated three times, thus allowing the dew point of the exiting gas to reach −74 °C or less before the start of any measurement. In a constant flow of 100 mL min^{-1} of argon, a concentration of about 10 ppm O_2 was measured to leak into the system.

The thermal analysis profile consisted of three stages. A graphical presentation of the temperature profile and gas atmosphere conditions applied in the furnace is given in Figure 4.1. During the first stage the sample material is reduced to stoichiometric UO_2 by heating to 700 °C in a flow of argon with 4 vol.% H_2. Then, after cooling to the target temperature T_{ox} (= 40, 70, 100, 130, 160, 190 or 250 °C), the furnace chamber is flushed for 3 h with argon (stage two). In the final stage, while maintaining the sample at an isothermal temperature, the flushing gas is changed to dry, synthetic air thus allowing oxidation of the freshly reduced samples.

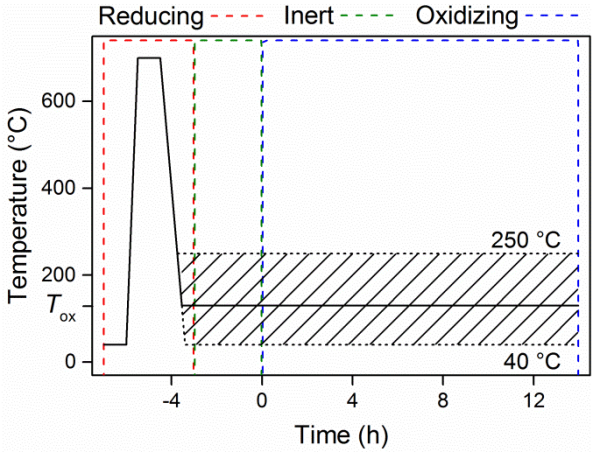

Figure 4.1. Schematic of the temperature profile applied in TGA. The oxidation temperature (T_{ox}) was chosen between 40 °C and 250 °C, as indicated on the graph. Colored dashed lines delimit the associated conditions in the furnace: reducing, inert and oxidizing.

Mass change was continuously recorded with an accuracy of ±14 µg (1σ). All TGA runs were corrected for drift and buoyancy by subtraction of a blank run under identical conditions. The thermocouple was calibrated using melting point standards (In, Sn, Bi, Zn, Al, Au) and validated with a selection of these metals on a regular basis. The absolute mass readout of the balance was calibrated using a reference weight of 2000.00 mg.

4.2.3 X-ray diffraction

X-ray diffraction was performed with a Philips X'Pert Pro diffractometer in parafocusing geometry (θ-θ configuration). Validation of zero point calibration was done on a weekly basis. An LFF X-ray tube (CuKα_1 = 1.5405929 Å)[62] was used as radiation source. A position-sensitive 1D detector with an active length of 2.122 ° (2θ) (PANalytical X'Celerator) was used, with a nickel filter placed in front to avoid CuKβ

contribution to the diffracted signal. The detector was operated in scanning mode. Diffractograms were measured through the range 20-141° (2θ) using a fixed divergence slit (½°) and copper beam mask in combination with 0.02 rad Soller slit assemblies. The exact measuring conditions (beam mask size and step size were optimized, depending on the sample preparation.

The reference oxide powders were prepared via the normal back-loading technique. The TGA produced samples could not be prepared according to this method due to the limited amount of material. Therefore, the latter powders were homogeneously dispersed onto a silicon zero-background sample holder, without the use of any adhesives. This allowed retrieving the powder after analysis. During sample preparation, transfer and measurement, the specimens were exposed to the normal lab environment (room temperature, relative humidity ~50%). The lattice parameters presented throughout the text are recalculated to their value at 20 °C, using the linear thermal expansion coefficient for UO_2 of 9.739×10^{-6} °C^{-1} near room temperature.[63] For U_3O_7 the same coefficient was assumed, as was also proposed for the case of U_4O_9 by Martin.[63, 64] Rietveld analysis of the X-ray diffractograms was performed with PANalytical HighScore Plus (v4.1). Details on the methodology can be found in Appendix III.

4.2.4 Electron microscopy

Transmission Electron Microscopy (TEM) was performed with a 300 kV JEOL 3010 microscope equipped with an in-column Gatan 794 MSC CCD camera and a side-entry double tilt specimen holder. A small amount of powder (< 1 mg) was randomly sampled and dispersed by isopropanol in a beaker. Short intervals (~10 s) of ultrasonic deagglomeration were applied to break up the soft agglomerates into individual grains. The suspension was then pipetted onto a holey carbon grid and the isopropanol was left to evaporate. Data analysis was performed with Gatan Microscopy Suite® (GMS) 2.

The structural information contained within HR-TEM images was analyzed by application of noise filtering over selected areas of the images. The method applied throughout this work consisted of a fast Fourier transform (FFT) procedure to convert the crystalline contribution in a real space image into lattice reflections of a reciprocal space image. A set of lattice planes was then selected by masking the corresponding reflections, excluding the central beam. The masked area was slightly smoothed at the edges (by 3-5 pixels) and subsequently reconverted into a real space image (inverse FFT), thus showing a filtered image of selected lattice planes.

4.3 Results

A systematic set of oxidized UO_2 powders differing in specific surface area was prepared by solid state synthesis and measured via *in-situ* thermogravimetric analysis. A consistent treatment was applied, in which a sample of precursor powder was always first reduced to stoichiometric UO_2 and subsequently oxidized at a selected temperature, ranging between 40 °C and 250 °C. All prepared powders were analyzed via XRD and a considerately chosen selection of samples was further analyzed using HR-TEM.

4.3.1 Thermogravimetric analysis

Mass increase curves showing the effect of oxidation on freshly reduced UO_2 powders are shown in Figure 4.2 (L, M, H), for all three precursor powders. The mass gain is expressed as an increase in average stoichiometry (O/U), here considered as homogeneous oxygen absorption. The oxidation experiments on precursor powders M at 190 °C and H at 160 °C and 190 °C were performed in two stages to avoid overheating of the sample material. During these TGA runs the reduced powders were first allowed to oxidize at a temperature of 130 °C before heating to higher temperatures.

The effect of surface area on oxidation rate is readily observed when comparing the curves of the individual samples. At any given time and temperature, the extent of oxidation is larger with higher specimen surface area, and the difference is most significant at temperatures between 40 °C and 100 °C. The total mass gain at the endpoint of each TGA run is listed in Table 4.2. During the flushing stage, following the reduction step, already a slight mass increase was measured due to uptake of oxygen impurities that enter the system. These amounts are included in the presented values.

Table 4.2. Average stoichiometry at endpoint of each TGA run.

T_{ox}	Average stoichiometry (± 0.02 O/U)		
(°C)	**L**	**M**	**H**
40	2.06	2.13	2.22
70	2.08	2.19	2.32
100	2.15	2.32	2.40
130	2.26	2.39	2.41
160	2.33	2.39	2.42
190	2.38	2.42	2.45
250	2.45	-	-

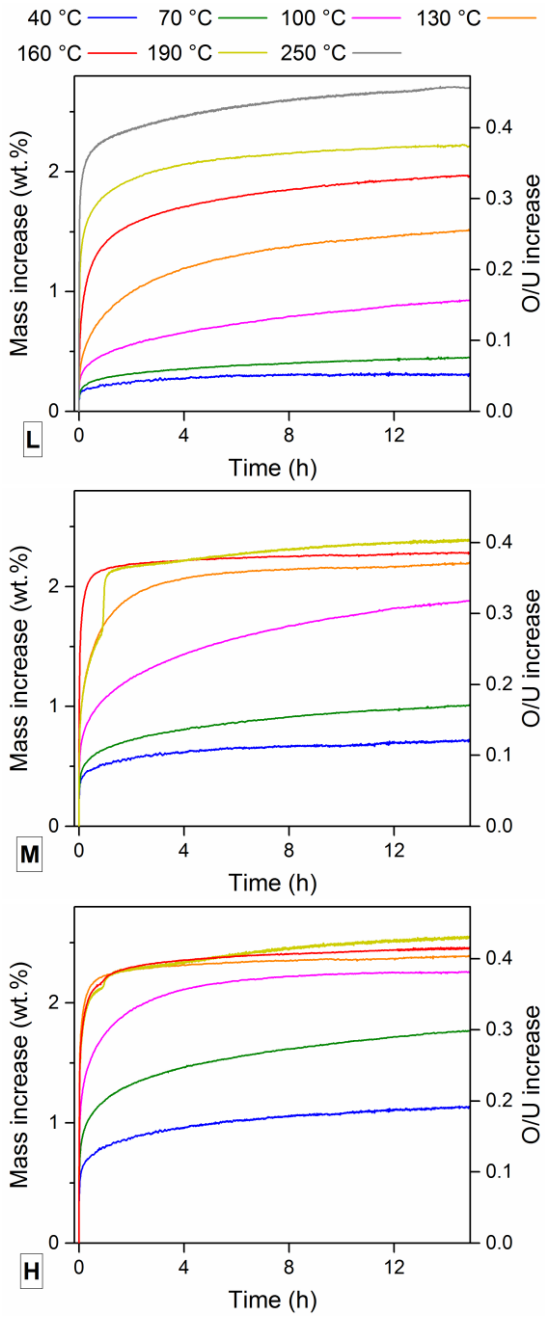

Figure 4.2. Experimental mass increase curves showing a decreasing rate of reaction up to an average stoichiometry close to 2.40. At the highest temperatures applied the reaction appears to accelerate again. Oxidation of precursor powders M at 190 °C and H at 160 °C and 190 °C were performed in two stages to avoid overheating.

At all but the highest temperatures investigated the TGA data shows a decreasing rate of mass increase as the reaction progresses. Quite notably, the curves level off as the mass increase exceeds about 2.2 wt.% (O/U ≈ 2.37). The temperature at which this intermediate state is reached depends on the powder surface area: T_{ox} = 190 °C for samples L, 130 °C ≤ T_{ox} ≤ 160 °C for samples M and 100 °C ≤ T_{ox} ≤ 160 °C for samples H. The corresponding average stoichiometry lies in the range 2.38 ≤ O/U ≤ 2.42 for all three sample types, the exact value increasing slightly with higher sample surface area. At 250 °C, sample L shows an accelerated rate as compared to the behavior at lower temperatures. A similar behavior is observed for samples M and H already at 190 °C. At 40 °C a stable mass value was obtained only for sample L, illustrating limited extent of oxidation at low temperature and with larger surface area.

Thermal analysis was repeated with an extended isothermal dwell time (+ 10 h) on two different samples. At 160 °C precursor powder L oxidized to O/U = 2.35. At 100 °C precursor powder M reached an O/U = 2.37. Oxidation was still on-going at the endpoint of the measurement, albeit with a low reaction rate. Likely, with an unlimited dwell time at the chosen temperatures, mass increase will reach a limiting value at or just below the above mentioned range 2.38 ≤ O/U ≤ 2.42.

4.3.2 X-ray diffraction

The crystallographic changes that occur during the oxidation of UO_2 are assessed with respect to three reference states: $UO_{2.03}$, U_4O_9, U_3O_7. Therefore, X-ray diffractograms of these reference oxides were evaluated using the Rietveld method. Figure 4.3 shows a selected region for the three diffractograms, all corrected for specimen displacement and normalized to the $(111)_p$ reflected intensity. The subscript 'p' refers to parent structure indexing, i.e. the presented data relates to the average structure of the U_4O_9 and U_3O_7 superstructures.[1, 38, 48] The decreased lattice parameter of U_4O_9 as compared to that of $UO_{2.03}$ results in a significant shift of the peak maximum to higher Bragg angles. The tetragonal symmetry in U_3O_7 is shown clearly by the splitting of the $(200)_p$ reflection into $(200)_p$ and $(002)_p$ components.

For all reference samples a fluorite-type parent structure is assumed, with additional occupation of octahedral interstitial sites by oxygen. The space groups are $Fm\bar{3}m$, $F\bar{4}3m$ and $P4_2/nmm$ (origin choice 2) for $UO_{2.03}$, U_4O_9 and U_3O_7, respectively.[38, 48] The composition of the unit cells is summarized in Table 4.3. These structural models present the ideal, undistorted state for fluorite-type uranium oxides. In reality, the incorporation of additional oxygen atoms induces distortion which mainly affect the oxygen sublattice.[65] Such information is, however, ineffectively probed with XRD, allowing assessment of the diffraction data using the undistorted parent structures. An

overview of the parameters evaluated using Rietveld refinement is given in Table 4.4. The U_4O_9 lattice parameter corresponds to values found by other researchers, when recalculated to 20 °C.[1, 38] Excellent agreement was obtained between experimental data and the fitted profile. Bragg *R*-factors were equal to 0.021, 0.032 and 0.036 for the used $UO_{2.03}$, U_4O_9 and U_3O_7 models, respectively. Diffractograms displaying the fitted Rietveld pattern and difference profile over the complete angular range are available in Appendix III (Figures AIII.1−AIII.3).

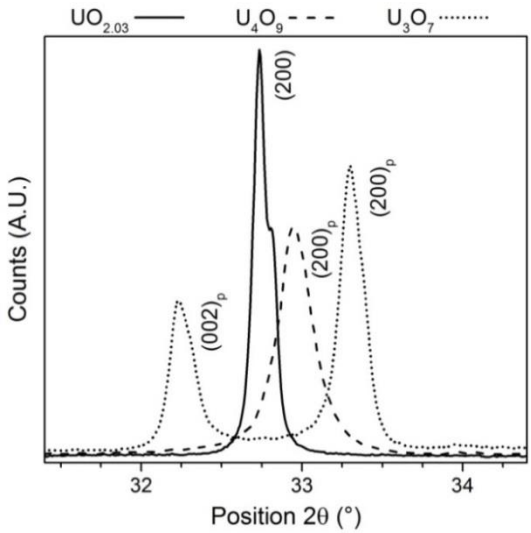

Figure 4.3. X-ray diffractograms showing the $(200)_p$ reflections of $UO_{2.03}$ and U_4O_9 and the $(200)_p$ + $(002)_p$ reflections of U_3O_7 ($CuK\alpha_{1,2}$).

Table 4.3. Composition of the parent structure cells used as input in the Rietveld refinement. The contribution of anion sites (both fully and partially occupied) is negligible; they are mentioned here to present the theoretical unit cell.

	$UO_{2.03}$		U_4O_9		U_3O_7	
Atoms	**Site**	**occ.**	**Site**	**occ.**	**Site**	**occ.**
U	4*a*	1	4*a*	1	4*f*	1
O	8*c*	1	4*c*	1	2*a*	1
	4*b*	0.03	4*d*	1	2*b*	1
			4*b*	0.24	4*c*	1
					4*e*	0.34
Average O/U	2.03		2.24		2.34	

Table 4.4. Parameters obtained after parent structure Rietveld refinement of the $UO_{2.03}$, U_4O_9 and U_3O_7 X-ray diffractograms.

	Lattice par. (pm)		Temperature factor B_{iso}	Agreement factors		
	a	***c***	**U (Å²)**	R_{exp}	R_{wp}	χ
$UO_{2.03}$	546.79(2)	-	0.401(4)	0.051	0.085	1.667
U_4O_9	543.62(2)	-	0.387(8)	0.069	0.116	1.681
U_3O_7	537.99(2)	554.91(2)	0.535(6)	0.048	0.090	1.875

All samples produced during TGA and discussed above, were subsequently analyzed via X-ray diffraction. Due to the small quantities, specimens for X-ray analysis could not be prepared via the usually preferred back-loading technique. Instead, the sample powders were dispersed onto a zero-background holder, i.e. a silicon crystal cut such that no diffracting conditions are met. By tuning the detector acquisition settings and optimizing the optics, high-quality diffractograms were recorded over the range 20-145 ° 2θ. Figure 4.4 (L, M, H) shows extracts of the $(200)_p$ reflection for each of the samples produced under the various conditions. The presented region is chosen for the purpose of illustration as it presents a better peak-to-noise ratio than the higher angular region. Complete diffractograms are given in Appendix III (Figures AIII.4−AIII.6). The data presented here are corrected for specimen displacement and normalized to the $(111)_p$ diffraction peak intensity. Asymmetric peak broadening and peak shifts towards higher angles can be readily observed upon comparing the different diffractograms. Also, the appearance of the tetragonal $(002)_p$ reflection near 32.2 ° 2θ can be distinguished. The onset of tetragonal deformation appears to occur at lower temperatures for samples with higher surface area.

The zero-background setup did not decrease the detection limit of crystalline impurities in the X-ray diffractograms. This was verified by preparing a powder mixed with U_3O_8 and measured under identical conditions. Impurity concentrations above 1 wt.% were readily detectable in the current XRD setup. Nevertheless, no traces of U_3O_8 were detected in the diffractograms of the oxidized samples, which were measured in a 2θ range to include the α-U_3O_8 (001) reflection specifically for this reason.

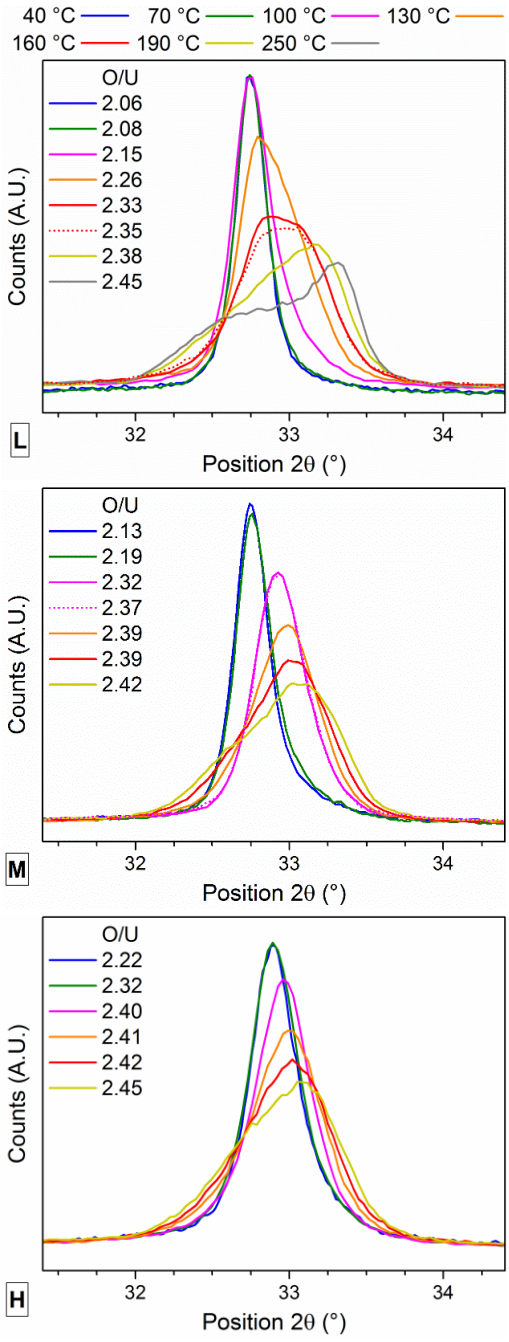

Figure 4.4. X-ray diffractograms showing the superimposed $(200)_p$ reflections of the oxidized powders ($CuK\alpha_{1,2}$). Dashed lines present data of the samples oxidized with an extended time (25 h).

The presence of other crystalline uranium oxides was evaluated via full pattern fitting (Rietveld method). Three possible phases were considered: $UO_{2.03}$, U_4O_9 and U_3O_7, each with input parameters equal to those obtained for the reference compounds (see Table 4.4). As a starting point, scale factors of the three phases were successively refined for each of the oxidized samples. This showed that asymmetric peak broadening and subsequent peak shift could be adequately modeled by the introduction of U_4O_9 in the fitted profile. With increasing oxidation temperature the U_4O_9 content increases while the contribution of remaining $UO_{2.03}$ diminishes and eventually disappears. A significant further increase in weighed-profile agreement factors was obtained by the introduction of the U_3O_7 phase, which refined to an appreciable content only in samples oxidized at temperatures of 100 °C (samples H), 130 °C (samples M), 160 °C (samples L) and higher.

The prior evaluation was used to identify possible phases present in each of the oxidized samples, the chosen criterion was a contribution larger than 1 wt.% in the fitted profile. Phases with a smaller contribution were discarded. Thereafter, the fit was improved by individually refining Cagliotti and line profile parameters of the selected phases. This procedure is justified both for the type of samples (L, M, H) as their crystallite size differs significantly from those of the reference powders, and for the phases themselves ($UO_{2.03}$, U_4O_9, U_3O_7) as the latter two are associated with nanosized domain formation (see following HR-TEM results and recent studies).[2, 43] An overview of the expected and weighed-profile agreement factors obtained after the first Rietveld analysis is reported in Appendix III (Table AIII.1).

Ample data is available on the variability of the tetragonal distortion in U_3O_7,[6, 18, 22] generally attributed to a nonstoichiometric character (U_3O_{7-z}).[3] Therefore, the tetragonal unit cell parameters (a, c) of the previously introduced U_3O_7 phases were additionally refined, hereafter referred to as U_3O_{7-z}. A considerable improvement of the fit (between 14 % and 40 % reduction in R_{wp} factors) was obtained (see Table AIII.1). An overview of the crystalline phases and their associated weight fraction in each of the samples, is presented in Figure 4.5. Powders oxidized at equal temperatures contain an increased content of U_4O_9 and / or U_3O_{7-z} for powders with higher specific surface area. If one assumes that the stoichiometry of the individual compounds is equal to those of the reference powders (O/U = 2.03, 2.24 and 2.34, respectively), an average stoichiometry can be readily calculated (Figure 4.5**,** white dots). The average stoichiometry derived from the weight fractions determined by XRD, shows a similar *trend* to what is observed in TGA (Figure 4.5**,** white squares), but the *values* of the average stoichiometry derived from the XRD observations are systematically lower than the values obtained by TGA. Since in the XRD analysis only the crystalline compounds are accounted for, any contribution from amorphous phases might go unnoticed, as will be discussed below.

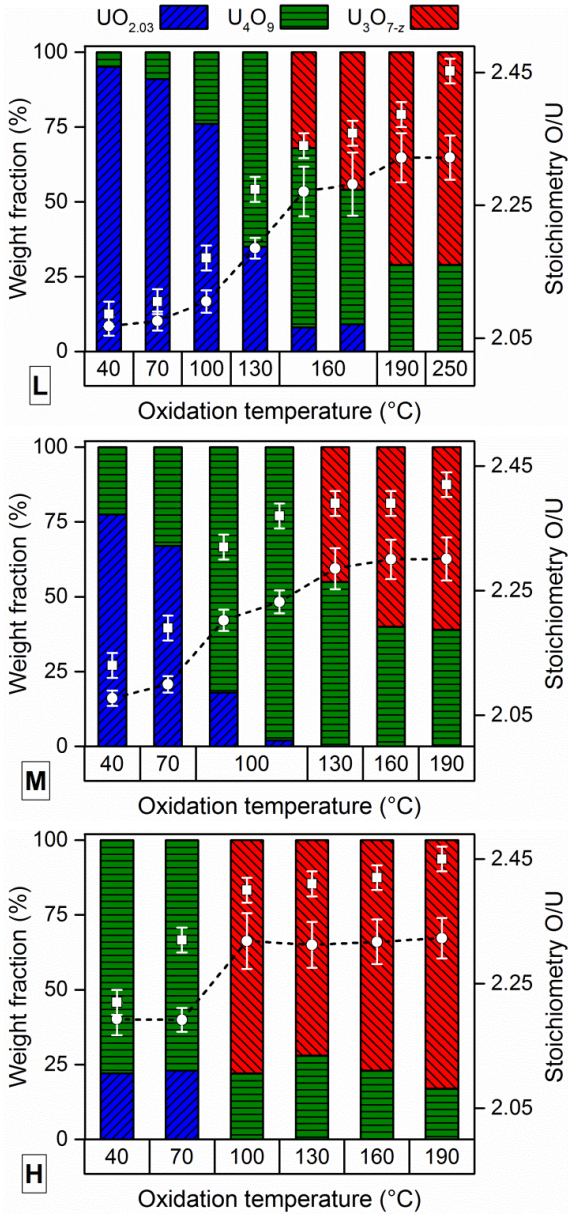

Figure 4.5. Overview of the weight fractions attributed to the different crystalline phases present in the oxidized samples (derived from Rietveld refinement of the X-ray diffractograms). The precision of phase analysis was, on average, 1 wt.% (1σ). Right-hand side data of samples L at 160 °C and M at 100 °C refer to samples oxidized with an extended time (25 h). Stoichiometry values as measured via TGA are represented by white squares. The average stoichiometry, calculated from the weight fractions of the different phases, is presented by white dots.

The lattice parameter evolution of the U_3O_{7-z} phase is presented in Figure 4.6, together with parent cell lattice parameter values of the U_3O_7 reference sample. A clear trend is visible: with increasing oxidation temperature the tetragonal distortion, i.e. the ratio *c*/*a*, increases. This feature is here more clearly illustrated by the dashed lines, which represent parabolic fits to the data grouped per lattice parameter value ($84.3\ \% \leq R^2 \leq 86.0\ \%$). At the intersection of both fitted curves, which presents the condition $c/a = 1$, the lattice parameter is found equal to 544 (2) pm (1σ). This value lies within the range of reported U_4O_9 lattice parameters at room temperature.[1, 38] Another important observation is that the measured lattice parameters for U_3O_{7-z} are still appreciably different to those of the reference U_3O_7, notwithstanding the fact that most of these samples are already severely oxidized (up to O/U = 2.45).

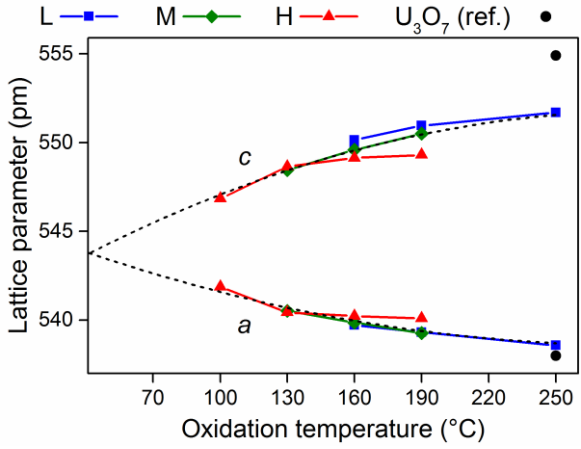

Figure 4.6. Evolution of the U_3O_{7-z} lattice parameters, as measured by XRD Rietveld refinement in samples oxidized at the given temperature. For comparison, also the parent structure lattice parameters of the U_3O_7 reference powder have been added to the graph. Dashed lines represent a parabolic fit to the data, grouped per lattice parameter value *a* or *c*.

4.3.3 Transmission electron microscopy

A selection of samples for HR-TEM analysis was considerately chosen as to cover a wide range of oxidation extent. Based on the XRD Rietveld assessment powders were selected containing either mostly $UO_{2.03}$ (sample L, 40 °C), U_4O_9 (sample H, 40 °C) or U_3O_{7-z} (sample H, 100 °C). The effect of oxidation temperature on the crystallinity of the oxidation products was evaluated by investigating powders with an equal U_4O_9 or U_3O_{7-z} concentration to those previously selected, but obtained at higher temperatures (Samples H, 70 °C and 160 °C, respectively). Figure 4.7 shows bright field (BF) images of samples L (40 °C) and H (70 °C). Two sharply defined features are observed

for each of the samples, indicated by the arrows. These features, hereafter referred to as nucleation sites, were recurring throughout all samples and appeared with larger dimensions in samples oxidized at a higher temperature (ranging between 5 and 15 nm in diameter). HR-TEM analysis focused on these areas, and the edges of the grains.

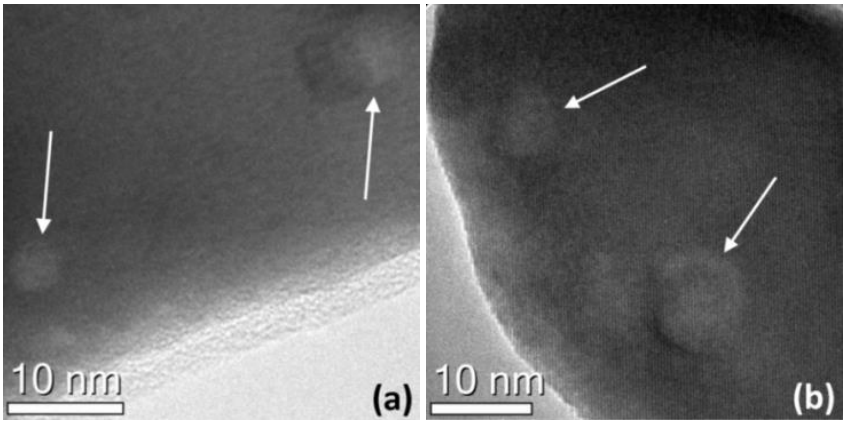

Figure 4.7. (a) BF image of sample L oxidized at 40 °C, (b) BF image with lattice resolution of sample H oxidized at 70 °C. Both grains show two distinct features at the surface. The slightly blurred-out region at the grain surface of (a) results from amorphous scatter of the holey carbon grid.

The analyzed samples did not show any structure defects close to the surface of the grains, nor in the proximity of the nucleation sites. Figure 4.8-4.11 (b) show fast Fourier transformed (FFT) patterns and noise filtered images of the $\{111\}_p$-equivalent planes corresponding to the selected large area, for samples H oxidized at different temperatures. Artefacts which appear near the bottom corners in the images are due to the delimited area for Fourier transformation not being completely contained within the grain under investigation (see e.g. the bottom right corner of Figure 4.8 (b)). Here, the discussion focusses on $\{111\}_p$-equivalent planes as there have been reports of lattice defects along these planes both in stoichiometric and hyperstoichiometric UO_2.[28, 66] The nanostructure of sample L oxidized at 40 °C (Figure AIII.7 in Appendix III) appeared equal to that of sample H oxidized at 40 °C (Figure 4.8). An additional HR-TEM image of sample H oxidized at 100 °C is also available in Appendix III (Figure AIII.8). A discrete surface layer, i.e. a region near the surface which would, a priori, exhibit some sort of discontinuity, was nowhere observed.

FFT patterns of the HR-TEM images show intense reflections which are compatible with the fluorite structure. They can be associated to any of the previously mentioned parent structures for $UO_{2.03}$, U_4O_9 and U_3O_{7-z}. Occasionally, faint satellite reflections are observed, resulting from crystal superstructures. The precision with which reciprocal lattice spacings (***d****) can be determined from Fourier transforms does not

allow to distinguish between the ***d**** -values associated with the different intermediate compounds (they differ only about 1% for the low order reflections). The appearance of satellite reflections, however, can be used to distinguish between these compounds. Along a $[1\bar{1}0]_p$-zone oriented pattern U_4O_9 will show superlattice reflections corresponding to ¼ $\{112\}_p$,[67] whereas U_3O_7 will show satellites along ⅓ $[002]_p$.[48]

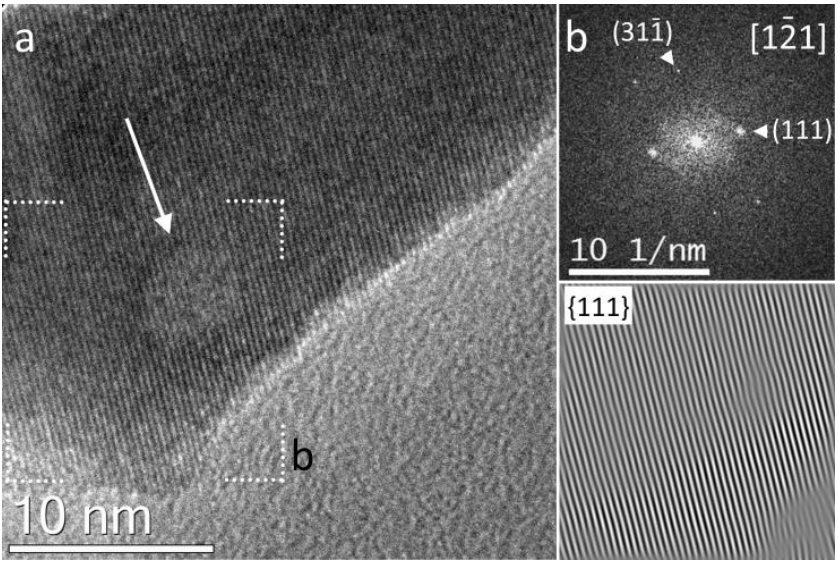

Figure 4.8. (a) HR-TEM image of sample H oxidized at 40 °C, with a small nucleation site indicated by the arrow. (b) FFT pattern of the delimited area and filtered image showing the corresponding {111} lattice planes. No superstructure reflections are observed via FFT and no lattice defects are present near the grain surface or in the proximity of the nucleation site.

Sample L oxidized at 40 °C did not show the presence of a superstructure in the analyzed grains (Figure AIII.7). This observation is as expected since, according to XRD analysis, this powder contains mostly $UO_{2.03}$. Sample H, on the other hand, likely contains over 75 wt.% of U_4O_9 phase (Figure 4.5). Nevertheless, no superstructure reflections were recognized in FFT patterns of the HR-TEM images (see Figure 4.8).

The local crystal structure is further evaluated on the basis of small area FFT analysis. FFT patterns of sample H oxidized at 70 °C show satellites corresponding to ¼ $\{112\}_p$ in a very limited region, close to the surface of the grain. Similar intensities are no longer observed in patterns taken more towards the bulk, see Figure 4.9 (c)-(e). This observation is again surprising in the context of the prior XRD analysis, where the crystal structure of this sample was attributed mostly to the U_4O_9 phase, similar to the H sample oxidized at 40 °C. As already mentioned, no crystallographic difference was observed between the area corresponding to a nucleation site and its surroundings.

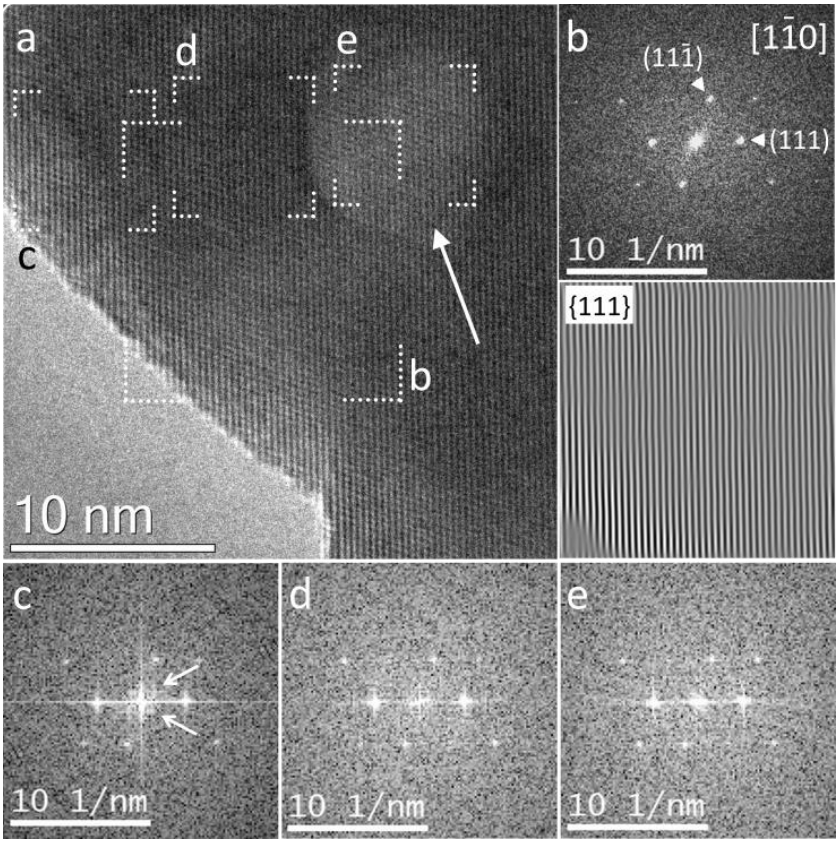

Figure 4.9. (a) HR-TEM image of sample H oxidized at 70 °C, showing a large nucleation site. (b) FFT pattern of the indicated area and filtered image showing the corresponding $\{111\}_p$ lattice planes with no lattice defects. (c)-(e) FFT patterns of the small areas, showing superstructure reflections corresponding to ¼ $[112]_p$ and ¼ $[11\bar{2}]_p$ in a pattern taken at the grain surface.

Most of the grains of sample H oxidized at 100 °C did not contain modulated structures, according to the analysis of HR-TEM images. Occasionally modulation was observed in the bulk of the grain and sometimes extending out to the surface, visible by contrast modulations in real-space images (Figure 4.10 (a) and Figure AIII.8 (a)). FFT patterns of these areas showed the typical U_4O_9 satellites. Small domains clearly absent of modulation were found near the grain surface (areas delimited by the dashed lines). The fact that modulation was only occasionally observed can be seen to correspond to an increased extent of unmodulated domains in most of the grains. Considering the XRD Rietveld assessment for this sample, i.e. 75 wt.% attributed to the U_3O_{7-z} phase, these domains likely consist of U_3O_{7-z} having a disordered defect structure.

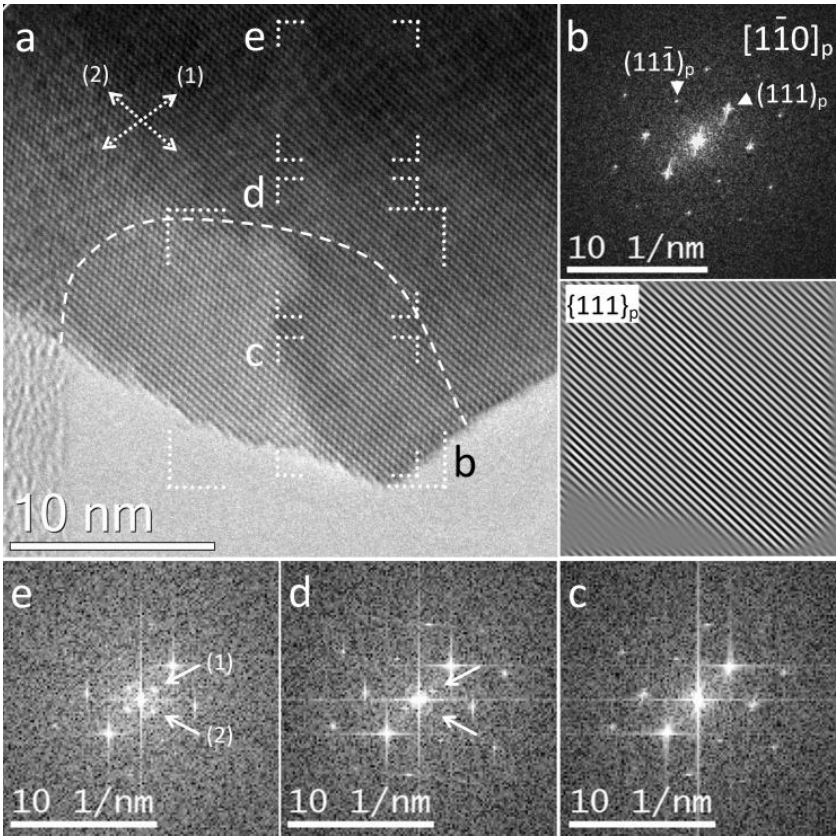

Figure 4.10. (a) HR-TEM image of sample H oxidized at 100 °C. (b) FFT pattern of the indicated area and filtered image showing the corresponding $\{111\}_p$ lattice planes with no lattice defects. (c)-(e) FFT patterns of the small areas, showing superstructure reflections corresponding to ¼ $[112]_p$ and ¼ $[11\bar{2}]_p$ becoming more intense and less diffuse in patterns taken towards the grain bulk. The region delimited by the dashed line presents a crystalline domain without superstructure, markedly different from the rest of the grain, which contains contrast modulation ripples in the HR-TEM image (orientations of the corresponding wave vectors indicated by dotted arrows).

The TEM observations on sample H oxidized at a temperature of 160 °C were less than optimal due to instability of the material, resulting from charging effects. Similar difficulties were already encountered, but to a much lower extent, in sample H oxidized at 100 °C. This observation indicates that an increasingly larger fraction of badly conducting material is present in the samples oxidized at higher temperatures. In BF imaging mode nucleation sites were again observed, scattered over the surface of the grains and having diameters up to 15 nm. The few grains for which HR-TEM analysis was possible showed practically no type of modulation, very faint satellites according

to the U_4O_9 superstructure were only occasionally encountered. A protrusion on the surface of an oxidized grain is observed (Figure 4.11 (a)), understood to be a nucleation site seen from a side projection. The protruding matter is clearly amorphous: the lattice interference pattern of the bulk grain ends at the boundary between grain surface and nucleation site (Figure 4.11 (a-b)) and no crystalline contribution is measured in a Fourier transformed pattern of an area corresponding to the protrusion (Figure 4.11 (c)).

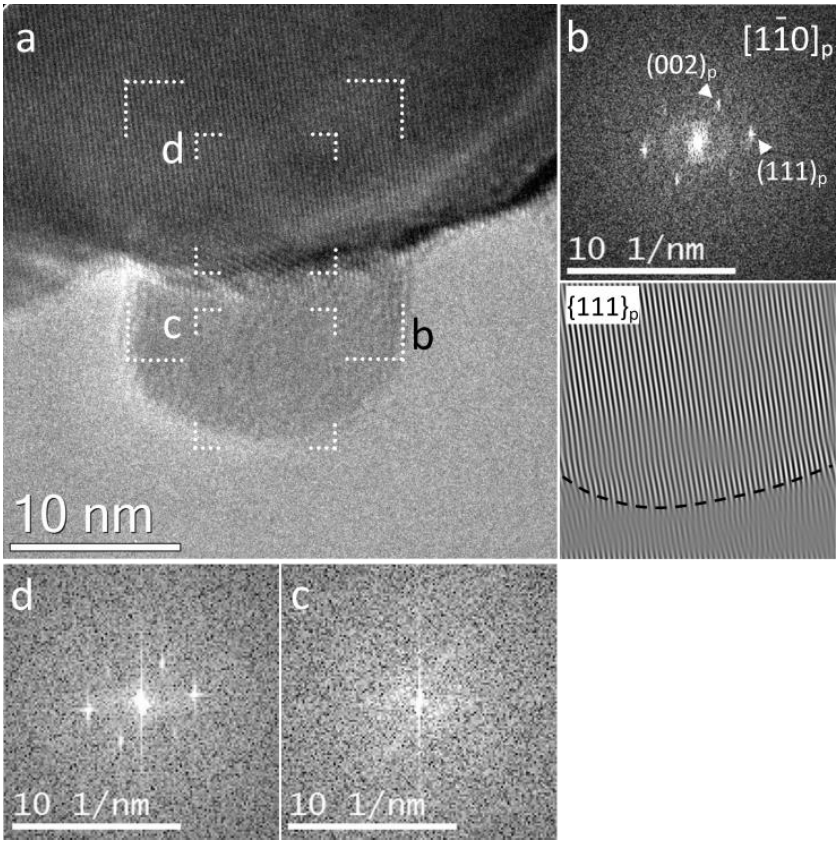

Figure 4.11. (a) HR-TEM image of sample H oxidized at 160 °C, showing amorphous matter protruding out from the grain surface. (b) FFT pattern of the indicated area and filtered image showing the corresponding $\{111\}_p$ lattice planes. The dashed black line indicates the interface between the crystalline and amorphous phase. (c)-(d) FFT patterns of the small areas, showing loss of crystalline reflections in the amorphous phase.

4.4 Discussion

The current investigation aimed to better understand the mechanism of oxidation in fine UO_2 powders. Various powders with either low (L, 4.0 $m^2 g^{-1}$), medium (M, 9.3 $m^2 g^{-1}$) or high (H, 21.1 $m^2 g^{-1}$) specific surface area were first reduced to stoichiometric UO_2 and subsequently oxidized at temperatures between 40 °C and 250 °C. The oxidation progress was measured by *in-situ* TGA and structural analysis was performed by XRD and HR-TEM.

TGA data shows that an intermediate state of oxidation is reached as the average stoichiometry approaches 2.40, the exact value varies slightly with surface area. This is considerably higher than the value of 2.33 which is often reported.[2, 6, 7] Usually, the intermediate state is attributed to complete oxidation of UO_2 into U_3O_7 without subsequent U_3O_8 formation: $UO_2 \rightarrow U_4O_9 \rightarrow U_3O_7$.[3] During low temperature oxidation in air, as the composition exceeds 2.33, one may expect that hyperstoichiometric phases of U_3O_7, U_3O_8 or UO_3 are formed.

The oxidized powders were further analyzed via XRD (Rietveld method) and HR-TEM. The purpose of Rietveld refinement was to quantify the crystalline constituents formed within each sample. The structural information of three well-characterized reference uranium oxide compounds ($UO_{2.03}$, U_4O_9, U_3O_7) was used for the phase quantification of the oxidized samples. The X-ray data are interpreted on the basis of the unit cell parameters of the fluorite-based parent structure. In the current XRD setup no superlattice reflections were detected for U_4O_9 and U_3O_7, but the structural differences between $UO_{2.03}$, U_4O_9 and U_3O_7 reference compounds were readily distinguished in the parent structure reflections.

X-ray diffractograms of the oxidized powders show the evolution of asymmetrical peak broadening and eventually a peak shift towards larger Bragg angles. In powders which were oxidized at temperatures up to 130 °C (samples L), 100 °C (samples M) or 70 °C (samples H) this was adequately modelled via the introduction of a U_4O_9 phase in the Rietveld refinement. Some early works report that at low oxidation temperatures (T < 160 °C), instead of cubic U_4O_9 a pseudo-cubic, tetragonal phase is formed with unit cell parameters almost identical to those of U_4O_9, and with *c*/*a* ratio smaller than 1 (≈ 0.986).[7, 46, 68] This phase was sometimes called α-U_3O_7 to distinguish it from "regular" U_3O_7 (or β-U_3O_7), which has a *c*/*a* ratio larger than one. The existence of the α-U_3O_7 phase has become doubtful in recent years, as it has not been observed with modern techniques such as synchrotron X-ray diffraction.[3] Similarly, we found no evidence for a tetragonal phase with *c*/*a* ratio smaller than 1 in any of the samples, and also the HR-TEM investigations confirmed that the typical U_4O_9 modulation sets in for the samples oxidized at temperatures as low as 70 °C.

We use the notation U_3O_{7-z} to refer to the range of tetragonal phases with continuously varying *c*/*a* ratio ($1.009 < c/a < 1.024$, see Figure 4.6). According to Rietveld analysis, the U_3O_{7-z} phase is observed only in powders oxidized above 100 °C for powder with high surface area (samples H), above 130 °C for powder with medium surface area (samples M) and above 160 °C for powder with low surface area (samples L). Refinement of the U_3O_{7-z} lattice parameters significantly improved the fit for the XRD data (see Table AIII.1). The tetragonal distortion (*c*/*a* ratio) was found to increase with increasing oxidation temperature (see Figure 4.6), and this is interpreted as a change in stoichiometry of the U_3O_{7-z} phase, as *z* approaches zero.

The reference U_3O_7 powder had a larger *c*/*a* ratio ($c/a = 1.031$) than the end value reached on the oxidized samples. The reference U_3O_7 sample was prepared by oxidation of as-received UO_{2+x} powder which had a low specific surface area (~2 $m^2\ g^{-1}$). Oxidation was performed at 250 °C in dry air for 7 h. During the heat treatment some U_3O_8 was formed, about 3.8 wt.% as quantified via Rietveld refinement and no U_4O_9 was observed. One of the L samples (4 $m^2\ g^{-1}$) was similarly oxidized at the same temperature, for an extended time of 15 h. Rietveld assessment of the X-ray data for this sample attributed about 25 wt.% to U_4O_9, the remaining part being U_3O_{7-z}, and no U_3O_8 was detected. Clearly, the powder particle size affects the oxidation process.

In a recent study by Quémard *et al.* it was also found that fine UO_2 powders (200 nm ≈ 2.7 $m^2\ g^{-1}$) showed a significantly decreased U_3O_8 formation rate, as compared to coarse-grained powders and pellets.[2] After a prolonged oxidation time (100 h) at 250 °C a conversion equivalent to O/U = 2.44 was reached, similarly to the oxidation behavior of our powders. It was proposed that oxidation of UO_2 at temperatures between 200 °C and 330 °C occurs by formation of a U_3O_7 layer and that this layer cracks upon reaching a critical depth (10^2-10^3 nm), thus providing fresh surfaces of underlying UO_2 for continuation of the reaction. In fine powders the critical layer depth cannot be reached and U_3O_8 formation is restricted to initiate at the surface of the particles, whereas a cracked layer would otherwise induce more available surface area.[2] Despite the substantial oxidation determined from the mass increase analysis (up to O/U = 2.45), neither XRD nor TEM could detect U_3O_8 in any of the nanometric powders (< 200 nm).

Average stoichiometry values measured via TGA were considerably higher than values calculated from the weight fractions associated to the crystalline components derived from XRD Rietveld refinement (see Figure 4.5). The latter values assume stoichiometry for the intermediate oxides equal to O/U = 2.03, 2.24 and 2.34 for the $UO_{2.03}$, U_4O_9 and U_3O_7 phases, respectively. Hyperstoichiometry has not been reported for U_4O_9, but a small hypostoichiometry field exists.[35, 37] The stoichiometry of the tetragonal U_3O_7 phases does not seem to significantly exceed O/U = 2.33,[3, 45, 46, 48] and

likely a broad hypostoichiometric U_3O_{7-z} domain exists in which the axial ratio *c*/*a* increases with increasing oxygen content.

The difference between the TGA derived O/U values and the values derived from the XRD analysis (Figure 4.5) becomes negligible only if the stoichiometry of the tetragonal phase in the oxidized samples would be between $2.40 < O/U < 2.55$. Considering, however, that the *c*/*a* ratio of the tetragonal phase in these samples was consistently smaller than that of the reference powder (for which O/U = 2.34), this seems unlikely. In addition, the structural changes that might be expected for a compound with O/U up to 2.5, i.e. further distortion of the tetragonal lattice to lower symmetry,[69, 70] are not observed in the diffraction data. Even if such changes would be unrecognizable within the experimental uncertainty the discrepancy would still remain for samples in which only cubic phases are identified. Alternatively, since no crystalline phases of higher oxides (e.g. U_3O_8) are observed, the difference can also be attributed to the presence of an amorphous phase, which remains undetected by XRD analysis.

In the TEM analysis circular-shaped nucleation sites were observed, consistently located on the surface of the oxidized grains. Their size was larger in samples oxidized at higher temperatures (see e.g. Figure 4.7). No lattice defects were found in the vicinity of these features, the electron diffraction patterns did not show additional reflections and the real space images did not show diffraction contrast effects near or in these areas and the rest of the grain. Figure 4.11 shows a well-delimited amorphous phase extending outwards from the sample surface which is interpreted as a nucleation site growing on the surface of the grain. The systematic absence of Moiré fringes related with other nucleation sites is a further indication that they also consist of an amorphous phase.

Our hypothesis is that for fine powders below a certain size limit (< 200 nm) oxidation occurs with formation of amorphous UO_3, which nucleates on the surface of the grains. This interpretation is consistent with the findings of Hoekstra *et al.* on room temperature oxidation of UO_2 powder with high surface area (~30 $m^2\ g^{-1}$).[7] For coarser powders (e.g. the prepared reference powders) oxidation favors formation of U_3O_8. Figure 4.12 presents the estimated amorphous UO_3 content from the difference in stoichiometry values (TGA−XRD, taking the stoichiometry of the U_3O_{7-z} phase equal to that of the reference U_3O_7 powder) for all oxidized powders. As a general trend, it is observed that the amount of amorphous UO_3 formed increases at higher oxidation temperatures.

All of the uranium oxides with partially filled 5f orbitals (UO_{2+x}, U_4O_9, U_3O_7, U_3O_8) are semi-conducting and are sufficiently conductive for electron beam observations (e.g. TEM, SEM, XPS, …). Electron conductivity values σ for UO_{2+x} and U_3O_8 are of

the order 10-10^{-3} Ω^{-1} cm^{-1}.[54] Pure uranium (VI) oxides, however, are insulators: UO_3 has a much lower conductivity $\sigma \approx 10^{-8}$ Ω^{-1} cm^{-1}.[71] We observed an increased electron beam instability (sample charging) during TEM analysis of samples oxidized at higher temperatures. Furthermore, all the analyzed grains showed the presence of nucleation sites, whose size increased with higher oxidation temperature. The evidence suggests that these areas, already identified as consisting of amorphous matter, could be amorphous UO_3. The presence of amorphous UO_3 effectively explains the discrepancies observed between TGA and XRD results.

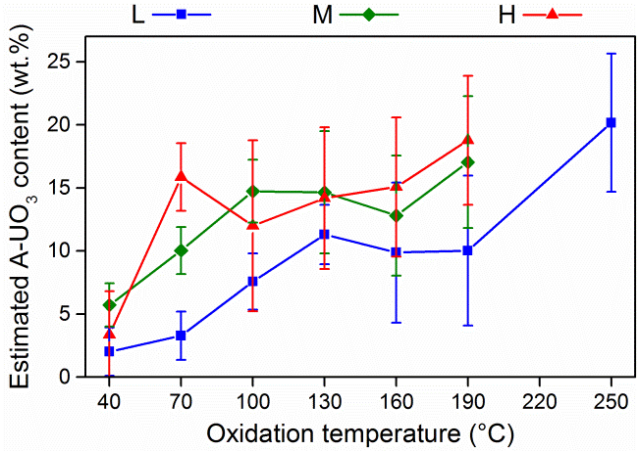

Figure 4.12. Estimated amorphous UO_3 (A-UO_3) content in the powder samples which were oxidized for 15 h, from the discrepancy between TGA and XRD average stoichiometry values. Vertical lines present the propagated error (1σ), taking into account the uncertainty on TGA and Rietveld refined values.

Amorphous UO_3 has a significantly lower density (6.8 g cm^{-3}) as compared to that of the fluorite-type uranium oxides (~11 g cm^{-3}).[54] Conversion of a volume within a grain of dense material into UO_3 would result in a significant amount of lattice strain. However, this was not readily observed during TEM analysis. Given that the nucleation sites appear to grow on the surface of the oxidized grains it may be expected that some strain is only induced at the interface between crystalline matrix and amorphous phase. Noise-filtered images of the $\{111\}_p$-equivalent planes (Figure 4.8-4.11) indeed show limited deformation in the vicinity of the nucleation sites.

Thomas *et al.* investigated oxidized, spent UO_2 fuel pellets.[28] They found distinct, large U_4O_9 domains (~500 nm thick) at the grain boundaries and a slight mismatch between the phase interfaces. In their analysis, U_4O_9 was identified on the basis of superlattice reflections in selected area diffraction patterns, since the small difference in parent structure lattice parameter of the two phases was undistinguishable. In the current work on fine powders, no discrete surface oxide layer was observed. This is also evidenced

by the absence of Moiré patterns throughout the analyzed grains. The intermediate oxides ($UO_{2.03}$, U_4O_9, U_3O_7) have very similar parent structure lattice spacings, e.g. $3.14 \leq d_{(111)} \leq 3.16$ Å. Superposition of discrete domains containing one of these compounds, unless considerably misoriented towards each other, is expected to produce Moiré fringes in HR-TEM images. One such example would be a surface coating of U_4O_9 or U_3O_7 on a bulk UO_2 grain. Regions containing U_4O_9 have been identified and these regions are not misoriented towards their surroundings, as evidenced by the analysis of FFT patterns.

Phase identification via TEM was based on the observation of domains showing long-period modulation in the HR-TEM images. As previously mentioned, the precision with which reciprocal lattice spacings are measured in FFT patterns of these domains does not allow to distinguish between the fluorite-based parent structures of the intermediate compounds $UO_{2.03}$, U_4O_9 and U_3O_7. Rietveld refinement of the X-ray diffraction data attributed over 75 wt.% of the crystalline matter in samples H oxidized at 40 °C and 70 °C to the U_4O_9 phase (the remainder being $UO_{2.03}$), see Figure 4.5. At 100 °C and above, a nearly constant fraction of about 25 wt.% U_4O_9 is observed, the remainder being U_3O_{7-z}. Surprisingly, the TEM analysis of the modulated domains gave partly conflicting results. The samples oxidized at 40 °C did not show any modulated phase at all (Figure 4.8 and AIII.7, Appendix III). Oxidation at 70 °C showed the typical U_4O_9 modulation in small domains located near the grain surface (Figure 4.9). Modulation was mainly absent after oxidation at 100 °C, however, in one grain the modulated U_4O_9 structure was readily observed (Figure 4.10 and AIII.8). Here, the U_4O_9 domains were located in the bulk of the grain, with unmodulated zones near the grain surface.

The HR-TEM observations at 40 °C and 70 °C indicate that in the early stage of oxidation a fluorite-type phase is formed with disordered oxygen defects, referred to as disordered U_4O_9. Long-range ordering of the defects with the formation of a modulated structure (ordered U_4O_9), but without changing the parent structure dimensions, occurs in the next stage. Belbeoch *et al.* introduced the notation $UO_{2.25}$ to refer to the phase without long-range ordering, while they used the notation U_4O_9 to refer to the modulated state.[72] They observed a phase transition around 65 °C between a low temperature pseudo-cubic (rhombohedral, $\alpha = 90.078°$) phase showing weak superstructure reflections and a cubic phase showing stronger reflections. The decrease in satellite intensity was more significant in fine grain-sized powders (< 1 µm).

Later observations by Naito confirmed the phase transformation first described by Belbeoch *et al.*, but he reported that the modulation is only affected in hypostoichiometric U_4O_{9-y}, stoichiometric U_4O_9 would not show different modulation intensities below or above the transition temperature.[73] Allen *et al.*, in their TEM work on oxidized, polycrystalline UO_2 samples (O/U = 2.24), observed islands showing

U_4O_9 modulation in electron diffraction patterns, surrounded by an apparently unmodulated matrix.[74] They distinguished between U_4O_9 and the matrix, having a disordered defect structure, for which they used the more general notation UO_{2+x} (but consistent with the notation $UO_{2.25}$ by Belbeoch *et al.*).

The phase which is generally referred to as U_4O_9 contains a small number of oxygen defects and exists in a narrow stoichiometry domain $2.235 \leq O/U \leq 2.245$, but does not include the exact 2.25 stoichiometry.[37] Since the deviation is so small the exact composition is usually disregarded. Cooper and Willis reassessed the refinement of the U_4O_9 crystal structure above the phase transition temperature, based on long-range ordering of cuboctahedral oxygen clusters and applying slightly more strict local symmetry restraints.[38] They obtained a theoretical composition of $U_4O_{8.944}$ ($O/U \approx 2.24$) for the average cell, which is in agreement with Willis' earlier findings.[65] The theoretical cell composition was subsequently used as a starting point in the assessment of the defect structure in the low-temperature phase.[75]

The present observations of long-range ordering can thus be interpreted in terms of deviations from the optimal stoichiometry which is required for the long-range ordering of the defect clusters ($U_4O_{8.944}$ or $O/U \approx 2.24$). When one deviates from this optimal stoichiometry, the intensity of the superstructure reflections decreases and eventually the ordering disappears. In the remainder, the term "disordered U_4O_9" or in short "U_4O_9 (dis)" is used to identify the state without superstructure reflections (previously called $UO_{2.25}$ in the notation of Belbeoch *et al.*)[72] and "ordered U_4O_9" or "U_4O_9 (ord)" identifies the long-range ordered structure. The notation U_4O_9 is maintained when distinction between the modulated and unmodulated phases is not relevant.

In the oxidation experiments at 40 °C and 70 °C, both $UO_{2.03}$ and disordered U_4O_9 coexist and one can thus expect that the U_4O_9 phase may not yet have reached the stoichiometry required for the development of long-range ordering. For the sample oxidized at 100 °C, the U_4O_9 phase is in equilibrium with tetragonal U_3O_{7-z}, and it may be expected that it has reached the appropriate stoichiometry and hence, the ordered phase U_4O_9 (ord) forms.

Well-crystallized U_3O_7 develops long-range ordering but with a different modulation wave vector than for U_4O_9 (ord).[48] In sample H oxidized at 100 °C, for which Rietveld refinement attributes over 75 wt.% of the crystalline matter to the U_3O_{7-z} phase and slightly less than 25 wt.% to U_4O_9, the TEM analysis could not reveal any zones with the modulation typical for U_3O_7. In one particular grain, domains showing long-period modulation were observed, but the superstructures were typical for U_4O_9 (ord). Whenever present, the modulated phases were observed in the bulk of the grain, with smaller domains of unmodulated structures near the grain surface. Although it is not possible to determine the slight tetragonal deformation from the HR-TEM

observations, one might expect that further oxidation starts at the grain surface and that the unmodulated domains near the grain surface are U_3O_{7-z}. The fact that no modulation was observed in other grains of this sample is then conform with XRD results (75 wt.% U_3O_{7-z}). An evaluation of the local stoichiometry in the unmodulated structures may provide more insight, for example performed via scanning TEM electron energy loss spectroscopy (EELS) analysis. In summary, our interpretation is illustrated in the schematic of Figure 4.13.

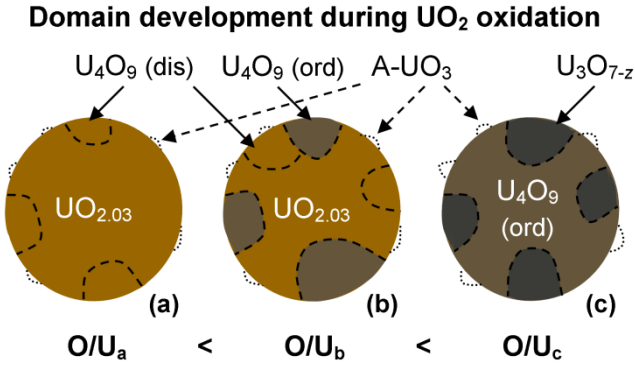

Figure 4.13. Interpretation of the XRD and HR-TEM results regarding domain formation during oxidation of UO_2 fine powders (cross-section of spherical particles). (a) Grain with a low degree of oxidation, consisting of a bulk phase of $UO_{2.03}$ and U_4O_9 (dis) domains without long-period modulation. (b) More oxidized grain, showing the evolution of ordered U_4O_9 domains and simultaneous formation of new U_4O_9 (dis) domains. (c) Strongly oxidized grain with the U_4O_9 (ord) phase extending throughout the bulk and domains of U_3O_{7-z} growing inwards from the grain surface. In all stages an amorphous phase (interpreted as amorphous UO_3 (A-UO_3)) is formed on the surface of the grains, growing in size with higher degree of oxidation.

Similar as for U_4O_9, it might be so that the long-range ordered modulation of U_3O_7 only develops within a narrow stoichiometry domain and that outside of this domain, the tetragonal distortion of the parent structure sets in, but long-range ordering of the oxygen defects does not occur. It remains unclear whether in the fine powders studied here the U_3O_{7-z} phase will eventually develop into long-range ordered U_3O_7. As already mentioned, none of the U_3O_{7-z} phases found in the fine powders displayed a tetragonal distortion (*c*/*a* ratio) equal to that of the coarse-grained U_3O_7 reference powder.

4.5 Conclusions

The oxidation mechanisms in fine UO_2 powders (< 200 nm) have been investigated. A variety of samples from three precursor powders having low (L, 4.0 $m^2 g^{-1}$), medium (M, 9.3 $m^2 g^{-1}$) and high (H, 21.1 $m^2 g^{-1}$) specific surface area were first reduced to stoichiometric UO_2 and subsequently oxidized under isothermal (40-250 °C) and isobaric conditions. The extent of oxidation was followed by *in-situ* TGA, and *post*-analysis of the powder samples was performed using XRD and HR-TEM.

According to TGA the average stoichiometry of the samples reached values between O/U = 2.06 and 2.45. At oxidation temperatures up to 190 °C (samples L) and 160 °C (samples M and H) the reaction rate was decreasing, eventually leveling off at O/U values close to 2.40. At higher oxidation temperatures the reaction progressed beyond this intermediate state. The crystalline constituents in the oxidized powder samples were quantified via Rietveld refinement of the X-ray diffraction data. Formation of increasing amounts of U_4O_9 in the early stage of oxidation explains the observed asymmetrical peak broadening and peak shift towards higher Bragg angles in the diffractograms. Tetragonal peak splitting occurring with extended oxidation is attributed to formation of a hypostoichiometric U_3O_{7-z} phase with variable tetragonal distortion ($c/a > 1$). For the fine powders used in this study, the U_3O_{7-z} phase remains considerably different from the reference U_3O_7 structure observed in coarser powder.

Even with high degree of oxidation no U_3O_8 was formed as evidenced by XRD analysis. A discrepancy exists between average stoichiometry values measured by TGA and those calculated from weight fractions attributed to the crystalline phases via XRD Rietveld refinement. The difference can be explained by the presence of significant amounts of amorphous UO_3, which remained undetected by XRD. HR-TEM analysis confirms that an amorphous phase nucleates on the surface of oxidized grains, and the nucleation sites appear to grow (from a few nm up to about 15 nm) with higher oxidation temperature.

The low temperature UO_2 oxidation mechanism appears to be remarkably different for fine powders (< 200 nm) as compared to coarser materials. Fully developed, long-range ordered U_3O_7 was not obtained, no U_3O_8 is formed and distinct surface layers were not observed. Oxidation above the solubility limit of UO_{2+x} proceeds via formation of higher oxides (U_4O_9 and U_3O_{7-z}) in nano-domains. Both modulated and unmodulated U_4O_9 appear to occur, which can be understood given the fact that long-range ordering of oxygen defects in U_4O_9 only takes place in a narrow stoichiometry domain around O/U = 2.24. No modulation has been observed in the U_3O_{7-z} phase, which might be attributed to a similar effect: given the fact that the tetragonal distortion (c/a ratio) always remained different in fine powders from that in coarser powders, the optimal stoichiometry for development of long-range order in U_3O_7 might not have been

obtained. To what extent the possible formation of amorphous UO_3 plays a role in this, remains to be investigated.

Acknowledgements

G.L. thanks SCK•CEN for a PhD fellowship. The authors thank S. Van den Berghe, K. Vanaken and P. Dries for providing laboratory support.

Appendix III: Additional information regarding the Rietveld refinement methodology followed and X-ray diffractograms showing the complete angular range. Additional HR-TEM images.

References

(1) L. Desgranges, G. Baldinozzi, G. Rousseau, J.-C. Nièpce, G. Calvarin, *Inorg. Chem.* **2009**, *48*, 7585.
(2) L. Quémard, L. Desgranges, V. Bouineau, M. Pijolat, G. Baldinozzi, N. Millot, J. C. Nièpce, A. Poulesquen, *J. Eur. Ceram. Soc.* **2009**, *29*, 2791.
(3) G. Rousseau, L. Desgranges, F. Charlot, N. Millot, J. C. Nièpce, M. Pijolat, F. Valdivieso, G. Baldinozzi, J. F. Bérar, *J. Nucl. Mater.* **2006**, *355*, 10.
(4) F. Valdivieso, V. Francon, F. Byasson, M. Pijolat, A. Feugier, V. Peres, *J. Nucl. Mater.* **2006**, *354*, 85.
(5) D. A. Dominey, *J. Inorg. Nucl. Chem.* **1968**, *30*, 1757.
(6) D. E. Y. Walker, *J. Appl. Chem.* **1965**, *15*, 128.
(7) H. R. Hoekstra, A. Santoro, S. Siegel, *J. Inorg. Nucl. Chem.* **1961**, *18*, 166.
(8) P. E. Blackburn, J. Weissbart, E. A. Gulbranson, *J. Phys. Chem.* **1958**, *62*, 902.
(9) S. Aronson, B. Roof, J. Belle, *J. Chem. Phys.* **1957**, *27*, 137.
(10) F. Grønvold, *J. Inorg. Nucl. Chem.* **1955**, *1*, 357.
(11) J. S. Anderson, L. E. J. Roberts, E. A. Harper, *J. Chem. Soc.* **1955**, 3946.
(12) L. E. J. Roberts, *J. Chem. Soc.* **1954**, 3332.
(13) K. B. Alberman, J. S. Anderson, *J. Chem. Soc.* **1949**, 303.
(14) I. F. Ferguson, J. D. M. McConnell, *Proc. R. Soc. London, Ser. A Mat.* **1957**, *241*, 67.
(15) M. J. Bannister, *J. Nucl. Mater.* **1968**, *26*, 174.
(16) J. E. Stubbs, A. M. Chaka, E. S. Ilton, C. A. Biwer, M. H. Engelhard, J. R. Bargar, P. J. Eng, *Phys. Rev. Lett.* **2015**, *114*, 1.
(17) G. C. Allen, P. A. Tempest, J. W. Tyler, *J. Chem. Soc., Faraday Trans. 1* **1988**, *84*, 4049.
(18) G. C. Allen, P. A. Tempest, J. W. Tyler, *J. Chem. Soc., Faraday Trans. 1* **1988**, *84*, 4061.
(19) P. Taylor, D. D. Wood, A. M. Duclos, *J. Nucl. Mater.* **1992**, *189*, 116.
(20) S. R. Teixeira, K. Imakuma, *J. Nucl. Mater.* **1991**, *178*, 33.
(21) T. K. Campbell, E. R. Gilbert, G. D. White, G. F. Piepel, B. J. Wrona, *Nucl. Technol.* **1989**, *85*.
(22) P. A. Tempest, P. M. Tucker, J. W. Tyler, *J. Nucl. Mater.* **1988**, *151*, 269.
(23) P. Taylor, E. A. Burgess, D. G. Owen, *J. Nucl. Mater.* **1980**, *88*, 153.
(24) P. Perio, *Bull. Soc. Chim. Fr.* **1953**, 256.
(25) H. Hering, P. Perio, *Bull. Soc. Chim. Fr.* **1952**, *76*, 351.
(26) L. E. Thomas, R. E. Einziger, *Mater. Charact.* **1992**, *28*, 149.
(27) R. E. Einziger, L. E. Thomas, H. C. Buchanan, R. B. Stout, *J. Nucl. Mater.* **1992**, *190*, 53.
(28) L. E. Thomas, R. E. Einziger, R. E. Woodley, *J. Nucl. Mater.* **1989**, *166*, 243.
(29) D. W. Shoesmith, *J. Nucl. Mater.* **2000**, *282*, 1.
(30) G. Leinders, T. Cardinaels, K. Binnemans, M. Verwerft, *J. Nucl. Mater.* **2015**, *459*, 135.
(31) N. A. Brincat, M. Molinari, S. C. Parker, G. C. Allen, M. T. Storr, *J. Nucl. Mater.* **2015**, *456*, 329.
(32) A. D. Murray, B. T. M. Willis, *J. Solid State Chem.* **1990**, *84*, 52.
(33) B. T. M. Willis, *Proc. Brit. Ceram. Soc.* **1964**, *No. 1*, 9.

(34) B. T. M. Willis, *Acta Crystallogr. A* **1978**, *34*, 88.
(35) D. Labroche, O. Dugne, C. Chatillon, *J. Nucl. Mater.* **2003**, *312*, 50.
(36) R. J. McEachern, P. Taylor, *J. Nucl. Mater.* **1998**, *254*, 87.
(37) W. Van Lierde, J. Pelsmaekers, A. Lecocq-Robert, *J. Nucl. Mater.* **1970**, *37*, 276.
(38) R. I. Cooper, B. T. M. Willis, *Acta Crystallogr. A* **2004**, *60*, 322.
(39) D. J. M. Bevan, I. E. Grey, B. T. M. Willis, *J. Solid State Chem.* **1986**, *61*, 1.
(40) F. Garrido, A. C. Hannon, R. M. Ibberson, L. Nowicki, B. T. M. Willis, *Inorg. Chem.* **2006**, *45*, 8408.
(41) D. A. Andersson, G. Baldinozzi, L. Desgranges, D. R. Conradson, S. D. Conradson, *Inorg. Chem.* **2013**, *52*, 2769.
(42) D. A. Andersson, J. Lezama, B. P. Uberuaga, C. Deo, S. D. Conradson, *Phys. Rev. B* **2009**, *79*, 024110.
(43) L. Desgranges, H. Palancher, M. Gamaléri, J. S. Micha, V. Optasanu, L. Raceanu, T. Montesin, N. Creton, *J. Nucl. Mater.* **2010**, *402*, 167.
(44) L. Nowicki, F. Garrido, A. Turos, L. Thomé, *J. Phys. Chem. Solids* **2000**, *61*, 1789.
(45) F. Garrido, R. M. Ibberson, L. Nowicki, B. T. M. Willis, *J. Nucl. Mater.* **2003**, *322*, 87.
(46) E. F. Westrum, Jr., F. Gronvold, *Phys. Chem. Solids* **1962**, *23*, 39.
(47) N. A. Brincat, M. Molinari, G. C. Allen, M. T. Storr, S. C. Parker, *J. Nucl. Mater.* **2015**, *467*, 724.
(48) G. Leinders, J. Pakarinen, K. Binnemans, T. Cardinaels, M. Verwerft, *Low temperature oxidation of uranium dioxide: an X-ray and electron diffraction study*, Poster presented at the 9th international conference on f-elements (ICFE-9), Oxford (UK), 6-9 September **2015**.
(49) B. Loopstra, *J. Appl. Crystallogr.* **1970**, *3*, 94.
(50) P. Taylor, *J. Nucl. Mater.* **2005**, *344*, 206.
(51) P. Taylor, R. J. McEachern, D. C. Doern, D. D. Wood, *J. Nucl. Mater.* **1998**, *256*, 213.
(52) K. O. Kvashnina, S. M. Butorin, P. Martin, P. Glatzel, *Phys. Rev. Lett.* **2013**, *111*, 1.
(53) S. D. Conradson, D. Manara, F. Wastin, D. L. Clark, G. H. Lander, L. A. Morales, J. Rebizant, V. V. Rondinella, *Inorg. Chem.* **2004**, *43*, 6922.
(54) I. Grenthe, J. Drozdzynski, T. Fujino, E. C. Buck, T. E. Albrecht-Schmitt, S. F. Wolf, *The chemistry of the Actinide and Transactinide elements, Vol. 1*, 3 ed., Springer, Dordrecht, **2006**.
(55) H. R. Hoekstra, S. Siegel, *J. Inorg. Nucl. Chem.* **1961**, *18*, 154.
(56) E. H. P. Cordfunke, *The Chemistry of Uranium*, Elsevier, Amsterdan, **1969**.
(57) T. Wadsten, *J. Nucl. Mater.* **1977**, *64*, 315.
(58) P. Taylor, D. D. Wood, A. M. Duclos, D. G. Owen, *J. Nucl. Mater.* **1989**, *168*, 70.
(59) A. Poulesquen, L. Desgranges, C. Ferry, *J. Nucl. Mater.* **2007**, *362*, 402.
(60) A. Leenaers, L. Sannen, S. Van den Berghe, M. Verwerft, *J. Nucl. Mater.* **2003**, *317*, 226.
(61) A. D. Whapham, B. E. Sheldon, *J. Nucl. Mater.* **1963**, *10*, 157.
(62) M. Deutsch, E. Förster, G. Hölzer, J. Härtwig, K. Hämäläinen, C. C. Kao, S. Huotari, R. Diamant, *J. Res. Natl. Inst. Stand. Technol.* **2004**, *109*, 75.

(63) J. K. Fink, *J. Nucl. Mater.* **2000**, *279*, 1.
(64) D. G. Martin, *J. Nucl. Mater.* **1988**, *152*, 94.
(65) B. T. M. Willis, *J. Chem. Soc., Faraday Trans. II* **1987**, *83*, 1073.
(66) H. Matzke, L. M. Wang, *J. Nucl. Mater.* **1996**, *231*, 155.
(67) H. Blank, C. Ronchi, *Acta Crystallogr. A* **1968**, *24*, 657.
(68) G. C. Allen, N. R. Holmes, *Appl. Spectrosc.* **1994**, *48*, 525.
(69) H. R. Hoekstra, S. Siegel, P. Charpin, *J. Inorg. Nucl. Chem.* **1968**, *30*, 519.
(70) H. R. Hoekstra, S. Siegel, F. X. Gallagher, *J. Inorg. Nucl. Chem.* **1970**, *32*, 3237.
(71) Z. M. Hanafi, F. M. Ismail, M. A. Khilla, N. H. Rofail, *Radiochim. Acta* **1990**, *49*, 35.
(72) B. Belbeoch, J. C. Boivineau, P. Perio, *J. Phys. Chem. Solids* **1967**, *28*, 1267.
(73) K. Naito, *J. Nucl. Mater.* **1974**, *51*, 126.
(74) G. C. Allen, J. T. Buswell, P. A. Tempest, *J. Chem. Soc., Dalton Trans.* **1983**, 589.
(75) L. Desgranges, G. Baldinozzi, D. Simeone, H. E. Fischer, *Inorg. Chem.* **2011**, *50*, 6146.

Chapter 5.

Low-temperature oxidation of fine UO_2 powders: thermochemistry and kinetics

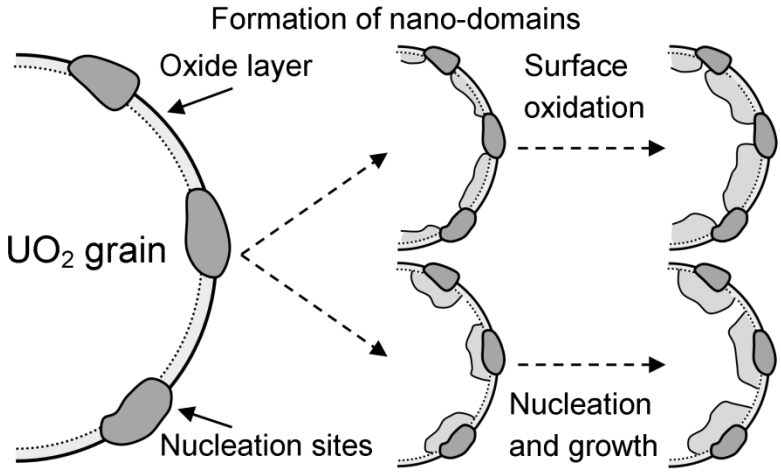

Manuscript in preparation: Gregory Leinders, Thomas Cardinaels, Koen Binnemans, Marc Verwerft

Author contributions

Gregory Leinders performed the experimental work, the interpretation of the data and the writing of this manuscript. He also contributed to the experimental strategy and the scientific ideas.

5.1 Introduction

The thermochemical behavior of uranium(IV) oxide (UO_2) under oxidizing conditions is being studied already for several decades. The main aim was to obtain a better understanding of the stability of UO_2, whose principal use has been as nuclear fuel, under in-reactor, long-term storage or final repository conditions.[1-6] The chemistry of the uranium-oxygen system is complex. Oxides with different stoichiometries can be formed as a result of oxidation, including non-stoichiometric oxides.[7-9] Especially the transition of UO_2 to the more thermodynamically stable oxide U_3O_8 has been the subject of numerous studies because the large volume expansion (about 36 %) associated with this conversion might be detrimental for the integrity of storage containers or fuel cladding.[10] Research mainly focused on oxidation of spent nuclear fuel by studying coarse fragments or sintered pellets,[11-15] while the oxidation of fine powders which are encountered in the front end of the nuclear fuel cycle is not often studied in the open literature.[16, 17]

The earliest stage in the oxidation process has been characterized as molecular or dissociative adsorption of oxygen.[18] The highly exothermic nature of the adsorption reaction is attributed mainly to chemical adsorption (chemisorption),[19] and this accounts for the pyrophoric behavior of fine, freshly reduced UO_2 powders in air.[6] During the course of oxidation, oxide ions are incorporated in the fluorite-type UO_2 structure ($Fm\bar{3}m$),[20] and at elevated temperatures a hyperstoichiometric solid solution (UO_{2+x} with $x \leq 0.25$) readily forms.[21, 22] However, the solubility limit of oxygen in UO_{2+x} decreases with temperature and below about 250 °C the limit corresponds to $0.01 \leq x \leq 0.03$.[23, 24] Oxidation then results in formation of higher uranium oxides (typically U_3O_7) near the reaction interface.[24, 25] Surface oxide layers of U_4O_9 (thickness of the order 10^2 nm) have also been observed on the grain boundaries of oxidized UO_2 fuel pellets.[26-28]

Diffusion of oxygen through surface oxide layers is considered to be the rate-limiting mechanism at temperatures above about 100 °C.[9] Hence, growth of the oxide layer has been interpreted by diffusion rate laws (e.g. following parabolic kinetics).[24, 29, 30] In fact, the process seems to be best modelled as two simultaneous and interdependent reactions $UO_2 \rightarrow U_4O_9$ and $U_4O_9 \rightarrow U_3O_7$.[31] In fine UO_2 powders the process is somewhat more complex, as oxidation appears to induce the sequential formation of U_4O_9 and U_3O_7 in nanosized domains throughout the grains,[16] and also the formation of UO_3 on the surface.[17, 32]

Below 100 °C oxygen diffusion is exceedingly slow, and only limited literature data is available in this region. Anderson *et al.* reported that oxidation still occurs, proceeding according to a logarithmic function of time.[33] Such reaction kinetics are usually associated with low-temperature oxidation processes which involve growth of very thin

(5−10 nm) oxide films on metallic surfaces.[34-36] A mechanism which explains the migration of ions through an oxide layer at temperatures considered too low for thermally activated diffusion was first described by Mott,[37] and later generalized by Cabrera and Mott,[38] Evans,[39] and Fromhold.[40] The authors argued that a potential difference will be set up over an oxide layer due to chemisorption of oxygen and the associated transfer of electrons from the bulk of the material to the surface. In very thin oxide films the resulting strong electric field enables the transport of ions, and oxide layer growth generally proceeds according to an inverse logarithmic rate law.[37, 38] Other closely-related rate laws have also been derived, depending on boundary conditions.[39, 40]

The rate of field-assisted oxidation decreases with increasing film thickness, and will eventually drop to negligible values at low temperatures. At more elevated temperatures, due to the increased probability for thermally activated diffusion, growth of the oxide layer may continue. Various metallic surfaces, including metallic uranium,[41, 42] follow these oxidation kinetics when exposed to oxygen.[43-45] A similar mechanism was proposed to be involved in the low-temperature region of UO_2 oxidation.[33]

In the present work the oxidation of fine UO_2 powders under dry, oxidizing conditions is investigated. Oxidation experiments were performed on several powders, differing in specific surface area, and were investigated by *in-situ* thermogravimetric analysis (TGA) and differential scanning calorimetry (DSC). The study aims to interpret the early stages of oxidation at temperatures between 40 °C and 250 °C, with particular attention to the occurrence of the *logarithmic* stage at temperatures below 100 °C, and the transition between the different oxidation stages.

5.2 Experimental

5.2.1 Sample preparation

Samples were prepared from two depleted UO_{2+x} batches (average O/U ≈ 2.1) produced via an Integrated Dry Route (IDR process) and supplied by FBFC International (Dessel, Belgium). The combined metallic impurity fraction was 136 µg g^{-1} and 47 µg g^{-1} in the two batches, as determined by Inductively Coupled Plasma Mass Spectroscopy (ICP-MS, ThermoFisher XSeries2). In order to obtain samples with different surface areas, a wet route dissolution process was used. The as-received powders were first dissolved in a 4 M HNO_3 aqueous solution and subsequently titrated with an excess of a 4M NH_3 aqueous solution. The precipitate formed was vacuum-filtered and dried at 80 °C for several hours to obtain bright yellow $(NH_4)_2U_2O_7$ (ammonium diuranate or ADU) powder.

Three uranium oxide precursor powders, having low (L), medium (M) and high (H) specific surface areas, were prepared from the ADU powder via thermal treatment in a Carbolite TZF1800 tube furnace with continuous flows of dry active gasses (dew point < -80 °C). Powder H was obtained by calcination of the ADU powder in synthetic air (N_2 / 21 vol.% O_2) at 550 °C for 30 min. X-ray analysis (Philips X'Pert Pro diffractometer) showed that the compound formed under these conditions was β-UO_3. Powders M and L were obtained by calcination in synthetic air at 650 °C for 30 min and 4 h, respectively. The compounds thus formed were identified as α-U_3O_8. Surface areas were measured by nitrogen gas adsorption (BET analysis using a Micromeritics TriStar II 3020). The results are shown in Table 5.1. Small amounts of the precursor powders were subsequently sampled, reduced to stoichiometric UO_2 and oxidized under specific conditions (see section 5.2.2). Theoretical spherical particle size (d_{BET}) corresponding to the UO_2 grains have been calculated from the surface area values and are added in Table 5.1.

Table 5.1. Precursor oxides (Precursor), specific surface area (SSA) and theoretical spherical particle size (d_{BET}) corresponding to the UO_2 grains.

	L	M	H
Precursor	U_3O_8	U_3O_8	UO_3
SSA ($m^2\ g^{-1}$)	4.0	9.3	21.1
d_{BET} (nm)[a]	137	59	26

[a]After reduction to UO_2

5.2.2 Simultaneous thermal analysis (STA)

STA (TGA and DSC) was performed with a Netzsch STA 449 ***F1*** Jupiter® thermogravimeter, coupled to a quadrupole mass spectrometer (403 D Aëolos®) to allow evolved gas analysis. An oxygen analyzer (Setnag OXYBOX'AIR) and dew point analyzer (Alpha Moisture Systems ADHT-BL) monitored the oxygen and water contents of the exiting gas. All gases were of high purity (99.9992%) with no measurable water content (dew point < −80 °C). A constant flow of argon gas (20 mL min^{-1}) was maintained through the balance compartment and leading into the furnace chamber, here referred to as the protective gas flow, resulting in increased balance stability. The flushing (active) gas entered the furnace chamber directly through a second inlet with a flow of 80 mL min^{-1}. The total exiting gas flow was therefore equal to 100 mL min^{-1}. The gas supply was controlled via mass flow controllers (Bronkhorst EL-FLOW), individually calibrated to the type of gas used.

Powder samples (20–35 mg each) were loaded in a small Pt/Rh crucible with lid and placed on the sample carrier, foreseen with a type S thermocouple (Pt-10% Rh/Pt). Thereafter the furnace was closed, degassed to 10^{-2} mbar and refilled with dry argon. This purging process was repeated three times, until the dew point of the exiting gas was less than -74 °C before the start of any measurement. In a constant flow of 100 mL min^{-1} of argon, a concentration of about 10 ppm O_2 was measured to leak into the system.

The thermal analysis profile consisted of three stages. A graphical presentation of the temperature profile and gas atmosphere conditions applied in the furnace is given in Figure 5.1. During the first stage the sample material is reduced to stoichiometric UO_2 by heating to 700 °C in a flow of argon with 4 vol.% H_2. Then, after cooling to the target temperature T_{ox} (= 40, 70, 100, 130, 160, 190 or 250 °C), the furnace chamber is flushed for 3 h with argon (stage two). In the final stage, while maintaining the sample at an isothermal temperature, oxygen is admitted to the flushing gas as to obtain an oxygen partial pressure of 0.1 vol.%, 0.4 vol.% or 16.8 vol.% O_2 in the total flow (protective + flushing gas).

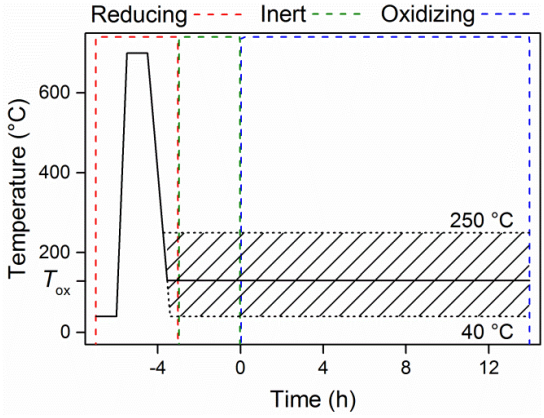

Figure 5.1. Schematic of the temperature profile applied in TGA. The oxidation temperature (T_{ox}) was chosen between 40 °C and 250 °C, as indicated on the graph. Colored dashed lines delimit the associated conditions in the furnace: reducing, inert and oxidizing (0.1 vol.%, 0.4 vol.% or 16.8 vol.% O_2).

Mass change was continuously recorded with an accuracy of ±14 µg (1σ). All STA runs were corrected for drift and buoyancy by subtraction of a blank run under identical conditions. The thermocouple was calibrated by melting point standards (In, Sn, Bi, Zn, Al, Au) and validated with a selection of these metals on a regular basis. Tabulated values for heats of fusion of these high-purity metals were used to calibrate the calorimeter. The absolute mass readout of the balance was calibrated using a reference weight of 2000.00 mg.

5.3 Results

5.3.1 Oxidation under limiting conditions at 40 °C

5.3.1.1 Reaction thermochemistry

Mass gain curves of oxidation experiments at 40 °C at different oxygen partial pressures are presented in Figure 5.2. Often, these curves are also expressed as an increase in average stoichiometry ΔO/U (see right hand vertical scale of Figure 5.2). Although homogeneous 'bulk' oxygen absorption does not occur at low temperatures (see introduction) such notation is a frequently used representation of mass increase. In this work the kinetic data will be interpreted via the mass increment per unit area of freshly reduced sample material, termed specific mass increment SMI (denoted as $\Delta W(\mathrm{t})$, in units mg m^{-2}):

$$\Delta W(\mathrm{t}) = \frac{m(\mathrm{t}) - m_0}{\mathrm{SSA} \cdot m_0} = \frac{\Delta m(\mathrm{t})}{\mathrm{SSA} \cdot m_0} \qquad \textbf{(5.1)}$$

with m(t) the recorded mass as a function of time, m_0 the mass at the start of the exposure experiment (at $t = t_0$), and SSA the specific surface area. This allows to compare results between the three precursor powders without *a priori* assuming a physical model such as formation of a surface oxide layer.[39]

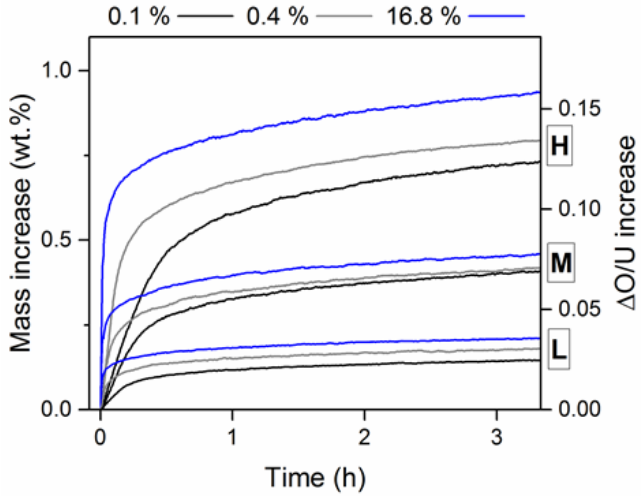

Figure 5.2. Mass gain curves of the oxidation experiments on the three precursor powders (L, M, H) under different oxygen partial pressures: black lines for 0.1 vol.% O_2, gray lines for 0.4 vol.% O_2 and blue lines for 16.8 vol.% O_2.

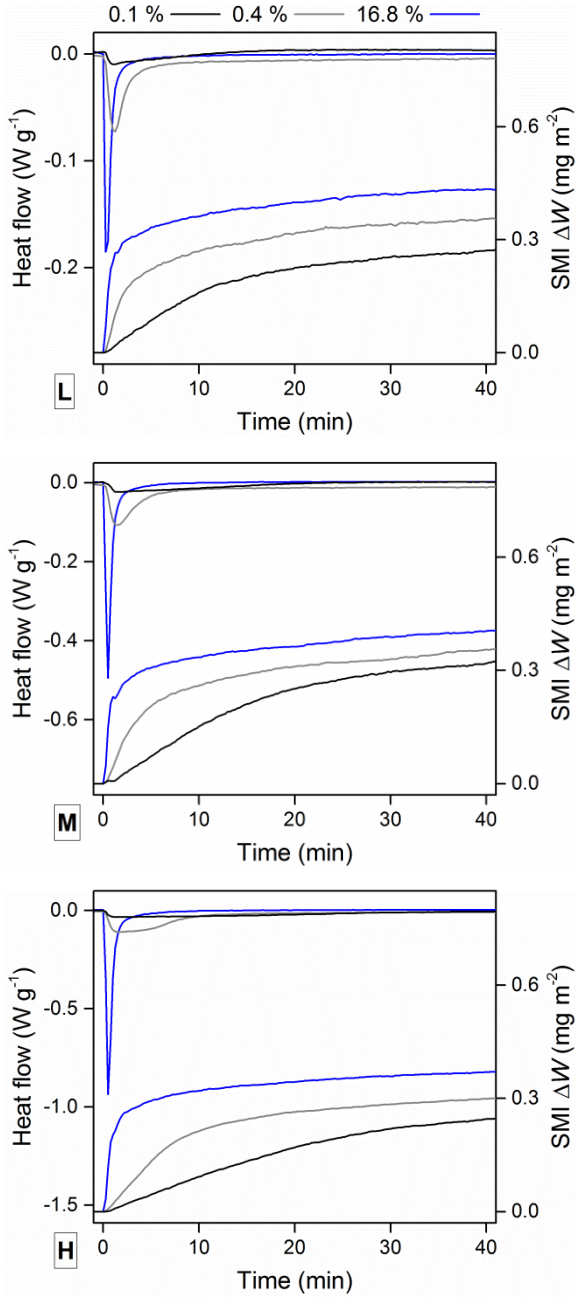

Figure 5.3. Mass gain curves (bottom curves, right axis specific mass increment SMI) and measured heat flow (top curves, left axis) during the first 40 min of the oxidation experiments at 40 °C on the three powder types (L, M, H), under different oxygen partial pressure. The color coding is equal to that used in Figure 5.2.

One observes a similar oxidation behavior for all three powders: a rapid mass increase in the early stage of oxidation, which levels off after typically 10 to 30 minutes. At the end of the oxidation experiment (200 min) the reaction still proceeds at a detectable rate in all samples. As would be expected the extent of oxidation increases with increasing specific surface of the powder and with increasing oxygen concentration of the gas.

Figure 5.3 presents a zoom-in of the initial 40 min of the oxidation reaction, also showing the measured heat flow. By convention, a negative heat flow represents an exothermal reaction. It is interesting to note that for identical oxygen content in the gas supply, the specific mass increment ($\Delta W(t)$) for the different types of powder evolves similarly.

The initial oxidation reaction is clearly exothermic, and the data show that the reaction heat is released over a longer period of time when the oxygen partial pressure decreases. The effect is also more pronounced with higher sample surface area and it will be shown further that this is due to the fact that the oxygen supply becomes the rate-limiting factor. As a result the endpoint of the exothermic reaction cannot be clearly identified from DSC curves measured under 0.1 and 0.4 vol.% O_2. Also, it is to be expected that during an extended exothermic reaction the transfer of heat in the DSC apparatus is more subjected to losses which are not accounted for in the measured signal (for example by convection). For this reason the DSC curves measured under reduced oxygen partial pressure were not quantitatively evaluated. For the samples which were oxidized under 16.8 vol.% O_2 the following values were measured, taking a horizontal baseline starting at time t_0 and ending at the baseline value (0 W g^{-1}): -4 ± 1 kJ mol^{-1} UO_2 (L), -8 ± 1 kJ mol^{-1} UO_2 (M) and -15 ± 1 kJ mol^{-1} UO_2 (H).

5.3.1.2 Stage I: linear oxidation kinetics

At the onset of oxidation the specific mass increment increases linearly (see Figure 5.3). This is best illustrated at low oxygen partial pressure, and with high surface area. After some time the increase starts to level off. The rate constant k_l in units mg m^{-2} min^{-1} during the initial oxidation stage evidently equals:

$$k_l = \frac{\Delta W(t)}{t - t_0}. \qquad \textbf{(5.2)}$$

Results for k_l are presented in Table 5.2. The oxygen supply clearly limits the initial reaction for all samples at low partial pressures (0.1 and 0.4 vol.% O_2). At higher partial pressure, the oxygen supply is no longer rate-controlling. We may, for example, calculate the time required until an amount of oxygen molecules corresponding to an

adsorbed monolayer on the UO_2 sample has entered the furnace. From the experimental conditions (gas flow rate, temperature, the amount of sample material present and its specific surface area, etc.), values of 19 s (0.4 s g^{-1}), 21 s (1.0 s g^{-1}) and 39 s (2.2 s g^{-1}) are obtained in 0.1 vol.% O_2 for samples L, M and H, respectively. Evidently, the relative values decrease proportionally as the oxygen supply increases: by a factor 4 in 0.4 vol.% O_2 and by a factor 168 in 16.8 vol.% O_2. Rate constants presented in Table 5.2 similarly show an increase by a factor of about 4 when increasing the oxygen content from 0.1 to 0.4 vol.% O_2. A further increase in oxygen partial pressure to 16.8 vol.%, however, does not lead to a corresponding proportional increase in rate constant values, and within experimental error the rate is equal in all powder types: 0.27 ± 0.02 mg m^{-2} min^{-1}. This shows that under these conditions the supply of oxygen is no longer rate-controlling and that the true material properties are being probed.

One may expect the earliest stage in the oxidation process to correspond to the chemisorption reaction of oxygen on the UO_2 grains.[18, 19] The accumulation of oxygen at the surface can in principle be imagined as formation of a surface oxide layer with an O/U > 2. The thickness of such an oxide layer Δy can then be estimated for spherical particles as:

$$\Delta y = R_\mathrm{i} \cdot \left[1 - (1 - A \cdot \Delta W \cdot \mathrm{SSA})^{1/3}\right] \qquad \textbf{(5.3)}$$

with

$$A = \frac{\mathrm{MM_{UO_2}}}{\mathrm{MM_O} \cdot (\mathrm{O/U} - 2)} \qquad \textbf{(5.4)}$$

where MM_{UO2} and MM_O are the molecular and atomic weights of UO_2 and O, respectively. The initial particle radius R_i of the reduced UO_2 grains can be derived from the BET specific surface area measurements, see Table 5.1.

The specific mass increment at the end of the linear stage ($t = t_1$) is nearly constant and independent of the specific surface area or oxygen content of the gas (see Table 5.2). It appears that the corresponding oxide layer thickness would be approximately equal in all samples, but the value depends on the choice of O/U, e.g. Δy(O/U = 2.25) = 1.2 nm, Δy(O/U = 2.33) = 0.9 nm, Δy(O/U = 3) = 0.3 nm.

Table 5.2. Rate constants for the initial linear oxidation stage as a function of surface area (L, M, H) and oxygen partial pressure (p_{O2}). Specific mass increment ΔW_1 at the end of the linear stage. Uncertainties are reported at 1σ level.

p_{O_2}	Rate constant k_l (mg m^{-2} min^{-1})		
	L	**M**	**H**
0.1	0.016 ± 0.005	0.015 ± 0.003	0.009 ± 0.001
0.4	0.07 ± 0.04	0.05 ± 0.01	0.026 ± 0.005
16.8	0.30 ± 0.04	0.28 ± 0.04	0.23 ± 0.04
	Specific mass increment ΔW_1 (mg m^{-2}) at the end of stage I		
	L (± 0.10)	**M (± 0.06)**	**H (± 0.04)**
0.1	0.20	0.19	0.18
0.4	0.20	0.18	0.18
16.8	0.22	0.21	0.18
Av. ΔW_1	0.21 ± 0.06	0.19 ± 0.03	0.18 ± 0.02

5.3.1.3 Stage II: inverse logarithmic oxidation kinetics

The kinetic curves all start to deviate from the linear trend after a specific mass increment ΔW_1 of about 0.2 mg m^{-2} is reached. In this second stage the oxidation reaction appears to follow the logarithmic decreasing trend which is commonly observed during oxidation of metallic surfaces at low temperatures.[42, 43, 45] Such behavior is consistent with formation of a very thin (5−10 nm) surface oxide layer in the initial oxidation stage. The proposed mechanism is one of field-assisted oxidation, where low-temperature ionic transport is enabled via a potential difference that is created over the oxide layer (visualized schematically in Figure 5.4).[38-40]

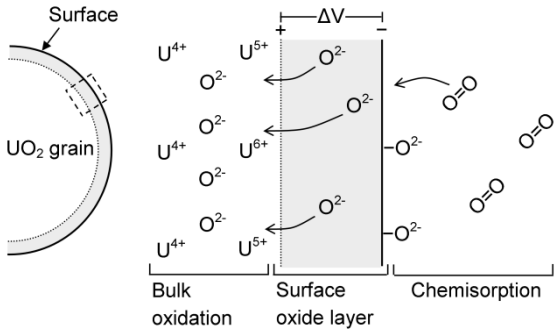

Figure 5.4. Schematic of the low-temperature oxidation mechanism. Oxygen is first chemisorbed on the surface of UO_2 grains, and subsequently migrates through a very thin surface oxide layer towards the bulk of the grain.

Of several closely-related rate equations which have been derived throughout the years, the approximate solution in the form of the inverse-quadratic logarithmic rate law is often applied:[45-47]

$$\frac{1}{\Delta y(\mathrm{t})} - \frac{1}{\Delta y_1} = -r \cdot \ln\left(\frac{\mathrm{t}-\mathrm{t}_1}{\Delta y(\mathrm{t})^2}\right) - r \cdot \ln(\tau), \qquad \textbf{(5.5)}$$

in which the constants r and τ correlate with several physical parameters of the oxidation reaction, including the ionic charge, the potential difference and oxidation temperature. A time shift $\mathrm{t}-\mathrm{t}_0$, with corresponding layer thickness Δy_1 is introduced to define the start of the second oxidation stage. In order to avoid having to assume a certain O/U ratio for the oxide layer, $\Delta y(\mathrm{t})$ is replaced by the mass increment $\Delta W(\mathrm{t})$ such that:

$$\frac{1}{\Delta W(\mathrm{t})} - \frac{1}{\Delta W_1} = -r \cdot \ln\left(\frac{\mathrm{t}-\mathrm{t}_1}{\Delta W(\mathrm{t})^2}\right) - r \cdot \ln(\tau) \qquad \textbf{(5.6)}$$

Eq. (5.6) is a function of the type $y = a \cdot x + b$ and allows to verify whether the kinetic data follow inverse logarithmic kinetics.

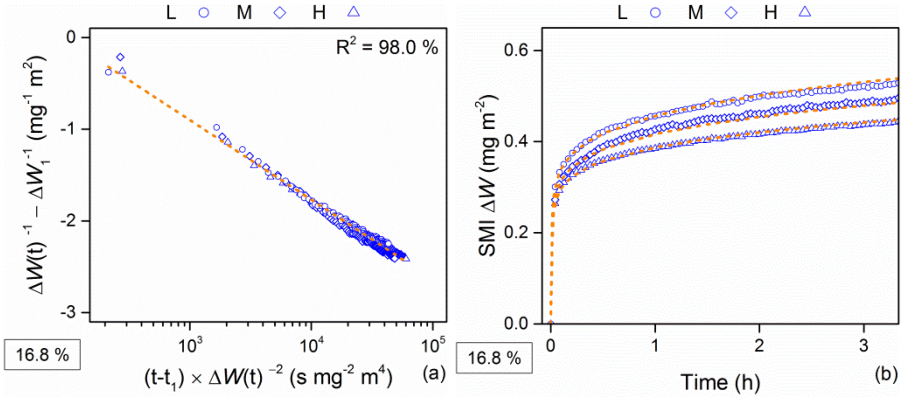

Figure 5.5. (a) Logarithmic time plot corresponding to the kinetic data of all samples (L, M, H) measured under 16.8 vol.% O_2, see Eq. (5.6). The dashed line presents the linear fit to the data. (b) Mass gain curves of the oxidation experiments measured under 16.8 vol.% O_2. The dashed line presents the fit to the kinetic curves, using the reaction parameters in the linear and inverse logarithmic oxidation stage.

The kinetic curves measured under 16.8 vol.% O_2 show excellent linear correlation in a logarithmic time plot (see Figure 5.5 (a)), consistent with the inverse logarithmic rate law. The obtained constants are $r = 0.376 \pm 0.001$ mg^{-1} m^2 and $\tau = 0.011 \pm 0.001$

$mg^2\ m^{-4}\ s^{-1}$. In Figure 5.5 (b) a plot of $\Delta W(t)$ from Eq. (5.2) and Eq. (5.6), using the derived reaction constants as input, is compared to the original kinetic data and good agreement is observed for each sample. The kinetic curves measured under a limiting oxygen supply also show a good linear correlation, but the discrepancy between individual samples is more significant (the figures are available in Appendix IV). Under these conditions the effect of the sample size cannot be ruled out.

5.3.2 Oxidation in 16.8 vol.% O_2 at various temperatures

5.3.2.1 Reaction thermochemistry

Oxidation experiments in dry synthetic air (16.8 vol.% O_2) at different temperatures (T_{ox} = 40, 70, 100, 130, 160, 190, 250 °C) and for substantial longer oxidation times have been reported in Chapter 4, and the corresponding mass gain curves are repeated in Appendix IV. Some of the higher oxidation temperatures were not tested in samples M and H to avoid overheating of the material (for samples M: $T_{ox} \leq 160$ °C, for samples H: $T_{ox} \leq 130$ °C).

DSC data for all oxidation experiments are presented in the top of each graph in Figure 5.7. Reaction enthalpy was quantified by integration of the DSC signal, taking a horizontal baseline starting at time t = 0 and ending at the baseline value (0 W g^{-1}). Such values are usually expressed as a function of the increase in average stoichiometry ΔO/U, instead of mass increase, according to the generalized reaction:

$$UO_2 + \frac{\Delta O/U}{2} O_2 \rightarrow UO_{2+\Delta O/U} \qquad \textbf{(5.7)}$$

for which the reaction enthalpy ΔH_r under standard conditions is defined as ($\Delta H_f°(O_2)$ = 0):

$$\Delta H_r = \Delta H_f°\left(UO_{2+\Delta O/U}\right) - \Delta H_f°(UO_2). \qquad \textbf{(5.8)}$$

The results are presented in Figure 5.6, and show an excellent linear correlation:

$$\Delta H_r = -162 \pm 1 \times \Delta O/U \ \ [\text{kJ mol}^{-1} UO_2]. \qquad \textbf{(5.9)}$$

Reaction enthalpy values ΔH_r calculated from tabulated standard formation enthalpy values ($\Delta H_f°$) for different ΔO/U values are presented in Table 5.3. A comparison is made against ΔH_r values calculated from Eq. (5.9). The difference is only marginal,

and in fact, the uncertainty intervals overlap. This shows that Eq. (5.9) can be used to accurately estimate formation enthalpy values for generic $UO_{2+\Delta O/U}$ compounds:

$$\Delta H_f^\circ\left(UO_{2+\Delta O/U}\right) = \Delta H_r + \Delta H_f^\circ(UO_2), \quad \textbf{(5.10)}$$

with ΔH_f° (UO_2) = − 1085 ± 1 kJ mol^{-1}.[48]

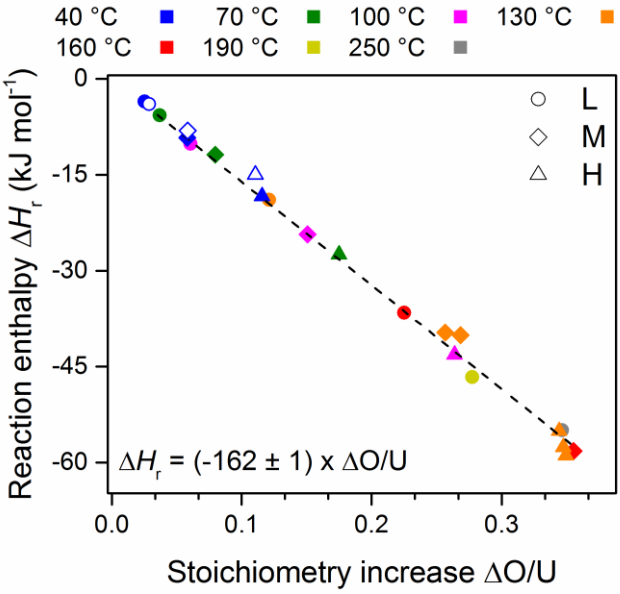

Figure 5.6. Reaction enthalpy values as a function of increase in average stoichiometry ΔO/U, corresponding with oxidation experiments performed at various temperatures. Non-colorized symbols correspond with the data reported in section 5.3.1.1. A linear fit of the experimental data points is shown by the dashed black line.

Table 5.3. Comparison between reaction enthalpy values for the formation of uranium oxide compounds from reported data and values calculated using the correlation for ΔH_r as a function of ΔO/U (Eq. (5.9)).

$UO_{2+\Delta O/U}$	$UO_{2.25}$	$UO_{2.33}$	$UO_{2.67}$
ΔO/U	0.25	0.33	0.67
ΔH_r (ref)[8, 48]	− 43 ± 2	− 56 ± 2	− 107 ± 1
ΔH_r (Eq. 5.9)	− 40.5 ± 0.3	− 53.5 ± 0.3	− 108.5 ± 0.7
Difference	3 ± 2	3 ± 2	− 2 ± 2

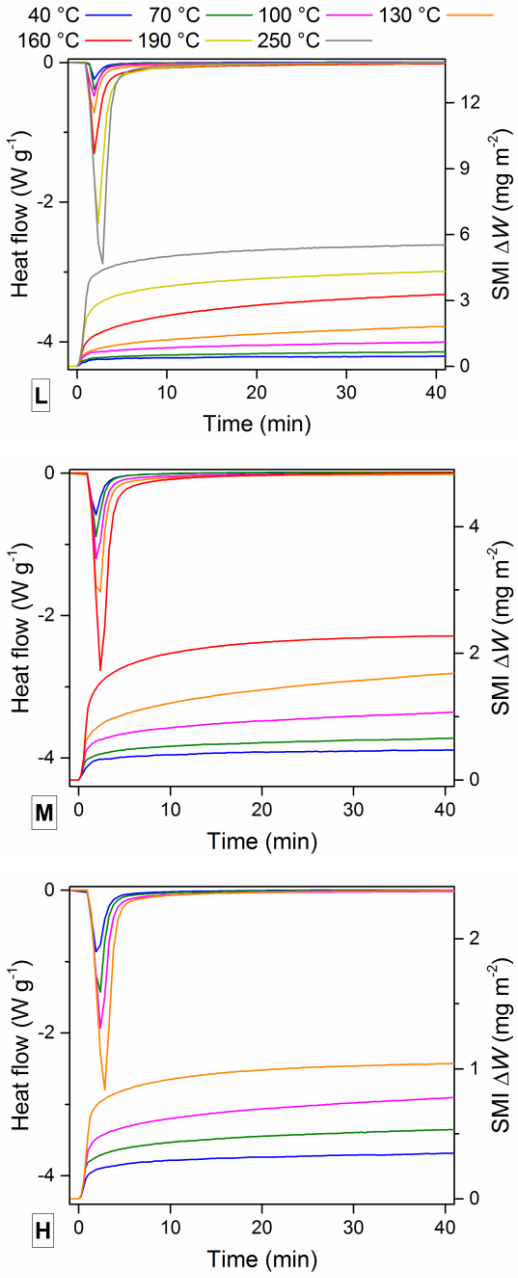

Figure 5.7. Mass Mass gain curves (specific mass increment SMI) and measured heat flow during the first 20 min of the oxidation experiments in 16.8 vol.% O_2 on the three powder types (L, M, H) at different temperatures. Experiments were not conducted at temperatures above 160 °C for samples M and above 130 °C for samples H to avoid overheating.

5.3.2.2 Stage I: linear oxidation kinetics

The linear oxidation rate of the initial reaction stage was observed in all curves (Figure 5.7), and results for the rate constant k_l are presented in Table 5.4. For powders L and M, similar values were obtained in the 40 °C runs as earlier observed (Table 5.2), but not so for sample H, which shows a deviating value. Also for higher oxidation temperatures, the values for sample H were lower than for the other two samples. Likely, the oxygen content in the gas supply was limiting for the oxidation experiments on samples H in this series of experiments, for which larger samples were used than for the experiments presented in section 5.3.1. If the values for sample H are considered outliers for the above reason the results are in fact very consistent: the rate constant is unaffected by surface area and it increases with temperature, showing Arrhenius behavior. From an Arrhenius plot of the data (see Figure 5.8) a pre-exponential factor (A) of 43 ± 8 mg m^{-2} min^{-1} and an activation energy (E_a) of 13.3 ± 0.5 kJ mol^{-1} is obtained:

$$k_l = A \cdot e^{-E_a/R \cdot T} = 43 \cdot e^{-13.3 \times 10^3 \text{ J} \cdot \text{mol}^{-1}/R \cdot T}. \quad \textbf{(5.11)}$$

Table 5.4. Rate constants for the initial linear oxidation stage as a function of surface area (L, M, H) and oxidation temperature (T_{ox}). Uncertainties are reported at 1σ level.

T_{ox} (°C)	Rate constant k_l (mg m^{-2} min^{-1})		
	L	M	H
40	0.28 ± 0.04	0.25 ± 0.04	0.19 ± 0.04 [a]
70	0.42 ± 0.06	0.41 ± 0.06	0.29 ± 0.04 [a]
100	0.63 ± 0.06	0.57 ± 0.08	0.30 ± 0.06 [a]
130	0.78 ± 0.08	0.73 ± 0.08	0.34 ± 0.06 [a]
160	1.2 ± 0.1	0.9 ± 0.1	-
190	1.4 ± 0.2	-	-
250	2.2 ± 0.2	-	-

[a] Reaction constant affected by the oxygen supply

Similar as in section 5.3.1.2, the mass increment corresponding with the initial oxidation stage appears to be independent of particle size, but it is clearly influenced by oxidation temperature (Figure 5.7). As was previously illustrated, if the initial oxidation stage is assumed to form a homogeneous surface oxide layer, the thickness of this layer may be estimated using Eq. (5.3). In the temperature range under

investigation (40 °C ≤ T_{ox} ≤ 250 °C), depending on the hypothesis for O/U of the oxide layer, the layer thickness would range between 1 – 15 nm (O/U = 2.25), 1 – 11 nm (O/U = 2.33), or 0.3 – 3 nm (O/U = 3). Surface layers with dimensions of the latter type (0.3 – 3 nm) could not have been distinguished in the HR-TEM analysis reported in Chapter 4, and their presence can therefore not be excluded.

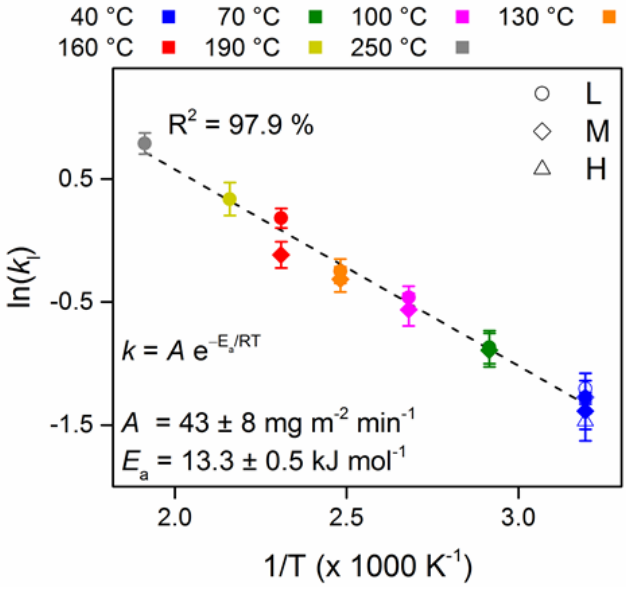

Figure 5.8. Arrhenius plot of the rate constants k_l in the linear oxidation stage.

In Chapter 4 also the results of X-ray diffraction and Rietveld analysis on all of the samples under investigation have been reported. This allowed identifying the crystalline constituents formed as a result of the oxidation reaction. Upon comparing average O/U values calculated from Rietveld analysis and values measured by TGA a significant mass deficiency was measured. This was interpreted as resulting from the presence of an amorphous fraction which had formed during oxidation, evidenced also by small nucleation sites for amorphous matter (presumably UO_3) on the surface of the grains. In the present analysis it is found that the reported mass deficiency corresponds almost exactly with the mass increase measured during the initial oxidation stage: if TGA-derived O/U values are corrected to exclude these amounts, good agreement with average O/U values calculated from Rietveld analysis is obtained, see Figure 5.9 (L, M, H). Thus, we identify the initial oxidation stage (chemisorption) to correspond to the development of the amorphous phase both as a surface oxide layer and as small nucleation sites distributed over the surface of the grains.

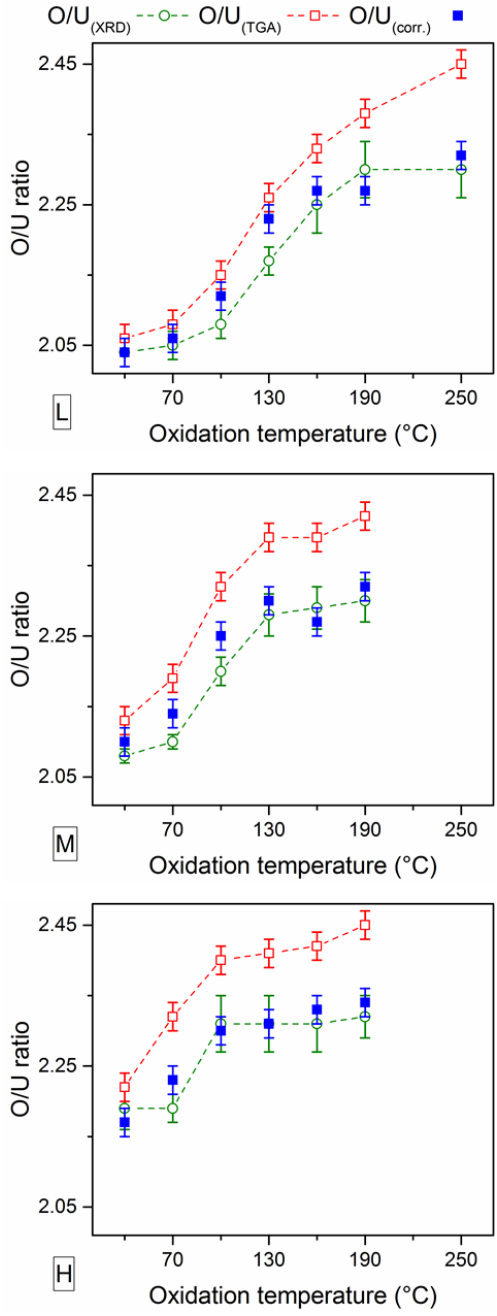

Figure 5.9. Comparison of calculated, measured and corrected average O/U values: marked in green color are values calculated from Rietveld analysis, marked in red color are the values originally measured by TGA, and marked in blue color are the corrected O/U values, which correspond well with Rietveld-derived values.

5.3.2.3 Stage II and III: inverse logarithmic and parabolic oxidation kinetics

The results of Rietveld analysis described in Chapter 4 showed that the development of both U_4O_9 and U_3O_7 may occur, depending on the extent of oxidation. HR-TEM analysis subsequently revealed that these higher oxides were formed in nanosized domains distributed throughout the grains. This heterogeneity can be interpreted as resulting from the nucleation sites created in the first oxidation stage: (1) Oxidation locally stops once these sites reach a critical dimension but continues at the remainder of the surface, or conversely, (2) oxidation occurs preferably around the nucleation sites (schematically represented in Figure 5.10).

The first mechanism will be diffusion-controlled if the available surface for oxidation is large compared to the surface inhibited by the nucleation sites, and is expected to show logarithmic or parabolic kinetics, depending on temperature. The second mechanism is a type of nucleation-and-growth reaction, expected to display sigmoidal kinetics. The current analysis will be restricted to the kinetic data of oxidation experiments in which only the U_4O_9 phase was distinguished as a crystalline oxidation product. The simultaneous development of U_4O_9 and U_3O_7 results in mixed oxidation kinetics which cannot be deconvoluted without knowledge of the specific reaction mechanisms. This limits the dataset to experiments which were performed at $T_{ox} \leq 130$ °C for samples L, and at $T_{ox} \leq 100$ °C for samples M (the kinetic data of samples H are omitted because the oxygen supply was limiting, as mentioned earlier).

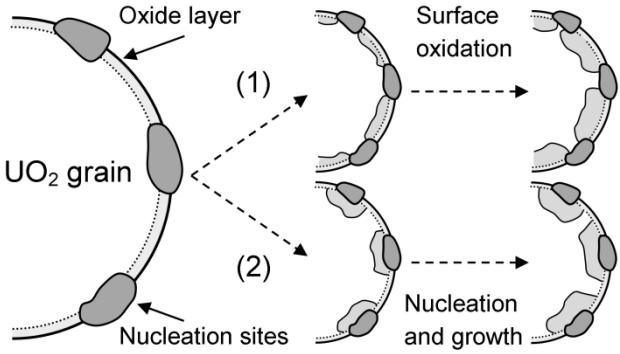

Figure 5.10. Schematic illustration of the proposed mechanisms for the development of domains during stage II and stage III oxidation of UO_2 grains: (1) Oxidation is inhibited near nucleation sites and continues at the rest of the surface, (2) oxidation occurs preferably around nucleation sites formed in stage I.

The kinetic data was evaluated against the known rate laws for diffusion-controlled reactions (1) and nucleation-and-growth mechanisms (2),[49] and was also tested for

logarithmic kinetics since these were already observed at the lowest oxidation temperature (see section 5.3.1.3). None of the curves appeared to follow sigmoidal reaction kinetics. Instead, the inverse logarithmic rate law was confirmed for oxidation temperatures up to and including 100 °C, see Figure 5.11 (a) The kinetic data measured at 130 °C, on the other hand, closely follows the Jander diffusional rate law and marks the beginning of stage III oxidation, see Figure 5.11 (b):[50]

$$\left(1-(1-\alpha)^{\frac{1}{3}}\right)^2 = k_J \cdot (t - t_1) \qquad \textbf{(5.12)}$$

with α defined as:

$$\alpha = \frac{\Delta W(t) - \Delta W_1}{\Delta W_\infty - \Delta W_1} \qquad \textbf{(5.13)}$$

An overview of the reaction constants obtained after fitting the kinetic curves is presented in Table 5.5. The reported uncertainties present the statistical errors (1σ) related to the fitting procedure. Good agreement is obtained between the reaction constants at 40 °C presented here and those reported in section 5.3.1.3; the difference gives a measure for the stochastic variation between repeat experiments: $\delta r = \pm 1 \times 10^{-3}$ g^{-1} m^2 and $\delta\tau = \pm 0.4$ mg^2 m^{-4} s^{-1}.

Table 5.5. Reaction constants obtained after fitting the kinetic data to the inverse logarithmic rate law and the Jander rate law.

T_{ox} (°C)	Inverse logarithmic		Jander
	r (mg^{-1} m^2)	τ (mg^2 m^{-4} s^{-1})	k_J (× 10^3 min^{-1})
40	0.377 ± 0.001	0.42 ± 0.02	-
70	0.324 ± 0.001	0.014 ± 0.001	-
100	0.276 ± 0.001	0.048 ± 0.001	-
130	-	-	0.5674 ± 0.0001

The curves of oxidation experiments performed at 40 °C start to deviate from logarithmic kinetics towards the end of the measurement due to the oxidation reaction no longer proceeding at a detectable rate. The corresponding mass increment then equals approximately $\Delta W_\infty - \Delta W_1 = 0.5$ mg m^{-2}. Translated into a surface oxide layer with O/U = 2.25 (= U_4O_9) the thickness is estimated at about 2 nm. Within the timeframe of the measurements the other kinetic curves did not reach a stable endpoint yet. Assuming here also for a moment the formation of a U_4O_9 oxide layer, the estimated thickness would be about 5−6 nm in samples oxidized at 70 °C, but in

samples oxidized at higher temperatures the thickness would exceed the radius of the particles. This illustrates that formation of a U_4O_9 oxide layer cannot be correct for these samples. Formation of some quantities of higher oxide must be involved.

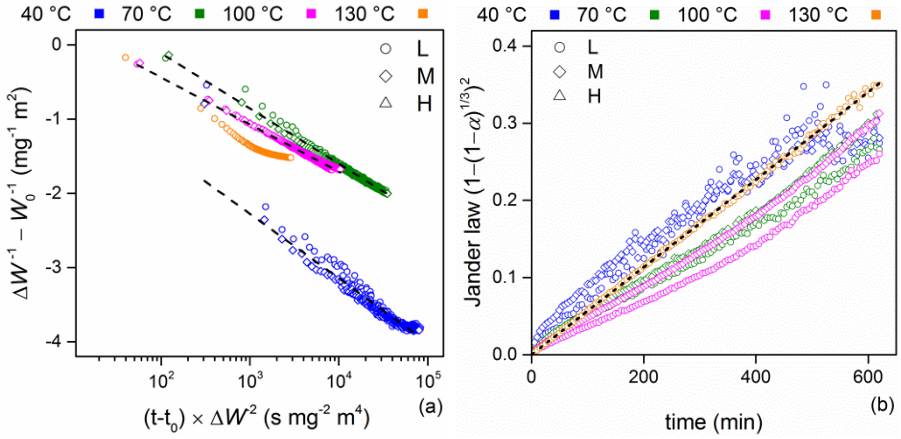

Figure 5.11. Evaluation of the selected kinetic data, as an inverse logarithmic function of time (a) and according to the Jander rate law (b). Dashed lines represent the linear fit to the curves. In (a) a good linear correlation is obtained for data measured at 40 °C (blue), 70 °C (green) and 100 °C (magenta), but not so for data measured at 130 °C (orange). Data measured at 40 °C show deviation from the trend towards the end of the measurement, corresponding with a decrease in reaction rate to negligible values. (b) A good linear fit is only obtained for data measured at 130 °C (orange), in accordance with results from plot (a).

5.4 Discussion

The exposure of freshly reduced UO_2 powders to an oxygen containing atmosphere resulted in the release of a substantial amount of heat. Roberts, and Ferguson and McConnell showed that this reaction step corresponds to physical and chemical adsorption of oxygen on the surface of the grains.[18, 19] In the current experiments, when the oxygen content was not limited in the gas supply the initial adsorption reaction occurred rapidly. As a result well-defined heat flow curves could be measured via DSC at various oxidation temperatures (see Figure 5.7). By integration of the heat flow a consistent set of reaction enthalpy values were obtained.

For convenience the mass increase values corresponding with the exothermal reaction were expressed as increase in average stoichiometry ΔO/U, showing a linear correlation (see Figure 5.6):

$$\Delta H_r = -162 \pm 1 \times \Delta O/U \quad [\text{kJ mol}^{-1}\text{UO}_2], \qquad \textbf{(5.9)}$$

However, it should be mentioned that this notation does not represent the actual physics of the reaction, since under the experimental conditions considered no continuous phase field of $UO_{2+\Delta O/U}$ (= UO_{2+x}) exists.[21-24] Theoretically, one could determine which of the higher oxides (e.g. U_4O_9 or U_3O_7) is formed by comparing the experimental mass increase with calculated values from a given formation reaction, knowing the standard formation enthalpy values ($\Delta H_f°$) of the compounds involved, e.g.:[8, 48]

$$4\,UO_2 + \frac{1}{2}O_2 \rightarrow U_4O_9, \qquad \textbf{(5.14)}$$

$$\Delta H_r = \Delta H_f°(U_4O_9) - 4 \times \Delta H_f°(UO_2) = -43 \pm 2 \text{ kJ mol}^{-1}\ UO_2 \text{ reacted.} \qquad \textbf{(5.15)}$$

$$3\,UO_2 + \frac{1}{2}O_2 \rightarrow U_3O_7, \qquad \textbf{(5.16)}$$

$$\Delta H_r = \Delta H_f°(U_3O_7) - 3 \times \Delta H_f°(UO_2) = -56 \pm 2 \text{ kJ mol}^{-1}\ UO_2 \text{ reacted.} \qquad \textbf{(5.17)}$$

However, since the tabulated formation enthalpy values present the same linear correlation with ΔO/U as that found from the experiments (see Table 5.3), the result becomes trivial. For a given reaction enthalpy value the experimental mass increase will be consistent with either of the above reactions: a larger quantity of U_4O_9 formed (which weighs less than U_3O_7), or equivalently, a smaller quantity of U_3O_7 formed. Thus the DSC data cannot be used to distinguish between the type of higher oxide formed during the initial stage of the oxidation reaction.

Quantitative analysis of the kinetic data showed that the chemisorption reaction likely corresponds to the formation of the amorphous phase which appears on the surface of the oxidized grains (evidenced in Chapter 4). For all samples the corresponding specific mass increment was similar, at equal oxidation temperatures, and it explained the mass deficiency measured by Rietveld analysis (see Figure 5.9). From the results described in Chapter 4 amorphous UO_3 is expected to be formed in this stage. If a homogeneous surface oxide layer is assumed, the thickness is estimated to be between 0.3 nm (T_{ox} = 40 °C) and 3 nm (T_{ox} = 250 °C). The presence of nanosized nucleation sites (diameter from a few nm up to 15 nm, estimated occurrence of 1 – 5 per grain) at the surface even further reduce these values to dimensions which could definitely not have been distinguished in the preceding HR-TEM analysis. However, other investigators have also obtained evidence for the presence of U(VI) compounds on the

surface of oxidized UO_2 by means of surface sensitive techniques such as X-ray photoelectron spectroscopy.[17, 32]

The initial reaction displays a linear oxidation rate, which remains unaffected by powder surface area. Furthermore, the values show Arrhenius behavior (see Figure 5.8), with an activation energy which is much lower (13.3 ± 0.5 kJ mol^{-1}) as compared to, for example, the reported activation energy for the diffusion driven oxidation process active at higher temperatures (95−105 kJ mol^{-1}).[9] Other investigators have indeed mentioned that the activation energy of the adsorption process must be very low, given the reaction rate even at temperatures as low as −183 °C, but an activation energy has never been reported to our knowledge.[18, 19]

The surface heterogeneity induced by the nucleation sites is likely to act as a precursor for the development of higher oxides in domains upon further oxidation (see Figure 5.10). For this reason the kinetic data was evaluated against various known rate laws. Best agreement was obtained with the inverse logarithmic rate law at temperature up to and including 100 °C (stage II), and with the Jander rate law at 130 °C (stage III). Since both types of kinetics are associated with diffusion processes we conclude that further oxidation takes place at the available surface instead of as a process of nucleation-and-growth.

The mechanism associated with stage II is considered to be the electric field-assisted slow migration of oxide ions from the surface towards the bulk of the particles, commonly known as the Mott-Cabrera model, see Figure 5.4.[38] According to the theory an electrostatic field will be set up in an oxide layer due to adsorption of oxygen (i.e. a potential difference will exist across the surface oxide layer).[37-40] The electric field enables incorporation and slow migration of ionic species and explains the oxidation reaction which can be followed at temperatures where the rate of a thermally activated diffusion process is negligible or very low.[45]

The electrostatic migration mechanism is generally limited to an oxide layer thickness of 5−10 nm.[47] Since it is well established that U_4O_9 is the first higher oxide formed during oxidation under the present conditions,[9, 14] we estimated a U_4O_9 surface oxide layer thickness of 3 to 6 nm at oxidation temperatures up to 70 °C. In the HR-TEM study reported in Chapter 4 the U_4O_9 phase was indeed recognized in an area ($\sim 7 \times 7$ nm^2) just below the grain surface. At higher temperatures the assumption of such a surface layer is no longer valid and the formation of a higher oxide (e.g. U_3O_7) needs to be involved. Electron-energy loss spectroscopy (EELS) analysis may provide information required to identify the type of oxide formed, and allow for direct observation of increased oxygen content throughout the grains.

5.5 Conclusion

Low-temperature oxidation of fine UO_2 powders has been investigated by performing oxidation experiments on freshly reduced powders at various temperatures and under reduced oxygen content in the gas supply. The focus has been to analyze the reaction thermochemistry and to interpret the kinetics and corresponding mechanisms involved in the oxidation process.

The earliest stage of the oxidation process was characterized as a rapid, exothermic chemisorption reaction, corresponding to formation of the amorphous phase which was observed in the preceding HR-TEM study. An initial linear oxidation rate was measured which increased with oxidation temperature, and was unaffected by specific surface area. The rate constant displayed Arrhenius behavior with a corresponding low activation energy of 13.3 ± 0.5 kJ mol^{-1}.

The nucleation sites formed during the first stage likely induce the development of higher oxides in domains upon further oxidation. After the initial reaction, oxidation proceeds according to a different regime showing either inverse logarithmic kinetics ($40\ °C \leq T_{ox} \leq 100\ °C$) or parabolic kinetics (Jander rate law) at 130 °C. The occurrence of such diffusion-controlled rate laws suggests a process of surface oxidation instead of a process of nucleation-and-growth. At 40 °C, the oxidation reaction effectively stopped after reaching an equivalent U_4O_9 layer thickness of 2 nm. At more elevated temperatures the formation of a higher oxide must be involved.

Acknowledgements

G.L. thanks SCK•CEN for a PhD fellowship. The authors thank K. Vanaken and P. Dries for laboratory assistance and Dr. A. Dobney for the ICPMS analysis.

Appendix IV: Additional plots of the kinetic data (as-measured, as a logarithmic function of time, and with fitted curves).

References

(1) A. Leenaers, L. Sannen, S. Van den Berghe, M. Verwerft, *J. Nucl. Mater.* **2003**, *317*, 226.
(2) K. K. Bae, B. G. Kim, Y. W. Lee, M. S. Yang, H. S. Park, *J. Nucl. Mater.* **1994**, *209*, 274.
(3) P. Taylor, D. D. Wood, A. M. Duclos, *J. Nucl. Mater.* **1992**, *189*, 116.
(4) L. E. Herranz, F. Feria, *Prog. Nucl. Energy* **2009**, *51*, 201.
(5) J. Nakamura, T. Otomo, T. Kikuchi, S. Kawasaki, *J. Nucl. Sci. Technol.* **1995**, *32*, 321.
(6) M. J. Bannister, *J. Nucl. Mater.* **1968**, *26*, 174.
(7) C. Guéneau, A. Chartier, L. V. Brutzel, *Comprehensive Nuclear Materials, Vol. 2*, Elsevier, Amsterdam, **2012**.
(8) I. Grenthe, J. Drozdzynski, T. Fujino, E. C. Buck, T. E. Albrecht-Schmitt, S. F. Wolf, *The chemistry of the Actinide and Transactinide elements, Vol. 1*, 3 ed., Springer, Dordrecht, **2006**.
(9) R. J. McEachern, P. Taylor, *J. Nucl. Mater.* **1998**, *254*, 87.
(10) P. Taylor, D. D. Wood, A. M. Duclos, D. G. Owen, *J. Nucl. Mater.* **1989**, *168*, 70.
(11) L. Desgranges, G. Baldinozzi, G. Rousseau, J.-C. Nièpce, G. Calvarin, *Inorg. Chem.* **2009**, *48*, 7585.
(12) A. Espriu-Gascon, J. Llorca, M. Domínguez, J. Giménez, I. Casas, J. de Pablo, *J. Nucl. Mater.* **2015**, *467*, 240.
(13) L. Quémard, L. Desgranges, V. Bouineau, M. Pijolat, G. Baldinozzi, N. Millot, J. C. Nièpce, A. Poulesquen, *J. Eur. Ceram. Soc.* **2009**, *29*, 2791.
(14) G. Rousseau, L. Desgranges, F. Charlot, N. Millot, J. C. Nièpce, M. Pijolat, F. Valdivieso, G. Baldinozzi, J. F. Bérar, *J. Nucl. Mater.* **2006**, *355*, 10.
(15) F. Valdivieso, V. Francon, F. Byasson, M. Pijolat, A. Feugier, V. Peres, *J. Nucl. Mater.* **2006**, *354*, 85.
(16) G. Leinders, J. Pakarinen, R. Delville, T. Cardinaels, K. Binnemans, M. Verwerft, *Inorg. Chem.* **2016**, *55*, 3915.
(17) H. R. Hoekstra, A. Santoro, S. Siegel, *J. Inorg. Nucl. Chem.* **1961**, *18*, 166.
(18) L. E. J. Roberts, *J. Chem. Soc.* **1954**, 3332.
(19) I. F. Ferguson, J. D. M. McConnell, *Proc. R. Soc. London, Ser. A Mat.* **1957**, *241*, 67.
(20) B. T. M. Willis, *Proc. Brit. Ceram. Soc.* **1964**, *No. 1*, 9.
(21) D. Labroche, O. Dugne, C. Chatillon, *J. Nucl. Mater.* **2003**, *312*, 50.
(22) C. Guéneau, N. Dupin, B. Sundman, C. Martial, J.-C. Dumas, S. Gossé, S. Chatain, F. D. Bruycker, D. Manara, R. J. M. Konings, *J. Nucl. Mater.* **2011**, *419*, 145.
(23) B. E. Schaner, *J. Nucl. Mater.* **1960**, *2*, 110.
(24) P. E. Blackburn, J. Weissbart, E. A. Gulbranson, *J. Phys. Chem.* **1958**, *62*, 902.
(25) P. Taylor, E. A. Burgess, D. G. Owen, *J. Nucl. Mater.* **1980**, *88*, 153.
(26) L. E. Thomas, R. E. Einziger, R. E. Woodley, *J. Nucl. Mater.* **1989**, *166*, 243.
(27) R. E. Einziger, L. E. Thomas, H. C. Buchanan, R. B. Stout, *J. Nucl. Mater.* **1992**, *190*, 53.
(28) L. E. Thomas, R. E. Einziger, *Mater. Charact.* **1992**, *28*, 149.

(29) P. Taylor, *J. Nucl. Mater.* **2005**, *344*, 206.
(30) D. E. Y. Walker, *J. Appl. Chem.* **1965**, *15*, 128.
(31) A. Poulesquen, L. Desgranges, C. Ferry, *J. Nucl. Mater.* **2007**, *362*, 402.
(32) T. Wadsten, *J. Nucl. Mater.* **1977**, *64*, 315.
(33) J. S. Anderson, L. E. J. Roberts, E. A. Harper, *J. Chem. Soc.* **1955**, 3946.
(34) H. H. Uhlig, *Acta Metall.* **1956**, *4*, 541.
(35) S. K. Roy, S. C. Sircar, *Oxid. Met.* **1981**, *15*, 9.
(36) M. Martin, W. Mader, E. Fromm, *Thin Solid Films* **1994**, *250*, 61.
(37) N. F. Mott, *Trans. Faraday Soc.* **1947**, *43*, 429.
(38) N. Cabrera, N. F. Mott, *Rep. Prog. Phys.* **1949**, *12*, 163.
(39) U. R. Evans, *The Corrosion and Oxidation of Metals: Scientific Principles and Practical Applications*, St. Martin's Press, New York, **1960**.
(40) A. T. Fromhold, JR., *Theory of metal oxidation, Vol. 1 - Fundamentals*, North-Holland Publishing Company, Amsterdam, **1976**.
(41) A. G. Ritchie, *J. Less Common Met.* **1984**, *98*, 193.
(42) P. E. Gharagozloo, M. P. Kanouff, *J. Am. Ceram. Soc.* **2013**, *96*, 2943.
(43) F. J. Graham, H. C. Brookes, J. W. Bayles, *J. Appl. Electrochem.* **1990**, *20*, 45.
(44) A. K. Burnham, G. T. Jameson, *J. Vac. Sci. Technol., A* **1987**, *5*, 1713.
(45) D. Starodub, T. Gustafsson, E. Garfunkel, *Surf. Sci.* **2004**, *552*, 199.
(46) R. Ghez, *J. Chem. Phys.* **1973**, *58*, 1838.
(47) V. P. Zhdanov, B. Kasemo, *Chem. Phys. Lett.* **2008**, *452*, 285.
(48) R. J. M. Konings, O. Beneš, A. Kovács, D. Manara, D. Sedmidubský, L. Gorokhov, V. S. Iorish, V. Yungman, E. Shenyavskaya, E. Osina, *J. Phys. Chem. Ref. Data* **2014**, *43*, 013101.
(49) A. Khawam, D. R. Flanagan, *J. Phys. Chem. B* **2006**, *110*, 17315.
(50) W. Jander, *Z. Anorg. Allg. Chem.* **1927**, *163*, 1.

Chapter 6.

Conclusions and outlook

Conclusions

The objective of this PhD thesis was to obtain a better understanding of the oxidation mechanisms and kinetics in fine UO_2 powders, at low temperatures (< 250 °C). The reactivity of such powders towards oxygen is considered an important issue in the UO_2 nuclear fuel production process. Uncontrolled oxidation is undesirable and may even lead to a pyrophoric reaction, which is why passivation treatments are required. Also, the large volume increase associated with the crystallographic transformation into the higher oxide U_3O_8 may pose a threat on the integrity of storage containers. For these reasons the research focused on the thermochemical behavior of the oxidation reaction and on the solid-state modifications which are induced. Conditions which relate with the production of UO_2 nuclear fuels and with storage of UO_2 powders and pellets were considered.

The uranium-oxygen system has a complex crystal chemistry. Numerous mixed-valence uranium oxides exist, and many of these display a certain degree of non-stoichiometry. The reference state which forms the basis throughout the PhD research is UO_2. Therefore, the pure and stoichiometric UO_2 crystal structure ($Fm\bar{3}m$) was first investigated. UO_2 sintered pellets were prepared via powder metallurgical route, similar as is applied in industry. Special attention was paid to obtaining exact stoichiometry in the samples, which was also verified via *in-situ* thermogravimetric analysis (TGA) after correction for the presence of impurity elements.

Accurate lattice parameter measurements were performed via X-ray diffraction (XRD) and a consistent set of values was obtained. An evaluation of literature data from the past 50 years illustrated the discrepancy in reported lattice parameter values for UO_2. This difference has been largely attributed to the difficulty in obtaining exact stoichiometry, and to a smaller extent to the use of outdated X-ray wavelength values. The "generally accepted" value of a = 547.04(8) pm at room temperature, which dates back to the 1950s, was re-evaluated and a slightly higher and more precise value of a = 547.127(8) pm was proposed.

An important intermediate uranium oxide which is formed during low-temperature oxidation is U_3O_7. It is considered to be the main precursor for U_3O_8 formation. Despite being investigated already for several decades, its crystal structure remains subject to debate. Conditions for formation of U_3O_7 from UO_2 via oxidation were first investigated by performing *in-situ* simultaneous thermal analysis (TGA and differential scanning calorimetry, DSC). Polycrystalline powders were subsequently prepared and analyzed via X-ray and selected area electron diffraction techniques.

The crystal structure of U_3O_7 was found to show a commensurate, long-range ordering based on a tetragonal parent structure. By definition of three linearly independent wave vectors the corresponding real space periodicity could be consistently described in an expanded unit cell ($\mathbf{A} = \mathbf{a_p} - 2\mathbf{b_p}$, $\mathbf{B} = 2\mathbf{a_p} + \mathbf{b_p}$, $\mathbf{C} = 3\mathbf{c_p}$) with a unit cell volume fifteen times that of the parent cell (basis vectors $\mathbf{a_p}$, $\mathbf{b_p}$, $\mathbf{c_p}$). The long-range ordered crystal structure is interpreted as a fluorite-derived structure in which the cations keep the same stacking as in UO_2, and where the anions follow an ordered arrangement of eleven fluorite-like subcells, and four subcells in which the anions assume a distorted cuboctahedral arrangement. The cuboctahedra are arranged in layers perpendicular to the **C**-axis with an inter-layer distance of $1.5 \times \mathbf{c_p}$.

Fine UO_2 powders behave differently during oxidation, as compared to coarse powders or pellet fragments. Quite notably, formation of the higher oxides U_4O_9 and U_3O_7 is less distinguishable, and also the rate of U_3O_8 formation is lower. For this reason a detailed structural analysis of fine UO_2 powders which were subjected to *in-situ* oxidation experiments at low temperatures (< 250 °C) was performed. X-ray diffraction and high-resolution transmission electron microscopy (HR-TEM) techniques were applied.

By employing the Rietveld method the sequential formation of U_4O_9 and U_3O_{7-z} during the course of oxidation could be more clearly identified from XRD data. Remarkably, no U_3O_8 was formed, despite the high degree of oxidation reached in some of the samples (O/U up to 2.45). A discrepancy was found between mass increase measured via TGA and mass increase quantified from the fractions of the crystalline phases identified via XRD. The difference was attributed to the presence of an amorphous phase, which was later observed by HR-TEM. The TEM study provided more insight in the solid-state phenomena at the level of the individual grains. It was found that the U_4O_9 phase develops a long-range ordered structure with higher degree of oxidation in the grains, and this was first distinguished in nanodomains near the surface of the grains. A similar mechanism was understood to happen also in the U_3O_{7-z} phase.

Only limited experimental data are available concerning the low-temperature oxidation processes in fine UO_2 powders. For this reason kinetic and thermochemical data of *in-situ* oxidation experiments (TGA and DSC) on such powders were investigated. The effects of oxygen concentration in the gas supply (0.1 vol.%, 0.4 vol.%, 16.8 vol.% O_2) and oxidation temperature (from 40 °C to 250 °C) were considered.

The low-temperature oxidation process could be divided into three stages. The earliest stage was characterized as a rapid, exothermic chemisorption reaction, corresponding

with formation of the amorphous phase on the surface the grains. Both the occurrence of nucleation sites, and formation of a very thin surface oxide layer which could not be distinguished in the preceding HR-TEM study, were considered. An initial linear reaction rate was observed, displaying Arrhenius behavior. The corresponding activation energy was found to be very low (13.3 ± 0.5 kJ mol^{-1}). Nucleation sites formed during the first stage likely induced the development of higher oxides in domains upon further oxidation.

After the initial reaction, oxidation proceeded in a different regime showing either inverse logarithmic kinetics ($40\ °C \leq T_{ox} \leq 100\ °C$) or parabolic kinetics (Jander rate law) at 130 °C. The respective mechanisms in both stages assume the migration of oxide ions, either assisted by an electric field over the oxide layer (Mott-Cabrera theory, stage II), or as a thermally activated diffusion process (stage III), and thus suggested a process of surface oxidation instead of a process of nucleation-and-growth. At an oxidation temperature of 40 °C the oxidation reaction no longer proceeded at a detectable rate after reaching an equivalent U_4O_9 layer thickness of 2 nm. The inhibition of the reaction shows that uncontrolled oxidation in fine UO_2 powders may be avoided, provided that the temperature does not exceed 40 °C.

Outlook

The description of the U_3O_7 crystal structure was based on long-range ordering of distorted cuboctahedral oxygen clusters. With the size of the clusters kept as a constant, the variation of the distortion from the ideal cuboctahedral geometry was assessed by performing *Bond Valence Sum* (BVS) calculations. The distortion which resulted in a nominal valence state of uranium of 4.67 gave somewhat deviating results for three out of eight cation sites, which indicates that further refinement of the crystallographic model might be required. For this reason quantitative diffracted intensity data must be acquired.

It was shown that the use of single crystal electron diffraction techniques played a crucial role in the assessment of the U_3O_7 structure, however, its limitation was that the diffracted intensities could not be quantitatively interpreted. For this reason it is suggested to make use of precession electron diffraction in further studies. A range of other techniques is also available to complement the structural research in U_3O_7. To obtain a better comprehension of the local environment and valence state of uranium in the crystal structure X-ray absorption spectroscopy (XAS) and valence band resonant inelastic X-ray scattering (RIXS) can be considered.

Despite a high degree of oxidation in many of the oxidized, fine UO_2 powders, no U_3O_8 was formed. Instead, an amorphous phase was observed to nucleate from the surface of the grains. It was suggested that this phase might be amorphous UO_3, but this could not be indefinitely proven. Surface-sensitive spectroscopical techniques such as X-ray photoelectron spectroscopy (XPS) or electron energy loss spectroscopy (EELS) may provide more insight in the nature of the amorphous phase. Furthermore, by using scanning TEM with a subnanometer-scale spatial resolution and by performing EELS analysis a direct observation of differences in oxygen content throughout the grains may be obtained. Lastly, it would be interesting to perform continued oxidation experiments either at higher temperatures or for extended times to investigate whether and when U_3O_8 starts being formed in these fine UO_2 powders.

The research performed in the current PhD thesis focused on the effects of dry, oxidizing conditions. However, another important aspect is the possibility for reactions in moist conditions. Specifically, the combined influence of oxygen and water vapor are of interest. Such interactions have to be considered also within the context of nuclear fuel production and storage.

It is recognized that although the U-O system has been studied extensively already for several decades, novel insights in the oxidation process are still being obtained. The complicated oxidation chemistry relates to the various possible valence states which uranium ions can exhibit. It may be expected that a similar complexity exists in other actinide-oxide systems, particularly Pu-O and Am-O. However, much less experimental data is available due to the hazards involved in working with these elements (mainly their high radiotoxicity). Nevertheless, more detailed knowledge on the oxidation behavior of these systems is required within the context of mixed-oxide (MOX) nuclear fuel or transmutation target production. The methodology and the interpretation of experimental results in this PhD thesis can be directly transferred to such research.

Scientific output

Journal publications

"Low-temperature oxidation of fine UO_2 powders: a process of nanosized domain development"
G. Leinders, J. Pakarinen, R. Delville, T. Cardinaels, K. Binnemans, M. Verwerft, *Inorganic Chemistry* **2016**, *55*, 3915-3927.

"Accurate lattice parameter measurements of stoichiometric uranium dioxide"
G. Leinders, T. Cardinaels, K. Binnemans, M. Verwerft, *Journal of Nuclear Materials* **2015**, *459*, 135-142.

Manuscripts submitted or in preparation

"Assessment of the U_3O_7 crystal structure by X-ray and electron diffraction"
G. Leinders, R. Delville, J. Pakarinen, T. Cardinaels, K. Binnemans, M. Verwerft, submitted to *Inorganic Chemistry*.

"Low-temperature oxidation of fine UO_2 powders: thermochemistry and kinetics"
G. Leinders, T. Cardinaels, K. Binnemans, M. Verwerft, manuscript in preparation.

Participation to conferences

"Low-temperature oxidation of uranium dioxide"
G. Leinders, J. Pakarinen, R. Delville, T. Cardinaels, K. Binnemans, M. Verwerft
Poster and flash presentation at the ICfE 2015 Conference, Oxford (UK), September 6-9, 2015

"Production and verification of stoichiometric uranium dioxide"
G. Leinders, T. Cardinaels, K. Binnemans, M. Verwerft
Oral presentation at the ENYG forum 2015, Paris (FR), June 22-26, 2015

"The influence of particle characteristics on the passivation of UO_2 powders"
G. Leinders, T. Cardinaels, K. Binnemans, M. Verwerft
Oral presentation at the ChemCYS Chemistry Conference for Young Scientists, Blankenberge (BE), February 27-28, 2014

"UO_2 and ZrO_2 solid solutions"
G. Leinders, T. Cardinaels, K. Binnemans, M. Verwerft
Poster presentation at the ThUL School in Actinide Chemistry, Karlsruhe (DE), January 13-18, 2013

Appendix I.

Safety aspects

I.I Guidelines and legislation

The experimental work performed during this PhD research was entirely conducted in the laboratories of the Belgian Nuclear Research Center (SCK•CEN). In addition to the normal aspects of industrial safety and common lab practice, strict guidelines which permit handling radioactive substances were in effect. For this reason various training sessions had to be followed by the PhD candidate. Those specifically related to the radioactive nature of the used materials were: (1) a five-day course on radiation protection, (2) a training session on working with open radioactive sources, (3) a training session on working in fume hoods and glove boxes. All these aspects were combined in an extended risk analysis which had to be performed before starting new sets of experiments.

All work related to the manipulation of radioactive substances conforms with the "as low as reasonably achievable" (ALARA) principle. This implies that before starting any experiment an evaluation is performed of how the manipulation is most efficiently done, thus minimizing the exposure to personnel. The ALARA philosophy focusses on four main features: (1) the use of radiation shielding, (2) minimizing the time spent in the vicinity of the radioactive source, (3) keeping as much distance as possible from a radioactive source, without jeopardizing the manipulations, (4) the use of a radioactive source with the lowest possible activity.

The aforementioned guidelines are all related to safety-aspects and are setup to protect workers from exposure to dangerous non-radioactive and radioactive chemicals. In addition, the research had to comply with federal and European legislation concerning working with fissile and fertile materials. A detailed accounting of all fissile and fertile materials has to be kept, uniquely identifying each separate batch of material and registering the associated weights. Importantly, the location of each batch has to be exactly known. This implies that each transfer of fissile or fertile material has to be registered through a formal system. These rules additionally ensure that criticality cannot be reached, by setting limits to the maximum amount of fissile material allowed in a working unit (fume hood, glove box, hot cell) or storage unit (storage cabinets).

I.II Risk analysis approach

In the extended risk analysis the following aspects were evaluated:

1. Identification of the user
2. Identification of the experiment
   2.1. Description of the chemicals used or formed
   2.2. Location of the experiment
   2.3. Persons involved in the experiment
3. Description of the experiment and risk assessment
   3.1. Description of handling and techniques
   3.2. More detailed information about the experiment
   3.3. Hazards associated with the chemicals
   3.4. Other risks associated with the experiment
4. Assessment of the radioactive properties
   4.1. Identification of the responsible security personnel
   4.2. Description of the radioactive chemicals used or formed
   4.3. Practical information related to handling of the radioactive substances
   4.4. Estimation of the received dose
5. Overview of required precautionary measures
6. Identification of chemical waste
7. Identification of radioactive waste
8. Overview of the acceptance criteria and approval by hierarchy

I.II.I Dry powder processing: sample handling and preparation

Sample handling actions included: separating individual sample batches (~3 g) from a stock powder batch (~1-10 kg), weighing and transferring into suitable containers. Specimen preparation for analytical techniques included: back-loading and top-loading powder specimens for X-ray diffraction, dispersing powders on a sample stub for scanning electron microscopy, dispersing powder in a holey carbon grid for transmission electron microscopy, loading of powder in sealed glass vials for gas adsorption analysis, loading of powder in the *in-situ* thermal analysis device.

The associated risks are related to the nature of working with powders and include the possibility for inhalation of airborne powder particles and the possibility for surface contamination by settling of airborne powder particles.

The following precautionary measures were taken:

- All sample handling was carried out in fume hood environment and a visual check of the level of underpressure was carried out before the start of any work.
- The working surface of the fume hood was covered with paper towels. Additionally, all powder handling was performed in an additional tray in order to contain possible spillage. After the experiment, or additionally after any delicate manipulation the paper towels were carefully removed and replaced.
- After the experiment wipe tests of the surface were performed to check for any level of contamination.
- For transfer of specimens to analysis devices: each procedure was first evaluated by the radiation control officer. A wipe test was always performed to check for any level of surface contamination on the specimen holder. All transfers were done in closed containers.

I.II.II Dry powder processing: heat treatments

Heat treatments included: oxidation in air or under reduced oxygen levels at temperatures ranging between room temperature and 1000 °C, reduction in H_2:Ar (5:95 vol.%) or under reduced H_2 levels at temperatures ranging between room temperature and 1800 °C. Medium-scale experiments (~3-50 g) were performed in ceramic furnaces, small-scale (~20-2000 mg) *in-situ* experiments were performed in a simultaneous thermal analyzer.

The associated risks are related to working with thermal devices and specific gasses, and include risks for burning, fire and explosion. An additional risk is the possible pyrophoric oxidation reaction in fine UO_2 powders.

The following precautionary measures were taken:

- All used furnaces were equipped with an overtemperature control, which shuts off the power supply in case of uncontrolled heating.
- All used furnaces could be completely sealed from the laboratory environment. Seals (e.g. O-rings) were actively cooled to maintain their integrity.
- The operation of the furnace at high temperature (> 1000 °C) was checked with a thermal camera to evaluate the positioning of the furnace and the effect of heating on surrounding materials.
- The supply of gas (e.g. pressurized bottles) was foreseen from spacious corridors, calculated to allow unexpected release of their contents without risk for self-ignition.
- Freshly-reduced UO_2 powders were subjected to a passivation treatment before removal from the furnace. Fine and very fine UO_2 powders were only subject to heat treatment in separated small batches.

I.II.III Wet-chemical processing: dissolution and precipitation

Wet-chemical processing included: dissolution of uranium oxide powder in diluted nitric acid (4−8 M), titration of uranyl nitrate solutions with aqueous ammonia solutions (4 M), vacuum filtration of the formed precipitates.

The associated risks are related to working with acid and alkaline solutions and the formation of hazardous byproducts: NO and NO_2 gas during the dissolution of uranium oxide, ammonium nitrate (NH_4NO_3) during titration of a uranyl nitrate solution with ammonia.

The following precautionary measures were taken:

- All sample handling was carried out in fume hood environment and a visual check of the level of underpressure was carried out before the start of any work.
- Dilutions of the used chemicals from stock solutions were prepared according to common lab practice and adequately labeled.
- Titration with ammonia was performed dropwise and with intervals to avoid excessive heating due to the exothermic reaction.
- The exhaust of the vacuum pump was fed back into the fume hood to avoid any airborne contamination in the laboratory.

- The filtrate was transferred to a large dish and left to evaporate in the fume hood without applying external heating. The remainder was then soaked up with paper towels, which were subsequently collected in a separate waste bag.

Appendix II.

Supporting information for Chapter 3

General Rietveld refinement variables consisted of a Chebyshev polynomial (cubic with zero order term) and specimen height displacement (misalignment to the tangent of the goniometer circle). Phase-specific variables included the scale factor, lattice parameters and Cagliotti (*UVW*) and line profile (pseudo-Voigt) parameters. Additionally, the isotropic temperature factor for U sites was refined. Data quality was assessed through the expected (R_{exp}) *R*-factor, see Eq. (AII.1). The agreement between experimental data and fit was evaluated via the weighed-profile (R_{wp}) value, see Eq. (AII.2). The applicability of the used structural model was assessed by the intensity-based or Bragg (R_{Br}) *R*-factor (Eq. (AII.3)).

$$R_{\mathrm{exp}} = \sqrt{\frac{\#obs. - \#var.}{\sum w_i \cdot y_i(obs)^2}}, \qquad \textbf{(AII.1)}$$

$$R_{\mathrm{wp}} = \sqrt{\frac{\sum w_i \cdot (y_i(obs) - y_i(calc))^2}{\sum w_i \cdot y_i(obs)^2}}, \qquad \textbf{(AII.2)}$$

$$R_{\mathrm{Br}} = \frac{\sum |I_{hkl}(obs) - I_{hkl}(calc)|}{\sum I_{hkl}(obs)}. \qquad \textbf{(AII.3)}$$

where y_i is the intensity of the individual profile points in the scan, w_i the weight attributed to each observation *i* and I_{hkl} the total intensity of a group of reflections (*hkl*). I_{hkl}(calc) is calculated from the structure factor equation and includes allowances for the experiment and a scale factor.

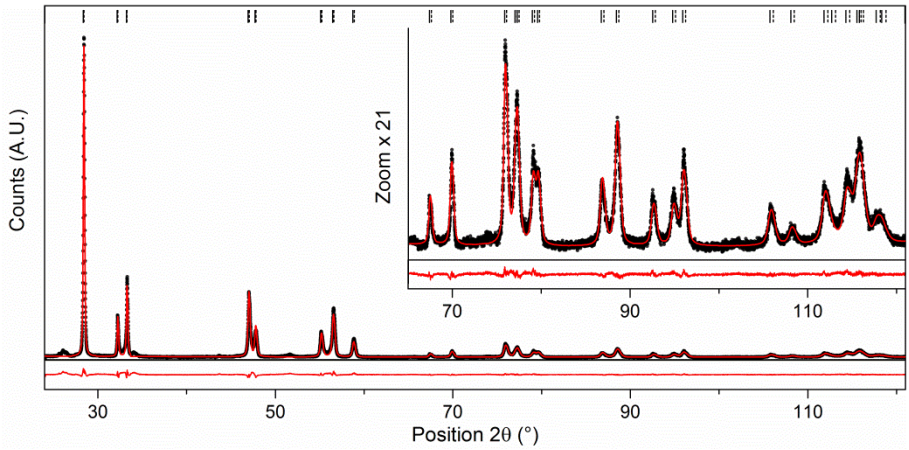

Figure AII.1. Experimental XRD data (dots) and fitted profile (red line) for the U_3O_7 powder prepared by oxidation in the TGA set-up (R_{wp} = 0.099). The difference profile is shown at the bottom. Peak maxima for Cu $K\alpha_1$ and $K\alpha_2$ are indicated at the top by solid and dashed lines, respectively. The inset shows a zoom-in of the higher order reflections. Contributions of U_3O_8 have not been taken into account in this fit.

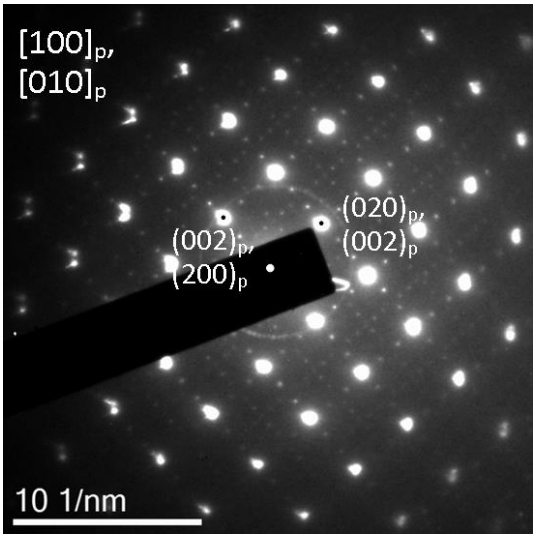

Figure AII.2. SAED pattern of twinned domains oriented along $[100]_p$ and $[010]_p$. Satellite reflections with a ⅔ periodicity along the **c***-axes are clearly observed. Additional reflections which can be distinguished at the equivalent positions $(0k\lambda)_p$: $\lambda = l \pm ⅓$ are the result of dynamical scattering effects, e.g. $(01⅔)_p = (10\bar{⅓})_p + (\bar{1}11)_p$.

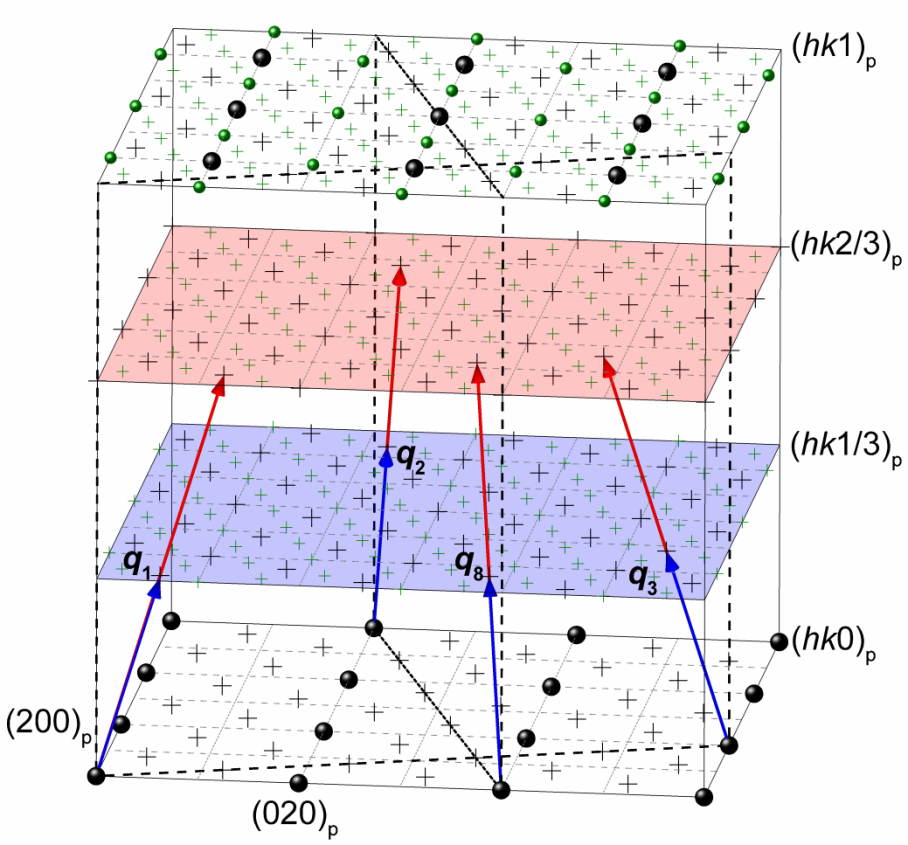

Figure AII.3. Reciprocal space map of the modulated U_3O_7 crystal structure. Parent structure and satellite reciprocal lattice points (restricted to first and second order) are represented by dots and crosses, respectively. Black color indicates fluorite type points and satellites constructed from these points, green color indicates non-fluorite type points and their derived satellites. First order satellites along wave vectors $\boldsymbol{q_1}$, $\boldsymbol{q_2}$, $\boldsymbol{q_3}$ and $\boldsymbol{q_4}$ (see Table 5 in the main text) are indicated by blue arrows, dashed lines mark their respective basal planes (i.e. $[3\bar{1}0]_p$ and $[130]_p$). Second order satellites are indicated by red arrows.

Appendix III.

Supporting information for Chapter 4

General Rietveld refinement variables consisted of a Chebyshev polynomial (cubic with zero order term) and specimen height displacement (misalignment to the tangent of the goniometer circle). Phase-specific variables included the scale factor, Cagliotti (*UVW*) and line profile (pseudo-Voigt) parameters. Where mentioned explicitly, lattice parameters were refined. Additionally, for the reference samples isotropic temperature factors for U sites were refined. Data quality was assessed through the expected (R_{exp}) *R*-factor, see Eq. (AIII.1). The agreement between experimental data and fit was evaluated via the weighed-profile (R_{wp}) and goodness-of-fit (χ) values, see Eq. (AIII.2) and (AIII.3). The applicability of the used models was assessed by the intensity-based or Bragg (R_{Br}) *R*-factor (Eq. (AIII.4)).

$$R_{\mathrm{exp}} = \sqrt{\frac{\#obs. - \#var.}{\sum w_i \cdot y_i(obs)^2}}, \qquad \textbf{(AIII.1)}$$

$$R_{\mathrm{wp}} = \sqrt{\frac{\sum w_i \cdot (y_i(obs) - y_i(calc))^2}{\sum w_i \cdot y_i(obs)^2}}, \qquad \textbf{(AIII.2)}$$

$$\chi = \frac{R_{\mathrm{wp}}}{R_{\mathrm{exp}}}, \qquad \textbf{(AIII.3)}$$

$$R_{\mathrm{Br}} = \frac{\sum |I_{hkl}(obs) - I_{hkl}(calc)|}{\sum I_{hkl}(obs)} \qquad \textbf{(AIII.4)}$$

With y_i the intensity of the individual profile points in the scan, w_i the weight attributed to each observation *i* and I_{hkl} the total intensity of a group of reflections (*hkl*). I_{hkl}(calc) is calculated from the structure factor equation and includes allowances for the experiment and a scale factor.

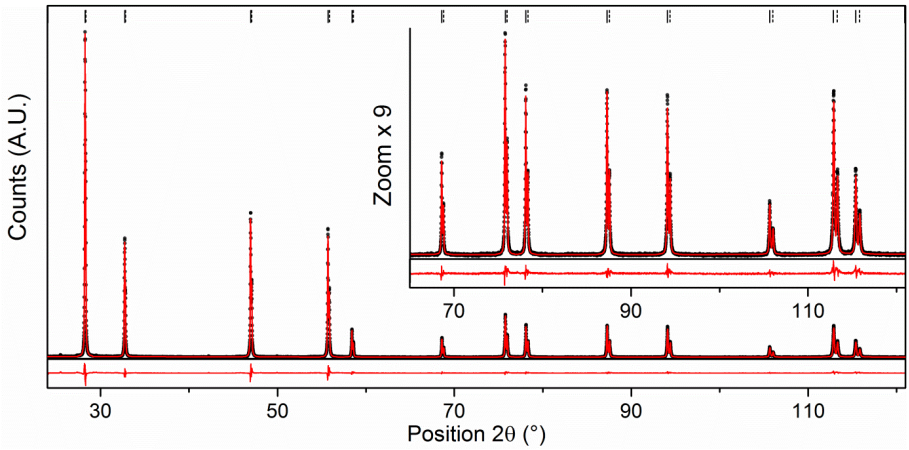

Figure AIII.1. Experimental XRD data (dots) and fitted profile (red line) for the $UO_{2.03}$ reference powder ($\chi = 1.667$). The difference profile is shown at the bottom. Peak maxima for $CuK\alpha_1$ and $CuK\alpha_2$ are indicated at the top by solid and dashed lines, respectively. Insert shows a zoom-in of the higher order reflections.

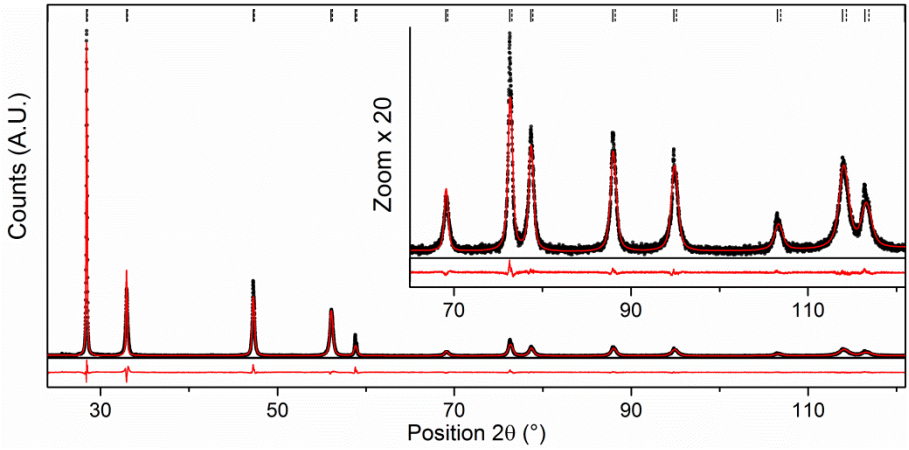

Figure AIII.2. Experimental XRD data (dots) and fitted profile (red line) for the U_4O_9 reference powder ($\chi = 1.681$). The difference profile is shown at the bottom. Peak maxima for $CuK\alpha_1$ and $CuK\alpha_2$ are indicated at the top by solid and dashed lines, respectively. Insert shows a zoom-in of the higher order reflections.

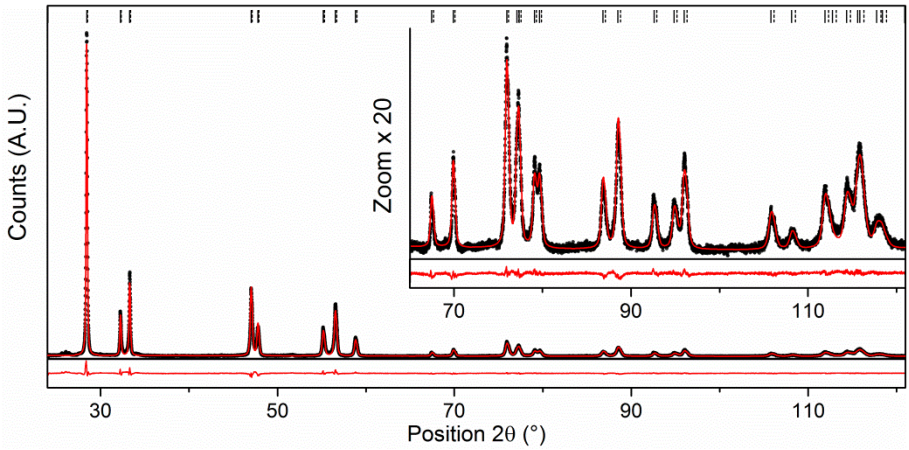

Figure AIII.3. Experimental XRD data (dots) and fitted profile (red line) for the U_3O_7 reference powder (χ = 1.875). The difference profile is shown at the bottom. Peak maxima for CuKα_1 and CuKα_2 are indicated at the top by solid and dashed lines, respectively. Insert shows a zoom-in of the higher order reflections.

Table AIII.1. Experimental and weighed-profile agreement indices obtained after Rietveld refinement of the XRD data, for each of the oxidized samples (L, M, H). Values listed under (I) result from the first assessment, restraining all lattice parameters. Values listed under (II) refer to the second assessment, with additional refinement of the U_3O_{7-z} lattice parameters. Values after dashed line refer to samples oxidized for an extended amount of time (25 h). Empty cells refer to non-existing data.

T_{iso} (°C)	L			M			H		
	R_{exp}	R_{wp} (I)	R_{wp} (II)	R_{exp}	R_{wp} (I)	R_{wp} (II)	R_{exp}	R_{wp} (I)	R_{wp} (II)
40	0.049	0.083	-	0.041	0.11	-	0.045	0.072	-
70	0.046	0.085	-	0.040	0.095	-	0.025	0.072	-
100	0.032	0.094	-	0.026	0.078	-	0.026	0.073	0.063
130	0.032	0.073	-	0.026	0.11	0.079	0.027	0.090	0.065
160	0.033	0.100	0.086	0.026	0.12	0.084	0.028	0.096	0.068
190	0.031	0.107	0.064	0.030	0.11	0.073	0.027	0.10	0.077
250	0.036	0.094	0.081	-	-	-	-	-	-
100	-	-	-	0.033	0.073	-	-	-	-
160	0.035	0.092	0.073	-	-	-	-	-	-

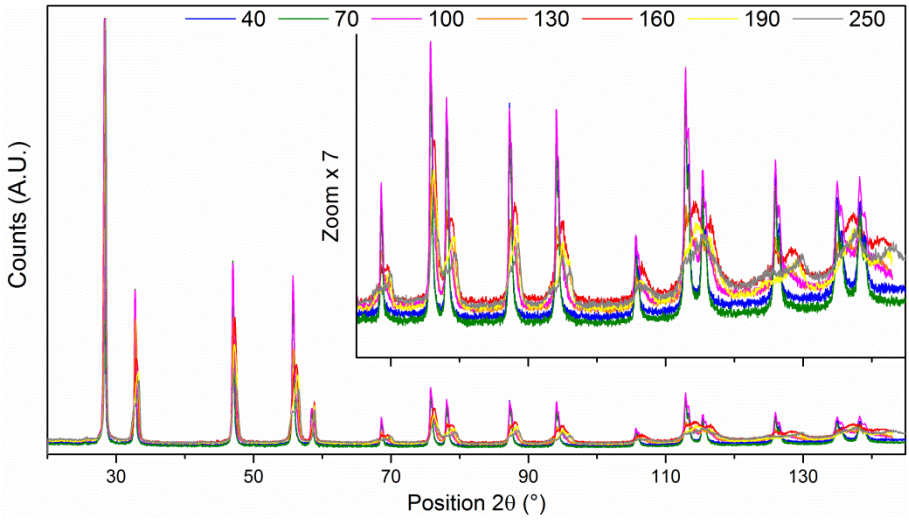

Figure AIII.4. Overlay of the XRD data measured for samples L, oxidized at various temperatures (°C). Intensity of the individual diffractograms normalized at the (111) reflection. Corrected for sample displacement. Insert shows a zoom-in of the higher order reflections.

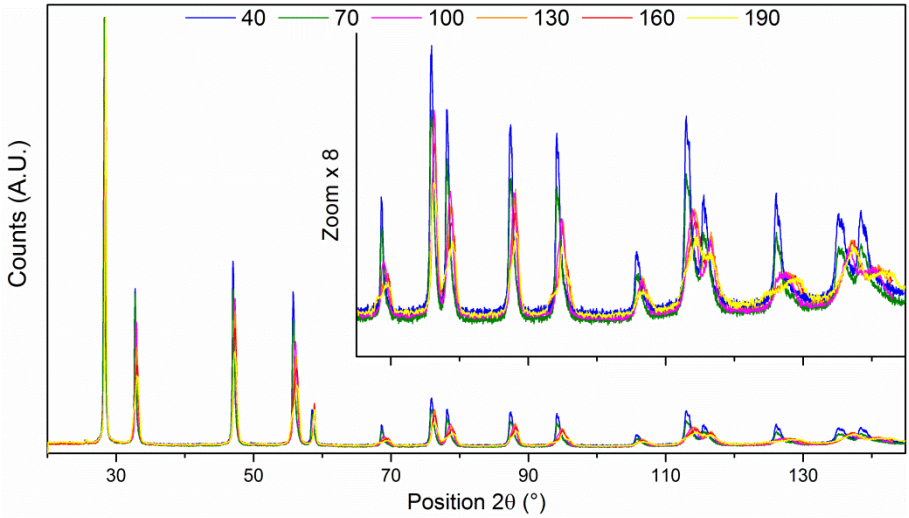

Figure AIII.5. Overlay of the XRD data measured for samples M, oxidized at various temperatures (°C). Intensity of the individual diffractograms normalized at the (111) reflection. Corrected for sample displacement. Insert shows a zoom-in of the higher order reflections.

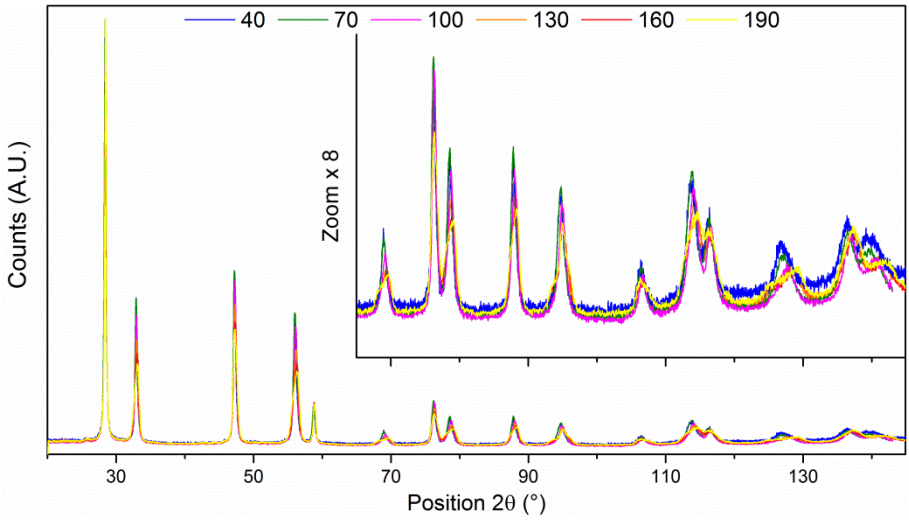

Figure AIII.6. Overlay of the XRD data measured for samples H, oxidized at various temperatures. Intensity of the individual diffractograms normalized at the (111) reflection. Corrected for sample displacement. Insert shows a zoom-in of the higher order reflections.

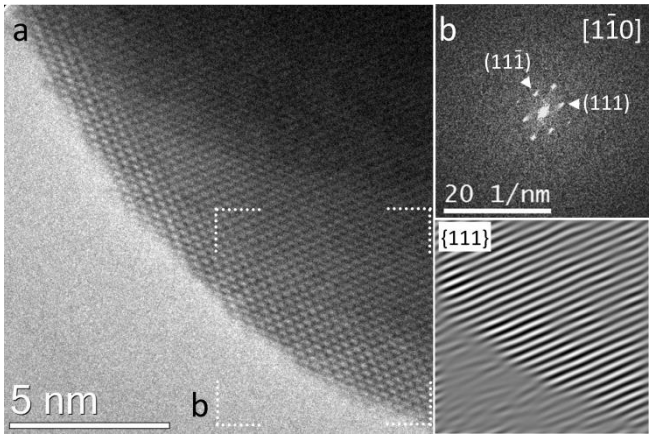

Figure AIII.7. HR-TEM image of sample L oxidized at 40 °C. (a) FFT of the indicated area and filtered image showing the corresponding {111} planes. The apparent mismatch in lattice planes to the bottom left of the image is an artefact due to filtering of part of the delimited area outside of the grain.

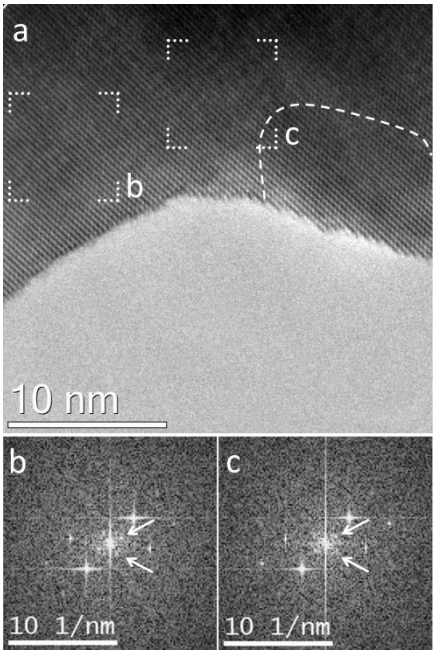

Figure AIII.8. (a) HR-TEM image of sample H oxidized at 100 °C, directly adjacent to the right-hand side of Figure 4.10 (a) in the main text. (b)-(c) FFT pattern of the small areas, showing superstructure reflections corresponding to ¼ $\{112\}_p$ close to the grain surfaces. Contrast modulation ripples can be seen throughout most of the real-space image. The region delimited by the dashed line presents a crystalline domain without superstructure.

Appendix IV.

Supporting information for Chapter 5

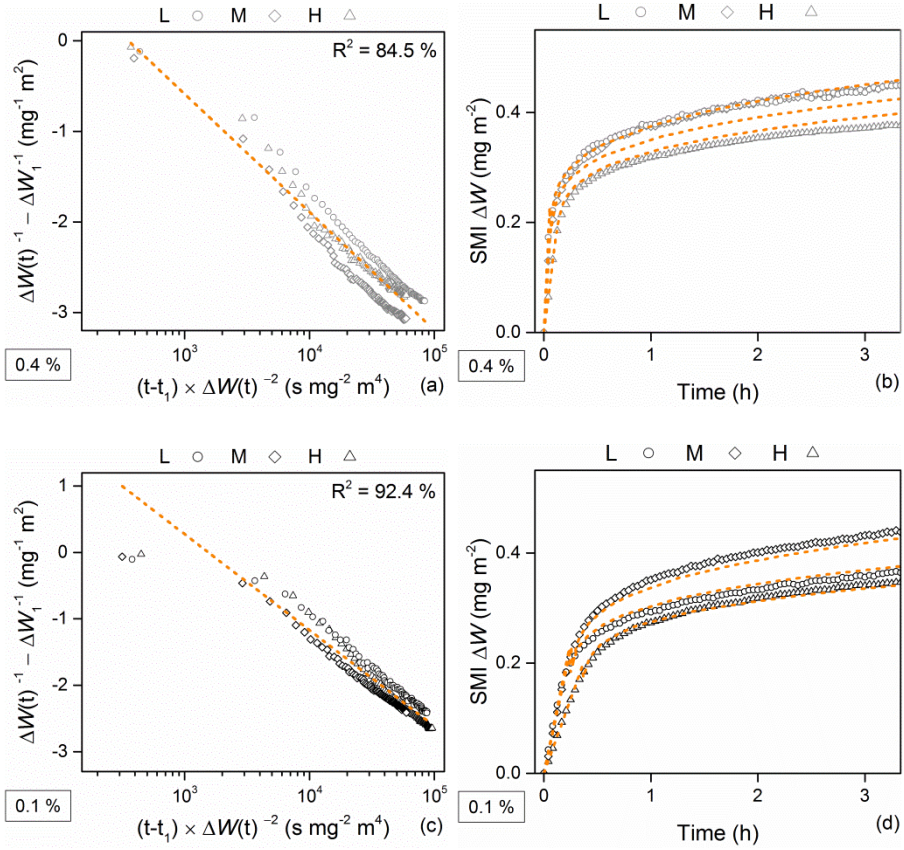

Figure AIV.1. (a, c) Logarithmic time plot corresponding to the kinetic data of all samples (L, M, H) measured under 0.4 and 0.1 vol.% O_2. The dashed line presents the fit to the data. (b, d) Mass gain curves of the oxidation experiments measured under 0.4 and 0.1 vol.% O_2. The dashed line presents the fit to the kinetic curves, from the reaction parameters in the linear and inverse logarithmic oxidation stage.

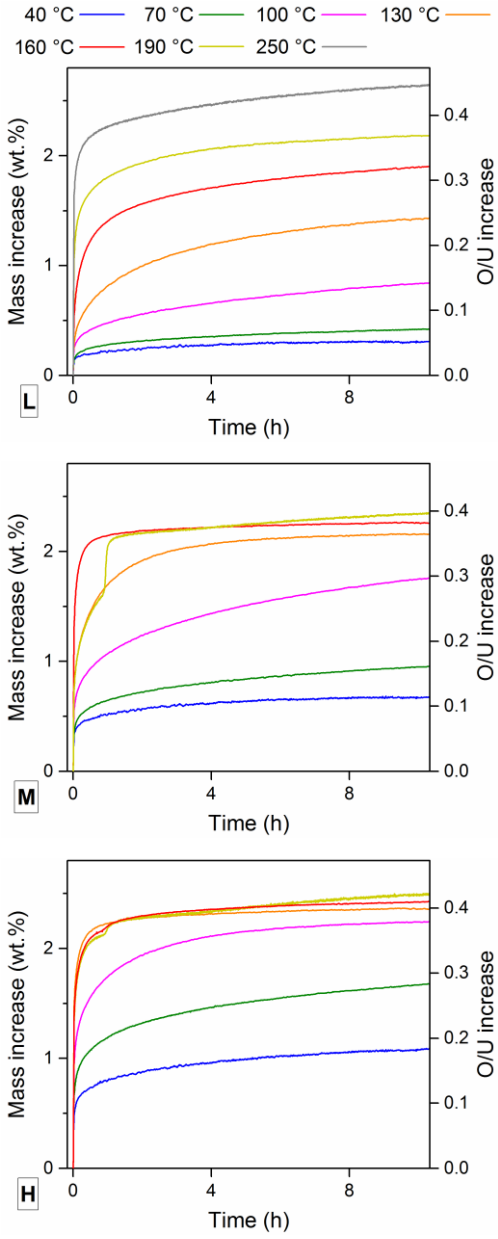

Figure AIV.2. Experimental mass increase curves showing a decreasing rate of reaction up to an average stoichiometry close to 2.40. At the highest temperatures applied, the reaction appears to accelerate again. Oxidation of precursor powders M at 190 °C and H at 160 and 190 °C was performed in two stages to avoid flash heating. During these STA runs the powders were, after their reduction, first allowed to oxidize at a temperature of 130 °C before heating to higher temperatures.